Study of the electromagnetic pumping systems of molten metals and molten salts

Cristian Robert Roman

UNIVERSITÉ DE GRENOBLE

THÈSE

Pour obtenir le grade de

DOCTEUR DE L'UNIVERSITÉ DE GRENOBLE

Préparée dans le cadre d'une cotutelle entre l'*Université de Grenoble* et *l'Université Politehnica de Bucarest*

Spécialité : **Matériaux, Mécanique, Génie civil, Electrochimie**
Arrêté ministériel : le 6 janvier 2005 -7 août 2006

Présentée par

Cristian Robert ROMAN

Thèse dirigée par **:**
Yves FAUTRELLE (Université de Grenoble, France)
Virgiliu FIRETEANU (Université Politehnica, Bucarest, Roumanie)

Préparée au sein des **Laboratoires SIMAP/EPM** et **EPM_NM**

Dans **les Écoles Doctorales IMEP2 (I**ngénierie - **M**atériaux, **M**écanique, **E**nvironnement, **E**nergétique, **P**rocédés, **P**roduction)

Titre

Study of the electromagnetic pumping systems of molten metals and molten salts

Thèse soutenue publiquement le **« 29/01/2014 »**, devant le jury compose de :
Pr. Alexandru MOREGA, président
Pr. Mouloud FELIACHI, rapporteur
Pr. Daniel ROGER, rapporteur
Pr. Jerzy BARGLIK, rapporteur
Pr. Yves FAUTRELLE, directeur de thèse côté Français
Pr. Virgiliu FIRETEANU, directeur de thèse côté Roumain

Université Joseph Fourier / Université Pierre Mendès France / Université Stendhal / Université de Savoie / Grenoble INP

Acknowledgements

The last four years have been ordained by God to meet special people, to see beautiful places and to learn a lot of new things that already are part of the package of my professional and life experience which constitutes the basis for my future. Now I look back with gratitude to those who brought their contribution so that these things could happen. Throughout these years some people, to whom I owe the completion of this project, were close to me and today I wish to thank them for their help.

First, I would like to thank my supervisors, professors Virgiliu Fireteanu and Yves Fautrelle. Under the guidance of professor Fireteanu I made the first steps towards finite element numerical modeling. He mainly supervised the parts of the thesis dealing with the electromagnetism and as a result of collaboration with him I learned a lot of things about electrical engineering, electric machinery, and especially about electromagnetic pumps. Professor Fautrelle led the research in the area of hydrodynamics and magnetohydrodynamic interaction. To him I owe my understanding of many new things in the field of magnetohydrodynamics and I am grateful for his warm welcome in Grenoble. They offered me moral support when needed and through them both I learned valuable life lessons.

As a result of the co-supervision agreement signed between Politehnica University of Bucharest and Grenoble Institute of Technology, a part of the doctoral studies were carried out at SIMAP-EPM laboratory in Grenoble. I would like to thank those who in this period manifested friendship and contributed to a favorable work climate. I would like to mention some of those who helped in solving various problems of scientific nature, Michael Dumont, Fatoumata Santara, Sébastien Letout, Annie Gagnoud and some of those who offered advices or with whom I had interesting discussions, Simona Epure, Florin Baltaretu, Lakhdar Hachani, Ahmed Nouri, Imants Kaldre, Wang Jiang and Raphaël Scapolan.

Both the first and last period of the thesis I spent in Bucharest in the EPM_NM laboratory team. I would like to thank Petrica Taras for the discussions on the thesis, but also to colleagues Felicia Gheorghe, Onur Nebi, Marcel Stamate, Alexandru Constantin whose diverse scientific activity vitalized and entertained the working environment.

I also thank the community of the *Machines, Materials and Electrical Drives Department* and especially to professor Alexandru Morega and associates Laurentiu Dumitran and Tiberiu Tudorache for their support in some scientific and administrative steps. Colleagues Bogdan Gorgan and Mirela Vihacencu brought their friendly input even from the beginning of the thesis.

I bring special thanks to the institutions that contributed to the completion of the thesis by providing financial support: project POSDRU 60203 *Dezvoltarea de cariere stiintifice competitive prin programe de burse doctorale (COMPETE)* and *Commissariat à l'énergie atomique et aux énergies alternatives (CEA Cadarache)*.

Family and close friends who have sustained and encouraged me throughout the preparation of this work had a very important role and I thank them very much.

Completion of this stage is not the end of the road. It is the beginning. In the big scheme of my life, the one that makes me value my thesis experience and to walk with confidence towards this beginning is God, to whom I bring honor.

Abstract

The actual concerns with respect to safe operation of existing nuclear plants and to designing special architectures envisaged for the fourth generation of nuclear reactors, corroborated with the increasing interest for efficiency and reliability of any equipment belonging to an energetic system, make that more and more research endeavors to be devoted to the study of various parts of these systems for a better understanding and optimization based on modern techniques of computer aided design. Among the types proposed for the fourth generation of nuclear reactors belong those that have as cooling agent molten salts, respectively liquid sodium. Many reactors of previous generations use mechanical pumps of special design for driving the coolants. Molten salts and liquid sodium, thanks to their physical properties, have the potential to be driven using electromagnetic pumps. Although the technology of electromagnetic pumping of electroconductive fluids was developed since the first half of the last century, currently it undergoes a revival due to the reconsideration of its multiple technological and security advantages.

This work is both an intimate study of the phenomena that occur as a result of the electroconductive fluids flow in the electromagnetic field of an electromagnetic pump – magnetohydrodynamic interaction - and a report on the capabilities and advantages of modern computational tools to facilitate design and optimization of electromagnetic pumps.

To achieve the principal goal of deeper understanding of the interdependent phenomena specific to electromagnetic pumps operation, two auxiliary objectives were considered. The first is related to the full exploitation of electromagnetic finite element models in order to retrieve as much information as possible about electromagnetic pumps behavior in a simplifying hypothesis that does not take into account the fluid dynamics. The second auxiliary objective is to build numerical models that couple the electromagnetism and the fluid dynamics, namely the two interdependent physics that govern the magnetohydrodynamic flow through channels of electromagnetic pumps.

In the section dealing with the study of electromagnetic pumping of molten salts, the thesis highlights specific problems related the generation of electromagnetic forces in fluids with low electrical conductivity and provides results with respect to applications where electromagnetic pumping of molten salts can be effective. With the electromagnetic numerical models were obtained important data about the influence of the number of electromagnetic poles and supply frequency on the Pressure – Velocity characteristic of annular linear induction pumps. Were analyzed the shielding effect generated by the metallic walls - with negative repercussions on pumps performances, braking effects exerted at pump inlet and pump outlet and the connection between the overload capacity and Pressure – Velocity characteristic of induction pumps. A special portion was devoted to the analysis of the time and space dependence of the electromagnetic force and to the study of the non-uniformities of electromagnetic quantities in azimuth direction of annular linear induction pumps.

In the chapter devoted to the magnetohydrodynamic interaction through coupled models, the thesis proposes two models that couple the electromagnetism and the fluid flow, one realized using multiphysic software and the second by coupling two different softwares. There are presented the advantages of the coupled models with respect to the results accuracy in comparison with electromagnetic models. It is presented the evolution of velocity, force and current densities profiles under the influence of the electromagnetic field and of different sodium mean velocities. It is shown that a good approximation of the electromagnetic pump efficiency requires the use of coupled models that take into account the hydrodynamic losses and the effects of the turbulent.

The contributions of the thesis are completed with significant observations related to the study methods and software tools used along the study process.

Keywords: magnetohydrodynamics, electromagnetic pumps, sodium, molten salts, ends effects, Hartmann effects, coupled electromagnetic – fluid dynamics finite element models

Résumé

Les préoccupations actuelles concernant l'exploitation sécuritaire des centrales nucléaires existantes et la conception d'architectures spéciales envisagées pour la quatrième génération de réacteurs nucléaires se combinent avec l'intérêt plus prononcé pour l'efficacité et la fiabilité de l'équipement d'un système énergétique. Cela fait que dans un souci de meilleure compréhension et optimisation basée sur des moyens modernes de conception assistée par l'ordinateur, l'étude de différentes parties de ces systèmes fait de plus en plus l'objet de recherches approfondies. Parmi les types proposés pour la quatrième génération de réacteurs nucléaires font partie ceux ayant comme agent de refroidissement les sels fondus, respectivement le sodium fondu. De nombreux réacteurs nucléaires de la génération précédente utilisent des pompes mécaniques de construction spéciale pour l'entraînement des liquides de refroidissement. En raison de leurs propriétés physiques, les sels fondus et le sodium liquide ont le potentiel d'être déplacés par les pompes électromagnétiques. Bien que la technologie de pompage électromagnétique des fluides conducteurs d'électricité ait été développée à partir de la première partie du dernier siècle, elle connaît maintenant un renouveau grâce à la reconsidération de ses nombreux avantages technologiques et de la sécurité d'exploitation.

Cet ouvrage est à la fois une étude approfondie des phénomènes qui se produisent en raison de l'écoulement du fluide dans le champ électromagnétique d'une pompe électromagnétique - interaction magnétohydrodynamique - et un rapport sur les capacités et les avantages des outils informatiques modernes pour faciliter la conception et l'optimisation des pompes électromagnétiques.

Afin d'atteindre l'objectif principal de la thèse, notamment une meilleure compréhension des phénomènes interdépendants spécifique à l'opération des pompes électromagnétiques, deux objectifs secondaires ont été considérés. Le premier objectif concerne la pleine exploitation des modèles électromagnétiques numériques en éléments finis afin d'obtenir autant d'informations que possible sur le comportement des pompes électromagnétiques, dans l'hypothèse où on ne tient pas compte de l'écoulement des fluides. Le deuxième objectif était la construction des modèles numériques qui réunissent l'électromagnétisme et la dynamique des fluides, respectivement des modèles numériques qui regroupent les deux phénomènes caractérisant l'écoulement magnétohydrodynamique dans les canaux des pompes électromagnétiques.

Dans l'étude dédiée au pompage électromagnétique de sels fondus, la thèse met en évidence des problèmes spécifiques liés à la génération de forces électromagnétiques dans les fluides faibles conducteurs d'électricité et fournit des résultats sur les applications où le pompage électromagnétique de sels fondus peut être efficace. À l'aide des modèles électromagnétiques nous avons obtenu des informations importantes sur l'influence du nombre de pôles électromagnétiques et de la fréquence d'alimentation sur la caractéristique Pression - Vitesse des pompes annulaires à induction. Ils ont été analysés le phénomène de blindage créé par les parois métalliques - avec des répercussions négatives sur les performances de la pompe, les effets de freinage exercés à l'entrée et à la sortie du canal de la pompe et la relation entre la capacité de surcharge hydrodynamique et la caractéristique Pression - Vitesse des pompes à induction. Une section spéciale a été consacrée à l'analyse de la dépendance de la force électromagnétique du temps et de l'espace et à l'étude de non-uniformitées des quantités de nature électromagnétique en direction azimutale dans les pompes annulaires à induction.

Dans le chapitre qui traite de l'interaction magnétohydrodynamique à base de modèles couplés, ils sont proposés deux modèles qui couplent l'électromagnétisme et l'écoulement. Un de ces modèles est réalisé avec un seul logiciel, tandis que le second est réalisé par le couplage de deux logiciels différents. Ils sont présentés les avantages des modèles couplés, en matière de la précision des résultats, par rapport aux modèles électromagnétiques. Il est également présenté l'évolution des profils de vitesse, de densité de force et de courant sous l'influence du champ électromagnétique et de l'écoulement de sodium à vitesses différentes. Il être montré que pour obtenir une bonne approximation de l'efficacité de la pompe électromagnétique il est nécessaire d'utiliser un modèle couplé qui prend en compte les pertes hydrodynamiques et l'effet de viscosité turbulente.

Les contributions de la thèse sont complétées par des observations importantes sur les méthodes de travail et les logiciels utilisés tout au long de l'étude.

Mot clé : magnétohydrodynamique, pompes électromagnétiques, sodium, sels fondus, effets d'extrémité, effets Hartmann, modèles éléments finis de type couplage électromagnétisme - écoulement.

Rezumat

Preocupările actuale în legătură cu exploatarea în siguranță a centralelor nucleare existente și în legătură cu proiectarea arhitecturilor speciale de reactoare nucleare pentru generația a patra, coroborate cu interesul tot mai pronunțat pentru eficiența și fiabilitatea oricărui echipament dintr-un sistem energetic, fac ca tot mai multe demersuri de cercetare să se îndrepte spre studiul diverselor subansamble ale acestor sisteme pentru o mai buna înțelegere și optimizare pe baza mijloacelor moderne de proiectare asistată de calculator. Din rândul tipurilor propuse pentru generația a patra de reactoare nucleare fac parte și cele care au ca agent de răcire săruri topite, respectiv sodiu topit. Multe reactoare nucleare de generație anterioară folosesc ca mijloc de antrenare a fluidelor de răcire pompe mecanice de construcție specială. Sărurile topite ăi sodiul lichid, datorită proprietăților fizice, au potențialul de a fi recirculate cu ajutorul pompelor electromagnetice. Deși tehnologia pompării electromagnetice a fluidelor electroconductoare a fost dezvoltată încă din prima parte a secolului trecut, în prezent cunoaște o renaștere datorită reconsiderării multiplelor avantaje tehnologice și de securitate în exploatare.

Lucrarea de față este atât un studiu al fenomenelor intime ce au loc ca urmare a curgerii fluidelor electroconductoare în câmpul electromagnetic al pompelor electromagnetice – interacțiune magnetohidrodinamică - cât și un raport despre capabilitățile și avantajele uneltelor moderne de calcul de a înlesni proiectarea și optimizarea pompelor electromagnetice.

Pentru a atinge scopul principal al tezei, și anume o înțelegere mai adâncă a fenomenelor interdependente specifice funcționării pompelor electromagnetice, au fost considerate două obiective secundare. Primul obiectiv se referă la exploatarea la maximum a modelelor electromagnetice numerice în element finit cu scopul de a obține cât mai multe informații cu putință despre comportamentul pompelor electromagnetice în ipoteza care nu ia în considerare curgerea fluidelor. Al doilea obiectiv a fost construirea unor modele numerice care cuplează electromagnetismul și curgerea, respectiv, cuplează modelele numerice ale celor două fenomene ce caracterizează curgerea magnetohidrodinamică din canalele pompelor electromagnetice.

În partea dedicată studiului pompării electromagnetice a sărurilor topite, teza evidențiază problemele specifice legate de generarea forțelor electromagnetice în fluide slab conductoare electric și oferă rezultate cu privire la aplicațiile unde pomparea electromagnetică a sărurilor topite poate fi eficientă. Cu ajutorul modelelor electromagnetice s-au obținut date importante despre influența numărului de poli electromagnetici și frecvența de alimentare asupra caracteristicii Presiune – Viteză a pompelor electromagnetice inelare de inducție. Au fost analizate fenomenul de ecranare creat de peretii metalici – cu repercursiuni negative asupra performanțelor pompelor, efectele de frânare exercitate la intrarea și la ieșirea din canalul de pompare și legătura dintre capacitatea de suprasarcină hidrodinamică și caracteristica Presiune – Viteză a pompelor de inducție. O secțiune specială a fost consacrată analizei dependenței de timp și a variației de la punct la punct a forței electromagnetice, precum și studiului neuniformităților mărimilor de natură electromagnetică în direcție azimutală în pompele inelare de inducție.

În capitolul despre interacțiunea magnetohidrodinamică pe baza modelelor cuplate, se propun două modele ce cuplează electromagnetismul și curgerea fluidelor, unul realizat cu ajutorul unui singur software și al doilea realizat prin cuplarea a două software-uri diferite. Sunt prezentate avantajele modelelor cuplate din punctul de vedere al acurateței rezultatelor în comparație cu modelele electromagnetice. Este prezentată evoluția profilelor de viteză, de densitate de forță și curent sub influența câmpului electromagnetic și a curgerii sodiului cu diferite viteze. Se arată că pentru a obține o buna aproximare a randamentului unei pompe electromagnetice este necesară utilizarea unui model cuplat ce ia în considerare pierderile hidrodinamice și efectele vâscozității turbulente.

Contribuțiile tezei se completează cu observații importante în legatură cu metodele de lucru și uneltele software utilizate de-a lungul procesul de studiu.

Cuvinte cheie: magnetohidrodinamica, pompe electromagnetice, sodiu, saruri topite, efecte de margine, efecte Hartmann, modele in element finit de tipul cuplaj electromagnetism-curgere

Content

Structure of the thesis

Electromagnetic pumping of electroconductive fluids is based on the interaction between the electromagnetic field and the electrical current present in the fluid. Thus, two branches of physics are involved, electromagnetism and fluid dynamics. The general objective of the thesis is the study of electromagnetic pumping systems for a better understanding of the intimate interdependent phenomena specific to electromagnetic pumps operation. To achieve this principal goal, two auxiliary objectives were considered. The first is related to exploitation to the most the electromagnetic finite element models in order to retrieve as much information as possible about electromagnetic pumps behavior in a simplifying assumption that does not take into account the fluid dynamics. The second auxiliary objective is to build a numerical model that couples the electromagnetism and the fluid dynamic, namely the two interdependent physics that govern the fluid flow through channels of electromagnetic pumps.

The thesis is structured in seven chapters, one annex and bibliography.

Chapter 1 contains the introduction in the subject. It is introduced the notion of magnetohydrodynamics as a discipline of physics of celestial bodies and as a branch of industrial electromagnetic processing of materials. It is given an overview of the works and important scientists with respect to the development of Earth's and Sun's magnetohydrodynamics. Further in the chapter it is briefly presented the history and state of the art regarding electromagnetic pumping. Presentations of the constructive types and of the operation principle of electromagnetic pumps are the subject of the last part of the chapter.

Chapter 2 is devoted to presenting theoretical aspects on numerical modeling, electromagnetism, fluid dynamics and magnetohydrodynamics used in the thesis. The first auxiliary objective is pursued in the next three chapters.

Chapter 3 deals with electromagnetic pumping of molten salts. Based on 2D and 3D finite element models, are evaluated and compared the parameters of the electromagnetic pumps, of induction type – with cylindrical, annular and rectangular channel and of conduction type with very low supply frequency.

Chapter 4 marks in the thesis the beginning of the study of electromagnetic pumping of sodium. Based on electromagnetic models coupled with translation motion of solid conductors, the chapter treats the behavior of small size annular linear induction pumps. Various results regarding the variation in time of the force and comparisons between results corresponding to 2D and 3D models are also presented.

Chapter 5 treats the subject of medium size electromagnetic pumps of induction type for sodium. A parametric study was done in order to obtain information on the influence of the supply frequency and number of poles on the characteristic curve Force-Velocity and on the pump efficiency characteristic. Further is highlighted the shielding effect of the metallic walls, the ends effect are presented and quantified. Significant information is presented about the startup, steady state operation and dynamic behavior of electromagnetic pumps. The three-dimensional structure of the electromagnetic field is studied with 3D models. It is evidenced the azimuth non-uniformity and its repercussions over global quantities. Based on time domain finite elements analysis, there are studied the ends effects and oscillations in time and variations in space of generated force.

Chapter 6 answers to the second auxiliary objective. It contains two coupled models that take into account properly the interaction between the electromagnetic

field and fluid dynamics. There are evidenced the influences of the electromagnetic field over the fluid flow and vice versa. It presents the dependence of various field quantities with the sodium velocity and the efficiency characteristic in the context of coupled model.

Chapter 7 summarizes the general conclusions and contributions that the thesis brings in the research field of electromagnetic pumping based on finite element numerical models.

The **Annex** contains a study on the topic electromagnetic stirring. The common element between electromagnetic stirring and electromagnetic pumping is the action of the Lorentz force. In the case of pumping, the Lorentz force balances the viscous forces and the pressure required in a closed hydrodynamic circuit. In the case of stirring in a closed volume, the Lorentz force balances only the viscous forces. This part of the thesis presents summarily the principles of electromagnetic stirring and analyzes the specificities of three electromagnetic stirring applications.

Chapter 1: Introduction

The interaction of fluids in motion crossed by electric current with electromagnetic fields provides a large variety of phenomena associated with electro-fluid-mechanical energy conversion. Effects from such interactions can be observed in liquids, gases, two-phase mixtures, or plasmas. Numerous scientific and technical applications exist, such as heating and flow control in metals processing, power generation from two-phase mixtures or high temperature gases, magnetic confinement of high-temperature plasmas — even dynamos that create magnetic fields in planetary bodies. Several terms have been applied to the broad field of electromagnetic effects in conducting fluids, such as magneto-fluid mechanics, magneto-gas-dynamics, and the more common one used here — magnetohydrodynamics, or "MHD", [1].

Fig. 1.1 presents the entire spectrum of technical branches belonging to the common body of Electromagnetic Processing of Materials (EPM).

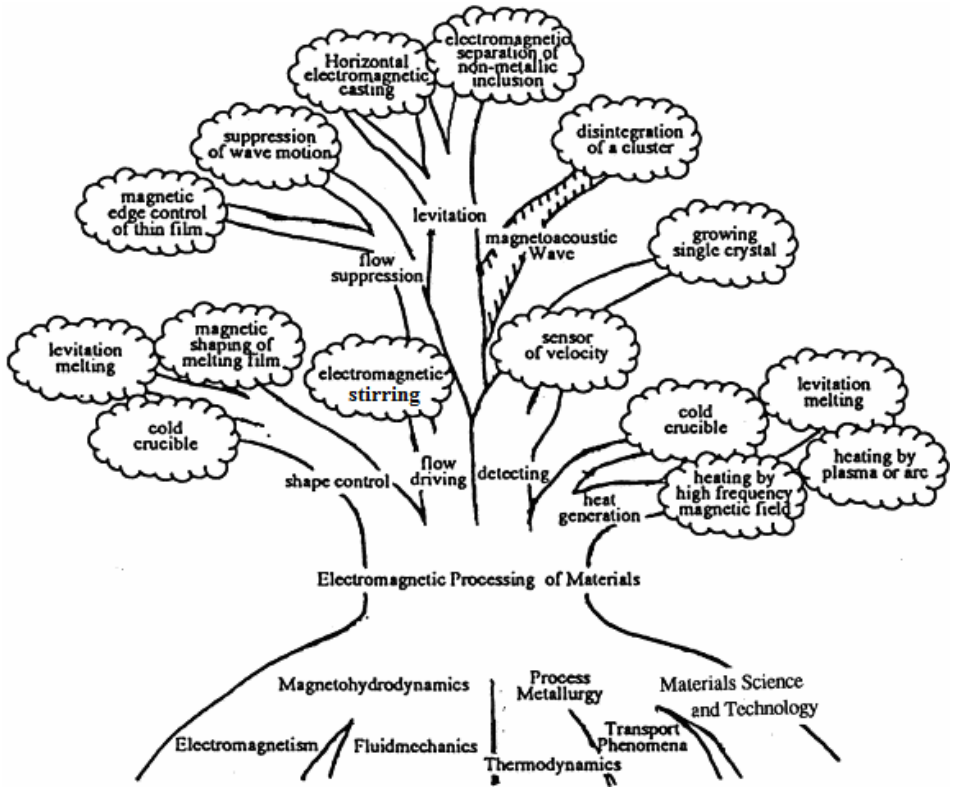

Fig. 1.1 The tree of the electromagnetic processing of materials, [2]

Electromagnetic pumping is a procedure of generating pressure in electroconductive fluid circuits by means of devices called electromagnetic pumps (EMPs). EMPs are of different constructive types and different sizes, but all of them are based on the principle of the electromagnetic force generation due to the current density and magnetic flux density interaction in the pumping channel. Electromagnetic pumping is part of MHD discipline. Before going deeper in the study of electromagnetic pumping, some general information on MHD is given.

In broad sense, MHD is a field of the Earth physics and astrophysics. In the specialty literature the Earth's core, Fig. 1.2a) is divided in outer core, from the 2890 km depth to 5150 km and the inner core from 5150 km to 6378 km. The Earth's core is composed mainly of melted iron, fact that determines some specialists to

affirm that this is the source that generates the terrestrial magnetic field. The MHD branch of science provides explanations for the gradually change in time of the Earth's magnetic field and for the rare and irregular phenomenon of Earth's magnetic poles inversion.

The Sun, which consists largely by ionized hydrogen, focuses the MHD interest in two main directions. First is that of the convective area, Fig. 1.2b), which generates the Sun's magnetic field. In the convective area the MHD phenomena are similar to those existent in the Earth's core.

The second interest direction from the MHD point of view is the solar atmosphere. It is made of solar corona and chromosphere and it is much less dense than the convective zone. A major problem is to explain the heating of the solar corona to temperatures up to 10^6 K order of magnitude while the photosphere, the neighboring region that separates the convective area from the cromosphere has 6000 K.

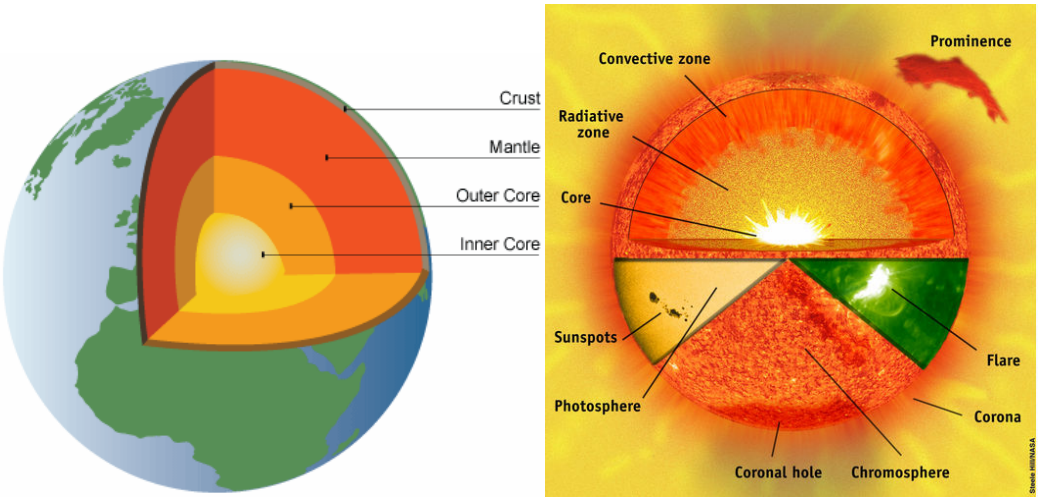

Fig. 1.2 Magnetohydrodynamics in the Earth's core and in the convective zone of the Sun

In [3] Agris Gailitis et al. presents a history of the dynamo effect theory how it became widely accepted as the only possible effect to explain the abundance of magnetic fields in the cosmos. Historically, the first explanation for the Earth magnetic field was given by Gilbert in 1600. He interpreted the Earth as a big loadstone. Later, Blackett in 1947 submitted the hypothesis that the large astronomical bodies might have dipole moments that are directly proportional to their angular momentum.

Dynamo theory describes the process through which a rotating, convecting, and electrically conducting fluid acts to maintain a magnetic field. This theory is used to explain the presence of anomalously long-lived magnetic fields in astrophysical bodies. The conductive fluid in the geodynamo is liquid iron in the outer core, and in the solar dynamo is ionized gas. This hypothesis, which was initially proposed by Joseph Larmor in 1919, has been modified due to extensive studies of magnetic secular variation, paleomagnetism (including polarity reversals), seismology, and the solar system's abundance of elements. Also, the application of the theories of Carl Friedrich Gauss to magnetic observations showed that Earth's magnetic field had an internal, rather than external, origin. There are three requisites for a dynamo to operate: an electrically conductive fluid medium, kinetic energy provided by planetary rotation, an internal energy source to drive convective motions within the fluid. In the case of the Earth, the magnetic field is induced and constantly maintained

by the convection of liquid iron in the outer core. A requirement for the induction of electromagnetic field is a rotating fluid. Rotation in the outer core is supplied by the Coriolis effect caused by the rotation of the Earth. The Coriolis force tends to organize fluid motions and electric currents into columns aligned with the rotation axis [4].

The first laboratory dynamo experiment was conducted by Lowes and Wilkinson in 1963 and 1968 on homogeneous dynamo, two iron cylinders, but not a fluid dynamo. The Riga experiments started with 1967 and have the purpose to verify the dynamo effect theory.

Dynamo theory is the only geophysical theory seriously considered today, [5], that explains the origin of Earth's main magnetic field in terms of a self-sustaining dynamo. In this dynamo mechanism, fluid motion in Earth's outer core moves the liquid iron across an already existing weak magnetic field and generates an electric current. Heat from radioactive decay in the core is thought to induce the convective motion. The electric current, in turn, produces a magnetic field that also interacts with the fluid motion to create a secondary magnetic field. Together, the two fields are stronger than the original and lie essentially along the axis of Earth's rotation. In the mid-1900s the German-born American physicist Walter M. Elsasser and the British geophysicist Edward Bullard had an enormous contribution to the theory development, [6] - [11].

Müller and Stieglitz in [12] did an important report on the self-excitation of magnetic field and dynamo effect demonstrations. Repeated measurements on the Earth's surface and more recently by satellites from space have shown that the magnetic field has a dipole structure by 90% while the other 10% are completed by higher order poles. Based on these measurements and on magneto-potential theory, isographs of the terrestrial magnetic field have been developed by several authors among others Bloxham and Gubbins in 1985, Jackson et al. in 2000 and Haak in 2001. The mean value of the magnetic flux density is about 0.04 mT at the surface, varying locally and in the short term, ten to several hundred years by up to 5%. An indicator for this is the movement of the magnetic north pole by several hundred kilometers to the northwest during the last 170 years. Moreover, reliable measurements recorded for the last 400 years have shown that local variations of the field drift towards west at a rate of 0.2 degrees per year and the field intensity weakens by about 0.07% per year [13]. Significant variations of the field have also been identified on time scales of thousands of years. The transition between different polarities occurred much faster in periods of several thousand years. Moreover, during the transition period the magnetic field intensity weakened significantly down to only 10% of its normal value. These randomly occurring events are called reversals. Fig. 1.3 shows the isolines of the radial component of the Earth's magnetic field at the Earth's surface after Haak, 2011.

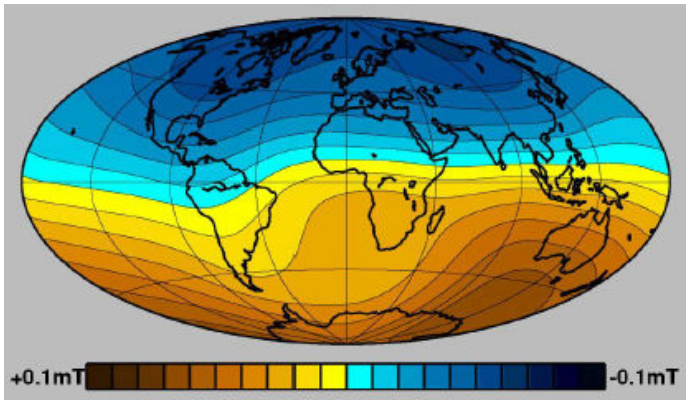

Fig. 1.3 Isolines of the radial component of the Earth's magnetic field at the Earth's surface

There are some other consecrated names for the pure MHD field: Hartmann and Lazarus who have done interesting experiments in liquids metals in 1937 ([14], [15]), Hannes Alfvén, who discovered the Alfvén wave during the World War II ([16], [17]), Thomas Cowling and Subrahmanyan Chandrasekhar who had important contributions on the geomagnetism science, [18].

The industrial MHD applications are in general related to electromagnetic pumps, electromagnetic stirrers, MHD generators, MHD propulsion, [19]-[21], and electromagnetic flowmeters [22], [23]. The electroconductive fluids that usually make the object of the industrial MHD are: molten metals or alloys and plasmas. Some of the suitable metals are: mercury, gallium, bismuth, tin, lead, aluminum, sodium, potassium, sodium-potassium alloys.

Plasmas are fluids obtained by ionization of gases at 2000–3000 K temperatures. The MHD of plasma developed in industry in relation to electrical energy generation through MHD conversion. MHD conversion is the technology through which electrical energy is directly produced from the kinetic energy of an electroconductive fluid at high temperature moving in electromagnetic field, Fig. 1.4.

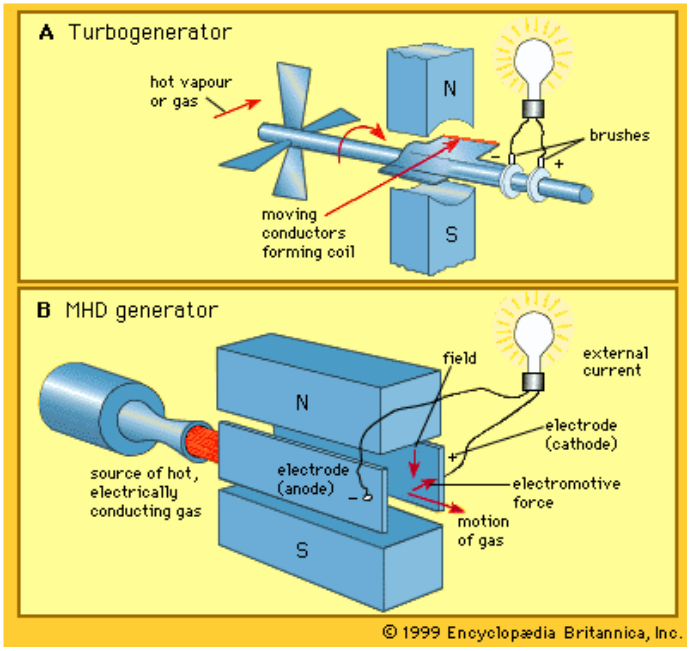

Fig. 1.4 Principle of MHD generators based on plasma jet relative to the classical generator based on rotation motion

In addition, plasmas are used in other applications otherwise impossible, like: processing of refractory materials where very high temperatures are needed, phase transformation processes which avoid the passing of the substance through intermediary phases, reactions that require high specific energy as pyrolysis and volatilization.

The industrial MHD of molten metals has been developed predominantly in applications of molten alkaline metals pumping in cooling systems of nuclear plants, [24]-[26]. The field also extended due to the MHD contributions in improvement of the transport, casting, stirring and purification processes of metals and alloys in metallurgical industry and contributions in pumping the soldering alloys in devices for making electrical connections. Electromagnetic levitation is another MHD procedure used in analyzing of molten metals samples when for obtaining a high degree of purity requires no contact with physical walls of an enclosure, [27].

Although electromagnetic pumping is strongly related to highly electrically conductive fluids, newer MHD applications with low conductive fluids have been researched and developed, [28]-[32]. Among them, an important application is electromagnetic pumping of molten salts which can be used in the field of electrical energy production from solar thermal energy or in the first cooling loop of Molten Salts Reactor (MSR), [33]. Other application can be molten glass stirring in various industrial applications, [34].

1.1 History and state of the art

While the electromagnetic pumping of low conductive fluids represent relatively recent studies and investigations, the history of electromagnetic pumping is related mainly to electromagnetic pumping of fluids of high electrical conductivity.

Even from the first half of the nineteen century it was known that when an electrical conductor traveled by electrical current is so moved in electromagnetic field, a force mutually perpendicular to the electromagnetic field and to the velocity of the conductor is exerted on the conductor. The negative charges tend to move in one direction, and the positive charges in the opposite direction, [35]. References [36]-[56] are testimonies for the early activities in the field.

It was recognized by Faraday as early as 1831 that one could employ a fluid conductor as the working substance in a power generator. To test this concept, Faraday immersed electrodes into the Thames river at either end of the Waterloo Bridge in London and connected the electrodes at mid span on the bridge through a galvanometer. Faraday reasoned that the electrically conducting river water moving through the earth's magnetic field should produce a transverse electromotive force. Small irregular deflections of the galvanometer were in fact observed, [57].

Practical MHD devices have been in use since the early part of the 20^{th} century. An MHD pump prototype was built in 1907, ([1], [58]).

Albert Einstein is known very much for his theories of relativity and the photo-electric effect. But also he was an inventor and produced numerous patents in at least seven countries during the period 1928–1936. One of the most useful inventions of the Einstein–Szilard collaboration was the Einstein–Szilard electromagnetic pump for circulating liquid metals as coolants dated in 25.05.1930, [59].

In 1928, AEG (Allgemeine Elektrizitats-Gesellschaft) built a prototype and exhibited it at the Leipzig trade fair but it was rather noisy. Later in the 1950s the Einstein–Szilard pump was utilized in the nuclear industry for cooling experimental breeder reactors. However, fabrication problems hindered the full development of this type of pump, ([60], [61]).

In the second part of the 20th century the MHD devices have been developed more and more and become useful for applications as stirring, levitation, transport and flow control in various metallurgical processes and others, [62].

Also in this period the capacity of MHD power generation grew significantly. The MHD conversion is the technology through which is obtained directly electrical energy from the kinetic energy of an electroconductive fluid at high temperature that is moving through electromagnetic field, ([63], [64]).

The efforts carried around the world to develop this technology were promoted because of the potential of the MHD generators to be much more efficient than the conventional steam facilities due to this direct conversion. Some of the advantages of the energy production through MHD conversion where highlighted:

- the MHD process has the potential of increasing the efficiency of the energy conversion up to 50-60 %;
- the MHD conversion is attractive for the industry due to the reduced quantity of cooling water and environment friendly character;
- MHD power generation is applicable no matter the source type for heat energy convertible in electrical energy. These sources can be of nuclear type, solar or from burning the fossil fuel.
- The increase of the reliability by eliminating moving parts.

Another type of MHD application developed in the last decade of the 20th century was the MHD ship propulsion in the seawater ([65], [66]) and control of the turbulent boundary layers to reduce drag, [67].

An important application of the MHD interaction that is studied in all the important atomic research groups was the magnetic confinement of plasma in order to obtain conditions necessary to sustain fusion reactions, [68].

The survey in the history of the MHD industrial applications shows that by now, the operation principles and the main drawbacks are known, the applications range is well diversified and the topic was studied by numerous research groups and a lot of papers have been devoted to the knowledge in the field, [69]-[72].

The actual researches in the field of electromagnetic pumps are closed related to the extraordinary development of the computer aided design software and of the computation resources, [73]-[82]. Beside the physical experimentation, these tools allow a deeper understanding of the intimate phenomena not sufficiently studied in the past and also the resume of design activity regarding new constructive solutions, [83].

The issue that continues to be a challenge even nowadays in the research and development of electromagnetic pumps is the flow instability, [84]. Instability occurs when there is some disturbance of the external or internal forces acting on the fluid. In practice it is very hard to suppress all possible small disturbances, and the problem of stable or unstable flow is a question of whether there exist disturbances that grow as time passes. Important works, [85]-[87], confirmed even from the ‘80s through experimental work that the instability of the flow through electromagnetic pumps is characterized by low frequency pulsation of the pressure and the sodium flow rate, non-uniform magnetic field along the azimuth, mechanical vibrations and fluctuations of winding voltage and current. The same studies affirm that the condition for instability occurrence is magnetic Reynolds number larger than unity.

In 1991 F. Werkoff, [88], presents a linear stability analysis in which, for the first time, edge waves are taken into account. He approaches the phenomena that limit the energetic efficiency of high-power machines, namely Joule losses in the liquid metal due to electromagnetic edge waves and flow inhomogeneities created by MHD

instability. Results are compared with experimental data from three large electromagnetic pumps (Soviet, French, and West German). It appears, surprisingly, that edge waves can either stabilize or destabilize the flow, depending on the characteristics of the induction machines.

The authors I.R. Kirillov, D.M. Obukhov, Hideo Araseki, Gennady V. Preslitsky, Anatoly P. Ogorodnikov were very active in the field for the last decades. In 2000 they performed an experimental and analytical study of double-supply-frequency pressure pulsation arising in annular linear induction pumps. In a large-scale induction pump, it is known that the supply frequency should be relatively low in order to satisfy a MHD stability criterion. Under such a low supply frequency, the double-supply-frequency pressure and flow rate pulsation generated in an induction pump may be of concern. The experimental data obtained in the work show that the amplitude of the pressure pulsation increases with decreasing supply frequency, number of poles and/or slip. The numerical results reveal that the pressure pulsation comes from a disturbance of the electromagnetic force near the stator ends, [89]. In [90] it is presented an experiment and a numerical analysis to proof the effect of linear winding grading at the stator ends of reducing the pressure pulsation. In addition, the experimental data reveals that the linear winding grading improves the pump efficiency.

Numerical models and computer codes for analysis of the local and integral characteristics of linear electromagnetic pumps, such as magnetic field distribution, pressure development, amplitude of pressure pulsation with double supply frequency and distribution of liquid metal velocity over the azimuth where proposed as result of the previous work, ([91], [92]).

In [93] the research group describes an experimental and analytical study of the MHD instability arising in an annular linear induction pump. In the experiment, the instability was investigated in detail using an electromagnetic pump of flow rate 7 m^3/min. The experimental results show again that the instability occurs when the magnetic Reynolds number is larger than unity and the instability becomes more intense as the slip increases. The numerical analysis reveals that when the magnetic Reynolds number is larger than unity, the azimuth non-uniformity of the applied magnetic field or of the sodium inlet velocity brings sodium vortices and hence a low frequency pressure pulsation occurs. In addition, the non-uniformity causes decreases of the developed pressure.

Other methods of suppressing the instability have been presented, [94]. The experimental data show that the winding phase shift suppresses the instability unless the slip value is so high, but brings about a decrease of the developed pressure. The numerical results indicate that the phase shift causes a local decrease of the electromagnetic force, which affects the developed pressure.

In 2012 it have been showed, [95], that there is a maximum flow rate for which a large-scale induction pump can be designed and manufactured to operate stably near the maximum efficiency point. On this basis, a parallel arrangement of several pumps in order to breakthrough this upper limit is proposed. It was proposed a method of measuring the sodium flow rate based on a correlation between the leakage electromagnetic field and the sodium flow rate. Other measuring solutions based on correlations between the sodium flow rate and the pump operation parameters (voltage, electric current, frequency and sodium temperature) were also proposed.

Japanese researchers are engaged in developing and manufacturing large electromagnetic pumps. In [96]-[99] there are presented experiments of electromagnetic pumps with rotating twisted magnetic field with gallium. They show

that a stator with out teeth or slots was more suitable in this case (uniformity of the magnetic flux density was remarkably better in the case with no core). The rotational velocity was much greater than the axial velocity for almost any value of the slip. The excessive rotational velocity has to be reduced in future designs of the pump. The optimum twist angle of the coil is larger than the present twist angle, 39°.

In 2004, Hiroyuki Ota et al. presents elements of design, fabrication and operation of a large capacity sodium-immersed self-cooled electromagnetic pump of 160 m^3/min flow rate, 2.8 bar head, more than 40% efficiency. The paper confirms the success of Large Electromagnetic Pumps usage in the Fast Breeders Reactors.

There are also Indian authors that are currently developing and proposing various constructive solutions for electromagnetic pumps in order to meet the Fast Breeders Reactors requirements, ([100], [101]).

Recently a Korean research group developed a MHD stability analysis of a liquid sodium flow inside the annular channel of a 372 mm long, 0.00167 m^3/s, 3 bar head electromagnetic pump with an idealized coil arrangement equivalent to a current sheet. It is proposed a magnetic field across the annular gap as a solution for avoiding perturbations that could lead to turbulence, flow separation or local cavitations. The calculations are based on analysis of the axisymmetric two-dimensional linear stability taking into account the perturbation on the developing direction [102].

1.2 Types of electromagnetic pumps and operation principle

The principal classifications of electromagnetic pumps can be made in function of operation principle and shape.

Depending on the way of generation the current density **J** in the pumping channel, electromagnetic pumps are of a) conduction type (also known as Faraday pumps), [103] and b) induction pumps. In general, both types include field coils for electromagnetic field generation.

Conduction pumps are built with rectangular channels due to the facility with which the directions of magnetic flux density and current density vectors can be correlated with the channel geometry thus the pumping force to result in the desired direction, as in Fig. 1.5. Imposition of the current density direction J_y is made by placing two electrodes on the two sides of the pump parallel with xOz plane, Fig. 1.5. The electrodes are in electrical contact with the electroconductive fluid and connected to a voltage supply of DC or AC type. The magnitude of the current flowing between the two electrodes depends on the voltage supply and fluid electrical conductivity.

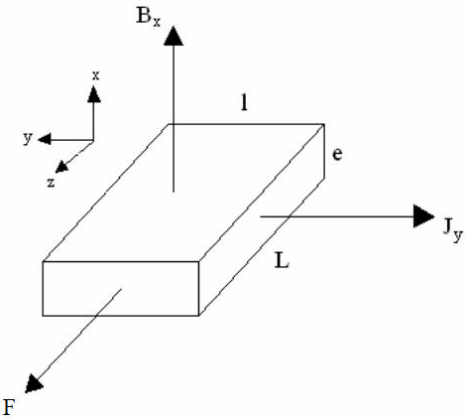

Fig. 1.5 Arrangement of the magnetic flux density, current density and force vectors in a rectangular channel of conduction pump

Another electromagnetic pump classification criterion is by the channel cross-section shape. Besides rectangular channels there are cylindrical and annular channels. Cylindrical and annular pumps are of induction type, therefore with AC supply and the particularity is that the field coils are the source for both current density and magnetic field. In the scientific literature the two types of pumps are called Cylindrical Linear Induction Pump (CLIP) and Annular Linear Induction Pump (ALIP). The induction pump configuration with rectangular channel is called Flat Linear Induction Pump (FLIP).

From the electromagnetic point of view, the CLIP, ALIP and FLIP types of electromagnetic pumps are linear electrical machines [104] - [107]. The electromagnetic configuration of the machine is such designed that the generated electromagnetic force (1.1), also known as Lorentz or Laplace force, entrains the mobile armature in rectilinear motion.

$$\mathbf{F} = \mathbf{J} \times \mathbf{B} \tag{1.1}$$

Fig. 1.6 gives a more complete classification of the two main categories of electromagnetic pumps function of electromagnetic sources and special channel shapes. Many papers are devoted to study and develop various kinds of electromagnetic pumps for diverse purposes, [108]-[135].

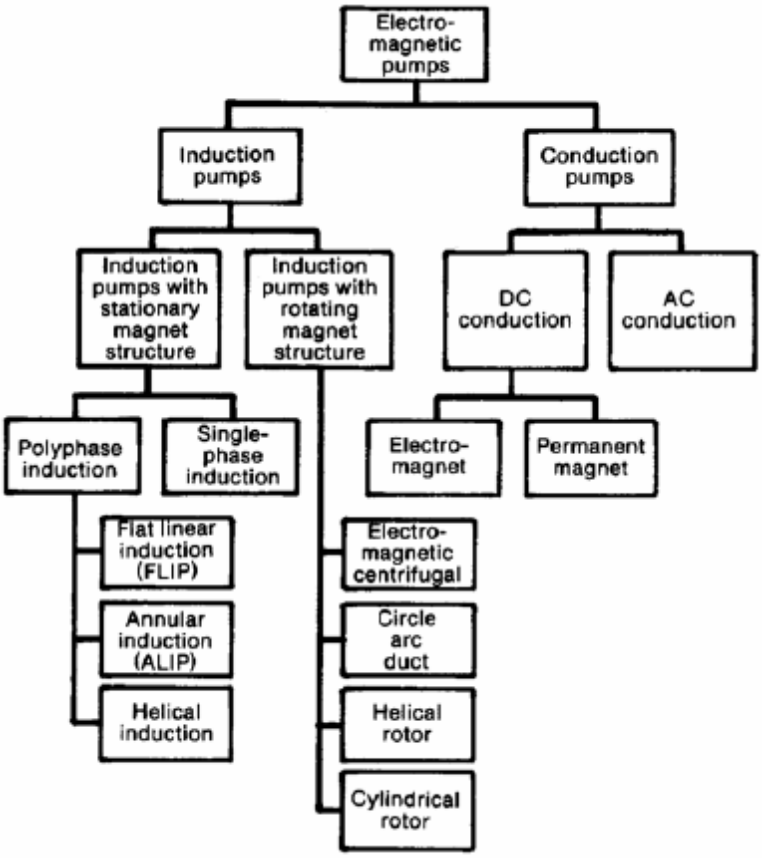

Fig. 1.6 Principal subclasification of EMPs

The CLIPs and ALIPs are particularizations of the linear induction machines, which derive from rotative induction machines. Fig. 1.7 presents in a didactic manner the principle relation that exists between rotative and linear machines. When the rotor and the stator, respectively mobile armature and fix armature are cut along a generatrix and unfolded in plane, a linear induction machine is obtained. The electromagnetic field produced by the new electromagnetic configuration is called

traveling field. If the fixed armature would be a channel containing an electroconductive fluid, the structure would be a FLIP.

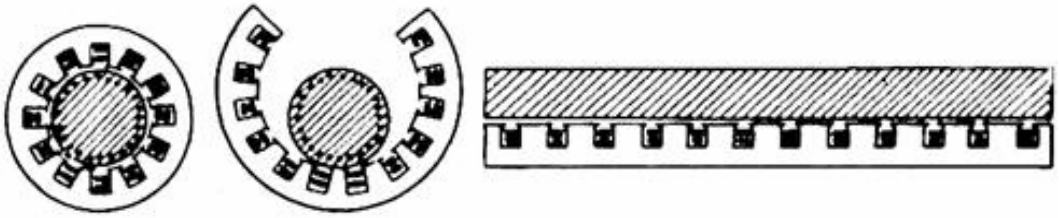

Fig. 1.7 Didactic obtaining of linear machine from rotative machine

Fig. 1.8 describes also didactically the obtaining of the inductor (fixed armature) of a CLIP or ALIP by continuation after the unfold of the fixed and mobile armatures b) of the asynchronous motor a), with the folding around an axis perpendicular to the first unfolding section cut and joining the winding ends belonging to the same slot in circular coils c).

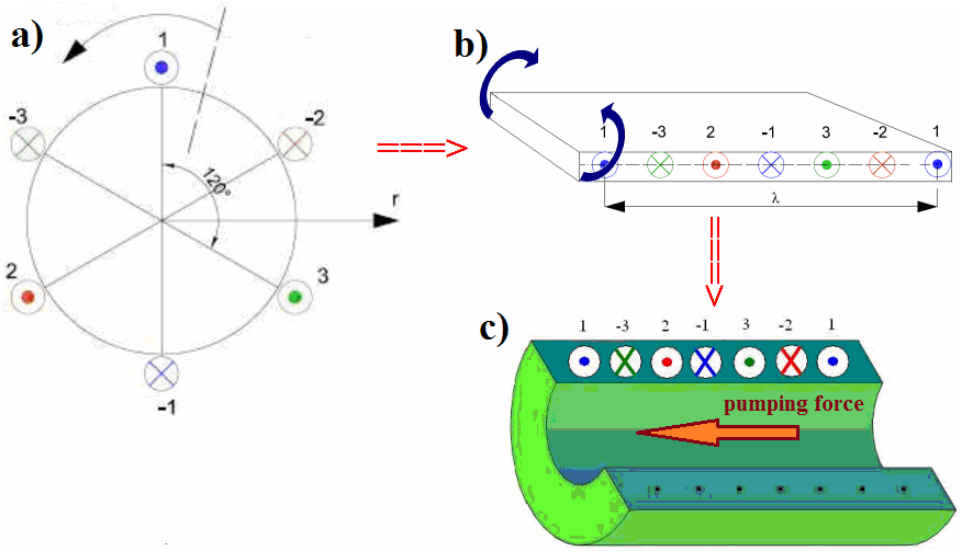

Fig. 1.8 Didactic obtaining of the cylindrical exterior inductor of CLIP or ALIP

Fig. 1.9 presents with more details the main components of the ALIP. The pump in Fig. 1.9 has only one active inductor, at exterior and magnetic cores at the interior side. In order to improve the pump performances, an interior inductor can be installed.

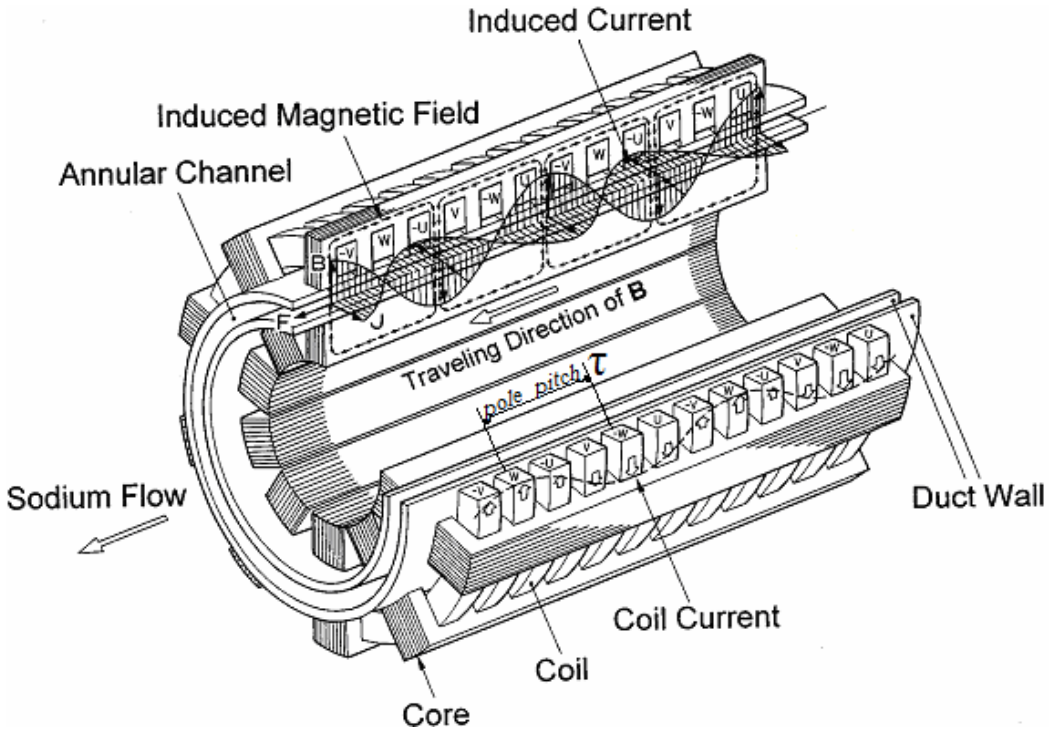

Fig. 1.9 Schematic drawing of ALIP, [89]

The traveling electromagnetic field is characterized by its synchronous speed $v_s=2f\tau$, where f is the inductor supply frequency and τ is the pole pitch length.

The principal drawbacks of the electromagnetic pumps are the ends effects. Unlike the induction machine with rotational field, which is endless along the motion direction, the linear induction machine or any other electromagnetic pump is characterized by strong field variation along the field traveling direction between regions just before the pump and immediately after entering the pump. Along the azimuth direction of the airgap of the rotative machine the field has only a cyclic variation due to alternating magnetic poles. The flow through a hydrodynamic circuit where an electromagnetic pump is installed is made in two types of media: in the presence, respectively in the absence of the electromagnetic field. This strong field variation at the pump inlet and outlet determines forces opposing to the flow, namely breaking effects, [136].

The reliability of the ALIPs in comparison with mechanical ones comes from the absence of any shaft or other moving part. This thing allows the full sealing of the liquid inside the pump. The ALIPs are free of any mechanic vibration as a result of operation principle and do not require any bearing and lubrication. These pumps can operate very well with liquid metals at high temperatures and present the advantage of force generation in the pumping channel contactless, namely by the electromagnetic induction phenomena.

1.3 Software tools used in the thesis

All the results presented in the thesis are obtained with software based on the finite element/volume method.

- FLUX 2D and 3D is professional software produced by CEDRAT, specialized in solving electromagnetic and thermal applications. It was used in chapters 3, 4, subchapters 5.2, 5.3 and paragraph A2 of annex A.

- COMSOL Multiphysic is an integrated environment that can solve applications of various types or coupled problems. It was used in subchapters 5.1, 6.1 and in paragraphs A1 and A3 of the annex A.
- FLUENT by Ansys is specialized in modeling flow, turbulence, heat transfer, and other types of phenomena. It was used in subchapter 6.2 where the MHD interaction in an ALIP for sodium is studied with a coupled model. The coupling is realized between COMSOL, used only for the electromagnetic calculation and FLUENT used to solve the hydrodynamic problem.

CONCLUSIONS

The introductory part of the thesis

- presents the objectives and structure of the thesis.
- defines the branch of physics called magnetohydrodynamics and precise its applicability in domains as astrophysics and industrial applications.
- presents an overview of the main events and scientists that are close related to the births and development of the MHD since its beginnings.
- contains the history and state of the art of electromagnetic pumping which is a review of the development of the field, principal achievements and main challenges still remaining.
- classifies the electromagnetic pumps after their shapes and operating principle and presents the main software tools used in the thesis.

Chapter 2: Theoretical aspects on numerical modeling, electromagnetic field, fluid dynamics and magnetohydrodynamics

Modern scientific research and development is based on computer aided design. Either a new solution is being tested, either a deeper understanding of phenomena is searched, numerical models represent the most economic and fast way of investigation. This chapter summarizes the most important elements of numerical modeling and theory of electromagnetic field, fluid dynamics and magnetohydrodynamics.

The first paragraph defines the numerical model of a physical phenomenon, gives the characteristics of finite element model and presents the steps to build it. In the paragraph devoted to electromagnetic field fundamentals are presented the regimes of the electromagnetic field, the general equations of the electromagnetic field and the equations of the steady state AC magnetic regime which is specific to electromagnetic pumps. Fundamental notions of fluid dynamics, such as laminar and turbulent flow, Reynolds number and Navier-Stokes equation that are used further in the thesis are defined in a special paragraph. The last paragraph presents the MHD equations and introduces notions specific to MHD as magnetic Reynolds number, interaction parameter, Hartman number and Hartmann layer.

2.1 Numerical models

The differential model of a phenomenon it the ensemble of the differential equation or partial differential equation that characterize the phenomenon and the conditions for the equation solution uniqueness. Finding the solution through analytical methods is possible only for very particular and simple cases. When complex geometries are involved or materials have non-linear properties the only way to solve the model is by numerical methods. The numerical solution of the differential model represents the numerical model of the phenomenon or of the device. The process of obtaining the numerical solution represents the numerical modeling of the phenomenon.

Through numerical modeling the partial differential equations become a system of algebraic equations whose solution represents an approximation of the solution of the state quantity in a discrete number of points belonging to the computation domain.

The procedure that gives the name of finite elements method (FEM) consist of dividing the 1D, 2D, 3D computation domain in elementary line segments, surfaces or volumes called generically finite elements, Fig. 2.1. The state quantity for each finite element is expressed through a combination of nodal values, which are values of the state quantities in the nodes of the finite element, and a set of known functions, called shape functions of the finite element. Some formulations of the studied phenomenon transform the differential model, respectively the partial differential equations and the solution uniqueness conditions, in a algebraic system of equations having as unknowns the values of state quantity in all the nodes of the finite element network, also called mesh.

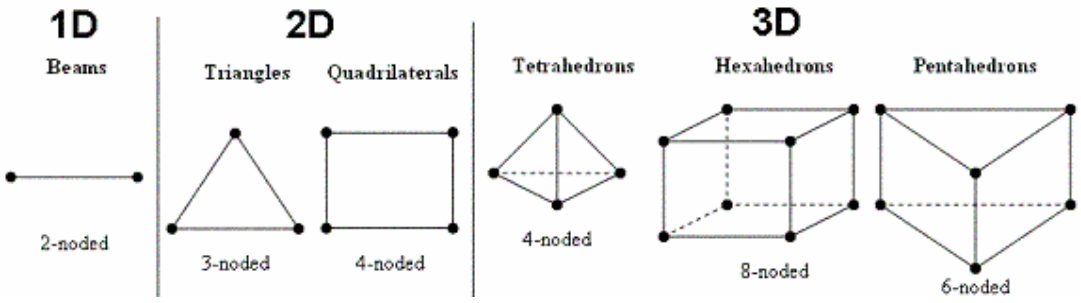

Fig. 2.1 Various types of finite elements

In general, the finite element method is preferred in the study of electromagnetic models. In computational fluid dynamics (CFD), the finite volume method (FVM) is predominantly used. Based on the control volume formulation of analytical fluid dynamics, the first step in the FVM is to divide the domain into a number of control volumes, also known as cells, where the state variable is located at the center of the control volume. The next step is to integrate the differential form of the governing equations over each control volume. Interpolation profiles are then assumed in order to describe the variation of the concerned variable between cell centers. The resulting equation is called the discretized or discretization equation. In this manner, the discretization equation expresses the conservation principle for the variable inside the control volume. The most compelling feature of the FVM is that the resulting solution satisfies the conservation of quantities such as mass, momentum and energy for any control volume as well as for the whole computational domain and for any number of control volumes. Even a coarse grid solution exhibits exact integral balances.

The most important advantages of numerical modeling are:

- it can treat complex computation domains
- it can treat non-linear equations, where the equation coefficients are dependent on equation unknowns
- it reduces significantly the cost and duration of the design stage
- it facilitates the optimization of the device before prototype stage

Practical implementation of a finite element model or finite volume model of a specific device consists in development of a computer program with the following structure: preprocessor, solver and postprocessor. These three parts of the program can exist separately or integrated in a single software.

The preprocessor performs the description of the computation domain geometry, physical characteristics and the computation domain discretization. The geometry can be built through the boundary description method or by constructive geometry method. In the boundary description method, volumes are defined by its constituent faces, each face is defined by its constituent edges and each edge is defined by two points. In the constructive geometry method, bodies are defined with Boolean operations with basic geometrical entities. Description of the physical characteristics means identification of the various type regions in the computation domain and assigning them with specific physical properties, specification of the sources and the boundary conditions. The principal types of boundary conditions are:

- Dirichlet conditions, when the value of the state quantity on the boundary is known;
- Neuman conditions, when the derivative of the state quantity relative to a local coordinate normal to the boundary is known. It can be distinguished:

homogeneous Neuman conditions, when the derivative is zero and non-homogeneous Neuman conditions, when the derivative has a known value.

- cyclic conditions, when a relation between two different boundary from the point of view of state quantity. There are:
    - periodicity conditions, when the state quantity has the same value in homologous points of different boundaries;
    - anti-periodicity conditions, when the state quantity has opposite values in homologous points of different boundaries;
    - translation conditions, when there is a constant difference between values of state quantity in homologous points of different boundaries.

In postprocessor, the user can extract the significant information related to the important local or global quantities. Also in the postprocessor, the numerical results are graphically presented for analysis and interpretation.

2.2 Fundamentals on electromagnetism [137], [138]

The electromagnetic field is a fundamental concept of the macroscopic theory of electromagnetism end represents one of the physical forms of existence of mater. It consists of two components predominantly interdependent, the electrical field and the magnetic field.

The **electric field** is produced by electrified bodies or by variation in time of the magnetic field. The macroscopic local and instantaneous state of the field is characterized by the vector quantities electrical field strength, $\mathbf{E}(\mathbf{r},t)$ and electrical flux density $\mathbf{D}(\mathbf{r},t)$ which are dependent of the position vector $\mathbf{r}$ and time variable t.

The **magnetic field** is produced by bodies traveled by electrical current, magnetized bodies, electrified bodies in motion or by variation in time of the electrical field. The macroscopic local and instantaneous state of the magnetic field is characterized by vector quantities magnetic field strength $\mathbf{H}(\mathbf{r},t)$ and magnetic flux density $\mathbf{B}(\mathbf{r},t)$.

The electric and magnetic macroscopic states of bodies are locally and instantaneously characterized through the following four quantities:

- volume density of the electric charge $\rho_v(\mathbf{r},t)$, which quantitatively defines the rate of electrical charges per volume unit;
- polarization $\mathbf{P}(\mathbf{r},t)$, defines the electric polarization state of bodies;
- conduction electric current density $\mathbf{J}(\mathbf{r},t)$, which describes the electrokinetic state;
- magnetization $\mathbf{M}(\mathbf{r},t)$, which describes the magnetization state of the bodies.

Relative to the behavior in time of the electrical and magnetic phenomena, the following regimes of the field exists:

- **unsteady general variable regime** of the electromagnetic field, in which the state variables have an aleatory variation in time. The transient regime is an example of unsteady regime.

- **unsteady periodical regime**, in which the quantities numerical values are repeating at regular interval of time, called period. A particular example of this regime is the **harmonic electromagnetic field**, where the time variation is expressed with sine and cosine functions.

In an unsteady regime the electric and magnetic fields are interdependent and the existence of the electromagnetic field is characterized by the electromagnetic waves. The particular case of the unsteady regime of the electromagnetic field, in which the time variation of the sate quantities is sufficiently slow that the contribution

of the electric field variation in time to the magnetic field generation can be neglected, is called **steady state AC magnetic regime (quasi-static magnetic field)**.

The particular case of the unsteady regime of the electromagnetic field, in which the time variation of the sate quantities is sufficiently slow that the contribution of the magnetic field variation in time to the electric field generation can be neglected, is called **steady state AC electric regime (quasi-static electric field)**.

- **steady regimes**, characterized by macroscopic state quantities invariable in time. In the case of the electromagnetic field in domains where bodies are immobile, these regimes are accompanied by energy transformations like transformation of the electromagnetic energy into thermal energy due to Joule effect. There are two variants of steady regimes, **stationary electric field** and **stationary magnetic field**.

- **static regimes**, which are particular cases of the stationary regimes of the electromagnetic field and in which energy transformation do not exist. These are the only regimes of the electromagnetic field in which electric and magnetic phenomena are independent and **electrostatic** and **magnetostatic regimes** can be differentiate.

General equations of the electromagnetic field

The local form of the general laws of the electromagnetic field in domains with immobile bodies characterized by continuity and smoothness of the physical properties consists of three evolution equations and two state equations:

Evolution equations:

- Faraday's law (electromagnetic induction law):

$$curl\boldsymbol{E} = -\frac{\partial \boldsymbol{B}}{\partial t} \tag{2.1}$$

- Ampère's law (magnetic circuit law):

$$curl\boldsymbol{H} = \boldsymbol{J} + \frac{\partial \boldsymbol{D}}{\partial t} \tag{2.2}$$

- Electric charge conservation law :

$$div\boldsymbol{J} = -\frac{\partial \rho_v}{\partial t} \tag{2.3}$$

State equations:

- Gauss' law (electric flux law):

$$div\boldsymbol{D} = \rho_v \tag{2.4}$$

- Gauss magnetism law (magnetic flux conservation law):

$$div\boldsymbol{B} = 0 \tag{2.5}$$

In points situated on discontinuity surfaces, on singularity curves or on singularity points, equations (2.1) – (2.5) become boundary conditions that express conditions of bound jump for the electromagnetic field state quantities. For an immobile discontinuity surface S, which separates immobile media with different properties, or which is characterized by the electric conduction current sheet $\mathbf{J}_s$ or by the surface electric charge density ρ_s, the boundary equations in the steady state AC magnetic regime are:

$$curl_s\boldsymbol{E} = \boldsymbol{n}_s \times \left[\boldsymbol{E}\right]_s = 0 \tag{2.6}$$

$$curl_s\boldsymbol{H} = \boldsymbol{n}_s \times \left[\boldsymbol{H}\right]_s = \boldsymbol{J}_s \tag{2.7}$$

$$div_s\boldsymbol{J} = n_s \cdot \left[\boldsymbol{J}\right]_s = -\frac{\partial \rho_s}{\partial t} - divb\boldsymbol{J}_s \tag{2.8}$$

$$div_s\boldsymbol{D} = n_s \cdot \left[\boldsymbol{D}\right]_s = \rho_s \tag{2.9}$$

$$div_s\boldsymbol{B} = n_s \cdot \left[\boldsymbol{B}\right]_s = 0 \tag{2.10}$$

In the expressions (2.6) – (2.10) are specified the notation and the definition of the curl and surface divergence operators relative to a surface S, where $\mathbf{n}_S$ is the unit versor normal on the S surface in the considered point. The $[\ ]_S$ represents the jump of the state quantity when crossing the discontinuity surface. The $\mathrm{divb}\mathbf{J}_S$ operator signifies the two dimensional divergence of the two dimensional vector $\mathbf{J}_s$ defined on the S surface.

In the general case of immobile media with arbitrary properties, the laws of material are expressed by the following constitutive laws:

$$\boldsymbol{D} = D(\boldsymbol{E}) \tag{2.11}$$

$$\boldsymbol{B} = B(\boldsymbol{H}) \text{ or } \boldsymbol{H} = H(\boldsymbol{B}) \tag{2.12}$$

$$\boldsymbol{J} = J(\boldsymbol{E}, \boldsymbol{B}) \tag{2.13}$$

The electromagnetic state of bodies in the presence of the electromagnetic field is defined with the constitutive parameters:

- electric permittivity, ε_e;
- magnetic permeability, μ;
- electrical conductivity, σ or its reverse, electrical resistivity, $\rho = 1/\sigma$.

A body is nonlinear electrically, magnetically or from the point of view of electrical conduction when its constitutive parameters are nonlinear dependent of the vectors **E** and **H** (or **B**).

A body is anisotropic electrically, magnetically or from the point of view of electrical conduction when its constitutive parameters are symmetrical tensors of second order in the tridimensional Euclidian space. The square matrixes associated to these tensors can be reduced to the following diagonal form:

$$\left[\overline{\overline{\mu}}\right] = \begin{bmatrix} \mu_1 & 0 & 0 \\ 0 & \mu_2 & 0 \\ 0 & 0 & \mu_3 \end{bmatrix} \tag{2.14}$$

where μ_1, μ_2, μ_3 represent the different values of the anisotropic material quantity along the three principal axes (polarization, magnetization and conduction axes).

A body is inhomogeneous when its constitutive parameters are scalar functions of point.

A body is nonpermanent and without hysteresis when its constitutive parameters are variable in time but depend exclusively on the instantaneous state of evaluation. In addition, the constitutive parameters of a body with hysteresis property depend on the states previous to evaluation.

In numerous applications, as the electromagnetic pumps, it is required the electromagnetic field calculation in computation domains with moving bodies.

It is defined R^0, a referential attached to a point belonging to the mobile body, which relative to the referential R attached to the computation domain is characterized by the position vector **r**(x,y,z) at time moment t and has the speed $\boldsymbol{v}$, much lower than the speed of light in vacuum.

The state quantities of the electromagnetic field, defined in its own referential R^0, satisfy in the points of continuous domains and with smooth electromagnetic properties the following general laws:

$$curl\boldsymbol{E}^0 = -\frac{\partial \boldsymbol{B}^0}{\partial t} + curl(\boldsymbol{v} \times \boldsymbol{B}^0) \tag{2.15}$$

$$curl\boldsymbol{H}^0 = \boldsymbol{J}^0 + \rho_v^0 \boldsymbol{v} + \frac{\partial \boldsymbol{D}^0}{\partial t} + curl(\boldsymbol{D}^0 \times \boldsymbol{v}) \tag{2.16}$$

$$div\boldsymbol{J}^0 = -\frac{\partial \rho_v^0}{\partial t} - div(\rho_v^0 \boldsymbol{v}) \tag{2.17}$$

$$div\boldsymbol{D}^0 = \rho_v^0 \tag{2.18}$$

$$div\boldsymbol{B}^0 = 0 \tag{2.19}$$

In equations (2.15) – (2.19) the space - time coordinates, speed $\boldsymbol{v}$ and the differential operators are expressed relative to the fix referential R.

For the points situated on a discontinuity surface S of physical quantities and velocity field, which separates two immiscible mobile regions, equations (2.15) – (2.19) become:

$$curl_s\boldsymbol{E}^0 = curl_s(\boldsymbol{v}_{\tau s} \times \boldsymbol{B}^0) \tag{2.20}$$

$$curl_s\boldsymbol{H}^0 = \boldsymbol{J}_s^0 + \rho_{s1}^0 \boldsymbol{v}_{1\tau s} + \rho_{s2}^0 \boldsymbol{v}_{2\tau s} + curl_s(\boldsymbol{D}^0 \times \boldsymbol{v}_{\tau s}) \tag{2.21}$$

$$div_s\boldsymbol{J}^0 = -\frac{\partial \rho_s^0}{\partial t} - divb(\boldsymbol{J}_s^0 + \rho_{s1}^0 \boldsymbol{v}_{1\tau s} + \rho_{s2}^0 \boldsymbol{v}_{2\tau s}) + (C_s \rho_s^0 - \frac{\partial \rho_s^0}{\partial n_s})\boldsymbol{v} \cdot \boldsymbol{n}_s \tag{2.22}$$

$$div_s\boldsymbol{D}^0 = \rho_s^0 \tag{2.23}$$

$$div_s\boldsymbol{B}^0 = 0 \tag{2.24}$$

where $\rho_{s1}^0 v_{1\tau s}$, $\rho_{s2}^0 v_{2\tau s}$ with $\rho_{s1}^0 + \rho_{s2}^0 = \rho_s^0$, represent densities of convection current sheet corresponding to the two faces of the discontinuity surface, $\mathbf{n}_s$ is the normal vector unit to the discontinuity surface and $C_s = -$ div$\mathbf{n}_s$ is the mean curvature of the discontinuity surface.

In the R^0 referential the constitutive equations are the same as in the case of immobile media. For example, an isotropic and homogeneous body, without hysteresis, without permanent polarization and magnetization and without imprinted electric field, has the following constitutive relations:

$$\boldsymbol{D}^0 = \varepsilon_e \boldsymbol{E}^0 \tag{2.25}$$

$$\boldsymbol{B}^0 = \mu \boldsymbol{H}^0 \tag{2.26}$$

$$\boldsymbol{J}^0 = \sigma \boldsymbol{E}^0 \tag{2.27}$$

In the fix referential R, for the same characteristics of the body, the constitutive equations are:

$$\boldsymbol{D} = \varepsilon_e(\boldsymbol{E}^0 + \boldsymbol{v} \times \boldsymbol{B}^0) \tag{2.28}$$

$$\boldsymbol{B} = \mu(\boldsymbol{H}^0 - \boldsymbol{v} \times \boldsymbol{D}^0) \tag{2.29}$$

$$\boldsymbol{J} = \sigma(\boldsymbol{E}^0 + \boldsymbol{v} \times \boldsymbol{B}^0) + \rho_v \boldsymbol{v} \tag{2.30}$$

Equations of the steady state AC magnetic regime of the electromagnetic field

This subchapter presents the mathematical model of the steady state AC regime of the electromagnetic field (quasi-static magnetic field) regime of the electromagnetic field. The electromagnetic finite element models developed along the thesis are based on this model.

This regime characterizes devices in which the electromagnetic field source consists of currents variable in time. The equations of the steady state AC magnetic in domains with immobile bodies are:

$$curl\boldsymbol{E} = -\frac{\partial \boldsymbol{B}}{\partial t} \tag{2.31}$$

$$curl\boldsymbol{H} = \boldsymbol{J} \tag{2.32}$$

$$div\boldsymbol{J} = 0 \tag{2.33}$$

$$div\boldsymbol{D} = \rho_v \tag{2.34}$$

$$div\boldsymbol{B} = 0 \tag{2.35}$$

Equation (2.35) allows defining an auxiliary quantity, **A**, called magnetic vector potential, and:

$$\boldsymbol{B} = curl\boldsymbol{A} \tag{2.36}$$

If (2.36) is introduced in (2.31) it is obtained:

$$curl\left(\boldsymbol{E} + \frac{\partial \boldsymbol{A}}{\partial t}\right) = 0 \tag{2.37}$$

which means the vector $\left(\boldsymbol{E} + \frac{\delta \boldsymbol{A}}{\delta t}\right)$ is irrotational, thus it can be expressed through the gradient of another auxiliary quantity, electric scalar potential V:

$$\boldsymbol{E} + \frac{\partial \boldsymbol{A}}{\partial t} = -gradV \tag{2.38}$$

The electric field strength,

$$\boldsymbol{E} = -gradV - \frac{\partial \boldsymbol{A}}{\partial t} \tag{2.39}$$

is the sum of the Coulombian electric field and the induced electric field strength. The current density **J** has two components, one corresponding to the Coulombian field – imposed by the exterior electric source and the second corresponding to the induced currents.

In order to ensure the univocally determination of the **A** and V potentials, it is necessary to impose in the computation domain a condition of the form:

$$div\boldsymbol{A} = \boldsymbol{f}(\boldsymbol{r}, t) \tag{2.40}$$

and on the boundary a condition of the form:

$$\boldsymbol{A} \cdot \boldsymbol{n}_{\Sigma} = g(\boldsymbol{r}_{\Sigma}, t) \tag{2.41}$$

In the general case, the local representation of the steady state AC magnetic field uses simultaneously both potentials. The equations to solve are:

$$curl\left(\frac{1}{\mu} curl\boldsymbol{A}\right) + \sigma \frac{\delta \boldsymbol{A}}{\delta t} = -\sigma gradV \tag{2.42}$$

$$div(\varepsilon_e gradV) + \varepsilon_e \frac{\delta}{\delta t}(div\boldsymbol{A}) + \rho_v = 0 \tag{2.43}$$

The imposing of the vector potential divergence (2.40) is in general correlated with the actual electromagnetic field problem. Thus, the most complex case is that in which the charges density ρ_v is not zero and both unknown potentials must be determined. In this case equation

$$div\boldsymbol{A} = \rho\sigma V \tag{2.44}$$

called Lorentz gauge condition, leads to the splitting of the system (2.42), (2.43) in equation of the vector potential, **A**:

$$curl\left(\frac{1}{\mu} curl\boldsymbol{A}\right) + \sigma \frac{\delta \boldsymbol{A}}{\delta t} = -grad\left(\frac{1}{\mu} div\boldsymbol{A}\right) \tag{2.45}$$

and the equation of the scalar potential, V:

$$-div(\varepsilon_e gradV) + \varepsilon_e \sigma\mu \frac{\partial V}{\partial t} = \rho_v \tag{2.46}$$

This model of the steady state AC magnetic field takes into consideration the most general electromagnetic phenomena. To solve the equations (2.45) and (2.46) means to find in each node of the mesh four unknown scalar quantities, namely the three components of the vector magnetic potential and the electric potential.

A second possibility to impose the univocally condition of form (2.40) takes into account that in all electromagnetic devices with steady state AC magnetic field the electric charges volume density is zero, $\rho_v = 0$. Taking into account the Coulomb gauge condition div$\mathbf{A} = 0$, the equation of the scalar potential (1.44) becomes:

$$div(\varepsilon_e gradV) = 0 \tag{2.47}$$

In this field model, the differential equations of the steady state AC magnetic field are:

$$curl\left(\frac{1}{\mu} curl\boldsymbol{A}\right) + \sigma\frac{\partial \boldsymbol{A}}{\partial t} = -\sigma gradV \tag{2.48}$$

$$div(\varepsilon_e gradV) = 0 \tag{2.49}$$

$$div\boldsymbol{A} = 0 \tag{2.50}$$

Sources of this field can be current densities imposed in some non-conductive regions of the domain, total current in some conductive regions, densities of current sheets and surface electric charge densities on the discontinuity surfaces.

Uniqueness of the solution of the system (2.48), (2.49), (2.50) is ensured when besides field sources there are known:

- physical properties: $\mu(\boldsymbol{r},t)$, $\sigma(\boldsymbol{r},t)$, $\varepsilon_e(\boldsymbol{r},t)$
- initial conditions (null conditions in general), through which values of the electric and magnetic field strength or potential values are imposed at initial time step.
- boundary conditions

In a 2D axisymmetric problem, with Oz axis of the cylindrical coordinate system (r,θ,z) being the symmetry axis, the conduction current density has an azimuth orientation, **J**[0,J(r,z,t),0]]. The field quantities are independent from the azimuth coordinate θ, and the magnetic vector potential has azimuth orientation, **A**[0, A(r,z,t),0]. The electric field has also azimuth orientation, **E**[0,E(r,z,t),0)]. Corroborating this with (1.40) means:

$$\frac{\partial V}{\partial z} = \frac{\partial V}{\partial t} = 0 \tag{2.51}$$

respectively that the electric potential depends only on the θ coordinate. From (2.39) results the following relation which shows that $\frac{\partial V}{\partial \theta}$ does not depends on z coordinate.

$$E(r,z,t) = -\frac{1}{r}\frac{\partial V}{\partial \theta} - \frac{\partial A}{\partial t} \tag{2.52}$$

2.3 Fundamentals on fluid dynamics [139], [140]

Fluid dynamics is a branch of fluid mechanics and is the science of fluids in motion. It includes aerodynamics, the study of air and other gases in motion and hydrodynamics, the study of liquids in motion. The fundamental laws of fluid dynamics are the following: conservation of mass, conservation of momentum, conservation of energy.

Compressibility is a measure of the relative volume change of a fluid or solid as a response to a pressure change. All fluids are compressible in some degree but in many situations the changes in pressure and temperature are sufficiently small that the changes in density are negligible. In this case the flow can be considered as an incompressible flow. The compressible flow refers mainly to gas flows.

There are called *viscous* flows are those in which fluid friction has significant effects on the fluid motion. It is called *inviscid* flow an approximation in which the viscosity is completely neglected.

Matter in any aggregation state is composed of molecules separated by interstices. On a macroscopic scale, materials have discontinuities. However, certain physical phenomena can be modeled assuming the materials exist as a *continuum*, meaning the matter in the body is continuously distributed and fills the entire region of space it occupies. A continuum is a body that can be continually sub-divided into infinitesimal elements with the same properties as the bulk material.

In continuum mechanics *stress* is a physical quantity that expresses the internal forces that neighboring particles of a continuous material exert on each other.

Stress inside a body appears in general as reaction to external forces as gravity and contact forces or to friction. Any deformation of a solid material generates an internal *elastic stress* that tends to restore the material to its original state. In liquids and gases, only deformations that change the volume generate persistent elastic stress. However, if the deformation is gradually changing with time, even in fluids there will usually be some *viscous stress*, opposing that change. Elastic and viscous stresses are usually combined under the name *mechanical stress*. Stress is defined as the average force per unit area that some particle of a body exerts on an adjacent particle, across an imaginary surface that separates them.

Quantitatively, the stress is expressed by the *Cauchy traction vector* **T** defined as the traction force **F** between adjacent parts of the material across an imaginary separating surface S, divided by the area of S. In a fluid at rest the force is perpendicular to the surface, and the stress is represented by the pressure. In a flow of viscous liquid, the force **F** may not be perpendicular to S, hence the stress across a surface must be regarded a vector quantity, not a scalar. The direction and magnitude generally depend on the orientation of S. Thus the stress state of the material must be described by a tensor, called the *Cauchy stress tensor*; which is a linear function that relates the normal vector **n** to the surface S to the stress **T** across S, Fig. 2.2.

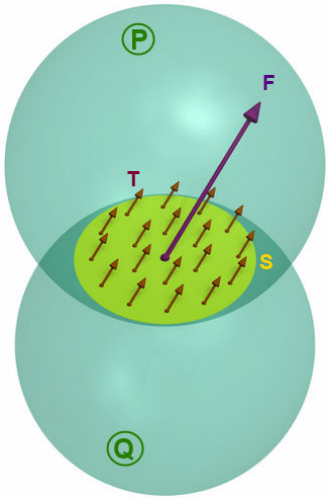

Fig. 2.2 The stress **T** across the surface S is the force **F** that particle P exerts on particle Q divided by the area of S

The *viscosity* of a fluid is a measure of its resistance to gradual deformation by shear stress. Viscosity is due to friction between neighboring layers of the fluid that are moving at different velocities. In the idealized situation when a layer of fluid is comprised between two parallel plates, if the speed of the top parcel is small enough,

the fluid particles will move parallel to it, and their speed will vary linearly from zero at the bottom to v at the top. Each layer of fluid will move faster than the one just below it, and friction between them will give rise to a force resisting their relative motion. In particular, the fluid will apply on the top plate a force in the direction opposite to its motion, and an equal but opposite to the bottom plate. An external force is therefore required in order to keep the top plate moving at constant speed. The magnitude F of this force is found to be proportional to the speed v and the area A of each plate, and inversely proportional to their separation y:

$$F = \eta A \frac{v}{y} \tag{2.53}$$

Thus is defined the *dynamic viscosity* η as the proportionality factor in (1.54). The *kinematic viscosity* is the dynamic viscosity divided by the fluid density.

A flow is *steady* when all the time derivatives of a flow field vanish. Steady-state flow refers to the condition where the fluid properties at a point in the system do not change over time.

Laminar flow occurs when a fluid flows in parallel layers, with no disruption between the layers. At low velocities the fluid tends to flow without lateral mixing, and adjacent layers slide past one another. There are no cross fluid currents perpendicular to the direction of flow, nor eddies or swirls.

Turbulent flow is a flow regime characterized by chaotic property changes. This includes rapid variation of pressure and velocity in space and time. Turbulent flows are unsteady by definition.

Reynolds number (Re) is a dimensionless number equal to the ratio of inertial forces to viscous forces which quantifies the relative importance of the two types of forces for given flow conditions. When Reynolds number is very low, Re<<1, it means that inertial forces can be neglected compared to viscous forces. High Reynolds numbers indicate that the inertial forces are more significant than the viscous (friction) forces.

Reynolds number can be defined with various relations for a number of different situations where a fluid is in relative motion to a surface, but generally it can be defined as:

$$\mathrm{Re} = \frac{d v L}{\eta} \tag{2.54}$$

where d is the mass density, v is the mean velocity, L represents a characteristic length dimension, η is the dynamic viscosity and ν the kinematic viscosity.

The flow of a fluid becomes more and more chaotic as the inertial forces become predominant relative to the viscous forces, namely Re is much higher than unit. For a pipe flow, the Re number in the range (2400 - 4000) represent the transition interval, where laminar and turbulent flows are possible. When Re is under 2400 the flow is laminar, when over 4000 turbulent, but the value of Re for which a flow becomes turbulent is depending on many variables.

Fig. 2.3 presents the typical parabolic shape of the flow profile in two laminar flows and the typical profile in case of a turbulent flow between two walls. Fig. 2.4 presents the flow past a rectangular object from laminar cases to more and more turbulent, as the Reynolds number increases.

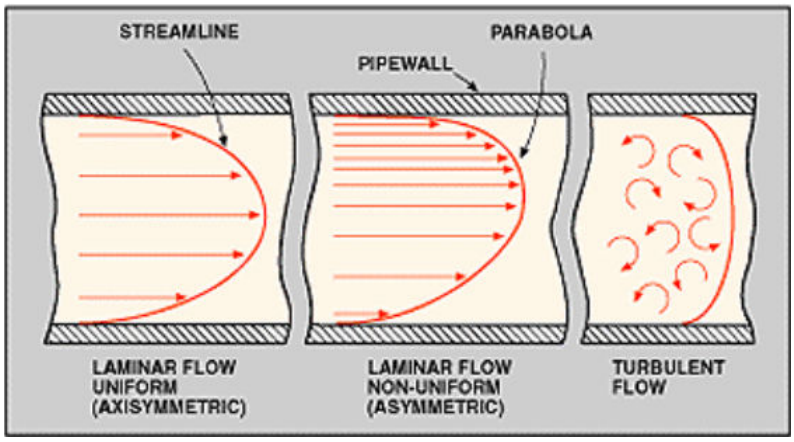

Fig. 2.3 Velocity profiles for laminar and turbulent flow

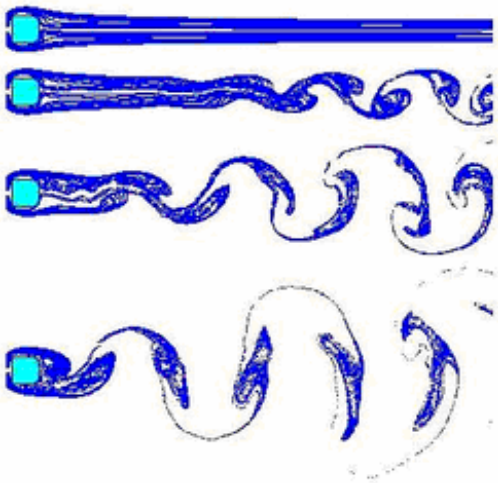

Fig. 2.4 Transition from laminar to turbulent flow past a rectangular object

The *Navier–Stokes equation* describes the motion of fluids. This equation arise from applying Newton's second law to fluid motion, together with the assumption that the stress in the fluid is the sum of a diffusing viscous term proportional to the gradient of velocity and a pressure term, hence the Navier-Stokes equation describes the *viscous flow*. For an incompressible flow of a Newtonian fluid with constant viscosity, the Navier-Stokes equation in vectorial form is:

$$d\left(\frac{\partial \boldsymbol{v}}{\partial t} + grad\,\frac{\|\boldsymbol{v}\|^2}{2} + rot\,\boldsymbol{v}\times\boldsymbol{v}\right) = -grad\;p + \eta\,div(\boldsymbol{grad}\;\boldsymbol{v}) + \boldsymbol{f} \qquad (2.55)$$

where d is the fluid mass density, v is the flow velocity, p is the pressure, η is the dynamic viscosity and f represent the body force density acting on the fluid. If the equation is written with del operator ∇ and the vector Laplacian ∇^2 operator it has the following expression:

$$d\left(\frac{\partial \boldsymbol{v}}{\partial t} + \boldsymbol{v}\cdot\nabla\boldsymbol{v}\right) = -\nabla p + \eta\nabla^2\boldsymbol{v} + \boldsymbol{f} \qquad (2.56)$$

The Navier–Stokes equation is a non-linear partial differential equation. The Navier–Stokes equation dictates not position but rather velocity. A solution of the

Navier–Stokes equations is called a velocity field or flow field, which is a description of the velocity of the fluid at a given point in space and time. Once the velocity field is solved, other quantities as flow rate may be found.

The left term represents the fluid's inertia. The term between brackets describes the acceleration and is composed of time dependent and convective effects. The non-linear quantity $\boldsymbol{v}\cdot\nabla\boldsymbol{v}$ represents the *convective acceleration*, which is an effect of time independent acceleration of a fluid with respect to space. While individual fluid particles are indeed experiencing time dependent acceleration, the convective acceleration of the flow field is a spatial effect, one example being fluid speeding up in a nozzle. Convective acceleration is present in most flows, one-dimensional incompressible flow being an exception.

The right side of the equation is a summation of divergence of stress (pressure and shear stress) and body forces. These forces consist of gravity forces but may include other types such as electromagnetic forces in MHD.

In some cases, such as one-dimensional flow the equation can be simplified to linear equations. The nonlinearity makes most problems difficult or impossible to solve and is the main contributor to the *turbulence*. Hence, any *convective* flow, whether turbulent or not, will involve nonlinearity. An example of convective but *laminar flow* would be the passage of a viscous fluid (for example, oil) through a small converging nozzle.

Regardless of the flow assumptions, a statement of the conservation of mass is necessary to complete the flow model. This is achieved through the mass continuity equation, given in its general form as:

$$\frac{\partial p}{\partial t}+\nabla\cdot(d\boldsymbol{v})=0 \tag{2.57}$$

If the Navier-Stokes equation is written in the cylindrical coordinates system r,θ,z, the following system of equations is obtained:

- on the r direction:

$$d\left(\frac{\partial v_r}{\partial t}+v_r\frac{\partial v_r}{\partial r}+\frac{v_\theta}{r}\frac{\partial v_r}{\partial\theta}+v_z\frac{\partial v_r}{\partial z}-\frac{v_\theta}{r}\right)=-\frac{\partial p}{\partial r}+\eta\left[\frac{1}{r}\frac{\partial}{\partial r}\left(r\frac{\partial v_r}{\partial r}\right)+\frac{1}{r^2}\frac{\partial^2 v_r}{\partial\theta^2}+\frac{\partial^2 v_r}{\partial z^2}-\frac{v_r}{r^2}-\frac{2}{r^2}\frac{\partial v_\theta}{\partial\theta}\right]+dg_r \tag{2.58}$$

- on the θ direction:

$$d\left(\frac{\partial v_\theta}{\partial t}+v_r\frac{\partial v_\theta}{\partial r}+\frac{v_\theta}{r}\frac{\partial v_\theta}{\partial\theta}+v_z\frac{\partial v_\theta}{\partial z}+\frac{v_r v_\theta}{r}\right)=-\frac{1}{r}\frac{\delta p}{\delta\theta}+\eta\left[\frac{1}{r}\frac{\partial}{\partial r}\left(r\frac{\partial v_\theta}{\partial r}\right)+\frac{1}{r^2}\frac{\partial^2 v_\theta}{\partial\theta^2}+\frac{\partial^2 v_\theta}{\partial z^2}+\frac{2}{r^2}\frac{\partial v_r}{\partial\theta}+\frac{v_\theta}{r^2}\right]+dg_\theta \tag{2.59}$$

- on the z direction:

$$d\left(\frac{\partial v_z}{\partial t}+v_r\frac{\partial v_z}{\partial r}+\frac{v_\theta}{r}\frac{\partial v_z}{\partial\theta}+v_z\frac{\partial v_z}{\partial z}\right)=-\frac{\partial p}{\partial z}+\eta\left[\frac{1}{r}\frac{\partial}{\partial r}\left(r\frac{\partial v_z}{\partial r}\right)+\frac{1}{r^2}\frac{\partial^2 v_z}{\partial\theta^2}+\frac{\partial^2 v_z}{\partial z^2}\right]+dg_z \tag{2.60}$$

where $\mathbf{g}_r$, $\mathbf{g}_\theta$, $\mathbf{g}_z$, $\mathbf{v}_r$, $\mathbf{v}_\theta$, $\mathbf{v}_z$ are the projection of the gravity, respectively velocity on the three direction of the coordinate system. The continuity equation is:

$$\frac{\partial p}{\partial t}+\frac{1}{r}\frac{\partial}{\partial r}(drv_r)+\frac{1}{r}\frac{\partial(dv_\theta)}{\partial\theta}+\frac{\partial(dv_z)}{\partial z}=0 \tag{2.61}$$

The unknowns of the system of equations composed by (2.58) – (2.60) are: the three components of the velocity, $\mathbf{v}_r = v_r(\mathbf{r},t)$, $\mathbf{v}_\theta = v_\theta(\mathbf{r},t)$, $\mathbf{v}_z = v_z(\mathbf{r},t)$, the pressure, $p = p(\mathbf{r},t)$ and the mass density $d = d(\mathbf{r},t)$, where r is the position vector of structure $\mathbf{r}[r_r, r_\theta, r_z]$.

In order to solve the system it is needed to know:

- *initial conditions* – by which is specified the repartition of the velocity field, pressure and mass density at the initial moment of the flow t = 0, in the entire domain occupied by the fluid
- *boundary conditions* – by which is specified the fluid parameters on the domain boundaries. At the contact with a solid surface is taken into account that the surface is impervious and due to friction the fluid particles are bonded to the surface of the solid body.

2.4 Fundamentals on magnetohydodynamics [141]

The MHD equations consist of:

Continuity equation:

$$\frac{\partial d}{\partial t} + \nabla \cdot (d v) = 0 \tag{2.62}$$

Cauchy momentum equation:

$$d\left(\frac{\partial}{\partial t} + \boldsymbol{v} \cdot \nabla\right) v = \boldsymbol{J} \times \boldsymbol{B} - \nabla p \tag{2.63}$$

where the term **J** x **B** is the electromagnetic (Lorentz) force.

Maxwell equations:

$$curl\boldsymbol{E} = -\frac{\partial \boldsymbol{B}}{\partial t} \tag{2.64}$$

$$curl\boldsymbol{H} = \boldsymbol{J} + \frac{\partial \boldsymbol{D}}{\partial t} \tag{2.65}$$

$$div\boldsymbol{B} = 0 \tag{2.66}$$

$$div\boldsymbol{D} = \rho_v \tag{2.67}$$

The constitutive equations:

$$\boldsymbol{D} = \varepsilon_e(\boldsymbol{E} + \boldsymbol{v} \times \boldsymbol{B}) \tag{2.68}$$

$$\boldsymbol{B} = \mu(\boldsymbol{H} - \boldsymbol{v} \times \boldsymbol{D}) \tag{2.69}$$

$$\boldsymbol{J} = \sigma(\boldsymbol{E} + \boldsymbol{v} \times \boldsymbol{B}) + \rho_v \boldsymbol{v} \tag{2.70}$$

Taking into account that the fluid velocity is present in the constitutive equations, it is obvious that the electromagnetic field can not be determined independently of the movement. The fluid motion induces an electromagnetic field, expressed by the constitutive equations and this field, that always satisfies the Maxwell equations, influences at its turn the fluid flow through the expression of the electromagnetic force density. It can be said that the mathematical expression of the MHD interaction resides in the constitutive equations. The solution of the Navier-Stokes equation is a velocity field which intervenes in the constitutive equations which leads to changes in the electromagnetic quantities. From the electromagnetic changes results the update of the electromagnetic force, which renews the flowing condition, respectively the velocity.

Other MHD aspects

It is defined the non-dimensional *magnetic Reynolds number*:

$$R_m = \frac{\mu}{\rho} vL \tag{2.71}$$

where μ is the magnetic permeability, ρ is the electric resistivity, v is a typical velocity scale of the flow and L is a typical length scale.

When this number is much lower than unity, advection is relatively unimportant, and so the magnetic field will tend to relax towards a purely diffusive state, determined by the boundary conditions rather than the flow. When the magnetic Reynolds number is much higher than one, diffusion is relatively unimportant on the length scale L. Flux lines of the magnetic field are then advected with the fluid flow, until such time as gradients are concentrated into regions of short enough length scale that diffusion can balance advection.

The *interaction parameter* is the ratio between the time scales of the convection of the fluid and action of the electromagnetic forces:

$$N = \frac{B^2 L}{\rho d v} \tag{2.72}$$

where B is the magnetic flux density, L is the characteristic length scale, ρ is the electric resistivity, d is the mass density and v a typical velocity of the flow.

Hartmann number characterizes the balance between the electromagnetic forces and the viscous forces:

$$Ha = BL\sqrt{\frac{1}{\rho\eta}} \tag{2.73}$$

where η is the dynamic viscosity.

The *Hartmann layer* represents the viscous limit layer thickness and has the following expression:

$$\delta_{Ha} = \frac{1}{B}\sqrt{\eta\rho} \tag{2.74}$$

This layer is also called *viscous sublayer* or *laminar sublayer*, because in this layer the flow is laminar even if the principal flow is turbulent. Fig. 2.5 presents the velocity profile of a turbulent flow near one wall. The velocity decreases in radial direction until at the wall it is null. Because of this, the Reynolds number decrease until the flow crosses the threshold from turbulent to laminar flow. The *turbulence generation layer* represents the thickness of the layer between wall and fully developed turbulent flow. It contains the viscous sublayer and a buffer layer in which the flow may be either laminar either turbulent. In the *outer layer* the flow is completely turbulent.

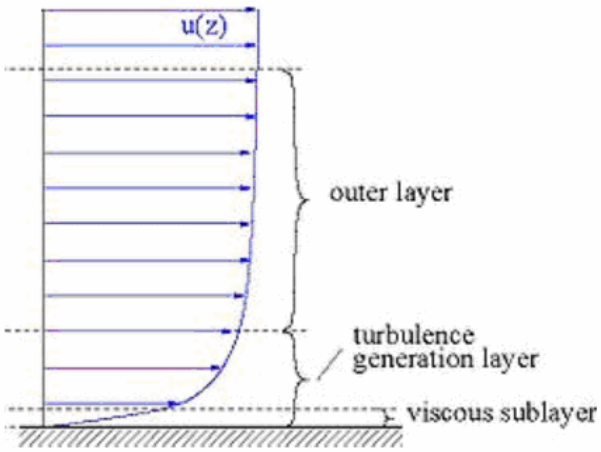

Fig. 2.5 Division of the turbulent profile

It is introduced the expression of an electromagnetic parameter always important in processing by induction: the *electromagnetic field penetration depth (skin depth)*:

$$\delta = \sqrt{\frac{2\rho}{\omega\mu}} \tag{2.75}$$

where $\omega = 2\pi f$ is the angular frequency (pulsation) and f is the supply frequency. The current density J in a conductor, respectively in the channel of an AC supply electromagnetic pump, decreases exponentially from its value at the surface, J_s according to the depth r from the surface after the law $J = J_s e^{-r/\delta}$, where δ is the skin depth. The skin depth is thus defined as the depth below the surface of the solid conductor at which the current density has decreased to 1/e of J_s.

The MHD flow in specific conditions as the electromagnetic pumps has many other characteristics as flattening of the velocity profile or important changes in the profiles of current and force under the influence of the electromagnetic field, which will be contemplated in chapter 6.

CONCLUSIONS

This chapter summarized theoretical aspects of numerical models, finite element models and the two physical phenomena mainly involved in the operation of electromagnetic pumps, namely electromagnetism and fluid flow.

The most significant part is found in the last paragraph, where the MHD equations are presented and the MHD interaction is explained based on the constitutive equations which from the mathematical point of view represent the link between quantities of the two different physics.

Chapter 3: Electromagnetic pumping of molten salts

This chapter is devoted to study the possibility of molten salts electromagnetic pumping. Certainly, the answer is meaningful for an entire range of electromagnetic processes where fluids with relatively high electrical resistivity are involved.

The electric resistivity of molten salts is in the range of $1.43 \cdot 10^{-3}$ to 10^{-2} Ωm, that is much higher than the one of metals that have the magnitude order of 10^{-6} to 10^{-8} Ωm. Unlike in the case of metals, the resistivity of molten salts decreases with the increase of the temperature. Molten salts have in general good qualities of a heat transfer agent, fact that can be very advantageous in some applications, [142]-[145].

Traditionally, molten salts such as sodium fluoride (NaF) and aluminum fluoride (AlF_3) are used as electrolyte in the aluminum production industry. Currently molten salts are envisaged for their thermal properties in two industrial applications: as a heat agent in the solar plants that generates electric energy by conversion of the Sun's energy and as a coolant in the Molten Salts Reactors (MSR). Fig. 3.1 presents the principal elements of a MSR from which is mentioned: reactor, control bars, pumps for molten salt, heat exchangers and the turbine unit that drives the turbine of the electric generator.

In the primary loop of heat extraction of a MSR, Fig. 3.1, the coolant is a mixture of molten slats which can operate at very high temperatures and still remaining at low pressure. The salts used in this purpose are much less reactive than the liquid sodium (used in Sodium Fast Reactors) and this constitutes an advantage with respect to the mechanical wear and the safety increase. In MSR the nuclear fuel is dissolved in the coolant thus the production of the fuel in the form of bars is not necessary anymore and the reactor structure becomes simpler. Molten salts are more efficient in heat removal from the reactor core and usage of molten salts as coolant has as effect the reduction of the quantity of piping in the primary loop and the decrease of the reactor cores dimensions as this components decrease themselves in size.

Oak Ridge National Laboratory made researches in the field of nuclear reactors with molten salts even from the 60ies. These researches have materialized through building and keeping in operation four years of a 7.4 MW_{th} experimental nuclear reactor with molten salts. The solution of uranium based fuel and the molten salt coolant had the formula $LiF\text{-}BeF_2\text{-}ZrF_4\text{-}UF_4$ (65%-30%-5%-0.1%). The experimental reactor had graphite moderator and the coolant was reaching approximately 650°C.

The current preoccupations with respect to finding the most efficient and secure architecture for the Generation IV of nuclear reactors take into account as a variant the MSR. The experiments of the Oak Ridge National highlight the technological advantages of using molten salts in the nuclear technique. The MSR plants have an increased security in exploitation and maintenance. The fluorine based salts are physically and chemically stable at atmospheric pressure, at intense heat and in radioactive medium. Because the molten salt remains at low pressure during entire operation cycle, in the reactor core do not exist high pressure vapors. This means that such a plant can not explode due to a too high accumulated pressure and that the core doesn't need a special pressure resistant construction. The mixture fuel – coolant operates at temperatures much higher than that of other coolants of other nuclear reactor types. The operation temperature of molten salts can vary from 650°C in tested systems up to 950°C in some projects. This fact allows using turbines with more efficient operation cycles.

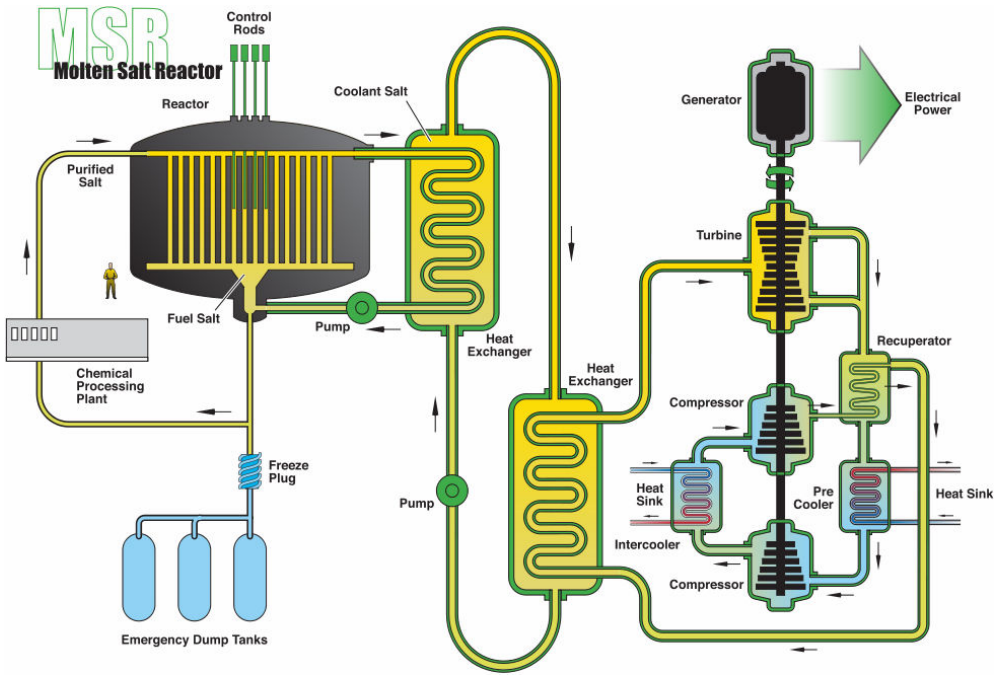

Fig. 3.1 Principle of heat transport in a Molten Salts Reactor, [146]

Regarding the use of molten salts as thermal agent due to its high heat capacity it is mentioned the tower systems, Fig. 3.2 and line focusing systems, Fig. 3.3. The tower systems are based on a concentric display of large mirrors called *heliostats* which follow the Sun direction and focus the solar energy unto a large tank situated on top of a tower. The tank contains a high heat capacity substance which when reached maximum temperature is directly used in a turbine – generator unit or deposited in insulated tanks for later use.

In the line focusing systems, a system of parabolic troughs focus the solar radiation on a pipes situated along the focal lines of the trough concentrators. The thermal agent is pumped through the piping and the heat accumulated is used in driving a steam turbine.

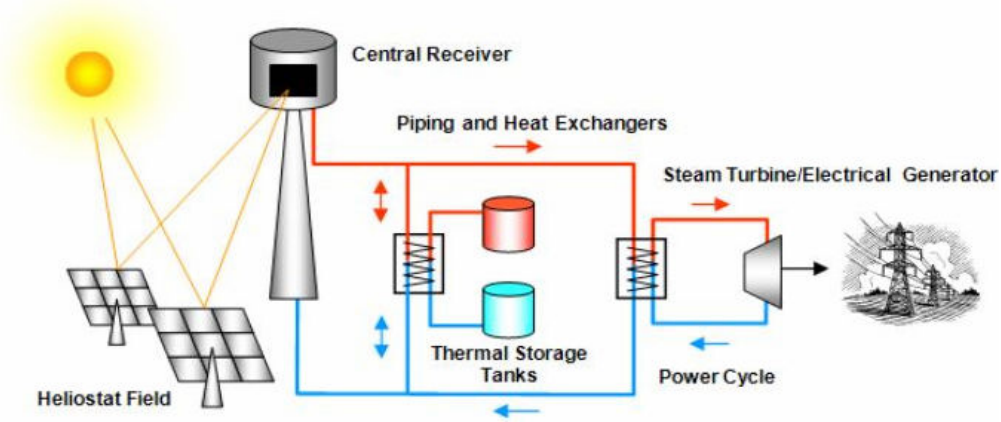

Fig. 3.2 Tower systems [147]

First liquids used in such systems were mineral oils, but newer plants, [148], based on molten salts. The molten salt mixtures best suited in the purpose of heat transfer are the so called *Solar Salt* (60% $NaNO_3$ and 40% KNO_3) and a salt with the commercial name HitecXL (48% $Ca(NO_3)_2$, 7% $NaNO_3$ and 45% KNO_3).

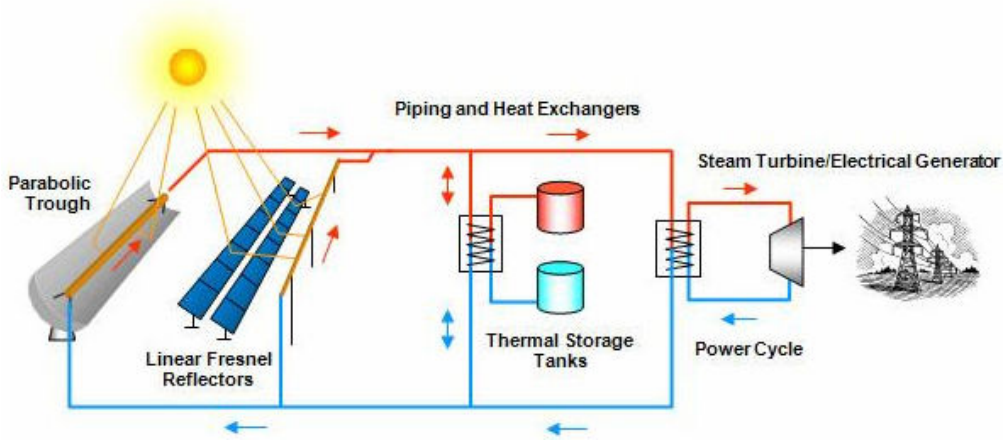

Fig. 3.3 Line focusing system [147]

The possible use of electromagnetic pumps in such Concentrated Solar Plants (CSP) can be a solution for the main challenge the molten salts raises in such applications. The solidification temperature of molten salts is relatively high. If synthetic oils become so viscous and consequently inoperable at 15°C, the *solar salt* solidifies at 220°C and the HitecXL, which has a higher price, solidifies at 120°C.

With the mechanical pumps the only possibility of preventing solidification during the night is a good piping insulation, adding extra heating sources and continuous circulation of the salt even if it is not collecting any energy during the night. If an induction pump would be used to drive the molten salt, the induced Joule power transformed in heat could prevent from solidification, it would be recovered by the turbine conversion and the extra heating sources would become pointless, [28].

The purpose of this chapter consists in investigation of the possibilities of electromagnetic pumping of molten salts applying the knowledge historically fixed relating the electromagnetic pumps for molten metals. For comparison reasons the models presented in paragraph 3.1 are applied also for liquid sodium. Based on the finite element models, in this chapter are evaluated and compared the parameters of the electromagnetic pumps, of induction type – with cylindrical, annular and rectangular channel and of conduction type with very low supply frequency. This measure is necessary in order to prevent the apparition of electrolysis in the case of pumping molten salts in pumps of DC current. The two materials of different electrical resistivity for which the electromagnetic pumping is tested have the following electrical resistivities: lithium fluoride (LiF) salt at 850°C, $\rho = 0.33 \cdot 10^{-2}$ Ωm and liquid sodium with $\rho = 0.33 \cdot 10^{-6}$ Ωm. The main objective consists in the evaluation of the correlations between the pumps geometrical, physical and supply parameters so that the pumps to ensure o reference value of the electromagnetic pressure $p_e = 10^5$ N/m^2. This pressure represents the ratio between the electromagnetic force and the area of the flowing section.

For the entire thesis some notions are specified:

- *Block-pumping* denotes the movement of the electroconductive fluid as a solid body.
- A *solid conductor* is characterized by non-uniform repartition of the current density along the conductor's thickness dependent on the penetration depth, (2.75).
- When using the expression *electromagnetic model / study* means that the calculation is strictly from the electromagnetic point of view, namely the

results are only electromagnetic quantities and the electroconductive liquid (molten salt, sodium, aluminum, etc) is considered as a solid conductor. The only type of motion considered in the electromagnetic models is translation motion, namely the electroconductive liquid is modeled in *block-pumping hypothesis*.

- A *magnetohydrodynamic model / study* imply renouncing to the solid conductor block-pumping hypothesis and considers the real flow of the electroconductive fluid, characterized by non-uniform velocity profiles as in Fig. 2.3.

3.1. Comparison between molten salts and sodium pumping based on 2D electromagnetic models

All the investigations in Chapter 3 are studies solved in the frequency domain. The molten salts, respectively sodium are immobile solid conductors regions.

3.1.1 Cylindrical linear induction pump for LiF (CLIP-LiF)

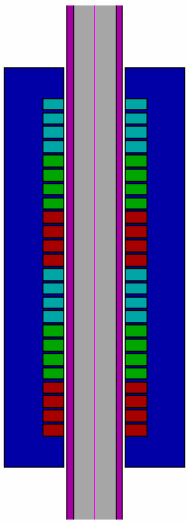

Fig. 3.4 Cylindric Linear Induction Pump

The electromagnetic structure in Fig. 3.4 corresponds to a three phased cylindrical inductor with two poles and eight circular coils per phase. The pole pitch is 720 mm and the length of the inductor is 1690 mm. The pumping cylindrical channel has the inner radius R_i = 100 mm and the inner and outer radius of the inductor are 145 mm, respectively 425 mm. The slots cross section is 50 mm x 100 mm and the mean value of the current density over the slots cross section is 6 A/mm^2. The phases of the current density in the three phase windings are 0º, -120º, +120º. The magnetic core is characterized by the magnetic saturation 1.4 T and by the initial relative permeability 300.

In order to create the reference value of the electromagnetic pressure p_e in the pump's channel, the necessary electromagnetic force is $F_{ec} = p_e \pi R_i^2 = 3140$ N. In Figs. 3.5 – 3.7 are represented the dependences on the supply frequency of the electromagnetic force, Joule power, and of the ratio between electromagnetic force and Joule power. From these graphic representations the conclusion is that the maximum pumping force corresponds to the frequency 280 kHz and that the value of the ratio pumping force over Joule power increases with the decrease of the frequency.

As it can be observed in Fig. 3.5, the desired value 3140 N of the pumping force corresponds to the frequency f_c = 30.5 kHz. Figs. 3.8 – 3.10 present the lines of the electromagnetic field, color map of the magnetic flux density, electromagnetic force density for phase 60º. Fig. 3.11 presents the module of the current density in the molten salt.

The value obtained for the Joule power developed in the molten salt is P_c = 116 MW and the reactive power of the pump is Q_c = 8090 MVAr.

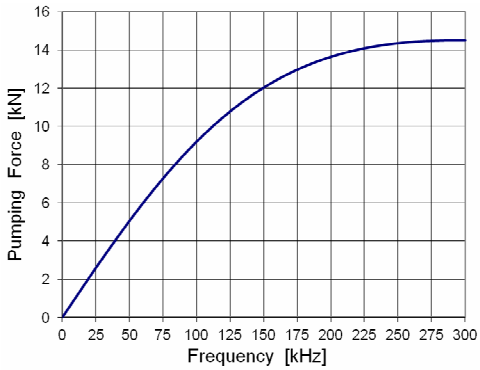

Fig. 3.5 Dependence of pumping Force on frequency, CLIP-LiF

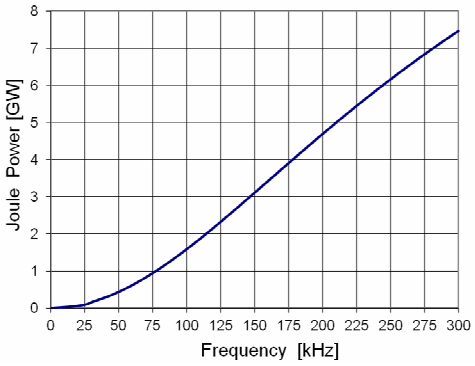

Fig. 3.6 Dependence of Joule power on frequency, CLIP-LiF

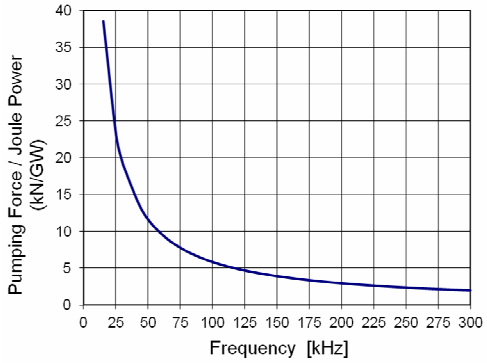

Fig. 3.7 Dependence of Pumping force/Joule power ratio On frequency, CLIP-LiF

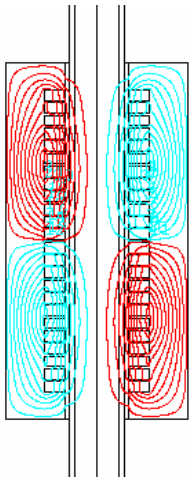

Fig. 3.8 Magnetic field lines, CLIP-LiF

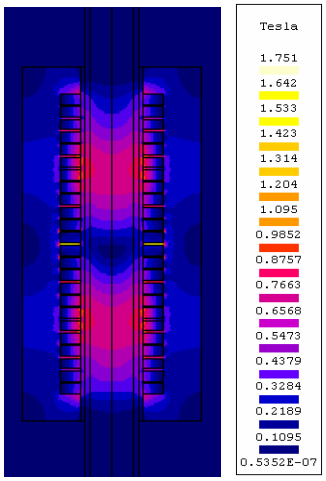

Fig. 3.9 Magnetic flux density, CLIP-LiF

If all the eight coils belonging to one phase of the inductor are series connected, and each coil has w turns, results the following rated values of the phase current and supply voltage:

$$I = 30000/w , \quad U = 155877w \tag{3.1}$$

If the eight coils are parallel connected, the rated values of the phase current and supply voltage are:

$$I = 240000/w , \quad U = 19484w \tag{3.2}$$

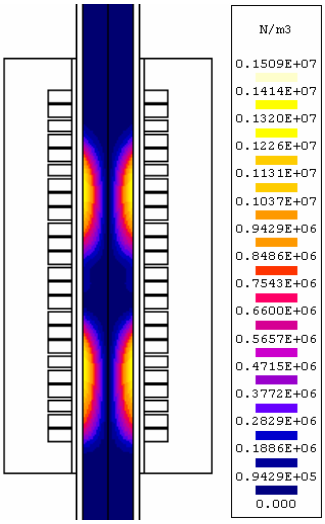

Fig. 3.10 Pumping force density, CLIP-LiF

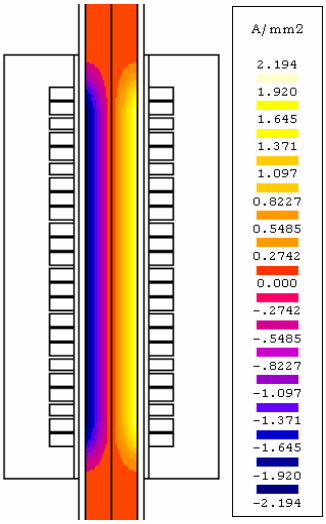

Fig. 3.11 Induced current density, CLIP-LiF

No matter the considered number of turns w, the two sets of rated data (3.1, 3.2) are technically impossible to be ensured, fact which leads to the conclusion that the cylindrical linear induction pump with medium supply frequency, 30.5 kHz, is not suitable for molten salts pumping.

3.1.2 Cylindrical linear induction pump for sodium (CLIP-Na)

The purpose of the models with sodium is not to design an optimum geometry and supply but to calculate the supply current density needed to generate the same rated electromagnetic pressure for the same flowing section when the forces are developed in a much electroconductive material.

The study for determination of frequency was not carried out anymore and the 50 Hz frequency was considered, taking into account the much higher conductivity of the liquid metal.

In order to produce the same force of 3140 N, it is necessary a mean current density over the slot cross-section of only 3.5 A/mm^2.

Regarding the active and reactive power induced in the channel, the differences are significant. The value obtained for the Joule power developed in the liquid sodium is P_c = 276 kW, and the reactive power of the pump is Q_c = 320 kVAr.

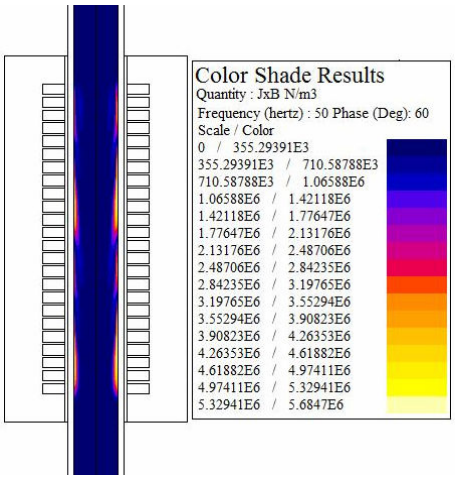

Fig. 3.12 Pumping force density, CLIP-Na

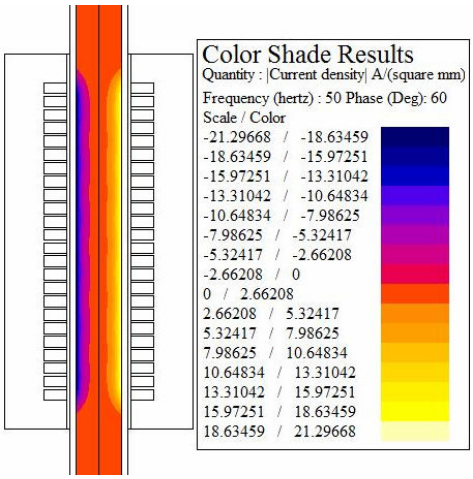

Fig. 3.13 Induced currents density, CLIP-Na

Fig. 3.9 highlights a smaller penetration depth in the case of sodium, which means a more pronounced diminution of the electromagnetic force density along the radial direction.

Thus, at 50 Hz, the recirculation phenomenon in the middle zone of the channel could be even more plausible in the sodium case. Fig. 3.10 represents the induced current color map where the values are much higher then those in Fig. 3.8. A supply of a lower frequency than 50 Hz could decrease the recirculation effect.

3.1.3 Annular linear induction pump for LiF (ALIP-LiF)

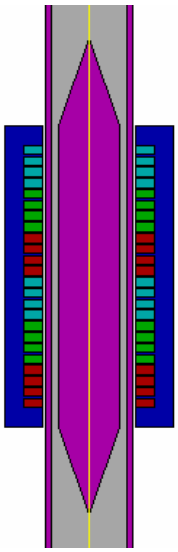

Fig.3.14 Annular linear induction pump

The structure in Fig. 3.14 corresponds to an induction pump with annular cross-section of the channel. The inductor of this pump is similar with the one presented above, with eight circular coils per phase, pole pith length 720 mm and inductor length 1640 mm. The ratio between the interior and exterior radii of the annular section of the channel is R_1/R_2 = 160 mm / 200 mm. The interior and exterior radii of the inductor have the values 245 mm, respectively 445 mm. The values of the slots dimensions and supply current density are the same as in the CLIP case.

The nonlinear magnetic core of the inductor is characterized by an saturation magnetic flux density 2 T and the initial relative permeability 3000. In order to obtain the reference value for the electromagnetic pressure, the electromagnetic force to develop is $F_{ea} = p_e\pi(R_2^2 - R_1^2) = 4524$ N. The dependences on the supply frequency of the electromagnetic force, Joule power and of the ratio electromagnetic force/Joule power are presented in Figs. 3.15 – 3.17 and show that the maximum pumping force corresponds to the frequency 150 kHz. The value 4524 N, imposed for the electromagnetic force corresponds to the frequency f_c = 5,9 kHz.

Figs. 3.18 – 3.20 show the results regarding the electromagnetic field lines, magnetic flux density color map and pumping force density for the phase 60º.

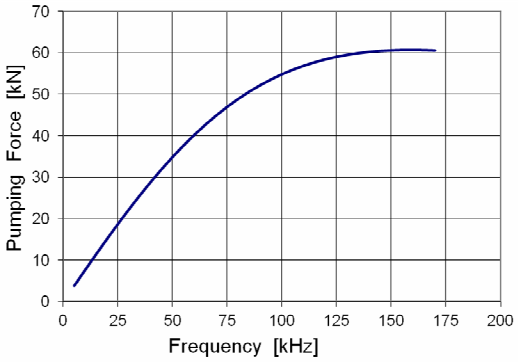

Fig. 3.15 Dependance of pumping force on frequency, ALIP-LiF

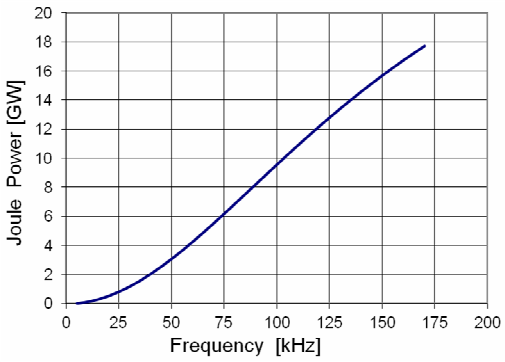

Fig. 3.16 Joule power dependance of frequency, ALIP-LiF

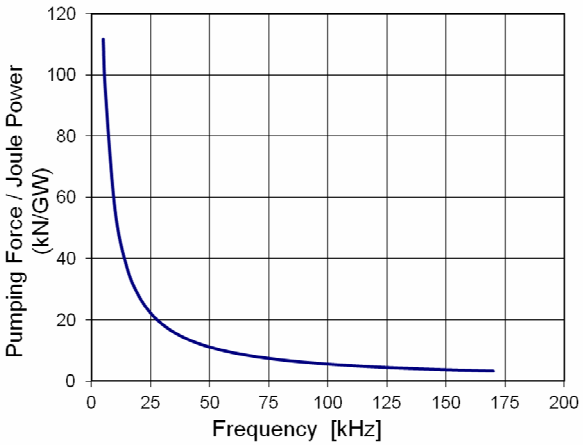

Fig. 3.17 Pumping force/Joule power ratio dependence of frequency, ALIP-LiF

Fig. 3.21 presents the color map of the current density in the molten salt. The Joule power developed in the molten salt is P_a = 47.8 MW and the reactive power of the pump is Q_a = 3420 MVAr.

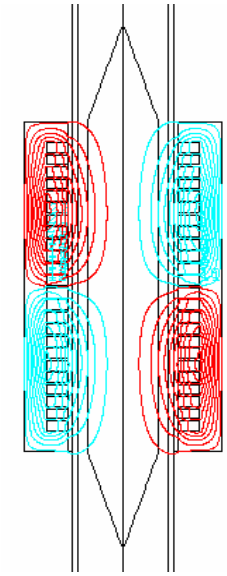

Fig. 3.18 Magnetic field lines, ALIP-LiF

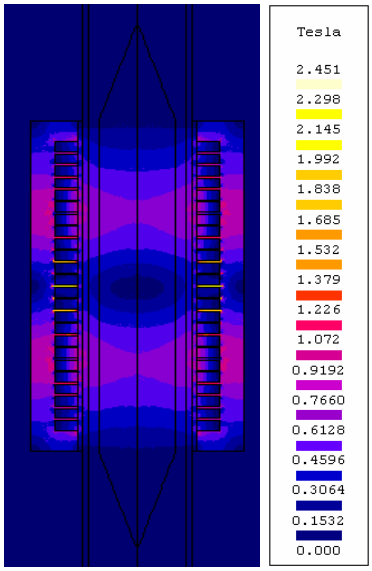

Fig. 3.19 Magnetic flux density, ALIP-LiF

If the eight coils belonging to one phase of the inductor are series connected and each coil has w turns, the rated values for the phase current and supply voltage:

$$I = 30000/w, \quad U = 65896w \tag{3.3}$$

If the eight coils are parallel connected, the rated values for the supply parameters phase current and voltage are:

$$I = 240000/w, \quad U = 8237w \tag{3.4}$$

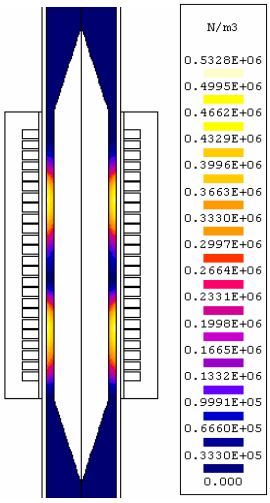

Fig. 3.20 Pumping force density, ALIP-LiF

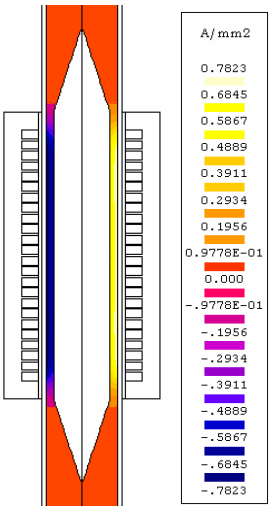

Fig. 3.21 Induced current density ALIP-LiF

Regardless the number of turn w, the two sets of rated data (3.3, 3.4) represent supply parameters technically impossible to realize, so that the annular linear induction pump with 5.9 kHz supply frequency is also lacking the practical interest. If in the axial cylindrical space of the channel a magnetic core would be set up, the performances of such configurations would increase, and maybe for a lower supply frequency, the rated supply parameters could become acceptable.

3.1.4 Annular linear induction pump for sodium (ALIP-Na)

In the case of annular pump model with sodium at 50 Hz it is necessary a current density over the coil cross-section of only 2.44 A/mm^2, in order to obtain the force 4524 N in order to ensure the reference electromagnetic pressure.
The Joule power developed in the molten sodium is P_a = 278 kW, and the reactive power of the pump is Q_a = 400 kVAr.

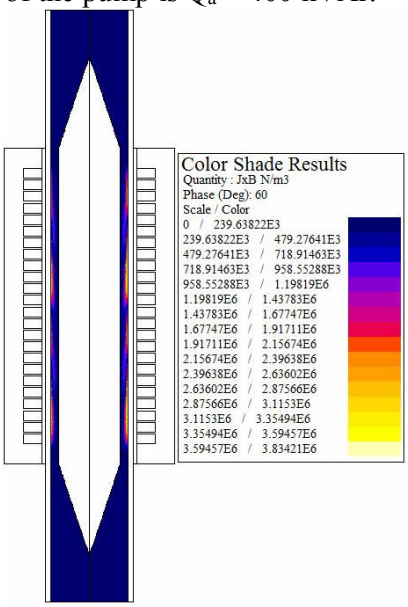

Fig. 3.22. Pumping force density, ALIP-Na

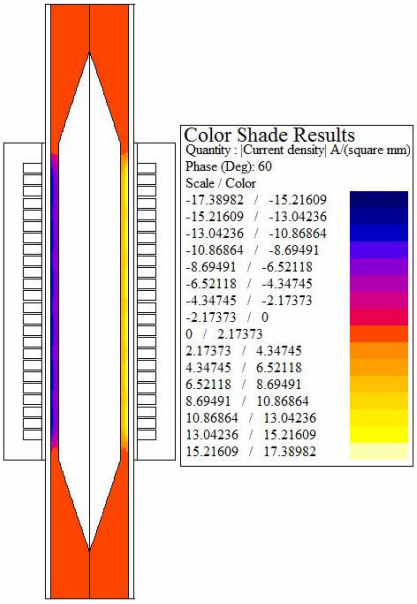

Fig. 3.23. Induced current density, ALIP-Na

Again, the pumping parameters are better in the case of sodium, and placing the inner cylinder eliminates the threat of sodium recirculation through the median zone of the channel. Thusly, this configuration could be suitable for sodium pumping.

3.1.5 Flat linear double-side induction pump for LiF (FLIP-LiF)

Fig. 3.24 presents the geometry of the 2D model of a flat linear induction pump with three phases, two poles, double-side inductor, and four coils per phase on each inductor side. The pole pitch length is 720 mm, the inductor length is 1840 mm and the pump height is 930 mm.

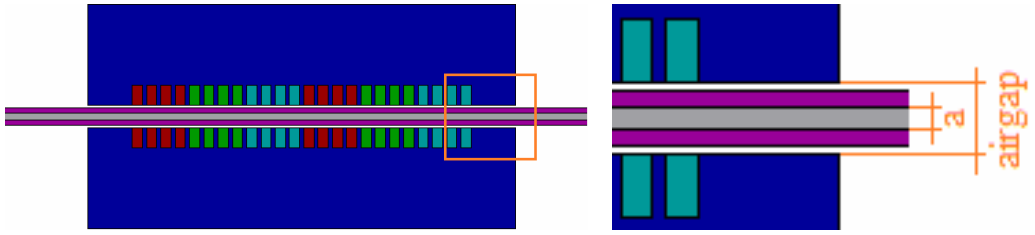

a) full device b) zoom

Fig. 3.24 Flat double-sided induction pump

The pumping channel has a rectangular cross-section with the inner thickness a = 40 mm. The pump airgap has the thickness 130 mm. The width of the two magnetic core sides, respectively the depth considered for the 2D computations, is b = 300 mm. The slots cross-section and the mean value of the current density over the coils cross-section are those of CLIP and ALIP pumps, respectively 50 mm x 100 mm and 6 A/mm^2. The phases of the current density in the three phase windings are 0º, -120º, +120º. The nonlinear magnetic core is characterized by the saturation 2 T and the initial relative permeability 3000. In order to create the reference value of the electromagnetic pressure in the molten salt, the rated pumping force is $F_{ef} = p_e \cdot a \cdot b = 1200$ N.

From the dependences on the supply frequency of the pumping force, the Joule power in the molten salt and the ratio electromagnetic force/Joule power, Figs. 3.25 – 3.27, it result that the maximum of the pumping force is reached for 30 kHz.

The rated value 1200 N of the pumping force is obtained for the FLIP rated frequency $f_f = 114$ Hz. The rated Joule power in the molten salt is $P_f = 422$ kW and the rated reactive power of the pump is $Q_f = 98$ MVAr.

Since the frequency f_f is not so far from the industrial network value, the version FLIP50, with 50 Hz frequency supply, was studied. This flat double-side pump version has the pole pitch length 1020 mm, the inductor length is 2540 mm, the inductor height is 1330 mm and the slot cross-section dimensions are 60 mm x 120 mm. The laminations of magnetic cores are characterized by high saturation 2.4 T and initial relative permeability 4000.

The rated value of the pumping force 1200 N is obtained with FLIP50 for a mean value of the current density over the coils cross-section of only 3.6 A/mm^2, lower than the value 6 A/mm^2 in case of CLIP and ALIP pumps.

Some of the results for the FLIP50 version are: pumping force $F_{ef50} = 1212$ N, the rated Joule power in the molten salt, $P_{f50} = 252.5$ kW and the rated reactive power $Q_{f50} = 51.7$ MVAr.

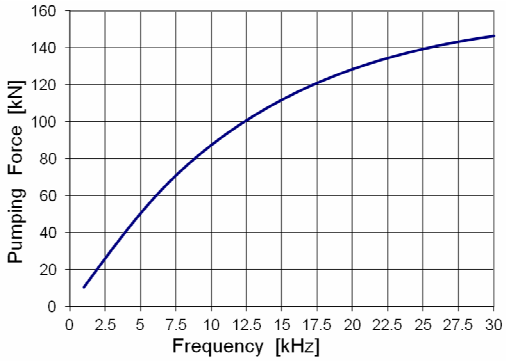

Fig. 3.25 Dependance of pumping force on frequency, FLIP-LiF

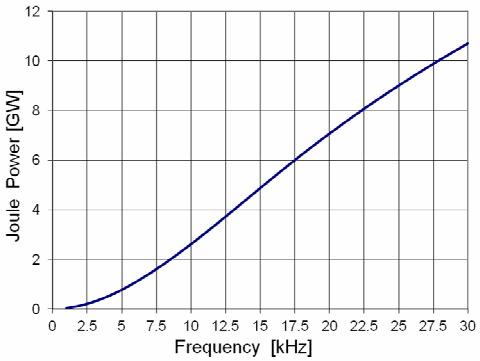

Fig. 3.26 Dependence of Joule power on frequency, FLIP-LiF

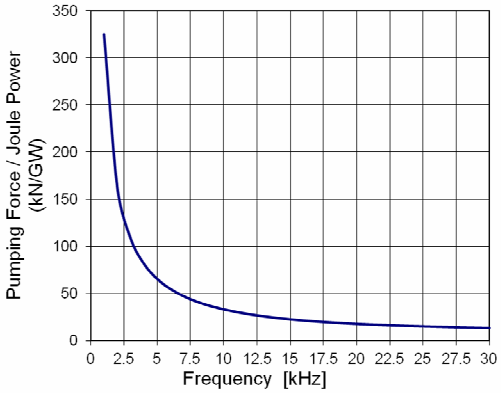

Fig. 3.27 Dependence of Pumping force/Joule power ratio on frequency, FLIP-LiF

With the two sides of FLIP50 inductor connected in parallel and the four coils of a phase per side connected in series, it result the rated phase current in [A] and the rated phase-to-phase supply voltage in [V]:

$$I = 51840/w\,, \qquad U = 576.5w \tag{3.5}$$

For $w_1 = 8$ turns/coil it results $U_1 = 4612$ V and $I_1 = 6480$ A and for $w_2 = 18$ turns/coil, $U_2 = 10376$ V and $I_2 = 2880$ A. These rated values of the FLIP50 electric power supply parameters are technically acceptable.

Figs. 3.28 – 3.30 show the FLIP50 results regarding the magnetic field lines, the magnetic flux density color map and the pumping force density for the phase 60º. Fig. 3.31 presents the module of the current density in the molten salt.

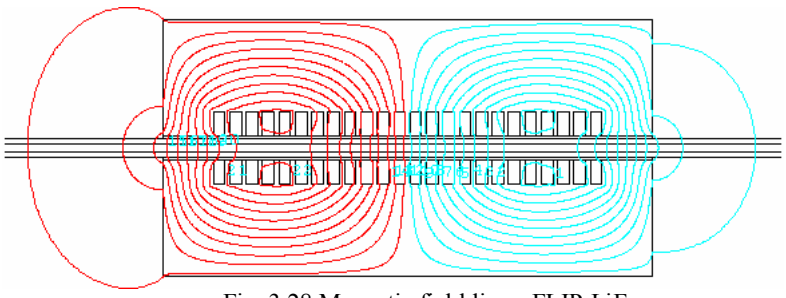

Fig. 3.28 Magnetic field lines, FLIP-LiF

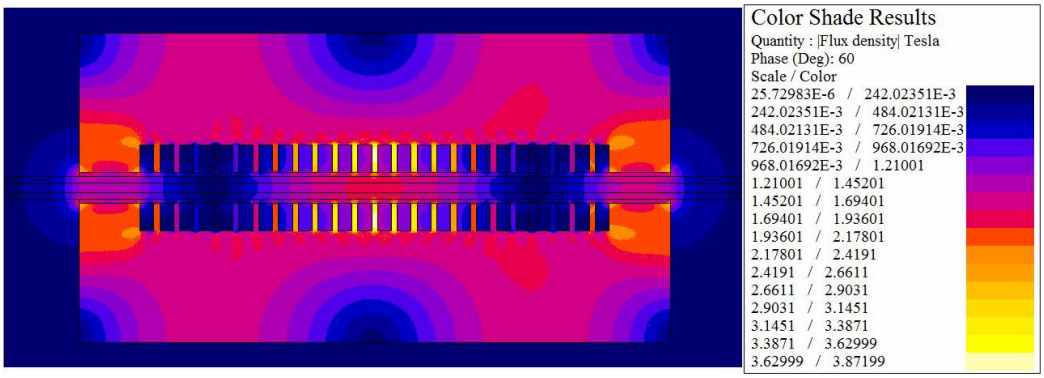

Fig. 3.29 Magnetic flux density, FLIP-LiF

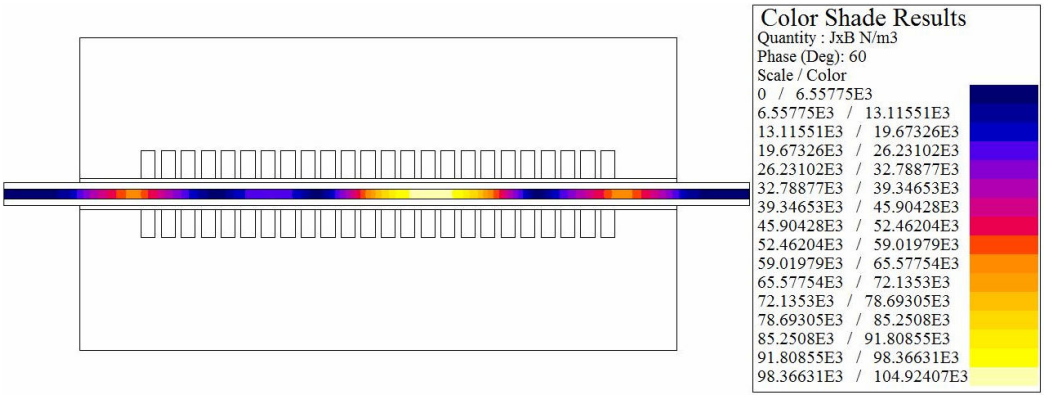

Fig. 3.30 Pumping force density, FLIP-LiF

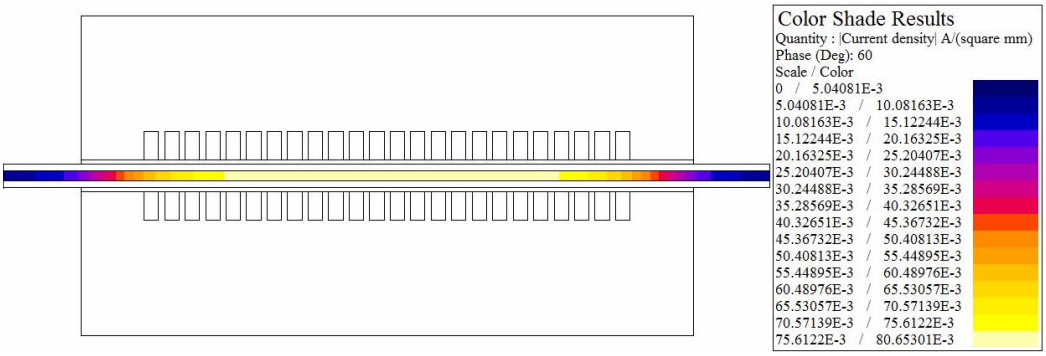

Fig. 3.31 Induced currents density, FLIP-LiF

3.1.6 Flat linear double-side induction pump for sodium (FLIP-Na)

The 1200 N force is ensured for the FLIP-Na pump for the supply frequency 50 Hz and current density over the slot cross-section 0.555 A/mm^2. The Joule power in the channel is insignificant, 14.4 kW, and the reactive power of the pump is 1.17 kVAr.

3.2 3D models for molten salts pumping

This subchapter deals with two 3D electromagnetic pump models for molten salt. The first model represents an extension of the investigation done through the model presented in paragraph 3.1.5. Studying a device with 2D models implies some simplifying hypotheses which suppose retrieving results with a certain degree of error. The 3D model treated in paragraph 3.2.1 shows how approximate the 2D model is.

Paragraph 3.2.2 is a 3D model of a conduction pump type, as presented in Fig. 1.5 of paragraph 1.2. In both models different influences of material properties or geometrical parameters are studied and the molten salt is considered an immobile solid conductor.

3.2.1 The 3D model of the flat linear double-side induction pump for LiF

The correspondent 3D model of the flat linear pump for LiF, 50 Hz was considered. In the 2D structure the coils ends are not taken into account, and since the pole pitch has the length 1020 mm, value much higher than the width of the magnetic core, which has the same size as the channel width, 300 mm, means that the evaluation of the pump parameters relative to the imposed electromagnetic pressure must be made with 3D models.

In the simulation it was taken into account the device symmetry from geometrical and phenomenological point of view with respect to the xOy plane, Fig. 3.32a) thus the actual computation domain in Fig. 3.32 represents only the superior half of the entire device. The supply frequency is 50 Hz. An approximation in this model consists in arranging the coils ends in the same plane, fact that doesn't affect the study of the generated travelling field.

Although the 3D model respects the dimensions, physical properties and the field sources from the 2D model, the generated pumping force is much lower. In comparison with the 1200 N resulted in the 2D model, the force in the 3D model is 30.9 N. The induced power in the molten salt is 5.1 kW, while for the 2D model was 252.5 kW.

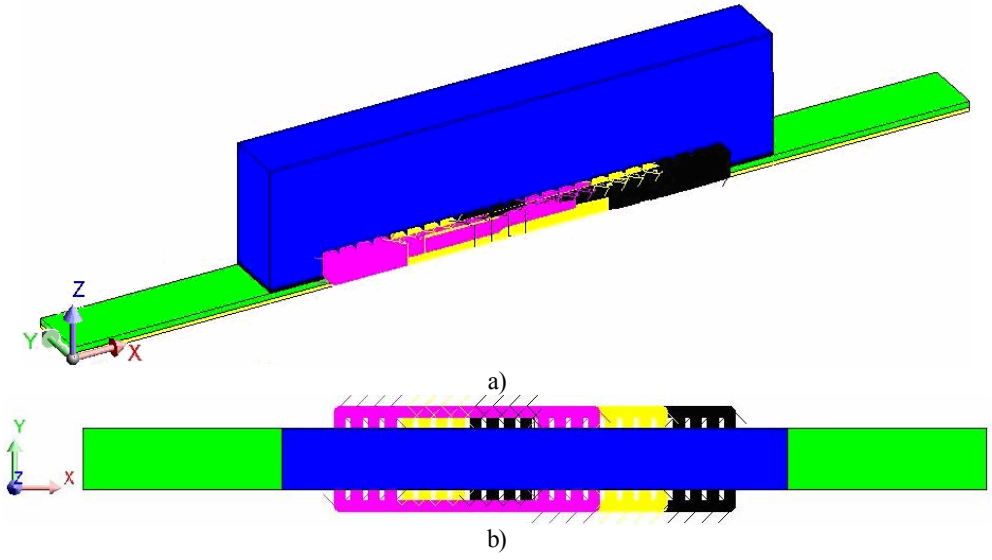

Fig. 3.32 Flat linear induction pump,3D model: a) 3D view, b) top view

Fig. 3.33 presents the vectors of the current density induced in the molten salt, and in Fig. 4.2b are represented the vectors of the electromagnetic force density. The currents form closed loops, respecting the trajectory imposed by the inductor's coils.

The difference between the two values of the force module relative to the 2D calculations, respectively 3D calculations, are due to the field analysis principle in a 2D model with software based on finite element method. The effect of the currents in the coil ends is not considered because in such a plane parallel structure only the currents with perpendicular direction on the xOz, Fig. 3.32a), plane of the model contribute to the electromagnetic field calculation. The force is maximum when the current density vector is perpendicular on the side walls of the channel, respectively having the direction of the Oy axis, Fig. 3.32b), and the magnetic flux density vector having normal direction on this, parallel with the Oz axis. One can see in Fig. 3.33a) that the local density of the induced current vectors parallel with Ox (which in the 2D calculation are not taken into account) is larger than the density of those with Oy direction.

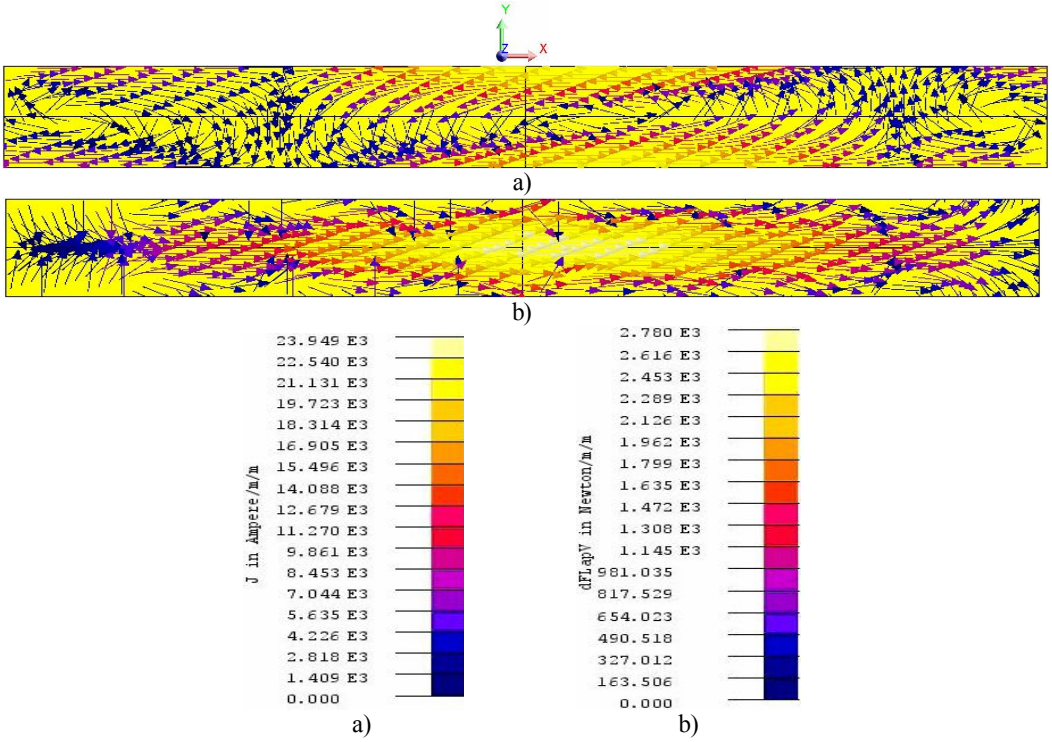

Fig. 3.33. a) Induced current density vectors, b) Pumping force density

It can be observed that in reality, the Ox component of the induced currents cancels in a great extent the pumping effect created by means of Oy component.
Knowing this fact, optimization of the pump model consists in finding methods of forcing the orientation of the induced currents towards the Oy direction, favorable for obtaining the maximal value for the pumping force.

The two studied methods are: widening of the channel in order to allow the current loops to extend more in the Oy direction and fixing of lateral short-circuiting bars on the two sides of the pump channel in order to force the elongation of the current lines on the Oy direction.

Influence of the channel width over the pumping force

Starting from the reference value of 300 mm, the channel width has been increased with a step of 40 mm until it became double.

Solving the model for each channel width is found that as the channel becomes wider, the loops of the induced currents are extending more in the Oy direction. Fig. 3.34 presents for the widths 300 mm, 460 mm and 600 mm the changes in the current lines.

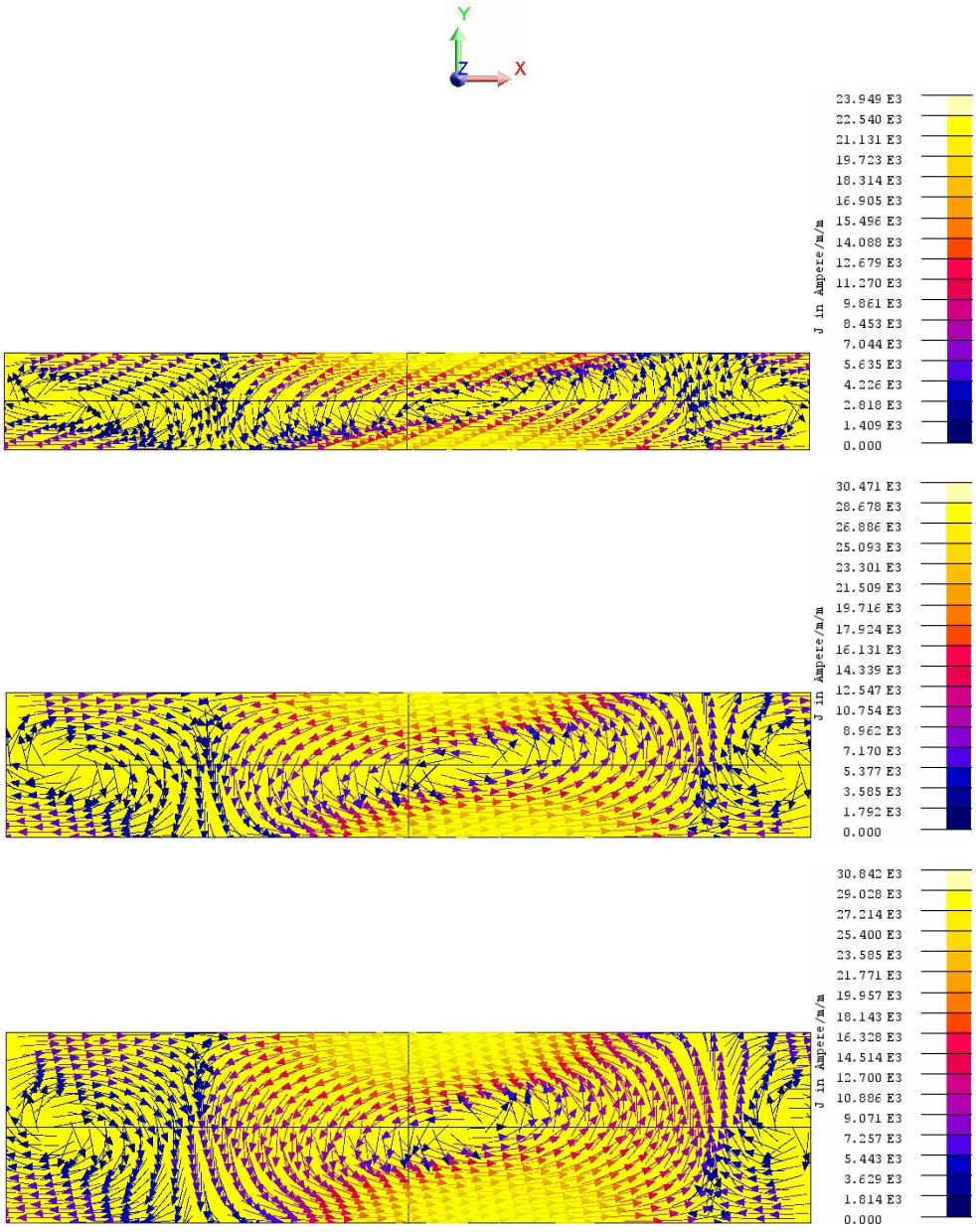

Fig. 3.34 Structure of the current density vectors for various channel widths; legends correspond to the arrows colors.

Fig. 3.35 presents the changes in the pumping force density vectors structure for the channel widths 300 mm, 450 mm and 600 mm, represented on a horizontal section xOy of the channel.

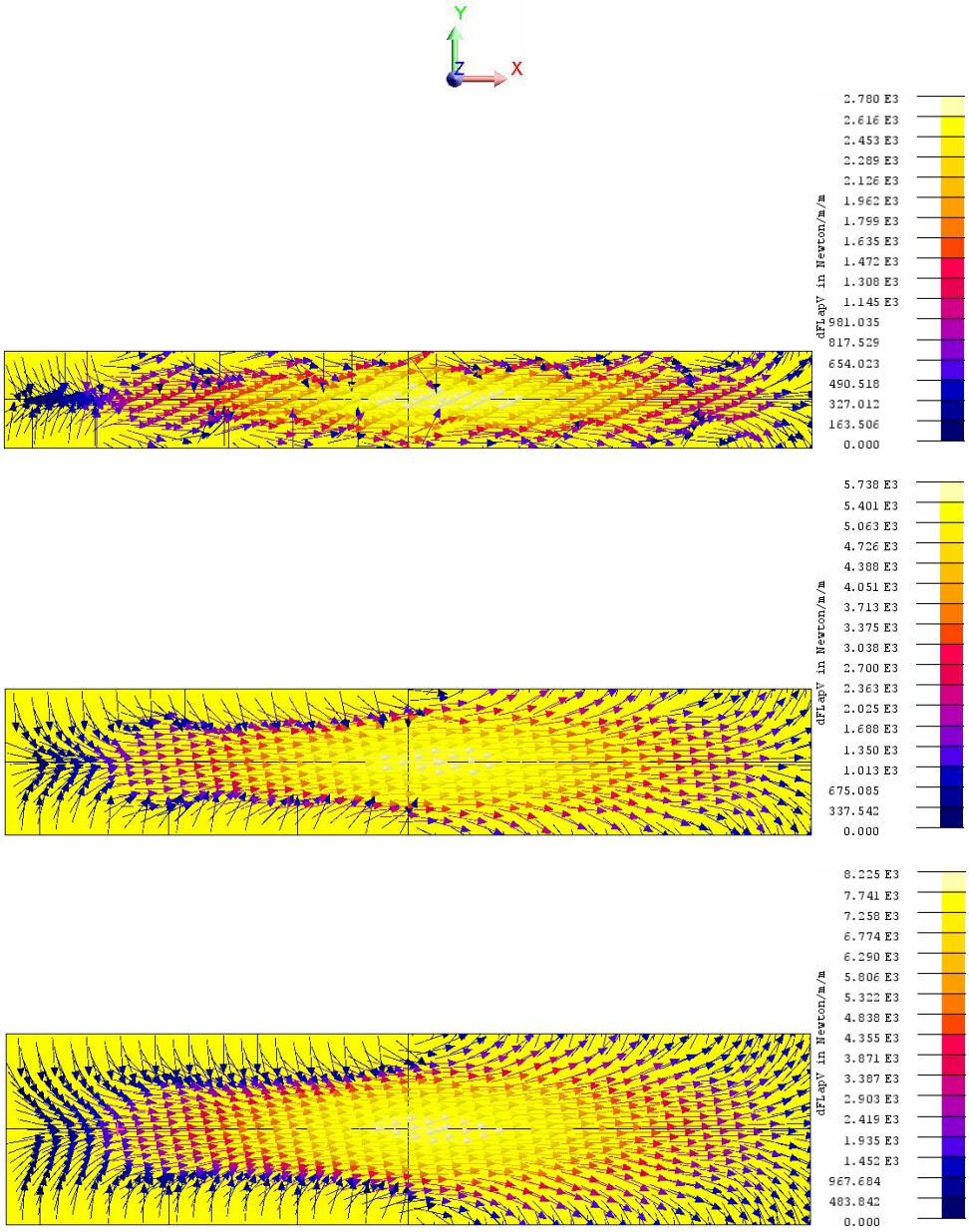

Fig. 3.35 Local orientation of the pumping force density vectors for various channel widths

Figs. 3.36 and 3.37 show the increase of the pumping force, respectively of the electromagnetic pressure along with the increase of the channel width, respectively channel cross section area.

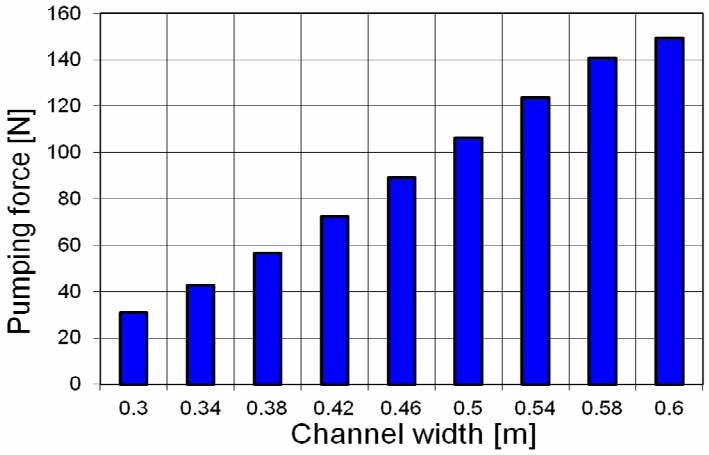

Fig. 3.36 Pumping force values for various channel widths

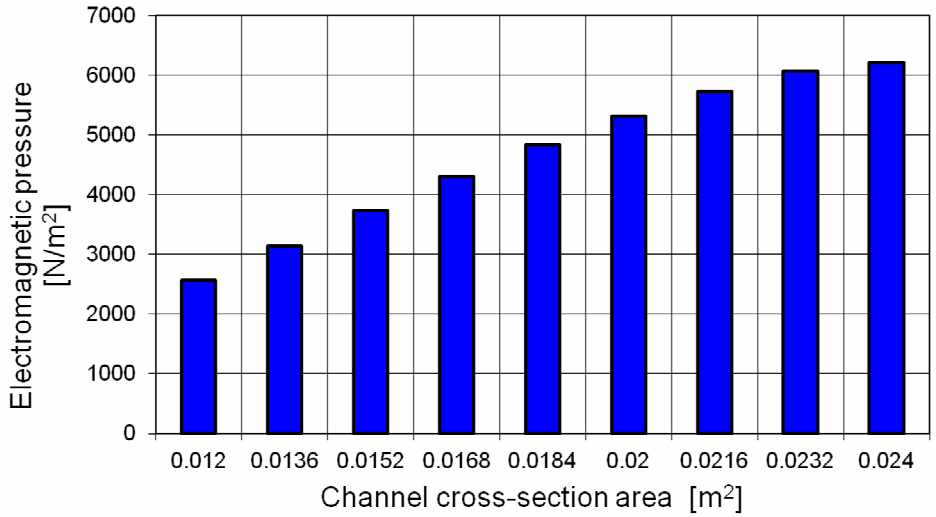

Fig. 3.37 Electromagnetic pressure corresponding to the channel cross-section area

It can be observed that the measure of increasing the channel width has significant results. By doubling the channel width, the electromagnetic force increases approximately five times which represents an approximately 2.5 times increase of the electromagnetic pressure.

Analyzing Fig. 3.37 it can be said that the growth rate of the electromagnetic pressure is decreasing towards the end of the range of channel cross-section area. This indicates that there is a saturation of the improving effect given by the increase of the channel width.

Influence of the short-circuiting bars

The two metallic bars 100 mm wide each, Fig.3.38 of higher electrical conductivity than that of molten salts are attached to the channel of reference width 300 mm. The bars are in direct contact with the molten salt and force the induced currents to orient after the preferential direction previously described. The bars resistivity is an important parameter. From the view point of the model solving, the currents direction can be controlled through parameterization of the resistivity of the two bars. The lower the resistivity is, the more the currents direction is closer to the optimum one from the view point of maximization the pumping force, namely parallel with the Oy axis.

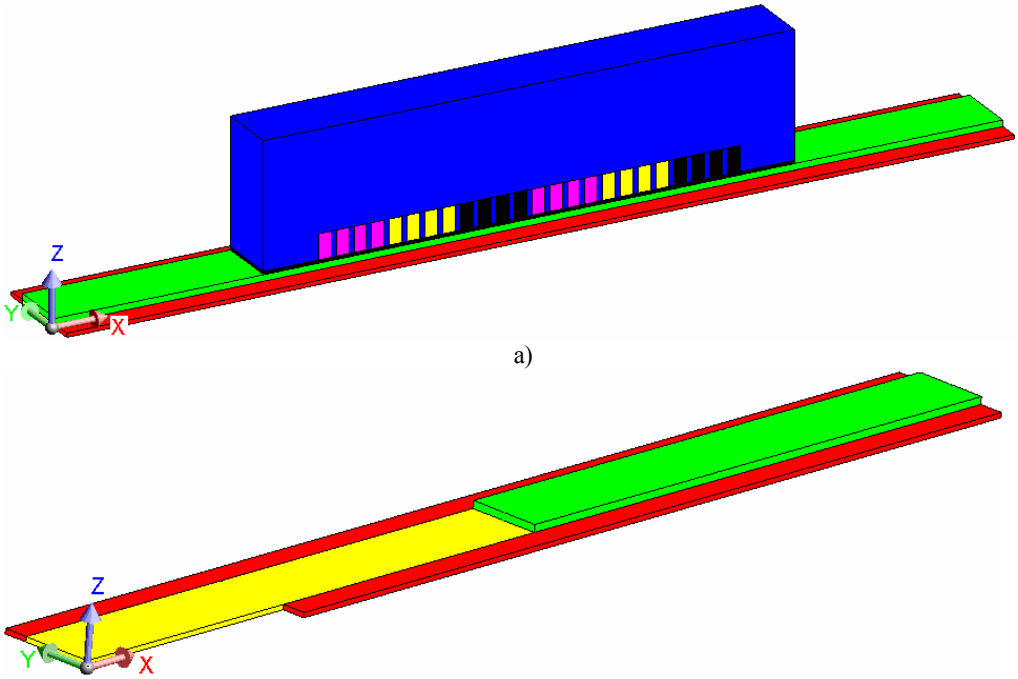

Fig. 3.38 Position of the two short-circuiting bars relative to sodium channel and pump's inductor

The purpose of studying the influence of the short-circuiting bars consists in finding the suitable resistivity, namely the material from which the bars could be realized, so that the flat induction pump of revised construction to generate the 1200 N force, necessary to ensure the reference electromagnetic pressure $p_e = 10^5$ N/m^2.

Fig. 3.39 presents the dependence of the generated force on various values of resistivity.

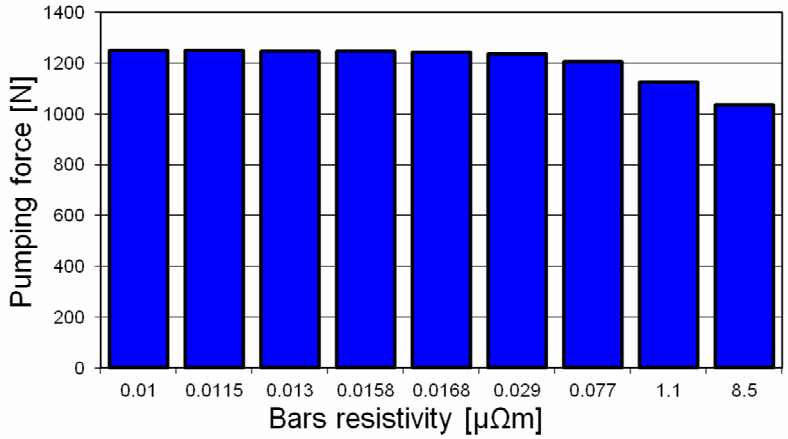

Fig. 3.39 Dependence of pumping force on bars resistivity

Fig. 3.39 reveals that there is a saturation of the improving effect that the short-circuiting bars have on the generated force with respect to the bars resistivity. Given be the fact that the very low values of resistivity on the abscise of Fig. 3.39 representation are fictive, a more complete study regarding the pump behavior for graphite, stainless steel and cooper bars is presented in Table I.

Table I. Pump characteristics for different bars material

Material	Graphite	Stainless Steel
Resistivity at 800°C [μΩm]	8.5	1.1
Pumping force [N]	1037	1125
Force acting on bars [N]	540	2500
Joule power in channel [kW]	361	514
Joule power in bars [kW]	130	388
Skin depth at 50 Hz, 800°C [mm]	207.5	74.6

Figs. 3.40 – 3.44 are representations with respect to orientation and module of current density and force density in the case of graphite bars, and Figs. 3.45 – 3.49 in the case of stainless steel bars, for phase shift 0 degrees.

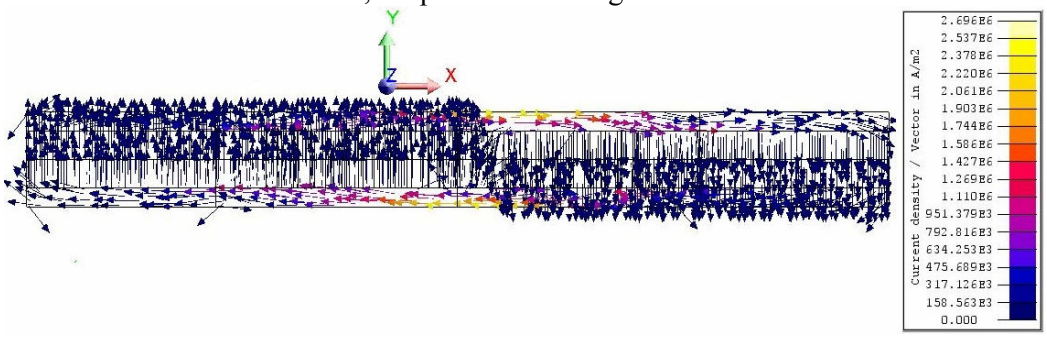

Fig. 3.40 Vectors of current density induced in molten salt and graphite bars

A first observation regarding the use of high conductivity short-circuiting bars is that the effect of current density orientation predominantly along Oy direction in the channel, Figs. 3.40, 3.45 has a great impact on the generated force. The pumping force increases from 30.9 N to 1037 N with graphite bars and to 1125 N for stainless steel bars.

Secondly, the bars are behaving as a second region with solid conductor properties in addition to the molten salt region. Orientation of the induced currents in the bars is along the Ox axis, according to the coils geometry and Lentz law. The values of the current density, respectively force in the bars are higher than those in the molten salt.

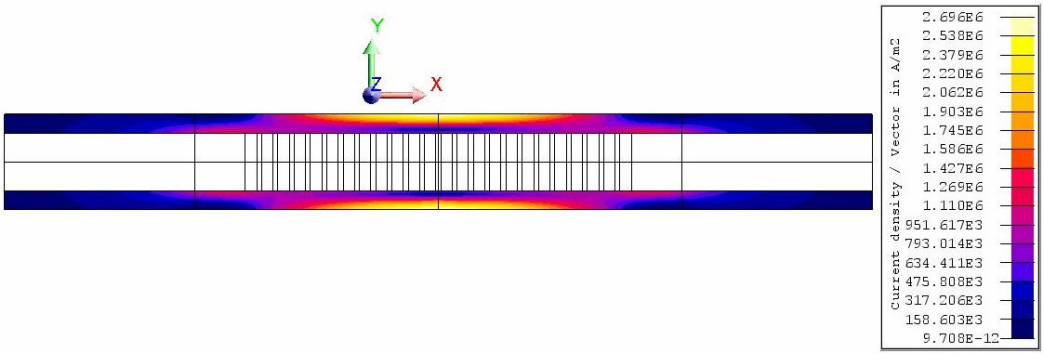

Fig. 3.41 Current density induced in the graphite bars

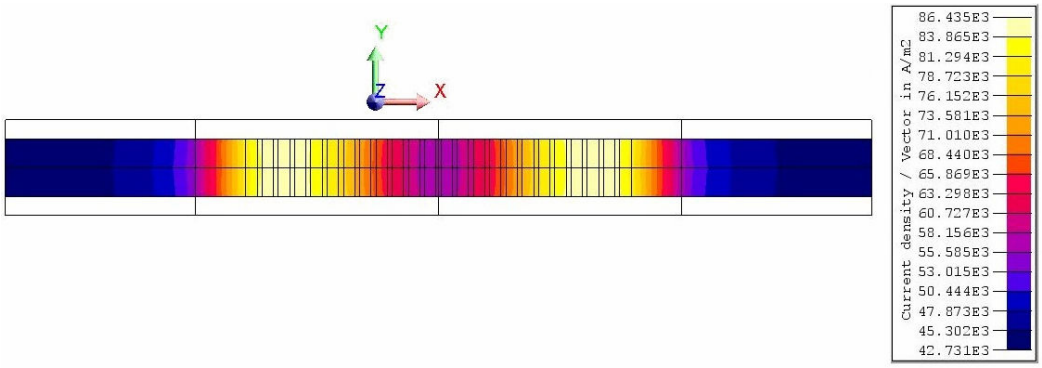

Fig. 3.42 Current density induced in the molten salt, graphite bars

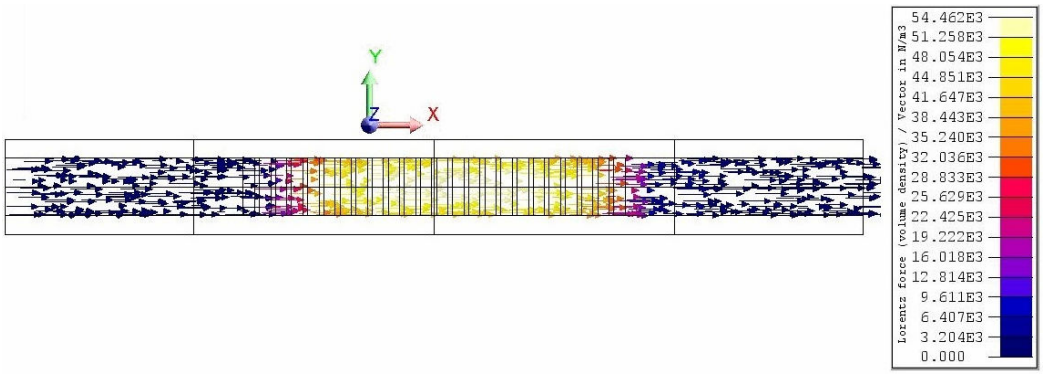

Fig. 3.43 Vectors of pumping force density developed in the molten salt, graphite bars

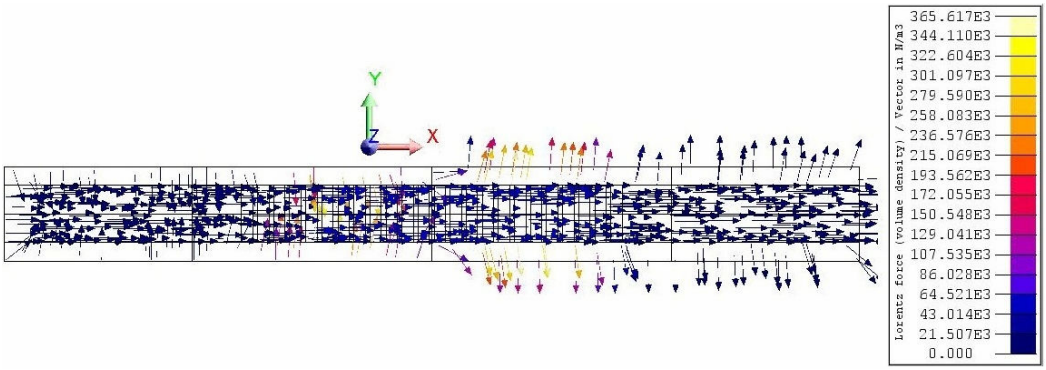

Fig. 3.44 Vectors of pumping force density developed in the molten salt and graphite bars

The force acting on the bars is oriented approximately along the Oy direction, Figs. 3.44, 3.49, because the currents induced in bars have direction quasi-perpendicular with respect the currents in the molten salt.

The effect of current density concentration near the solid conductor surface is much more pronounced for stainless steel bars, Fig. 3.46 than in the case of graphite bars, Fig. 3.41, since the difference between bars width and electromagnetic field penetration depth increases, Table I. This shows that a good design should consider a decrease of the bars width along with the decrease of the bars resistivity by choosing widths comparable with the penetration depth.

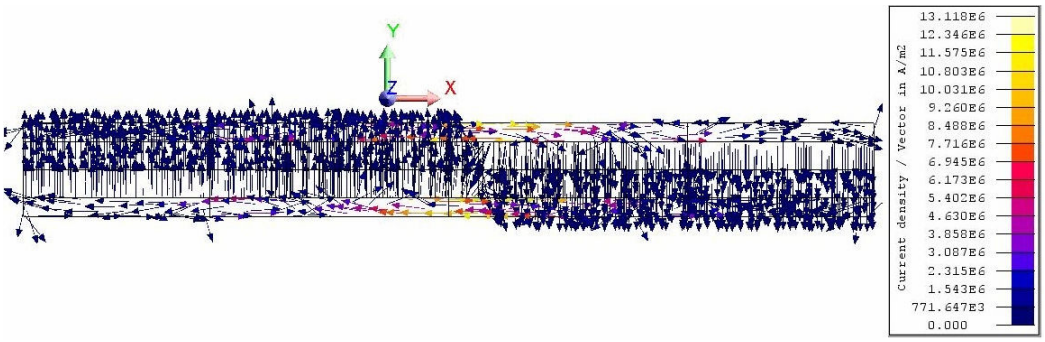

Fig. 3.45 Vectors of current density induced in molten salt and stainless steel bars

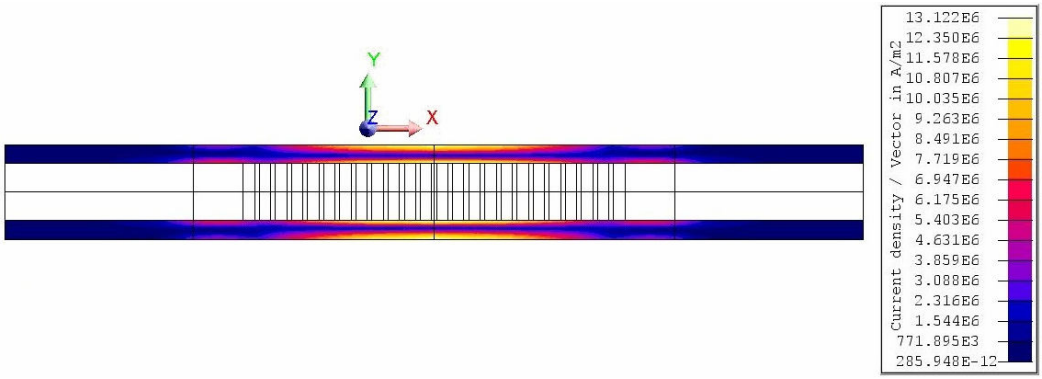

Fig. 3.46 Current density induced in the stainless steel bars

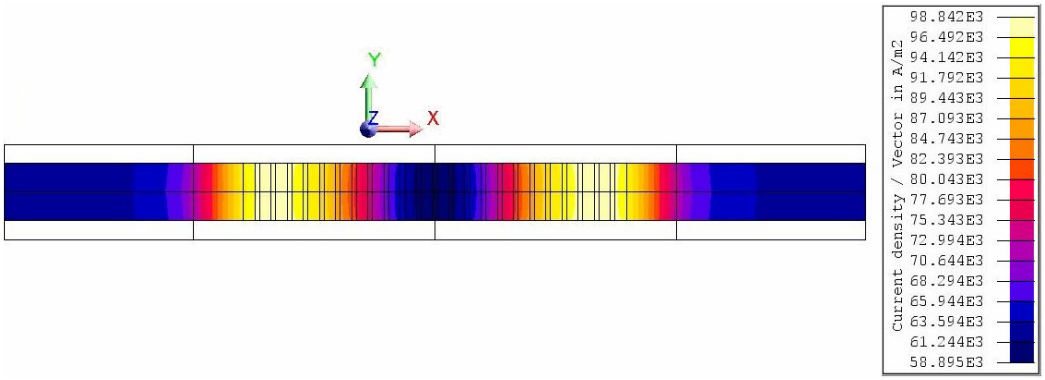

Fig. 3.47 Current density induced in the molten salt, stainless steel bars

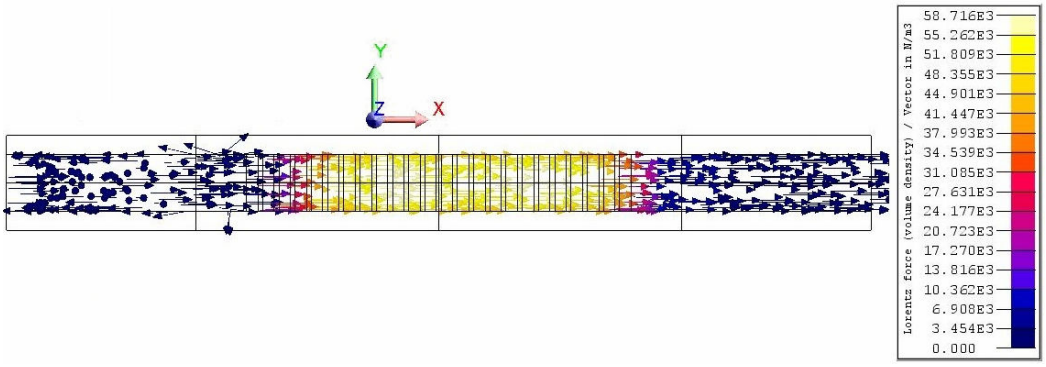

Fig. 3.48 Vectors of pumping force density developed in the molten salt, stainless steel bars

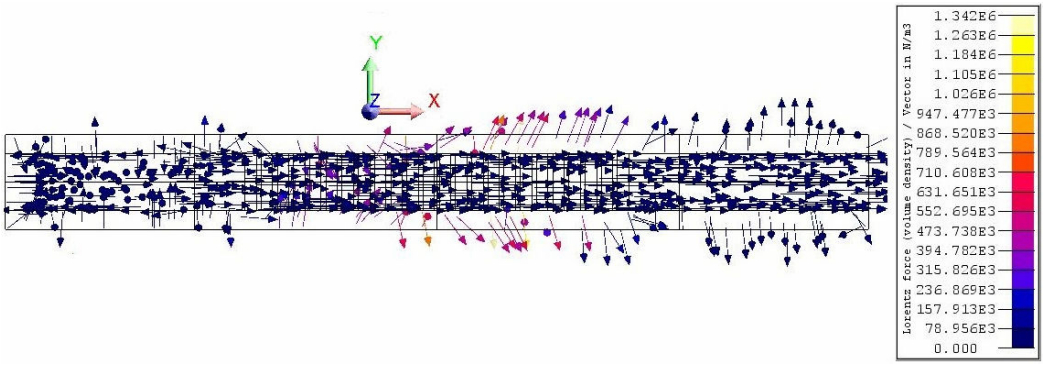

Fig. 3.49 Vectors of pumping force density developed in the molten salt and stainless steel bars

Comparing the results of the model with no short-circuiting bars and the model with graphite bars it was found that the pumping force increases 32.5 times at the expense of a 70 times increase of the induced Joule power. When passing from graphite bars to stainless steel bars, a supplementary force increase of 8.5 % is obtained but the Joule power induced in molten salt increases with 42 % and in the bars increases with 198 %.

3.2.2 The 3D model of the conduction pump

This type of pump is studied by means of a multiphysic coupling of two problems that models two types of phenomena that occur in the conduction pump, namely an electric conduction problem, in which the current density distribution in the molten salt is determined and a magnetostatic problem where the pumping force is determined.

Multiphysics principle

Each phenomenon is described by Maxwell's equations in corresponding form for the two field regime and takes into account the constitutive equations characterizing the conducting materials. The weak coupling that was accomplished supposes that the two systems of equations are separately solved, and a transfer of results takes place between the two systems [149].

The linking between the two standard applications, Fig. 3.50, was carried out "manually" and the first step in the operations succession was solving process with the Electric Conduction application in order to find the current distribution inside the molten salt channel. The second step was solving process with Magneto Static application, where the previously calculated current distribution is interpolated through a data exchange file (.DEX) and the value of the pumping force is computed.

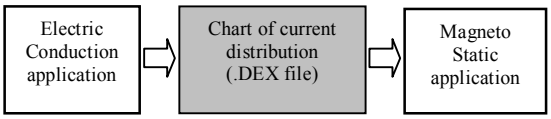

Fig. 3.50 Multiphysic technique

The physical quantities exchanged through the .DEX file are defined on an exchange support of nodes belonging to the mesh. The exchange support of this case is the volume region "molten salt". The condition in order to realize the multiphysic exchange was to have the same mesh structure in the area of interest, namely the molten salt channel.

Formulation and differential model of the electric conduction problem

The corresponding Maxwell's equations for an electrical system in the Electric Conduction application are:

$$curl\ \mathbf{E} = 0 \tag{3.6}$$
$$curl\ \mathbf{H} = \mathbf{J} \tag{3.7}$$

where **E** is the electric field and **J** is the current density.

The irrotational character of the field allows expressing it using the auxiliary quantity, *scalar electric potential* **V**. Thus, the associated equations for the regime are:

$$\mathbf{E} = -grad\ \mathrm{V} \tag{3.8}$$
$$div\ \mathbf{J} = 0 \tag{3.9}$$

The constitutive equation that characterize the conducting materials is:

$$\mathbf{J} = \sigma\mathbf{E} \tag{3.10}$$

where σ is the electrical conductivity.

The second order equation solved which constitutes the differential model of the electric conduction regime is:

$$div(\sigma\ grad(\mathrm{V})) = 0 \tag{3.11}$$

The conditions for the uniqueness solution require that the value of this potential be assigned to at least one point of the computation domain. In the conduction pump model an electric potential is imposed on the electrodes surfaces in electric contact with the molten salt.

Formulation and differential model of the magnetostatic problem

The corresponding Maxwell's equations for a magnetic system in the Magneto Static application are:

$$curl\ \mathbf{H} = \mathbf{J} \tag{3.12}$$
$$div\ \mathbf{B} = 0 \tag{3.13}$$

where **B** is the magnetic flux density, **H** is the magnetic field strength and **J** representss the density of DC currents in the computation domain.

Ecuation 3.13 allows to express this magnetic field using the auxiliary quantity *vector electric potential* **A**, defined as follows:

$$\mathbf{B} = curl\ \mathbf{A} \tag{3.14}$$

The material constitutive equation is:

$$\mathbf{B} = \mu\mathbf{H} \tag{3.15}$$

where μ is the magnetic permeability.

The following equation represents the differential model of the regime and it is solved by FLUX software with the finite elements method in the Magneto Static application:

$$curl[1/\mu \cdot curl\ \mathbf{A}] = \mathbf{J} \tag{3.16}$$

Geometry and physical properties

The DC supplied pump, Fig. 3.51, has 1685 mm height, the length along the Ox axis is 1720 mm and the width is 1000 mm. The air gap where the thermal insulated rectangular channel of the pump is placed has the thickness 85 mm. The

dimensions of the molten salt cross section region are 40 mm along Oz and 300 mm along Ox.

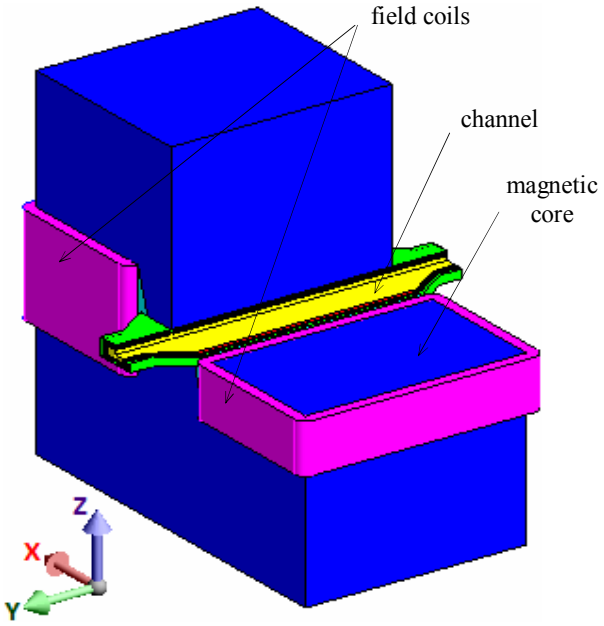

Fig. 3.51 Double section view of the conduction pump

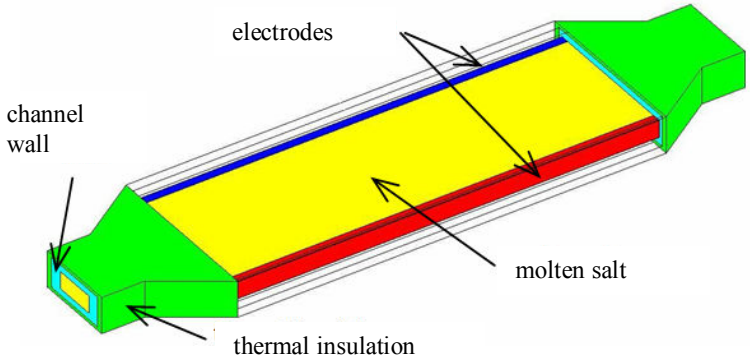

Fig. 3.52 Structure of the conduction pump channel

In the Magneto Static problem the following regions are defined: the two field coils, the magnetic core and the molten salt channel, Fig. 3.52. The field coils are coil conductor regions and the total current imposed in the stranded coil conductor is 145.5 kA. The magnetic core is a non conducting region with the relative permeability 4000 and high saturation magnetization of 2.4 T. The channel is a source region, with current density provided by the electric conduction problem through the data file.

In the Electric Conduction problem are defined two face regions representing the equipotential surfaces of the two electrodes, in electric contact with the molten salt. The two faces are assigned with 10 V, respectively –10 V potential.

According to the potential difference of 20 V applied, the generated current flow in the molten salt inside the pump channel, generates the current density to be imported in the Magneto Static problem. The molten salt in the channel has the resistivity $\rho = 0.33 \cdot 10^{-2}$ Ωm.

The boundary conditions in both problems are ensured by the presence of an infinite box enclosing the computation domain, Fig. 3.53. Inside the infinite box region, a Kelvin transformation is performed by the software, thus the relevant quantities can be computed at any distance up to infinite.

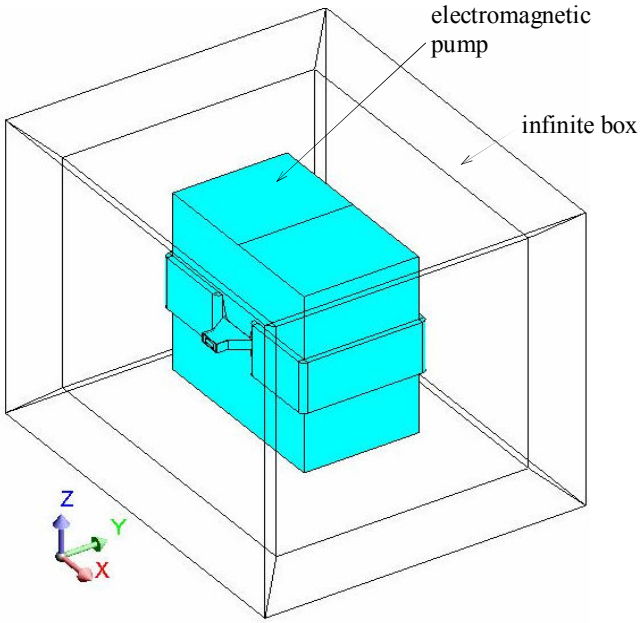

Fig. 3.53 Computation domain of the DC conduction pump

Results analysis and parametric study

The cumulated effect of the current injected by the electrodes and of the magnetic flux density given by the two DC field coils creates an Oy oriented, Fig. 3.57, total force of 462 N. The corresponding electromagnetic pressure for the channel cross section area of 0.012 m^2 is 0.39 bars. The dependence of electromagnetic force, respectively electromagnetic pressure on the potential difference is given in Table II.

Table II. DC conduction pump characteristics for various applied voltages

ΔU [V]	**F** [N]	**p** [bar]
20	462.0	0.39
40	924.7	0.77
60	1386.1	1.16
80	1848.2	1.54
100	2310.3	1.93
120	2772.1	2.31
140	3234.5	2.70
160	3696.6	3.1
180	4157.6	3.5
200	4618.0	3.8

Figs. 3.53 – 3.54 present the field quantities and orientations of the pumping force vectors, developed in the channel, for the case ΔU = 200V.

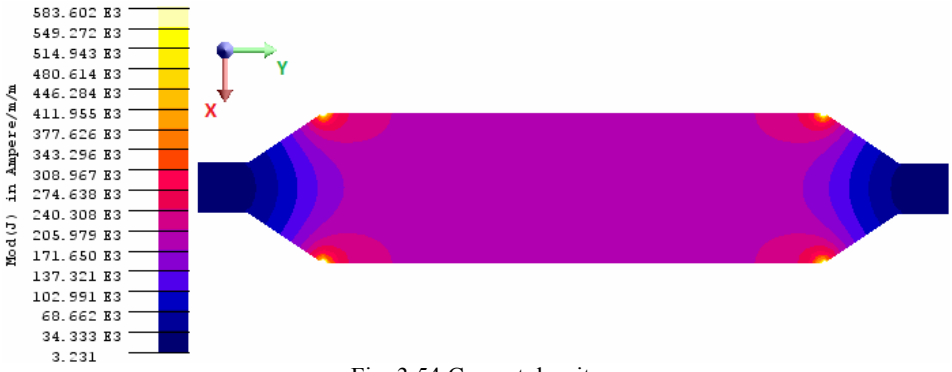

Fig. 3.54 Current density

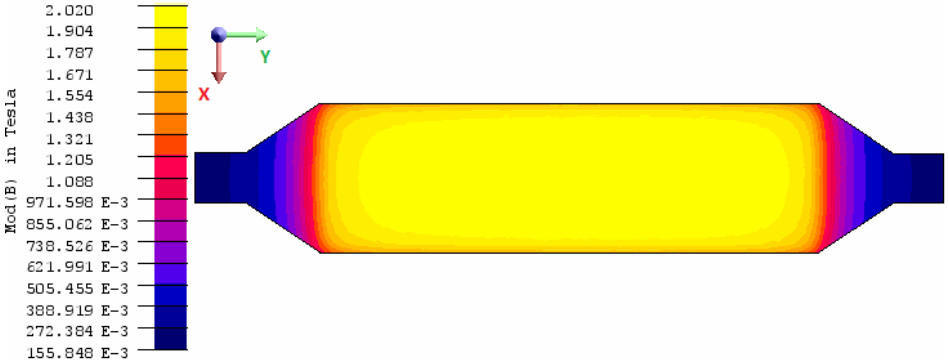

Fig. 3.55 Magnetic flux density in the xOy plane

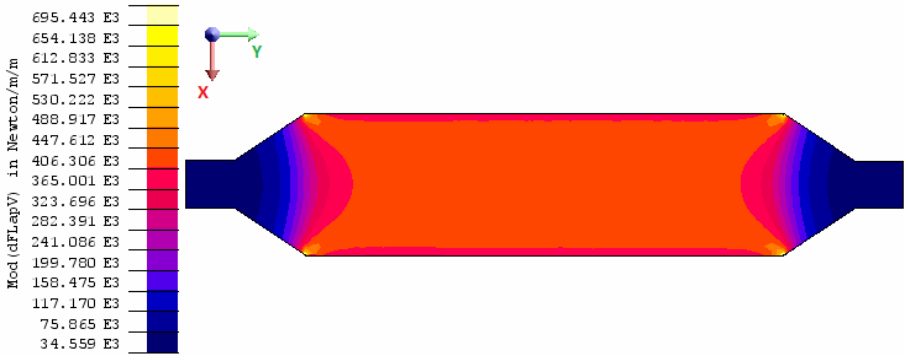

Fig. 3.56 Pumping force density

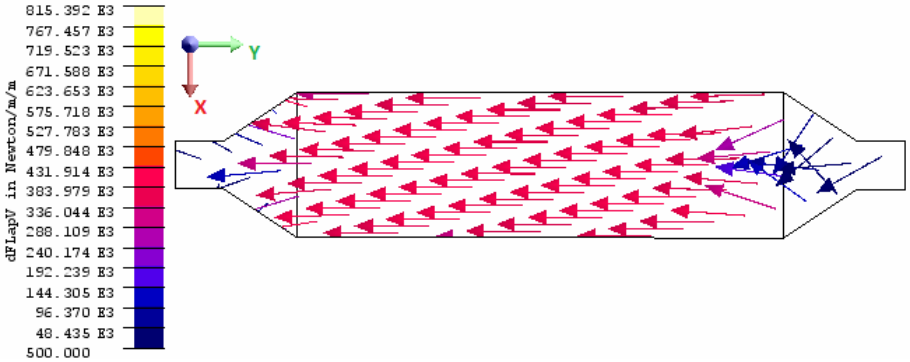

Fig. 3.57 Pumping force vectors

Fig. 3.58 presents the magnetic flux density on a cut plane parallel with xOz plane, through the middle of the magnetic core and molten salt channel.

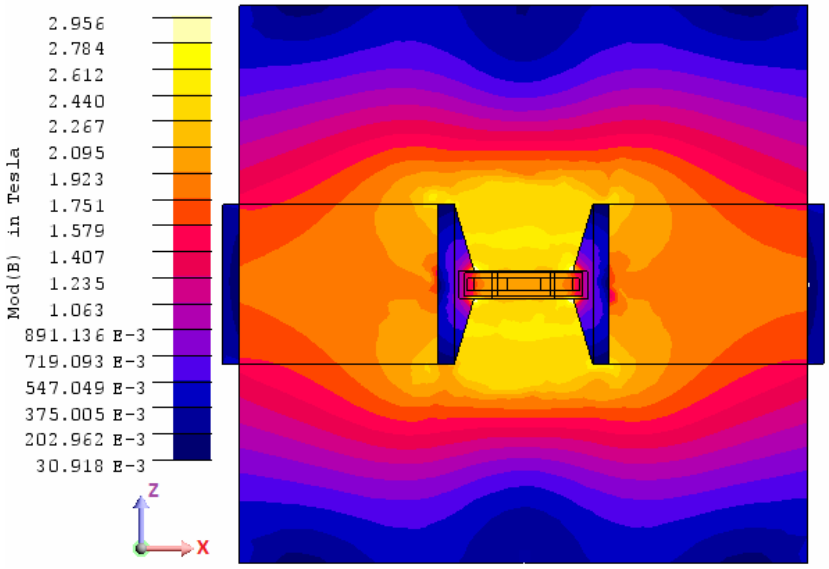

Fig. 3.58 Magnetic flux density in xOz plane

The magnetic flux passing through the molten salt depends on the air gap height, marked in Fig. 3.59 with a. While, the magnetic flux decreases with the increase of a, the magnitude of the resultant **J**, has more and more important values. In other words, for constant channel cross section area, the couple (a,b) influences the pumping force module, Fig.3.59.

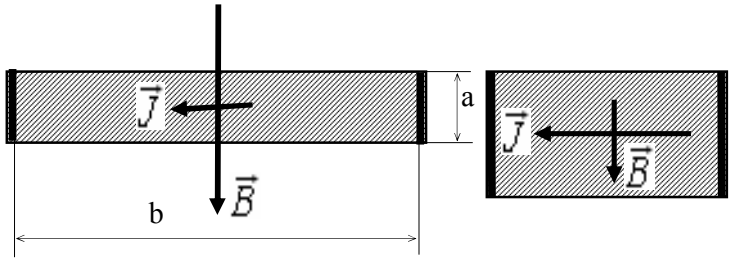

Fig. 3.59 Different channel shapes for constant cross-section area

The variation of the electromagnetic force and pressure when the channel cross section has different shapes given by the (a,b) couple and constant area was studied. Table III presents the values chosen for the (a,b) couple and the correspondent results for applied voltage 200 V.

Table III. Pumping characteristics for different channels shapes

a [mm]	**b** [mm]	**S** [m^2]	**b/a**	**F** [N]	**P** [bar]
40	300	0,012	7,50	4618	3,85
50	240		4,80	5491,8	4,58
60	200		3,33	6033,75	5,03
70	171,43		2,45	6458	5,38

One can see how the electromagnetic pressure increases as the b/a ratio decreases, in other words as the channel cross section becomes higher and narrower.

Another study is an analytical investigation on the influence of the pump extension in Oy direction, Fig. 3.51, denoted L, over pump efficiency. The applied voltage was modified accordingly, in order to keep the same pressure of p = 3.9 bar for any value of the parameter L from 1000 to 4000 mm. The current density over the

two coils cross section is 6.16 A/mm^2. The quantity Q = 0.06 m^3/s is the flow rate calculated as the product of the constant molten salts block velocity v = 5 m/s and the channel cross section area. In Table IV, η_{em} is the efficiency of the electro-mechanical conversion and takes into consideration as a useful power only the mechanical driving effect, Fig. 3.60.

Table IV. Efficiency dependence on L

L [mm]	**ΔU** [V]	**$P_{J\_channel}$** [kW]	**P_{J_coils}** [MW]	**η_{em}** [%]	**η** [%]
1000	200.00	1758.06	0.35	1.12	83.66
1200	166.67	1465.05	0.39	1.27	79.18
1400	142.86	1255.76	0.44	1.39	74.63
1600	125.00	1098.79	0.48	1.49	70.11
1800	111.11	976.70	0.52	1.56	65.71
2000	100.00	879.03	0.57	1.62	61.49
2200	90.91	799.12	0.61	1.66	57.47
2400	83.33	732.53	0.65	1.69	53.68
2600	76.92	676.18	0.70	1.70	50.14
2800	71.43	627.88	0.74	1.71	46.84
3000	66.67	586.02	0.78	1.71	43.78
3200	62.50	549.39	0.83	1.70	40.95
3400	58.82	517.08	0.87	1.69	38.34
3600	55.56	488.35	0.91	1.67	35.92
3800	52.63	462.65	0.96	1.65	33.70
4000	50.00	439.52	1.00	1.63	31.65

Depending on the possible application of such pump, the Joule power that transforms in heat can be considered a useful power. The electro-thermo-mechanical efficiency in this case is given by η, Fig. 3.61.

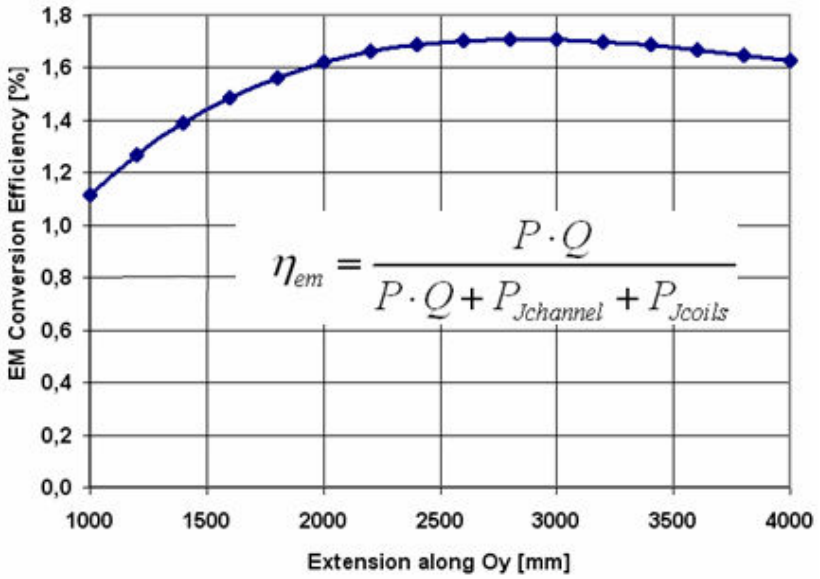

Fig. 3.60 Electro-mechanical conversion efficiency

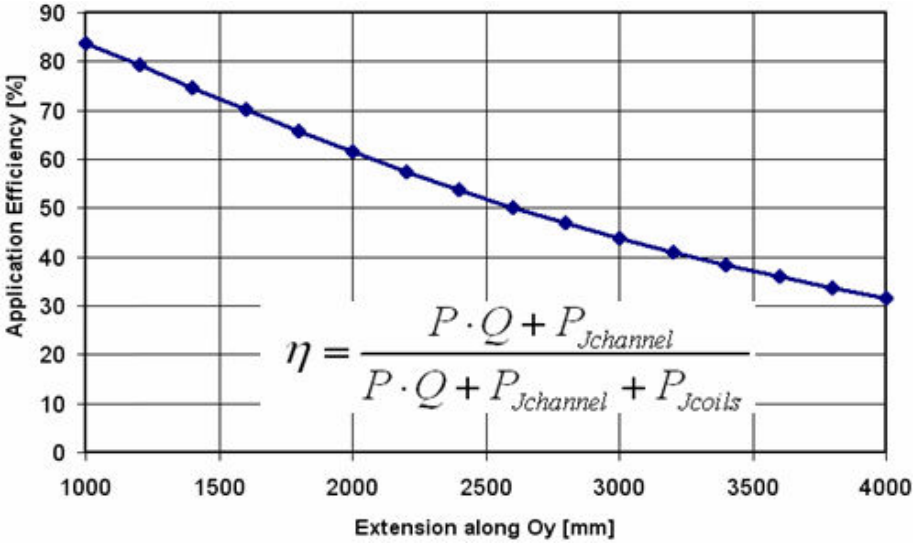

Fig. 3.61 Electro-thermo-mechanical efficiency

The parametric investigations show the influence of the channel's shape and applied voltage over the pumping force in a rectangular cross section channel, with molten salts. The efficiency of the electromechanically conversion has a maximum for the pump width around 3000 mm, after which increasing the Oy dimension of the pump is useless.

CONCLUSIONS

Investigation of electromagnetic pumping of molten salts is justified by the constructive reliability and safety of the electromagnetic pumps and by the nature of the applications where the pumps and molten salts are used, namely application in energy production industry, where the Joule power developed in the molten salt can be considered useful energy.

The CLIP and ALIP models studied in paragraph 3.1 proved to be not suitable for electromagnetic pumping of molten salts. Testing the two models for sodium pumping revealed that the pumping parameters are obtained for realizable supply conditions and that the optimum design of the supply and geometry of a pump is unique for a given electroconductive fluid and pumping parameters.

The complete study based on 2D and 3D models of the FLIP for molten salts firstly showed that numerical modeling although is a powerful tool the results are depending on the users understanding of the physical phenomenon and capacity of using the simplifying hypothesis without influencing the results. Thus it is concluded that the total force developed by the FLIP can be increased by increasing the channel width or using lateral short-circuiting bars of low resistivity.

The conduction pump presented in paragraph 3.2.2 has the best performances from all the pumps for molten salts studied in this chapter. The main advantage of this pump is the double possibility of controlling the force generated in the channel, namely by the supply voltage between the two electrodes and by the supply of the field coil. From the point of solving method, this application was coupling two types of problems, a problem of electric conduction and a magneto static problem.

Chapter 4: Electromagnetic study of the RMS sodium pump

In the previous chapter some insights about electromagnetic pumping of low electroconductive fluids, namely molten salts, have been reported. When high electroconductive fluids, as liquid sodium, are subject of electromagnetic pumping, things change with respect to pump geometry, electrical supply and efficiency. For example, at frequency 50 Hz the electromagnetic field penetration depth is 23.6 mm in sodium, $\rho_{Na} = 0.11 \cdot 10^{-6}$ Ωm, and 4088.7 mm in the lithium fluoride (LiF) molten salt, $\rho_{LiF} = 0.33 \cdot 10^{-2}$ Ωm. This shows that at high conductivities the pump supply frequency is low. This aspect is also important for the channel cross section dimensioning. In comparison with molten salts electromagnetic pumping, due to a greater conductivity of liquid metals, the induced currents and forces are much higher and the Joule power lower.

RMS pump is a design of a small scale annular linear induction pump. The study of this pump marked two important aspects in the chronology of the thesis preparation. Firstly it meant the beginning of the scientific collaboration between EPM_NM Laboratory in Bucharest with SIMAP-EPM Laboratory in Grenoble on the subject of electromagnetic pumping. The work was done in Bucharest based on data provided by SIMAP-EPM and had the purpose of putting together knowledge and practice from both sides in order to prepare further analyses for medium and large size electromagnetic pumps. Secondly, for the author it represented the first phase in the deeper study of the specific problems of electromagnetic pumps of ALIP type for sodium.

An *electromagnetic study* was done and the sodium was considered a solid body with *solid conductor* properties. Two cases are considered: a) the sodium region is immobile – case treated with frequency domain analysis models - and b) the sodium region is in motion – case treated with models of type step by step in time domain coupled with translating motion.

The structure and geometrical dimensions of the RMS pump are given in Fig. 4.1.

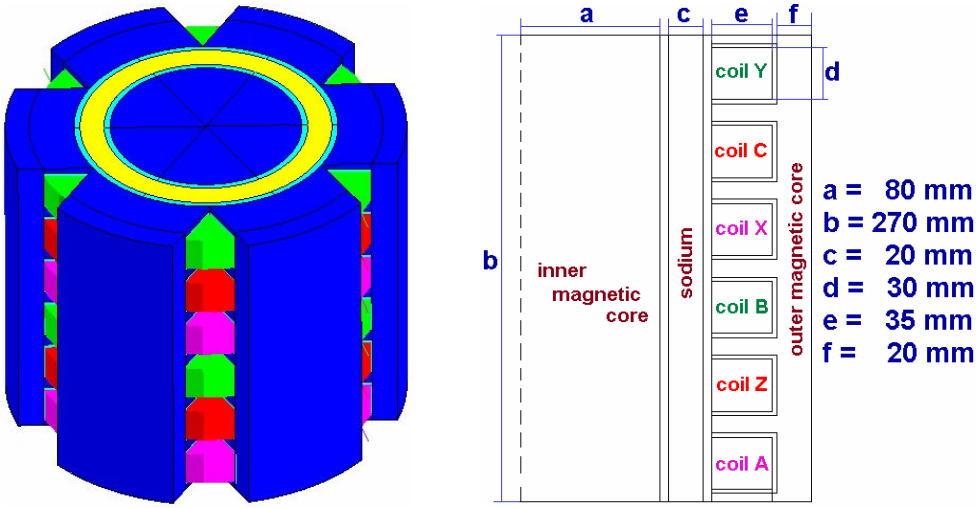

a) b)

Fig. 4.1 Structure and dimensions of the RMS pump

The nonlinear magnetic core is characterized by the saturation magnetization 2 T and relative initial magnetic permeability 1000. The resistivity of the only solid conductor in the computation domain, namely sodium is considered $0.11 \cdot 10^{-6}$ Ωm. The space between sodium region and inner and outer magnetic cores is nonconductive and nonmagnetic. The phases of the currents in the three phase windings are 0º for coil A, -120º for coil B, +120º for coil C, 180º for coil X, 60º for coil Y and -60º for coil Z.

For the presented geometry and based on frequency domain models in no moving conditions, a study of the electric supply parameters has been done. It was determined the number of turns per coil for technically acceptable values of current density over the coil cross section from the point of view of classical methods of winding cooling [153]. The number of turns was iteratively determined taking into account a 3 x 400 V, 50 Hz electric power supply, star connection of the inductor winding and three possible values of the current density. The values considered to be acceptable for current density are 2 A/mm^2, 3 A/mm^2 and 4 A/mm^2. For each of these cases, Table V presents the number of turns, generated pumping force and the phase current.

The traveling magnetic field is characterized by the synchronous velocity $v_s = 2f\tau = 13.5$ m/s, where f is the 50 Hz supply frequency and $\tau = b/2$ is the magnetic pole pitch length.

Table V

J [A/mm^2]	Number of turns	Force [N]	Phase current [A]
2	275	100	7.7
3	184	225	17.3
4	138	400	30.75

The value 3 A/mm^2 is taken as a rated value for the pump supply. All the following results in this chapter correspond to this supply.

4.1 2D axisymmetric models of RMS pump based on frequency domain analysis

The “Axial path” and “Radial path”, Fig. 4.2 are used as support in order to represent various field quantity spatial variation.

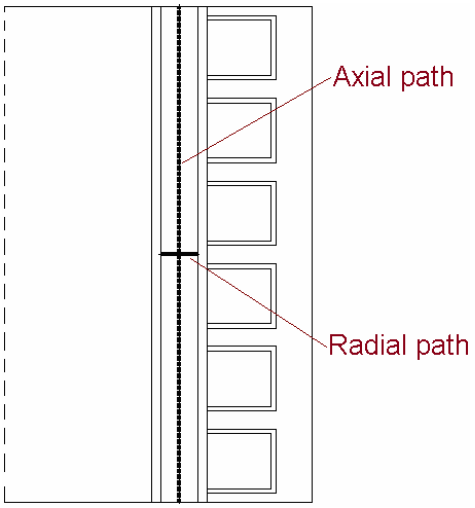

Fig. 4.2 Paths used for different representation

Fig. 4.3 presents the magnetic flux density variation along the *axial path* at various phase shifts of a time period. The wave shape corresponding to 180 degrees is identical with the one of 0 degrees thus Fig. 4.3 presents some selected variation curves of the cyclic variation of the magnetic flux. Comparing the curves from 0 degrees towards 180 degrees is an image of the comparison at successively time moments. The monotonous shifting towards right of the progressive wave is an image of the traveling electromagnetic field motion.

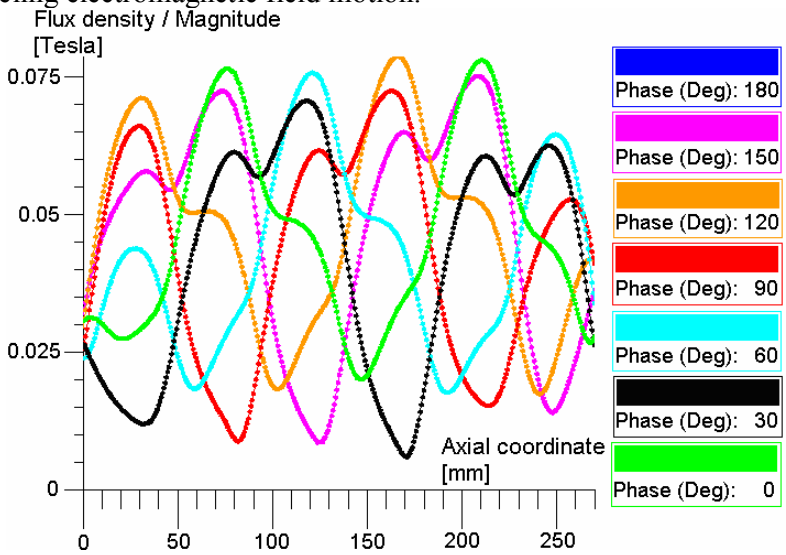

Fig. 4.3 Magnetic flux density along the axial path

The wave shapes in Fig. 4.3 are also an image for the two magnetic poles of the pump. The sequence tooth / slot in a configuration with one slot per pole per phase of the small size ALIP have an effect of sharpening the wave in the area of highest values of the wave. The influence of a slot is of the same importance as the influence of the pole change. This particular effect is much less intense in large size ALIPs with higher number of slots per pole.

The variation along the axial path of the current density is relevant for the influence of the slots, which create the variations presented in Fig. 4.4.

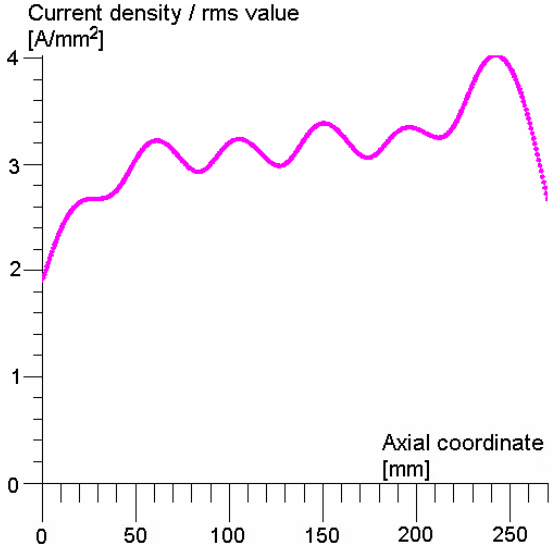

Fig. 4.4 Current density along the axial path

Fig. 4.5 presents for phase shift 30 degrees the axial and radial components and magnitude of the electromagnetic force density. The preponderantly negative values of the radial component are an indicator for the orientation towards the pump axis of this component. Considering that the motion of interest is axially, it is interesting to mention that the magnitude of radial component is higher than the axial component. The difference tends to be similar at any phase shift. This is an indication for the oblique direction of the resultant force.

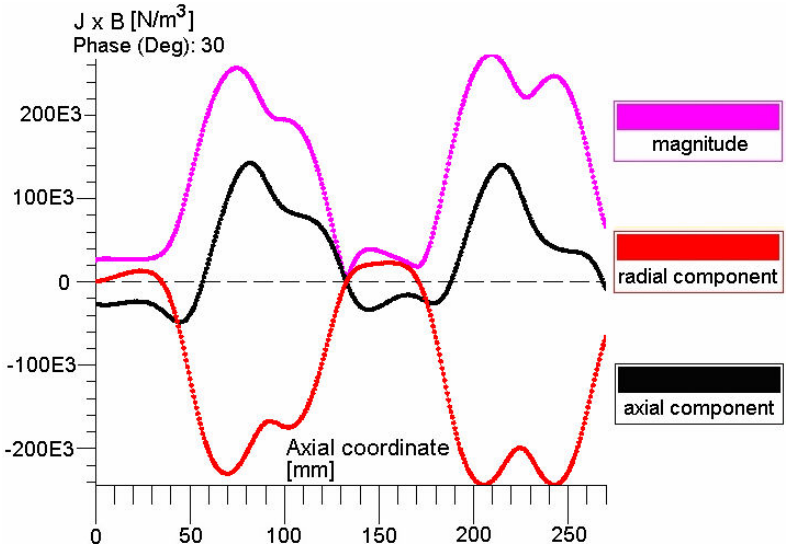

Fig. 4.5 Axial, radial components and the magnitude of the electromagnetic force along the axial path

The decay of the electromagnetic field from the exterior face towards the interior face of the sodium region is presented in Fig. 4.6 using the radial path. The decay direction is from the inductor active face towards the inner magnetic core is due to the skin effect of the sodium region, (2.75).

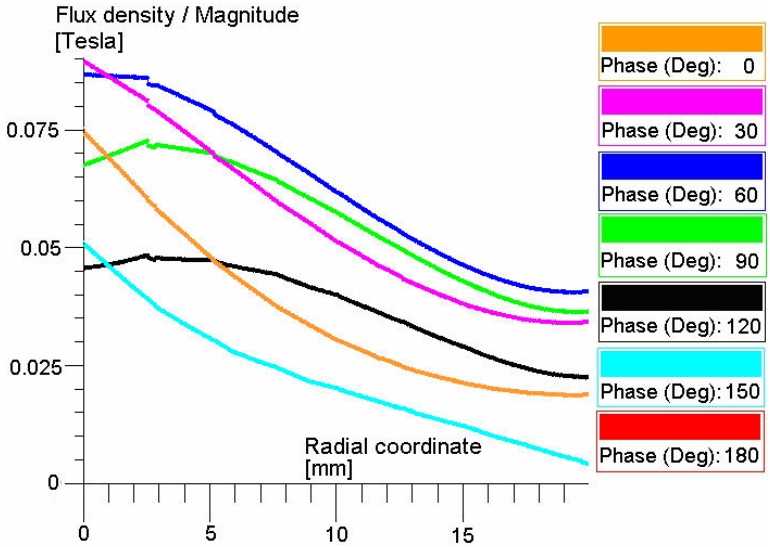

Fig.4.6 Magnetic flux density along the radial path

4.2 2D axisymmetric models of RMS pump based on time domain analysis coupled with motion and with circuit

The implicit parameter of a transient computation is *time* t. All the local and global quantities are functions of t.

The instantaneous values of the two current sources in the circuit model of the RMS pump, Fig. 4.7, are:

$$i_1(t) = \sqrt{2}\, I \sin \omega t\ ,\ \ i_2(t) = \sqrt{2}\, I \sin (\omega t - 2\pi/3) \qquad (4.1)$$

where I is the RMS value of the current related to each inductor slot, $\omega = 2\pi f$ is the pulsation and f = 50 Hz is the supply frequency.

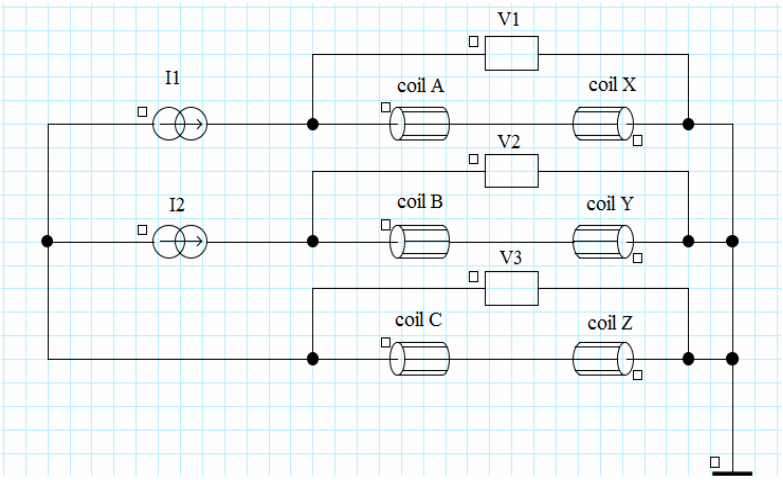

Fig. 4.7 The circuit model of RMS pump

The time and space dependent electromagnetic field characterizing the pump operation, whose source is the current density $\mathbf{J}_1(\mathbf{r},t)$ in the regions of inductor slots, can be expressed in term of the magnetic vector potential $\mathbf{A}(\mathbf{r},t)$, so that the magnetic flux density is $\mathbf{B} = curl\mathbf{A}$. The correlation between geometry, currents (4.1) and the current density $\mathbf{J}_1$, namely the electromagnetic field – circuit coupling, is ensured by the pump circuit model in Fig. 4.7.

The time dependence of the electromagnetic field is numerically treated through the step by step in time domain method. Thus, the term representing the induced current density in conductive regions with the electric conductivity σ, $\sigma(\partial\mathbf{A}/\partial t)$, is approximated by finite differences, $\sigma[\mathbf{A}^{(k)} - A^{(k-1)}] /\Delta t$, where k-1 and k define two successive moments t_{k-1} , t_k and $\Delta t = t_k - t_{k-1}$.

The position of sodium region is changing from the time t_{k-1} to t_k, namely in the *block – pumping* hypothesis. The state variable $\mathbf{A}(\mathbf{r}, t)$ of the electromagnetic field satisfies the equations:

$$curl[(1/\mu)curl\mathbf{A}] + \sigma(\partial\mathbf{A}/\partial t) = \mathbf{J}_1,\ \ div\mathbf{A} = 0 \qquad (4.2)$$

The 2D axisymmetric model of the RMS pump in the cylindrical coordinates system [r,θ,z] takes into account the properties $\mathbf{J}_1[0, J_1(r,z,t), 0]$ and $\mathbf{A}[0, A(r,z,t), 0]$ and the block motion of the sodium region along the pump axis Oz, Fig. 4.8. In this context, equation (4.2) is implicitly satisfied and the vector potential A(r,z,t) satisfies the equation:

$$\partial/\partial z[(1/\mu)\partial A/\partial z\ ] + \partial/\partial r[(1/\mu)\partial A/\partial r] - \sigma(\partial A/\partial t) = - J_1 \qquad (4.3)$$

The finite element solution of the unknown vector potential $A^{(k)}(r,z)$ at the current time step t_k considers the boundary condition of tangent magnetic field on the vertical limit of the computation domain and Kelvin transformation inside the infinite box region, Fig. 4.8a). With respect to the time variable t, the step by step scheme is applied and the initial condition $A^{(0)}(r,z) = A(r,z,0) = 0$ is considered.

Regarding the motion of the sodium region along the Oz axis, Fig. 4.8b), the velocity v is imposed and is invariable in time.

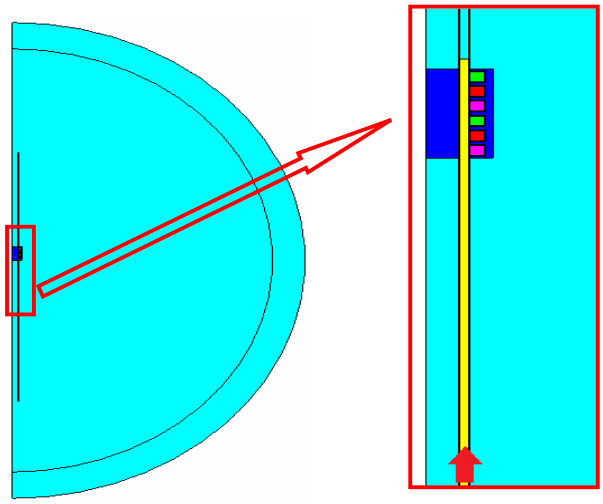

a) b)

Fig. 4.8 Computation domain of the RMS pump field-motion-circuit coupling transient 2D model

The known value of the sodium region at the time step t_k allows the computation of the displacement $v \cdot \Delta t$ of this region, respectively of the new position of the sodium region in the computation domain for the next time step $t_{k+1} = t_k + \Delta t$. Fig. 4.9 presents positions of the sodium region with respect to the inductor at different moments of time t_k.

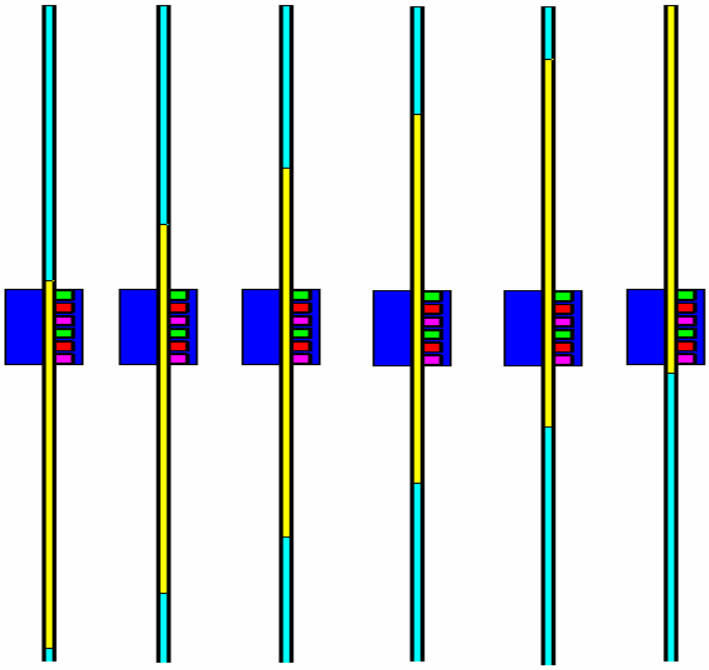

Fig. 4.9 Different positions of the sodium region at various moments, 2D model

Figs. 4.10 – 4.12 are representations of field quantities related the sodium region for three particular velocities: 0 m/s, the sodium is actually not moving or it characterizes the state in the moment of switching on the pump, 7 m/s which corresponds to the maximum force, Fig. 4.22 and 11.34 m/s which is close to the synchronous velocity. The representations are at phase 0º for the immobile case and at time step 0.0925 s for the cases with imposed speed 7 m/s, respectively 11.34 m/s.

Analyzing the magnetic flux distribution one can see that the range of values is approximately similar for the three cases. Also, the distribution of the magnetic flux density is similar in the first two cases. A very different distribution is observed for the 11.34 m/s.

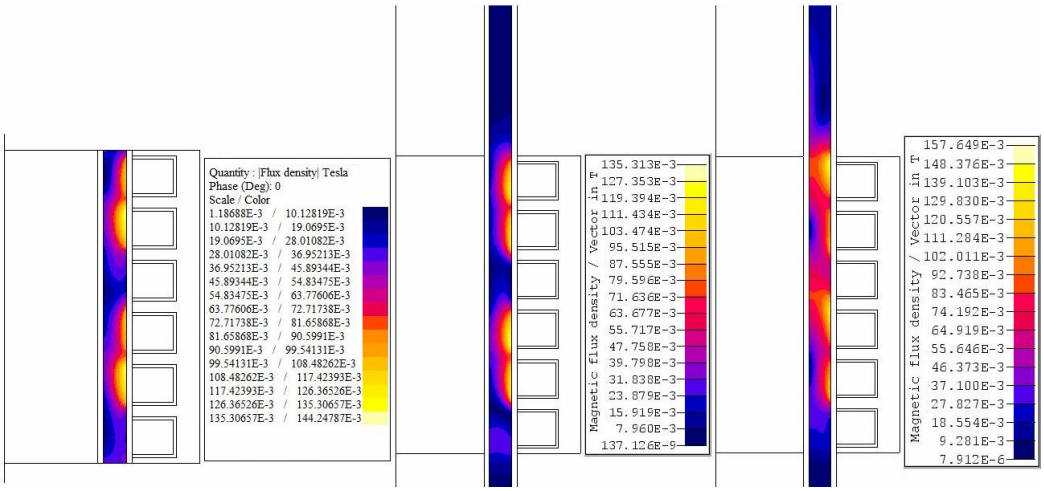

a) b) c)

Fig. 4.10 Module of magnetic flux density in sodium at velocities a) 0 m/s, b) 7 m/s, 11.34 m/s, 2D model

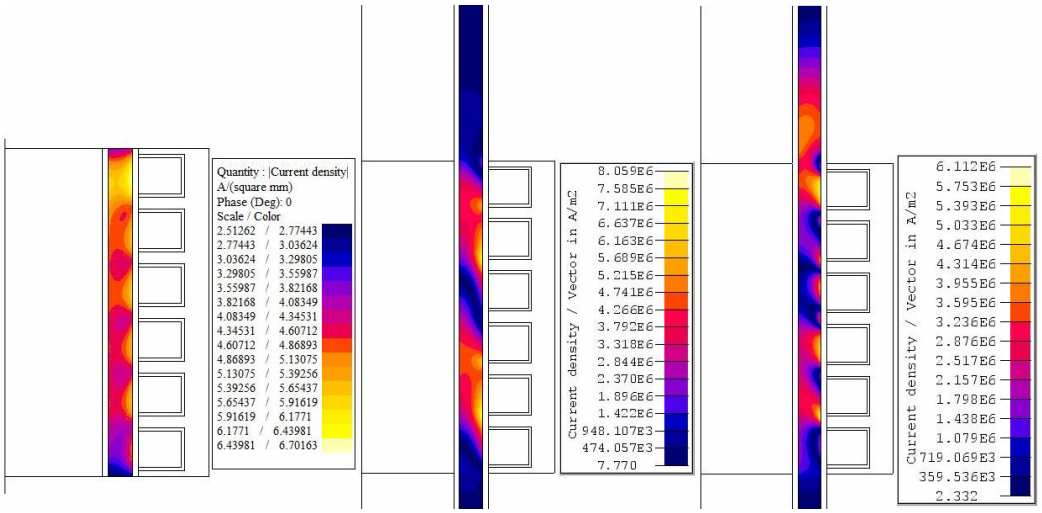

a) b) c)

Fig. 4.11 Module of current density in sodium at velocities a) 0 m/s, b) 7 m/s, 11.34 m/s, 2D model

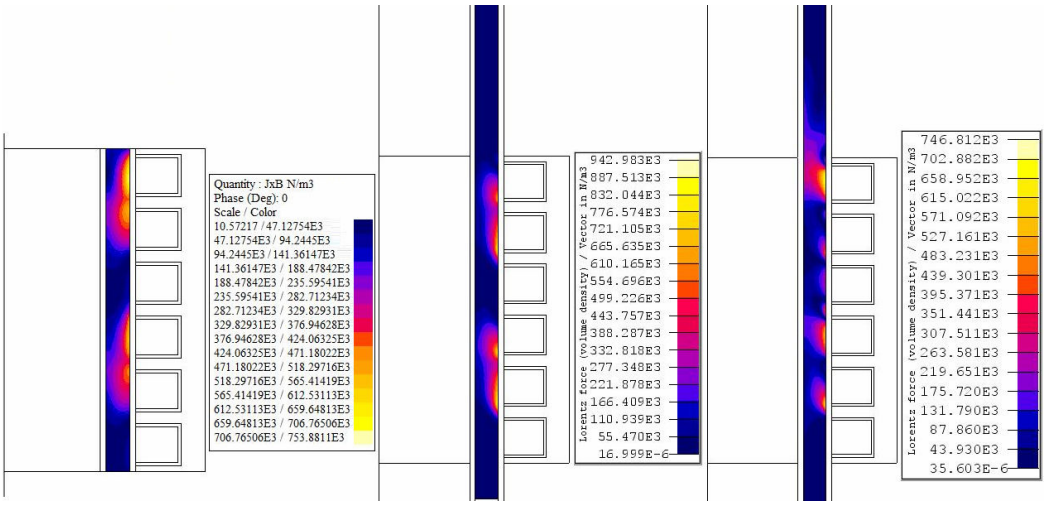

a) b) c)

Fig. 4.12 Module of force density in sodium at velocities a) 0 m/s, b) 7 m/s, 11.34 m/s, 2D model

The current density distribution is much more sensitive to sodium velocity than the magnetic flux. Passage from 0 m/s to 7 m/s brings an important change in the current distribution that have the aspect of oblique pulled upwards, in the motion direction. At 11.34 m/s the current density of important values is distributed in the region that exceeds the pump's inductor.

At high velocities, a double induction phenomenon is occurring. The induced current in sodium at 0 m/s is due to the time variable inductor currents of the pump. As the sodium velocity increases, another electromagnetic field is generated due to the motion of the electroconductive region, (2.15), (2.16). This is an explanation for the intensification of the magnetic flux, Fig. 4.10c) at the outlet. This second field induces at its turn supplementary currents, Fig. 4.11c). This phenomenon is also called entrainment of the electromagnetic field by the flow or the magnetic field is advected with the fluid flow, see paragraph 2.4.

The magnetic field and current generation at the outlet determine an intensification of the electromagnetic force, very visible at 11.34 m/s, Fig. 4.12c).

Fig. 4.13 presents the variation in time of the integral of axial force density for various velocities of the sodium region.

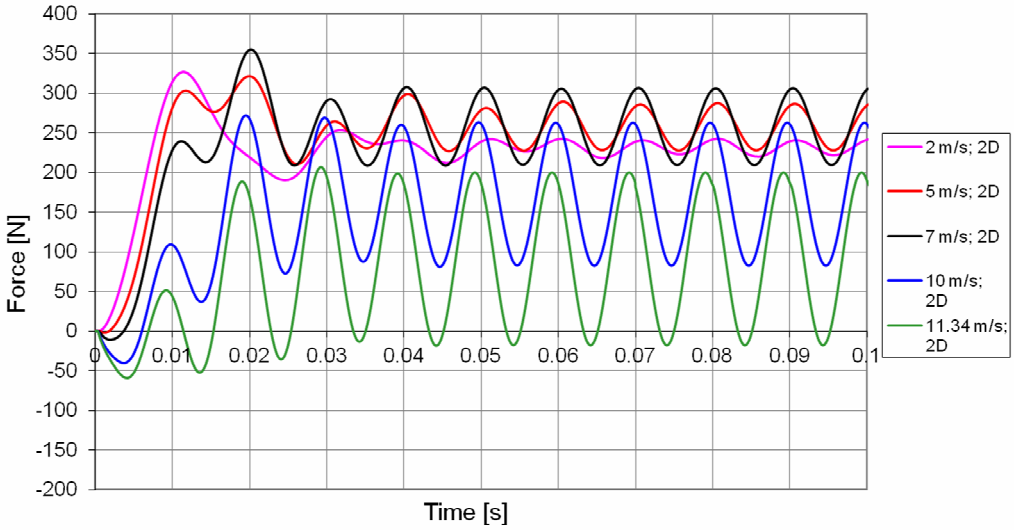

Fig. 4.13 Variation in time of the electromagnetic force for various imposed speeds 2D model

It can be observed that the mean values of the force in the stabilized regime are depending on velocity and the amplitudes increase with the increase of velocity. The time necessary for reaching stabilized regime is decreasing as the velocity increases. The frequency of the force is 100 Hz, which is double of the supply frequency.

4.3 3D models of RMS pump based on frequency domain analysis and time domain analysis coupled with motion and with circuit

The interest of a 3D model consists in evaluation of quantities in the azimuth direction. The geometry of the model used in the 3D simulation is reduced to 1/6 of the entire device, Fig. 4.14, by taking into account the geometrical and electromagnetic quantities symmetries with respect to the symmetry plane of each exterior magnetic core.

The motion in case of the transient models, Fig. 4.15, is considered in the same manner as in paragraph 4.2.

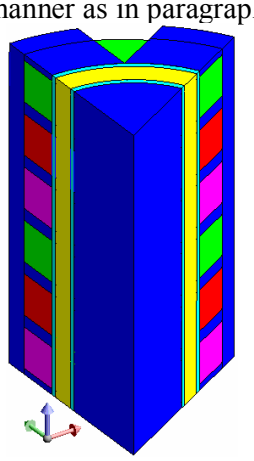

Fig. 4.14 Reduced geometry of the 3D model of RMS pump

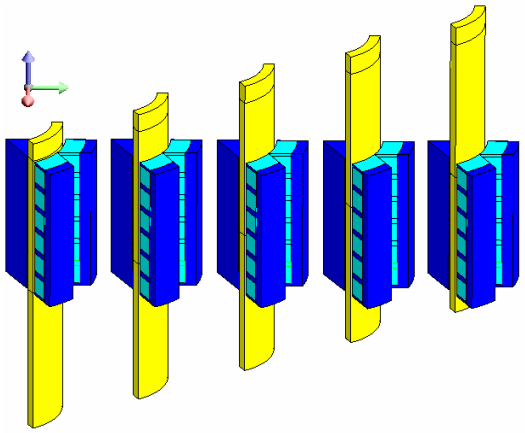

Fig. 4.15 Different positions of the sodium region at various moments, 3D model

Figs. 4.16 and 4.17 are representation of the azimuth component of the current density on the exterior, respectively interior sodium face for different velocities.

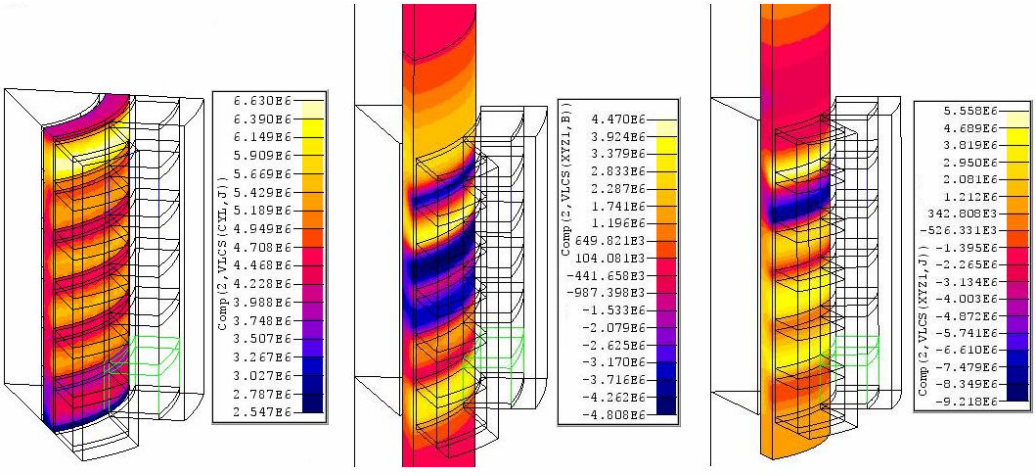

a) b) c)

Fig. 4.16 Azimuth component of current density on sodium exterior face for velocities a) 0 m/s, b) 7 m/s, 11.34 m/s

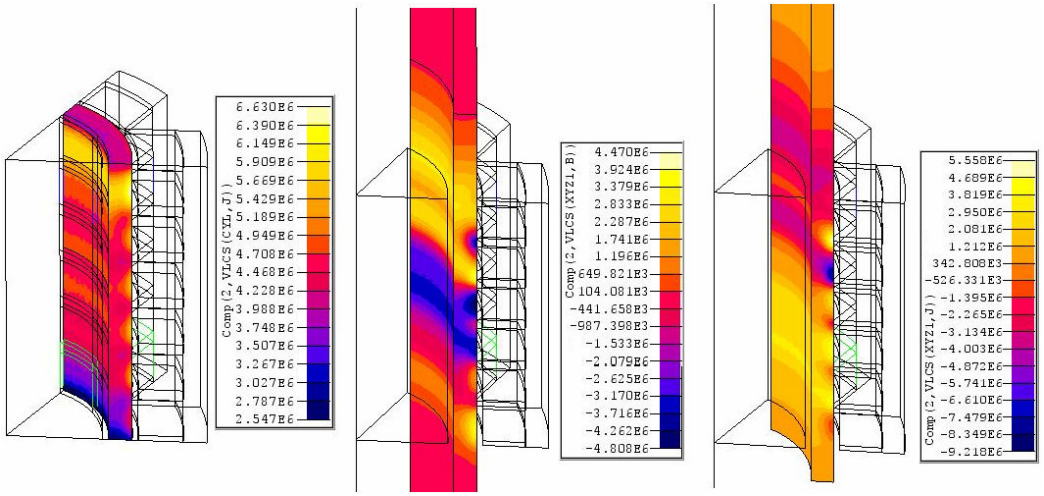

a) b) c)

Fig. 4.17 Azimuth component of current density on sodium interior face
for velocities a) 0 m/s, b) 7 m/s, 11.34 m/s

Fig. 4.18 presents the variation in time of the integral of axial force density for various velocities of the sodium region relative to the 3D model. The values are representative for the full geometry of the pump. The observations made for the variations determined with the 2D model, Fig. 4.13, are also valid. Some observations, nevertheless, can be made with respect to the relative differences between force variations in time in 2D and 3D models, at the same velocity.

Figs. 4.19 – 4.21 show that for a certain sodium velocity, the amplitudes of force are higher in the case of the 3D model and the mean value is higher in the case of the 2D model. The differences between the models are due to a better taking into account of the real situation, namely the phenomena along the azimuth direction.

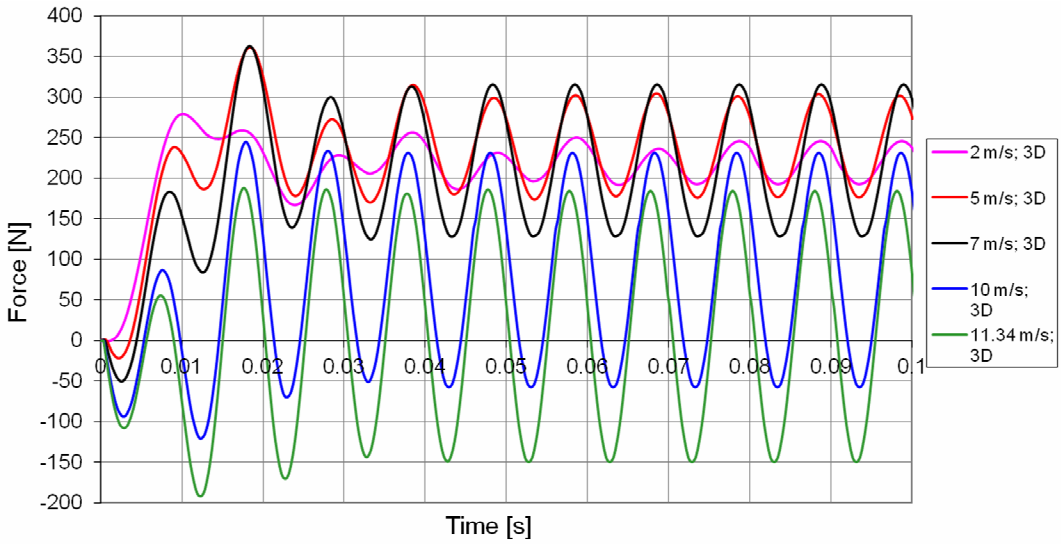

Fig. 4.18 Variation in time of the electromagnetic force for various imposed speeds, 3D model

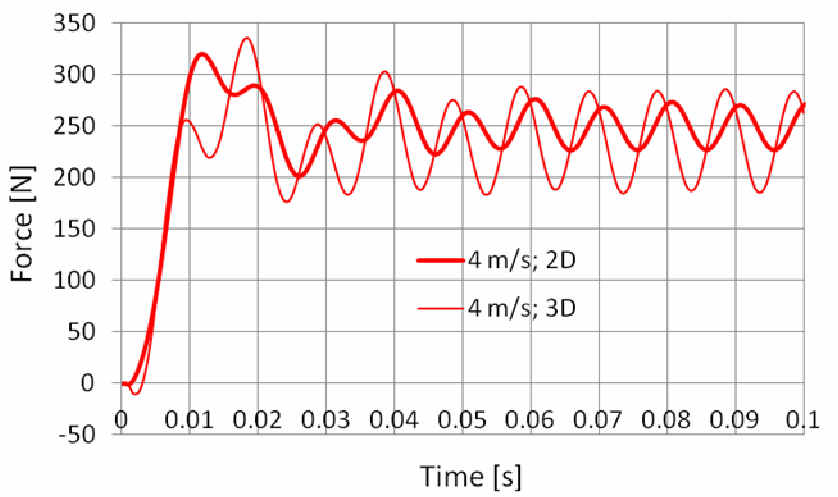

Fig. 4.19 Comparison between 2D and 3D models of RMS pump with respect to the variation in time of the electromagnetic force for sodium velocity 4 m/s

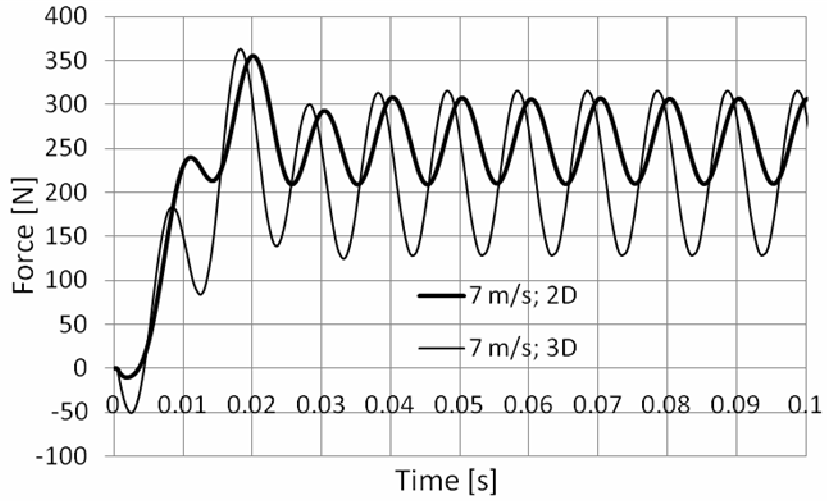

Fig. 4.20 Comparison between 2D and 3D models of RMS pump with respect to the variation in time of the electromagnetic force for sodium velocity 7 m/s

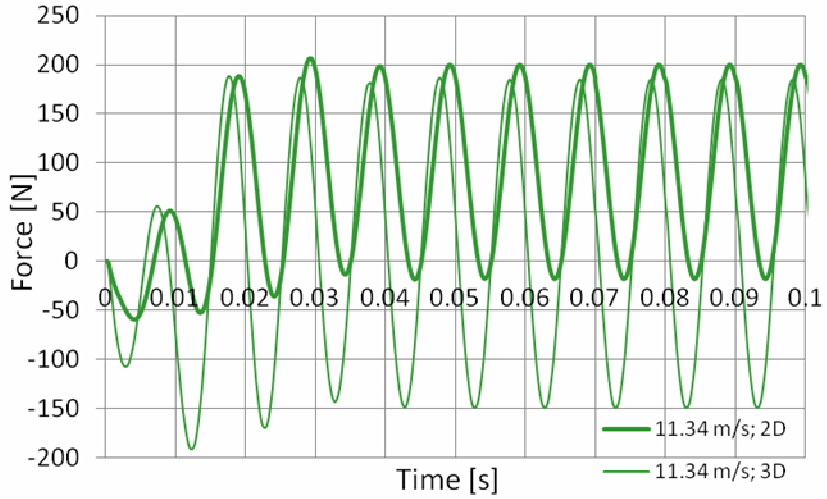

Fig. 4.21 Comparison between 2D and 3D models of RMS pump with respect to the variation in time of the electromagnetic force for sodium velocity 11.34 m/s

Based on the 2D and 3D transient magnetic models coupled with translating motion and circuit, namely by calculating the mean force in the stabilized regime for various sodium velocities it was determined the Force - Velocity characteristic of the RMS pump, Fig. 4.13 and 4.18. The lower values of the mean force observed for the 3D model have the correspondence in the Force – Velocity characteristic in that the characteristic of the 3D model is always under the characteristic of the 2D model.

Some remarks regarding the RMS pump characteristic can be made:

- the maximum force corresponds to the range 6 - 7 m/s for the 2D model and to 5 m/s for the 3D model
- The force becomes zero for the sodium velocity between 12.5 and 12.625 m/s according to the 2D model and between 11.34 and 12 m/s according to the 3D model.
- The difference between 2D and 3D model with respect to the force at 0 m/s is 3.86%. The difference between maximum force and force at 0 m/s is 17.8% for the 2D model and 14.5% for the 3D model, namely the slope of ascendant branch of the characteristic is very smooth.

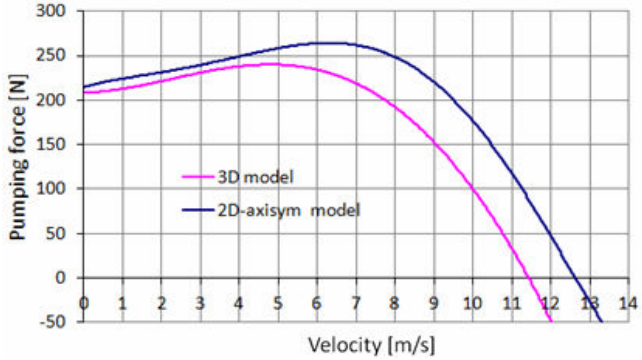

Fig. 4.22 Comparison between 2D and 3D models with respect to the Force – Velocity characteristic of the RMS pump

CONCLUSIONS

This chapter treated from the electromagnetic point of view a small size annular linear induction pump for sodium. The supply parameters and the pumping force were calculated for three technically acceptable current densities over the coil cross-section.

Based on the coupling electromagnetic field – circuit – motion, the variation in time of the electromagnetic force and the characteristic curve Force – Velocity were presented as they result from the 2D model, respectively 3D model. The most important aspects regarding these variations are:

- the mean value of the force in the stabilized regime is depending on velocity as the characteristic curve shows
- the amplitude of the force increases with the increase of velocity
- the time necessary for reaching stabilized regime is decreasing as the velocity increases
- the frequency of the force is always double the supply frequency
- the values of the force on the characteristic curve Force – Velocity corresponding to the 3D model are lower than the values on the curve corresponding to the 2D model due to better consideration of the ends effects and azimuth non-uniformities by the 3D model
- the mean force at a given sodium velocity is lower in the 3D model and the amplitude of the force is much higher in the 3D model.

Chapter 5: Electromagnetic study of PEMDYN sodium pump

The motivation of the studies undertaken in this chapter is related to the succession in time of the author's researches with respect to electromagnetic pumping. After the studies on the RMS pump, the PEMDYN pump followed. PEMDYN is a medium size annular linear induction pump for liquid sodium. The study of PEMDYN pump was occasioned by the collaboration of CEA Cadarache (Commissariat à l'énergie atomique et aux énergies alternatives) with SIMAP-EPM laboratory. The researches were carried out in Grenoble with CEA support. The results of the theoretical study will reflect in a future prototype of the PEMDYN pump for the analysis of possible causes for flow instabilities and testing various prevention solutions in order to obtain valuable information before building the very large electromagnetic pump [121] with possible application in ASTRID project [122].

This chapter is dedicated to an *electromagnetic study* of the PEMDYN pump and contains a study relating the influence of the supply parameters (frequency and number of poles) on the pump Force – Velocity characteristic, a characterization of the startup, steady state operation and dynamic behavior of ALIPs and a study of the azimuth electromagnetic field non-uniformities and oscillations in time and space variation of the force, based on 3D models.

The principal dimensions of PEMDYN pump, such as length, mean radius and thickness of the channel are prescribed. Different versions of the PEMDYN pump may be: with or without interior active inductor, namely double sided or single sided pump, with or without metallic channel walls. From the point of view of the finite element models, some studies may differ in that they model the inductor composed of coils and magnetic yoke with slots and teeth by its correspondent current sheet providing the traveling wave of the electromagnetic field. In each case, the conditions and assumptions of the study are presented.

5.1 Influence of frequency and number of poles on pump characteristics

Fig. 5.1 contains an axial cross section through the double sided PEMDYN pump, which is characterized by the following geometrical dimensions: magnetic yokes length 2200 mm, magnetic yokes width 40 mm, mean value of the pumping channel diameter 300 mm, thickness of the annular channel 50 mm, thickness of the metallic channel walls 5 mm. The length of the current sheets that models the interior and exterior three phased inductor is L_s = 2000 mm. The radial distance between the inner and outer current sheets is 70 mm. The actual computation domain of the 2D axisymmetric models used is selected in magenta.

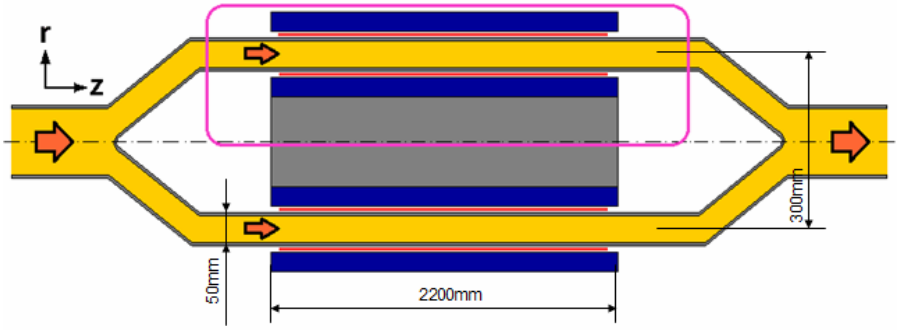

Fig. 5.1 Axial cross section of the PEMDYN pump

The inner and outer current sheets with respect to the channel are defined by the traveling wave of the line current $J_s(z, t) = J_0\cos(\omega t - kz)$ along the axial coordinate z. The frequency of this wave is $f=\omega/2\pi$, $J_0=83.5$ A/mm is the amplitude of the current sheet wave and $k=2\pi/\lambda$, where the wave length $\lambda=2\tau$ is the double of the pole pitch length τ.

The physical properties considered are: sodium resistivity, $\rho_{Na} = 0.13511\cdot10^{-6}$ Ωm, sodium relative permeability, $\mu_r = \mu/\mu_0 = 1$, relative permeability of the nonconductive linear magnetic yokes $\mu_r = 1000$ and channel walls resistivity, $\rho_{Steel} = 0.565\cdot10^{-6}$ Ωm.

Taking into account the fixed longitudinal extension of the current sheets, 2000 mm, the number of poles, is inversely proportional with the pole pitch. This pump can have only the following number of poles 2p = {2, 4, 6, 8, 10}. The corresponding values of pole pitch length are τ = {1000, 500, 333, 250, 200} mm.

5.1.1. Families of Force-Velocity characteristics

The literature and industrial experience recommend low supply frequencies for annular induction pump for sodium taking into consideration the electromagnetic field penetration depth. The influence of frequency and number of poles on the pump Force – Velocity characteristic was studied for the above specified number of poles and the following supply frequencies {5, 10, 15, 20} Hz.

The numerical models used in this section are of type frequency domain analysis with imposed speed. Solving a series of parameterized applications with the parameters frequency and number of poles, various results that describe the pump behavior are obtained. Figs. 5.2 – 5.6 present families of Force-Velocity characteristics for a certain number of poles and various frequencies.

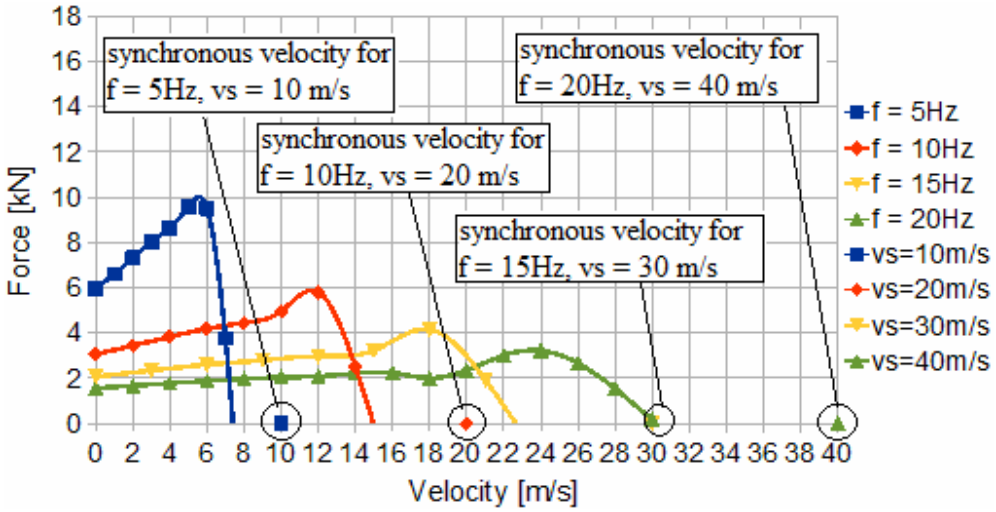

Fig. 5.2 Family of Force-Velocity characteristics for 2 poles configuration and various frequencies

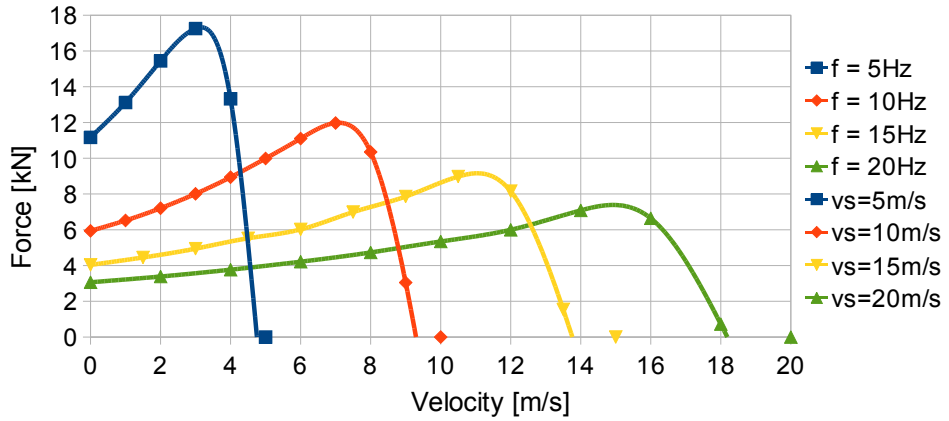

Fig. 5.3 Family of Force-Velocity characteristics for 4 poles configuration and various frequencies

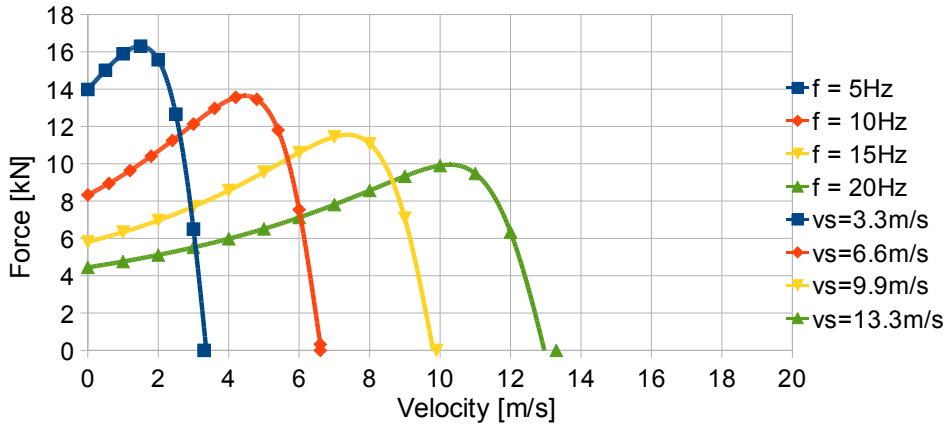

Fig. 5.4 Family of Force-Velocity characteristics for 6 poles configuration and various frequencies

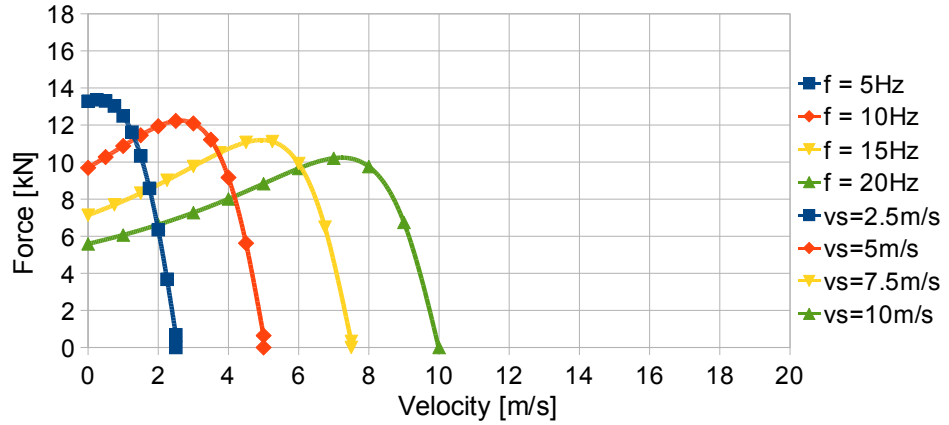

Fig. 5.5 Family of Force-Velocity characteristics for 8 poles configuration and various frequencies

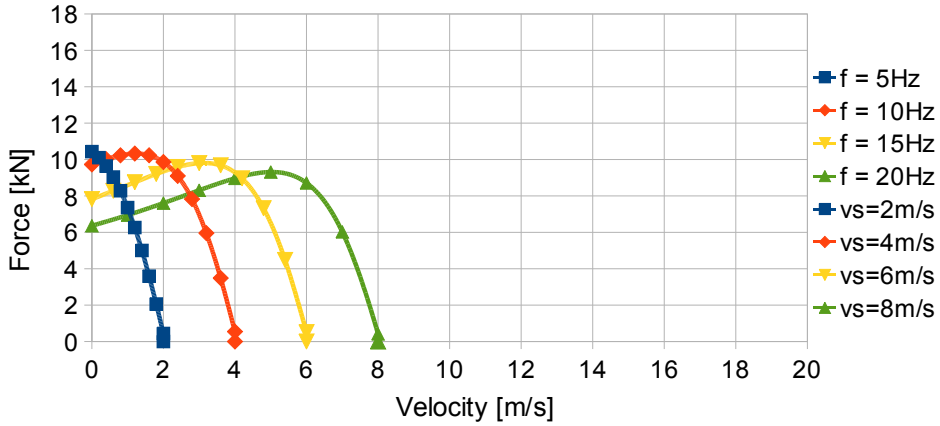

Fig. 5.6 Family of Force-Velocity characteristics for 10 poles configuration and various frequencies

The values of the synchronous velocity corresponding to each frequency and number of poles are marked on the abscissa axis. It can be observed that the value of the velocity for which the force is zero is, in some cases, much smaller than the synchronous velocity. This is most visible for the case 20 Hz, 2 poles, and it happens due to the shielding effect of the metallic walls and because of the important negative forces at the pump inlet and outlet. The shielding effect of the metallic walls refers to the fact that only a part of the power generated by the inductor is transferred towards the sodium, Fig. 5.15. The other part is developed in the metallic walls. There are two types of regions with induced currents: the sodium region which is mobile and the metallic walls, immobile regions.

It is assigned the notion *maximum force* to each characteristic Force-Velocity. It refers to the maximum value of the force for certain pair supply frequency - number of poles. It can be observed that for a given number of poles the maximum force decreases with the increase of the frequency and the velocity corresponding to the maximum force, increases.

As the frequency is lower and the number of poles goes higher, the pump characteristic passes more and more into a monotonous decreasing curve. In paragraph 5.2 is demonstrated that only the descending branch of the characteristic curve is stable at sudden load changes. In this context a pump with a characteristic curve monotonous descendent could be considered stable on the entire sodium velocities range.

Figs. 5.7 – 5.10 represent another method of organizing the families of Force-Velocity characteristics. For fixed supply frequency, the characteristics are presented for various numbers of poles.

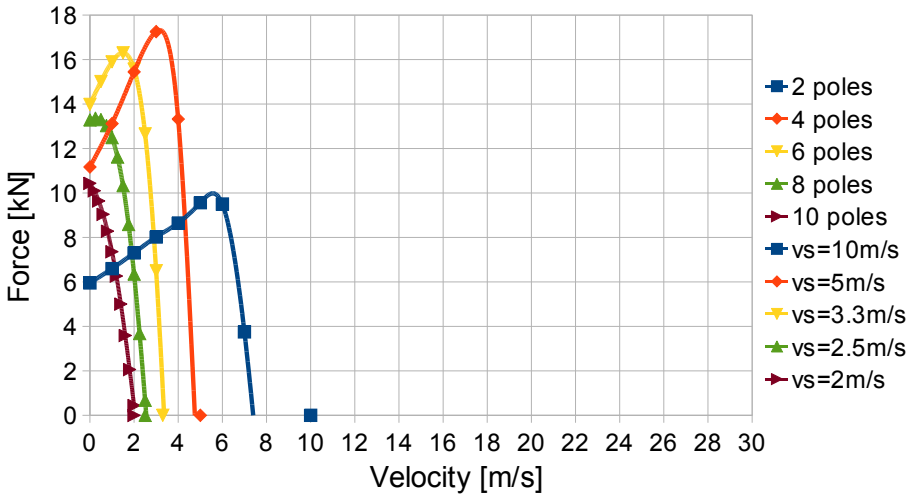

Fig. 5.7 Family of Force-Velocity characteristics for 5 Hz supply and various numbers of poles

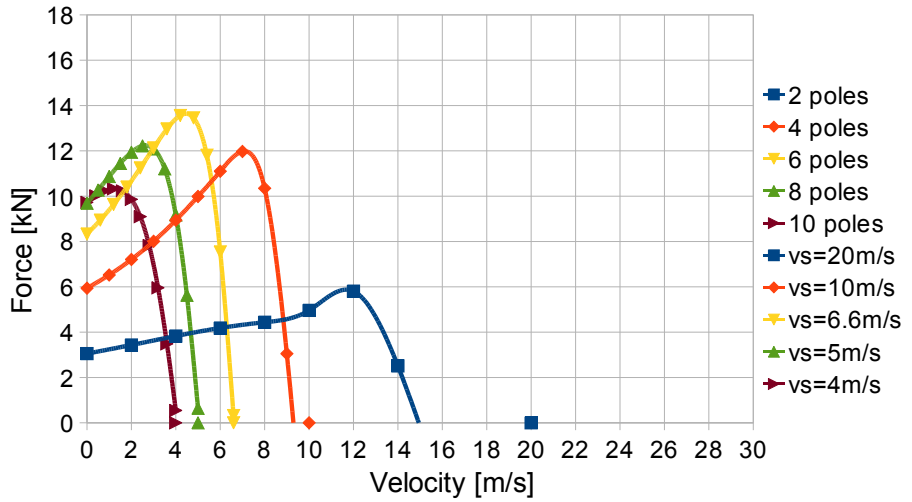

Fig. 5.8 Family of Force-Velocity characteristics for 10 Hz supply and various numbers of poles

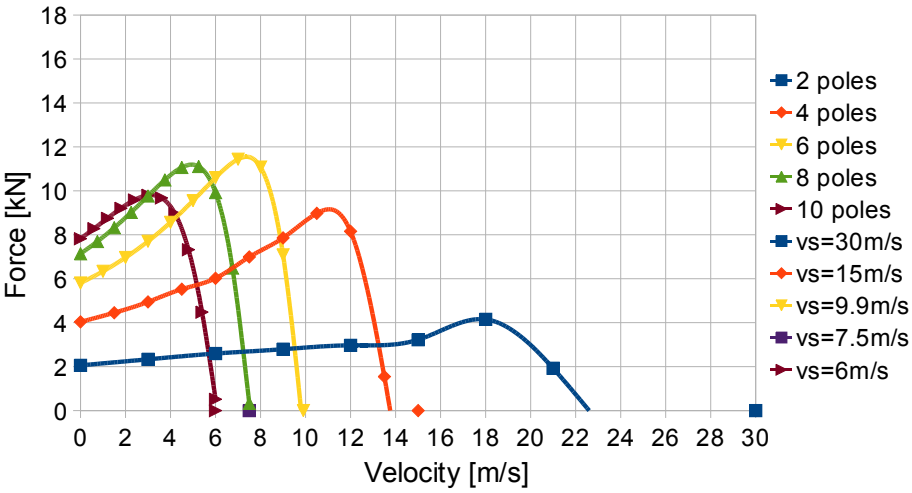

Fig. 5.9 Family of Force-Velocity characteristics for 15 Hz supply and various numbers of poles

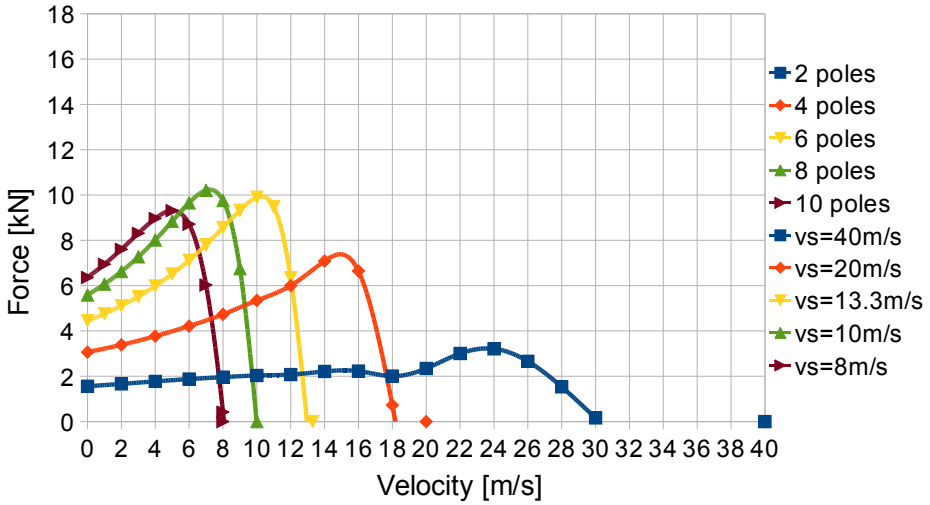

Fig. 5.10 Family of Force-Velocity characteristics for 20 Hz supply and various numbers of poles

Analyzing the characteristics for fix frequency it can be observed that for each frequency there is an optimum from the point of view of maximum force.

The decrease of number of poles and the increase of frequency is correlated with the relative difference between the synchronous velocity and the velocity for which force is zero. Namely, the difference between the two velocities increases as the pump has less number of poles and higher supply frequency.

For any annular induction pump can be defined the quantity called *slip* which represents the relative difference between the synchronous speed of the traveling electromagnetic field and the mean speed of sodium:

$$s = (v_s - v_{Na})/v_s \tag{5.1}$$

where v_s is the synchronous speed and v_{Na} is the mean speed of the sodium.

Figs. 5.11 – 5.14 present the pump characteristic expressed as Force function of slip at given frequency for various numbers of poles. The fact that the velocity corresponding to null force is much smaller than the synchronous velocity determines non-zero values of slip for null force.

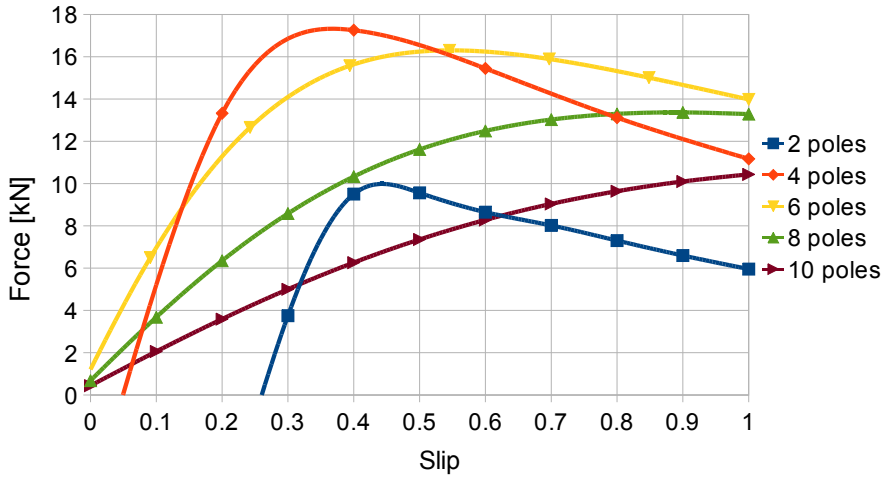

Fig. 5.11 Family of Force-Slip characteristics for 5 Hz supply and various numbers of poles

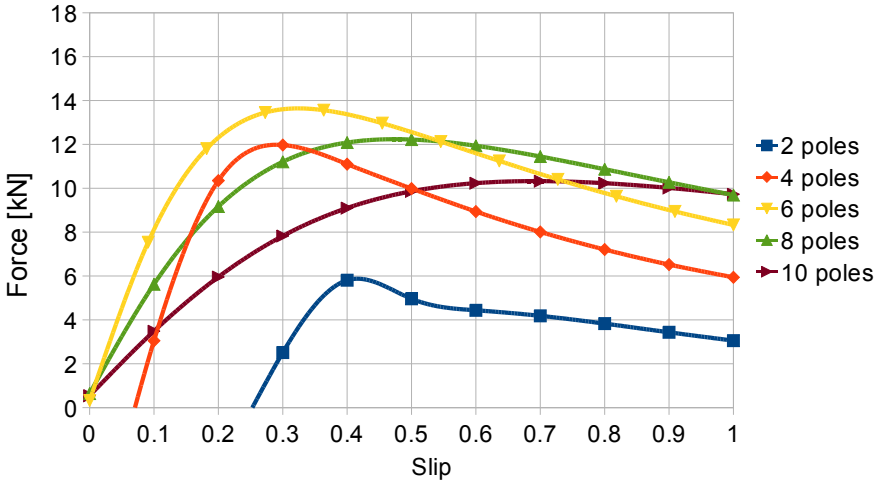

Fig. 5.12 Family of Force-Slip characteristics for 10 Hz supply and various numbers of poles

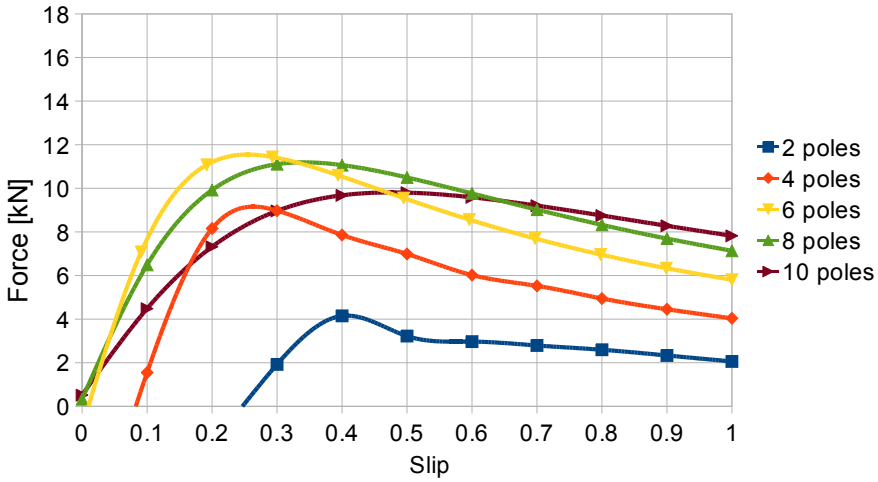

Fig. 5.13 Family of Force-Slip characteristics for 15 Hz supply and various numbers of poles

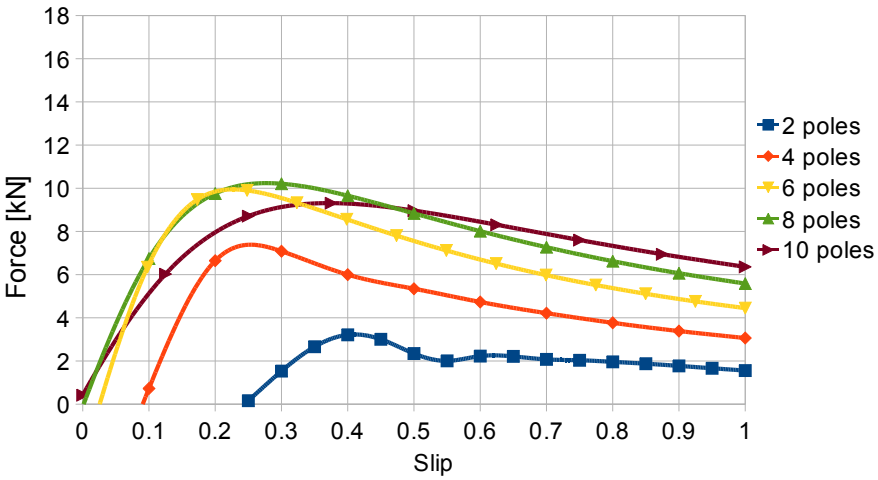

Fig. 5.14 Family of Force-Slip characteristics for 20 Hz supply and various numbers of poles

5.1.2 Influence of metallic walls

As mentioned, the fact that the force is null for a velocity smaller than the synchronous velocity is due to the combined effects of metallic walls shielding and negative forces at the pump ends. In order to quantify the shielding effect of the

metallic walls, the version with non-conductive walls of the 20 Hz, 2 poles configuration has been modeled. Fig. 5.15 gives information about the share that the electro-conductive walls have to the characteristic modification in comparison with the negative forces. The force is zero at approximately 30 m/s for configuration with metallic walls and at approximately 32 m/s in the case of non-conductive walls configuration which is closer to the synchronous velocity 40 m/s, Fig. 5.10. The conclusion is that the shielding effect is only 20% responsible for the difference between synchronous velocity and null force velocity. The other 80% are due to the ends effects.

Fig. 5.15 also highlights the loss of efficiency due to the shielding effect. The current and force densities induced in the walls with no kinematic effect determine the important differences with respect to the force values in the two cases.

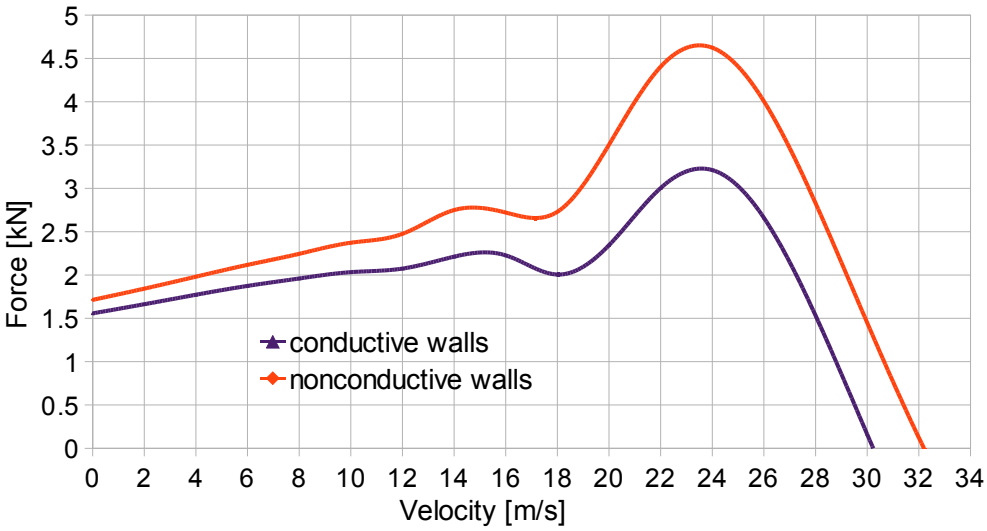

Fig. 5.15 Influence of the metallic walls on the Force – Velocity characteristic of the 20 Hz, 2 poles PEMDYN pump version

5.1.3 Dependence of global characteristics on frequency and number of poles

This paragraph gives information about the effect of the two parameters, frequency and number of poles, on the global quantities that characterize the pump operation, as electromechanical power, Joule power and efficiency.

If only the maximums of the characteristics in Figs. 5.2 – 5.6 or 5.7 – 5.10 are retained, Fig. 5.16 presents the dependence of these maximum forces on frequency and number of poles. It places the configurations 5 Hz, 4 poles and 5 Hz, 6 poles as best choices from the point of view of maximum force generated by the pump.

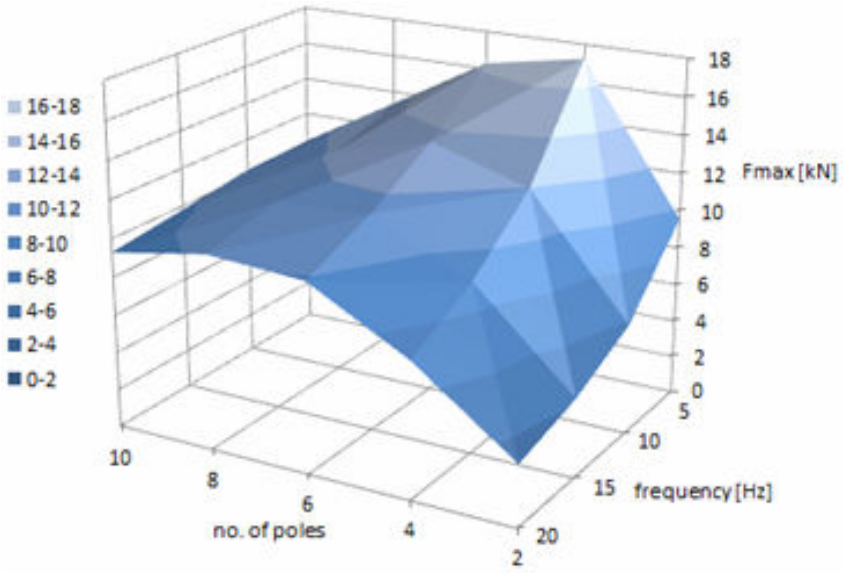

Fig. 5.16 Dependence of maximum force on frequency and number of poles

For the configuration with six poles there are given in addition the characteristics for the supply frequencies 30, 40, 50 Hz, Fig. 5.17. They show that with the increase of the frequency, the maximum forces are decreasing and the descendant branch, where the pump operates, corresponds to very high velocity. This behavior is similar when configurations with other numbers of poles are studied for frequencies higher than 20 Hz.

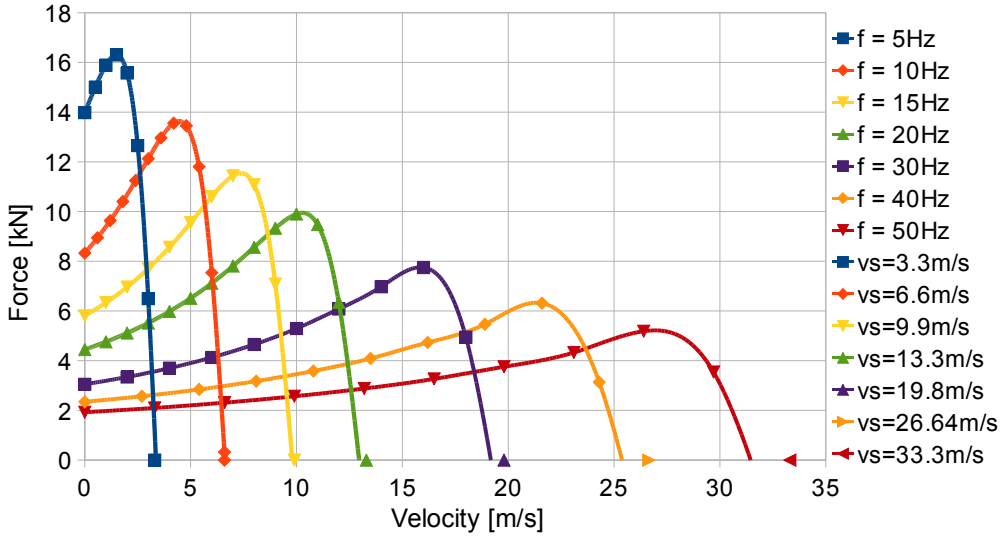

Fig. 5.17 Force – Velocity characteristics for PEMDYN configuration with 6 poles and supply frequency in the range [5 - 50] Hz

The electro-mechanical power corresponding to *maximum force* is calculated as the product of maximum force and the corresponding velocity. The dependence of this quantity on frequency and number of poles is presented in Fig. 5.18. It reflects the convective action of the electromagnetic field. The maximums of the representation are obtained for the configurations 20 Hz, 4 poles and 20 Hz, 6 poles.

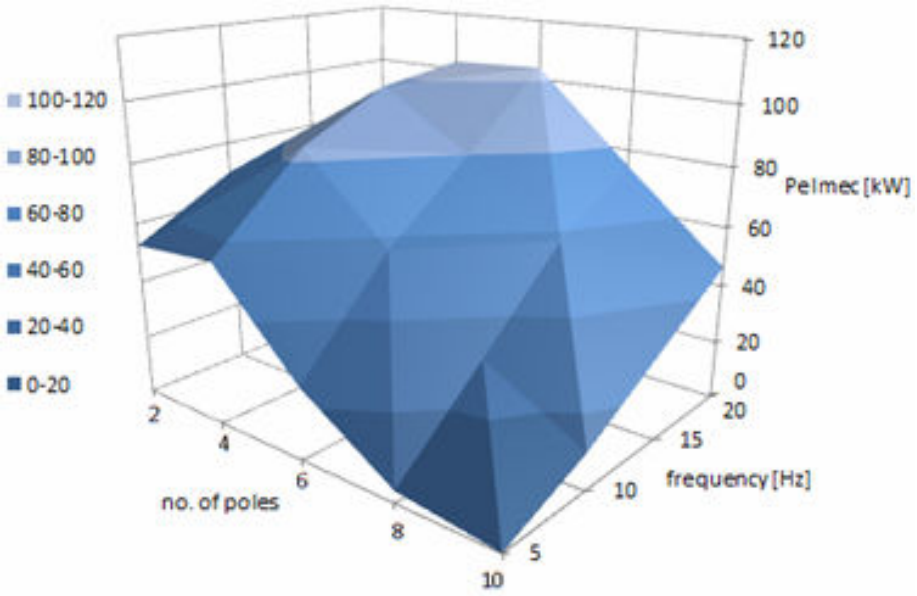

Fig. 5.18 Dependence of maximum electro-mechanical power on frequency and number of poles

The dependence on number of poles and frequency of the Joule power developed in sodium and in the metallic walls, Fig. 5.19, show that the configurations 20 Hz, 2 poles and 20 Hz, 4 poles are the most power consuming.

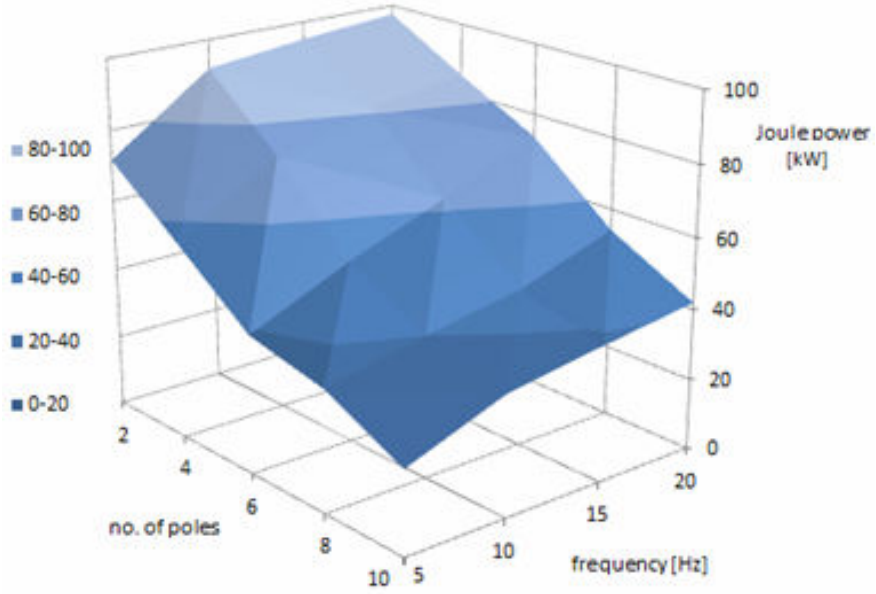

Fig. 5.19 Dependence of maximum Joule power on frequency and number of poles

The efficiency is defined as the percent ratio between electromechanical power and the sum of electromechanical power and Joule power. From the point of view of the efficiency the best configuration is 20 Hz, 6 poles. Configurations 20 Hz, 8 poles; 20 Hz, 4 poles and 20 Hz, 10 poles have the maximum efficiency only a few percents lower than the 20 Hz, 6 poles pump configuration. The calculated efficiency is a measure of quantification of the degree to which the pumping effect the electromagnetic field exercise on the sodium is more important than the heating effect the electromagnetic field has through the Joule power.

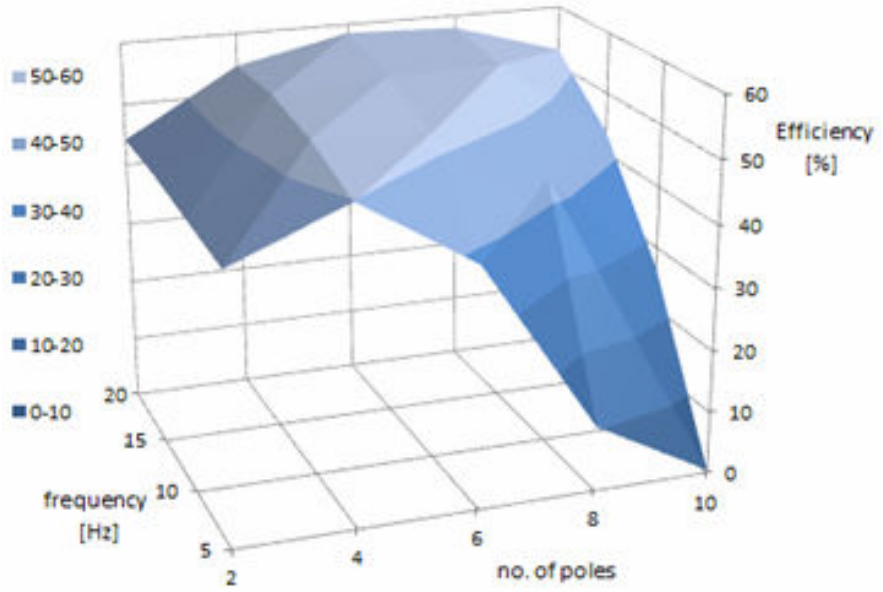

Fig. 5.20 Dependence of the maximum efficiency on the frequency and number of poles

To be noted that the evaluation of pump efficiency must take into account the Joule losses in coils and losses in the magnetic materials.

5.1.4 Ends effect quantification

In order to characterize various pump configurations from the point of view of the ends effects, the following scheme has been used. The Joule power developed in sodium and walls and the integral of the axial force density have been calculated a) only in the *inductor region* and b) *entire length* of the computation domain. By inductor region is understood the region comprised between the limits of the current sheets. The cross-hatched region in Fig. 5.21 represents the margins that were not taken into account when referring to inductor region.

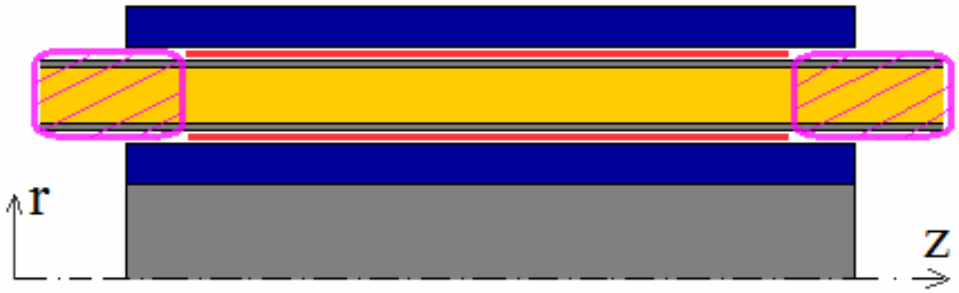

Fig. 5.21 Dividing the calculation domain for ends effects quantification

Table VI show the differences between calculations that take into account only the inductor region and calculations that includes the rest of the domain, with respect to the induced power and generated force. The ends effects consist in diminishing the total pumping force due to the negative forces and increasing the total Joule power due to the induced currents in the ends parts due to the field entrainment outside the pump at high velocities.

A *pump configuration* is characterized by a certain pair supply frequency – number of poles and excepting the two parameters it respects the other general data of the PEMDYN pump. The table says that the ends effects determine an increase of the Joule power with 10.2%, 8.7%, 12.7% for the three pump configurations and a decrease of force with 8.6%, 1.4% and 11.6%.

Table VI

		5 Hz, 2 poles	20 Hz, 6 poles	20 Hz, 2 poles
Joule Power in Na and walls [kW]	Inductor region	64.26	67.05	85.04
	Entire length	71.61	73.50	97.46
Force [kN]	Inductor region	10.46	10.04	3.63
	Entire length	9.56	9.90	3.21

Figs. 5.22–5.24 present the dependence of the induced Joule power on the sodium velocity for three pump configuration. For each pump configuration, there are separately given the dependence on velocity of the Joule power in sodium for the inductor region and for the entire channel and Joule power in walls, also for inductor region and entire wall length. For each pump configuration there are mentioned the synchronous velocity v_s, the velocity corresponding to maximum force v_{fmax} and the velocity corresponding to null force v_{f0}. For each velocity one can determine the share from the total Joule power induced in sodium or in the walls, only in the inductor region or in the entire length of the pump. The curves that are of real interest are those referring to the entire channel and entire length of the walls, *PJ-Na (entire channel)* and *PJ-walls (entire wall length)* because their sum gives the total Joule power developed in the pump at a certain velocity. The curves relative to only the inductor region represent theoretical calculations because they don't refer to an independent phenomenon. The interest of such calculation is to know the influence of the ends effects on the efficiency.

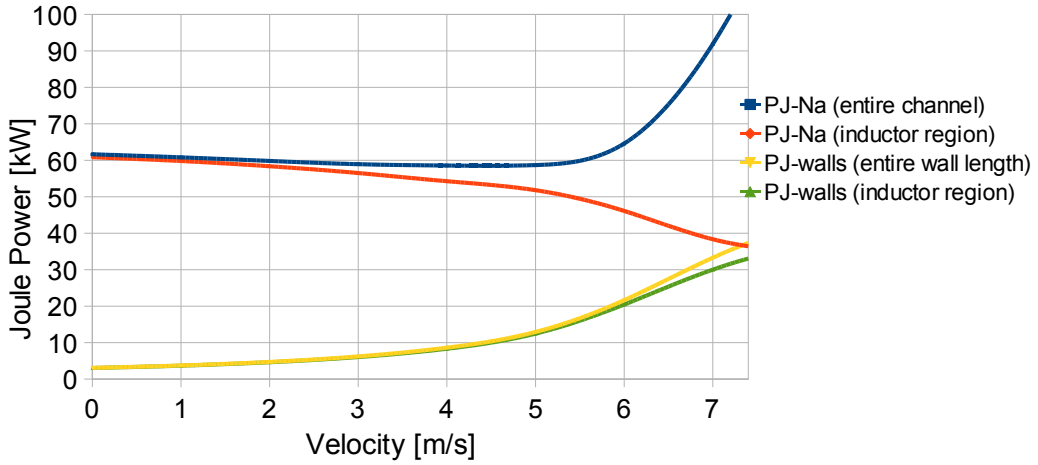

Fig. 5.22 Joule power – Velocity characteristic of the 5 Hz, 2 poles configuration;
v_s = 10 m/s, v_{Fmax} = 5.5 m/s, v_{F0} = 7.4 m/s

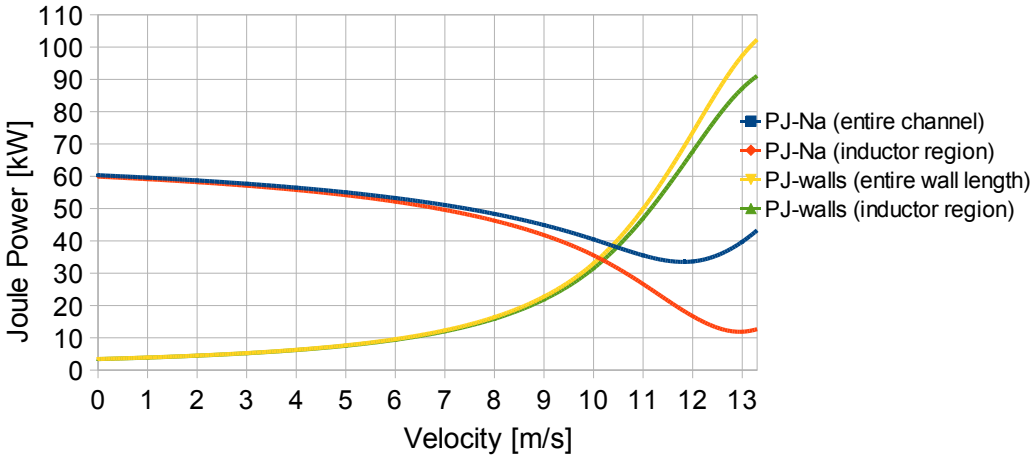

Fig. 5.23 Joule power – Velocity characteristic of the 20 Hz, 6 poles configuration;
$v_s = 13.3$ m/s, $v_{Fmax} = 10.5$ m/s, $v_{F0} = 13$ m/s

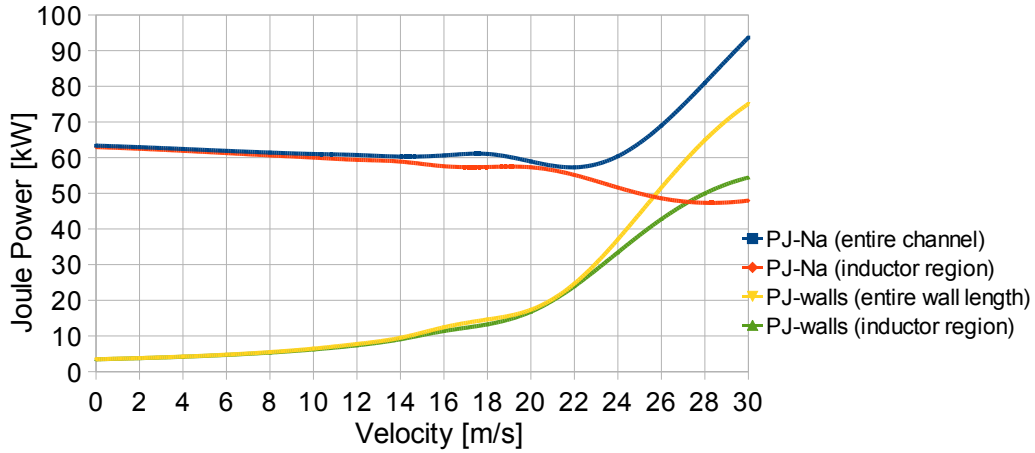

Fig. 5.24 Joule power – Velocity characteristic of the 20 Hz, 2 poles configuration;
$v_s = 40$ m/s, $v_{Fmax} = 24$ m/s, $v_{F0} = 30$ m/s

It can be observed that for low velocities, respectively in the range between zero and around velocity corresponding to maximum force or for the ascendant branch of the Force–Velocity characteristic, there is no major difference between the power induced only in the inductor region or induced in the entire pump length, whether it is about power in sodium or in the walls. This means that the ends effects are not so important relative to the differences of power generation in the inductor region or in the entire length. In the range of velocities between velocity corresponding to maximum force and velocity corresponding to null force, respectively for the descendant branch of the Force–Velocity characteristic, important differences between power generated in the inductor region and in the entire length of the pump, start to appear. This means that for the range of velocities where usually the rated velocity is, the induced power in sodium and in the channel is of higher values in the region immediately after the pump outlet than in the entire pump length due to the electromagnetic field entrainment and secondary induction phenomenon (paragraph 4.2).

Regarding the power in the entire wall length it can be said that is monotonous increasing with the increase of velocity, curve “PJ-walls(entire wall length)” in Figs. 5.22-5.24. The power induced in sodium for the entire pump length, curve

"PJ-Na(entire channel)", Figs. 5.22 – 5.24 is slightly decreasing from null velocity towards a value closed to the velocity corresponding to maximum force when it starts again to increase. It is noted that for the pump configuration 20 Hz, 6 poles, the values of power induced in the entire sodium length at any velocity of the descendant branch are lower then any power induced at the low velocities of the ascendant branch.

5.1.5 Field quantities for different pump configurations and velocities

Fig. 5.25 presents the magnetic flux density and electromagnetic field lines of the PEMDYN pump configurations 20 Hz, 2 poles and 20 Hz, 6 poles when the sodium region moves with 24 m/s, respectively 10 m/s which represent the velocities corresponding to the maximum force of the two configurations. The lines of the magnetic field highlight the two poles, respectively the six poles of the two structures. The entrainment of the magnetic field is evidenced by the field lines and magnetic flux density extended along an important length over the pump outlet. The extension of the field over the pump outlet is proportional with the sodium velocity.

Figs. 5.26 and 5.27 show the differences related the field quantities for 20 Hz, 2 poles and 20 Hz, 6 poles pump configurations when sodium is moving with low, respectively high velocity. Fig. 5.26b) is a zoom at the outlet region of Fig. 5.25a) and presents the magnetic flux density, electromagnetic field lines and electromagnetic force at sodium velocity 24 m/s and 2 m/s, Fig. 5.26a). Some remarks can be made with respect to Fig. 5.26:

- the field entrainment is practically inexistent at 2 m/s and at 24 m/s extends beyond the pump outlet over approximately two thirds of the pump length;
- the magnetic flux density in sodium corresponding to the entrained field is of higher values than in the inductor region; this explains why at high velocities the Joule power density in sodium is higher in the region after pump outlet than in the inductor region, as presented by the difference between *PJ-Na (entire channel)* and *PJ-Na (inductor region)* in Fig. 5.24;
- at low velocities the negative forces at the outlet are inexistent or very small, but Fig. 5.26b) gives information about the important negative forces near the pump outlet developed at high velocities.

The principle of the observations made for 20 Hz, 2 poles configuration regarding the differences between low velocity and high velocity remain valid for 20 Hz, 6 poles pump configuration. The field entrainment at 10 m/s is on a length comparable with the pole pitch length and the negative forces reported to the positive forces just before the outlet are lower than in the 20 Hz, 2 poles, 24 m/s case.

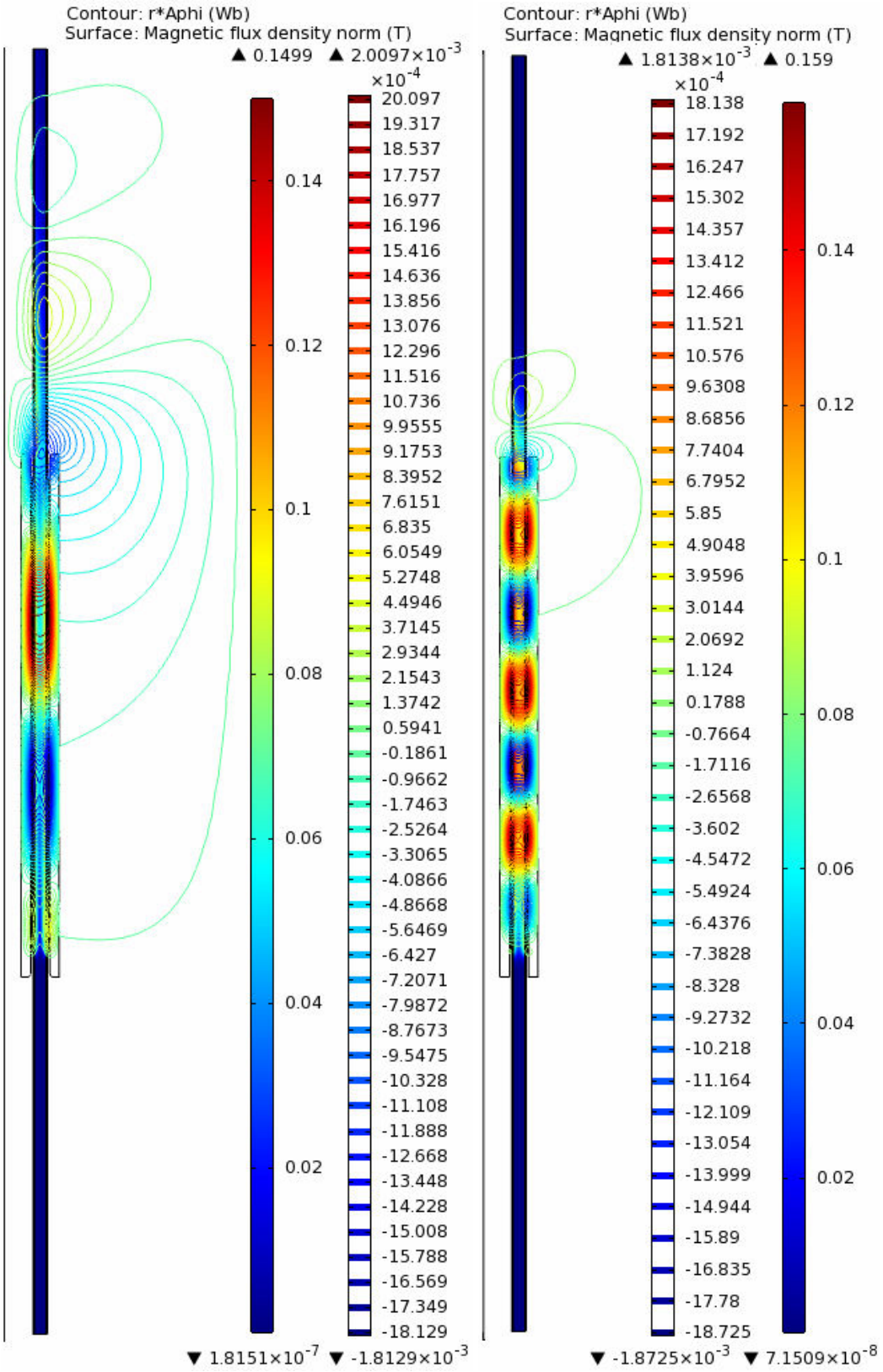

a) 20 Hz, 2 poles, v_{Na} = 24 m/s = v_{Fmax} b) 20 Hz, 6 poles, v_{Na} = 10 m/s = v_{Fmax}

Fig. 5.25 Electromagnetic field lines and magnetic flux density for two pump configurations at different sodium velocities

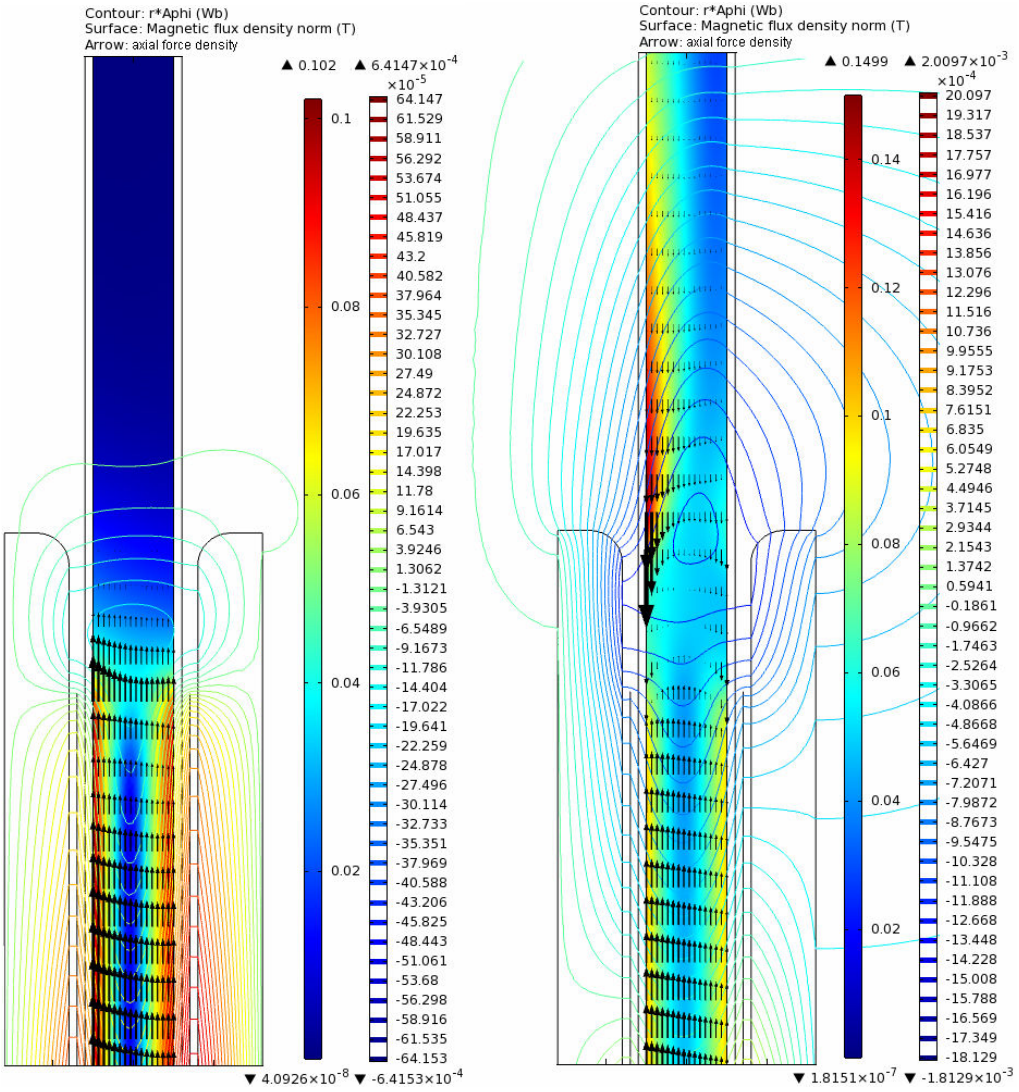

a) v_{Na} = 2 m/s

b) v_{Na} = 24 m/s = v_{fmax}

Fig. 5.26 Electromagnetic field lines, magnetic flux density in colors and axial force density in arrows for the 20 Hz, 2 poles configuration for low and high velocities of the sodium region (outlet zoom)

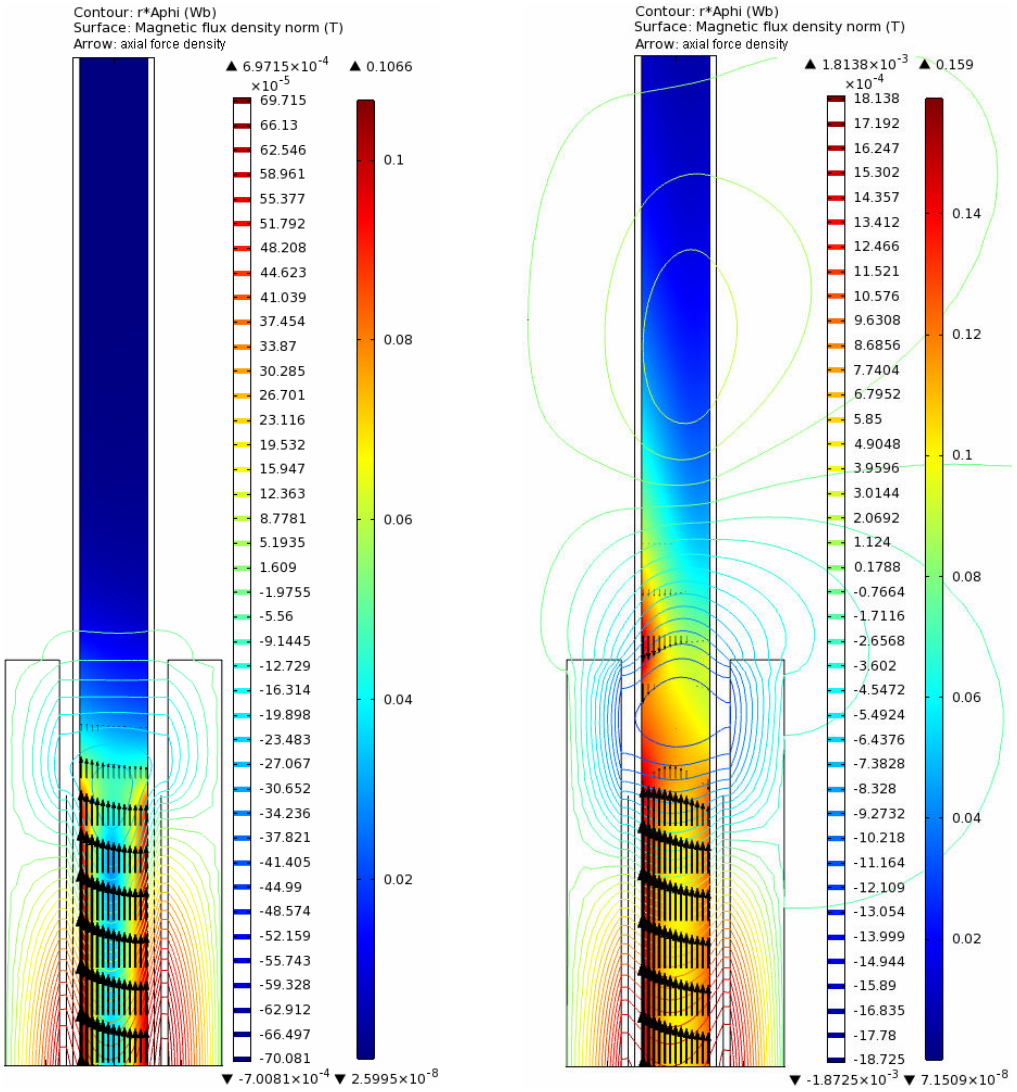

a) v_{Na} = 2 m/s b) v_{Na} = 10 m/s = v_{fmax}

Fig. 5.27 Electromagnetic field lines, magnetic flux density in colors and axial force density in arrows for the 20 Hz, 6 poles configuration for low and high velocities of the sodium region (outlet zoom)

Fig. 5.28 presents the longitudinal component of the force density in colors and arrows for three pump configurations and sodium velocities. The relative comparison of the three pictures is possible due to the representation in the same colors scale and arrows scale. The sodium velocities 24 m/s, 5.5 m/s and 10 m/s correspond to the maximum force generated by the 20 Hz, 2 poles, 5 Hz, 2 poles and 20 Hz, 6 poles pump configurations. Fig. 5.18 gives information about the ends effects at the pump inlet, namely about their intensity and length of propagation. Depending on pump configuration and sodium velocity, the negative forces may extend towards the pump outlet on a length equal to a quarter of the pump length, Figs. 5.29–5.31.

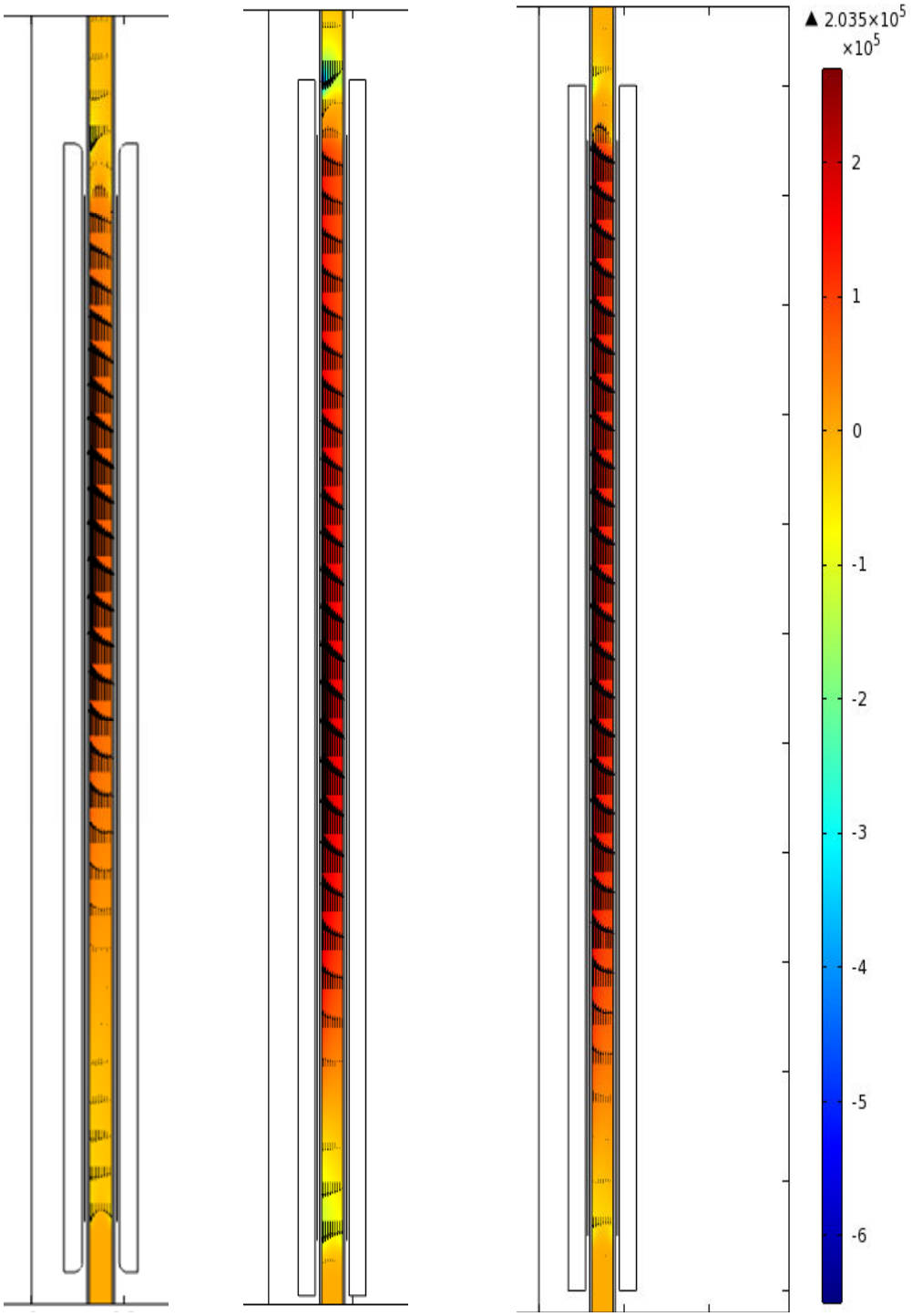

a) 20 Hz, 2 poles, v_{Na}=24 m/s b) 5 Hz, 2 poles, v_{Na}=5,5 m/s c) 20 Hz, 6 poles, v_{Na}=10 m/s

Fig. 5.28 Longitudinal component of the force density in colors and arrows for three pump configurations and sodium velocities

Another method of evaluation the ends effect on the total force generated by the pump is by plotting the variation of the force along the pump. Figs. 5.29–5.31 are representations of the axial force density variation along an axial path situated in the middle of the channel thickness for various velocities ranging from zero to a value between the velocity corresponding to maximum force and the velocity for null force.

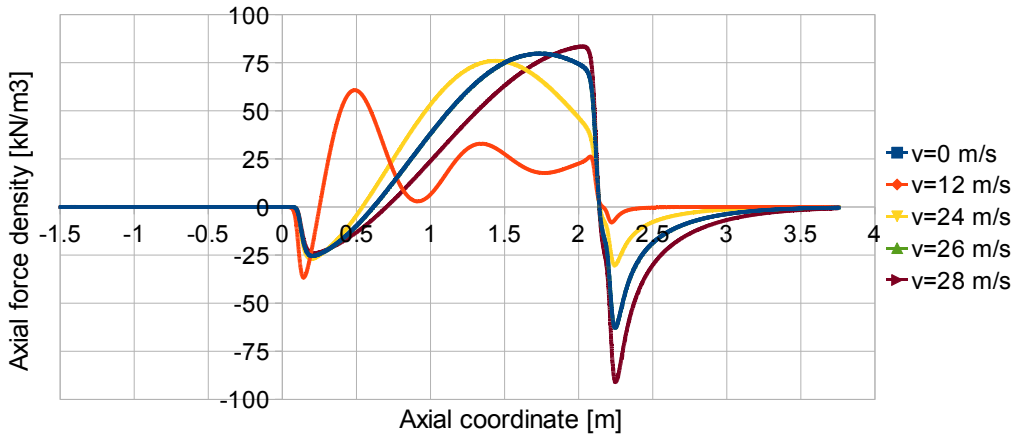

Fig. 5.29 Longitudinal profile of the axial force density for pump configuration 20 Hz, 2 poles at various sodium velocities

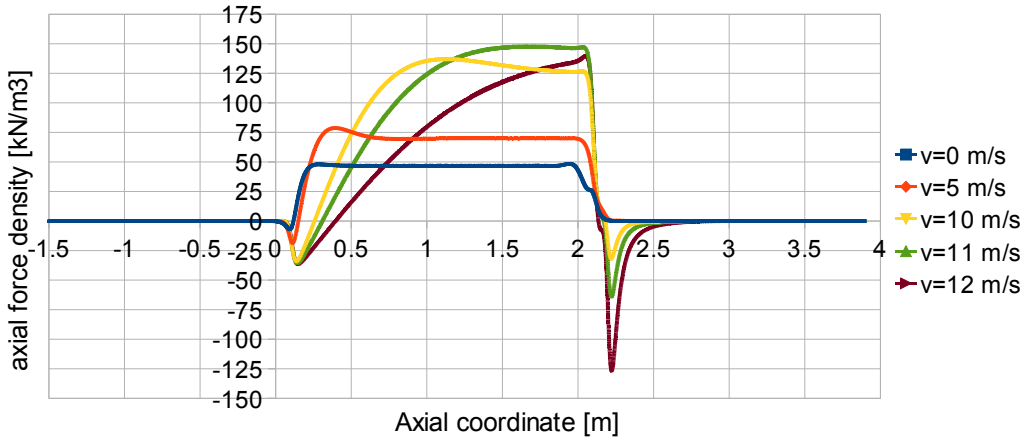

Fig. 5.30 Longitudinal profile of the axial force density for pump configuration 20 Hz, 6 poles at various sodium velocities

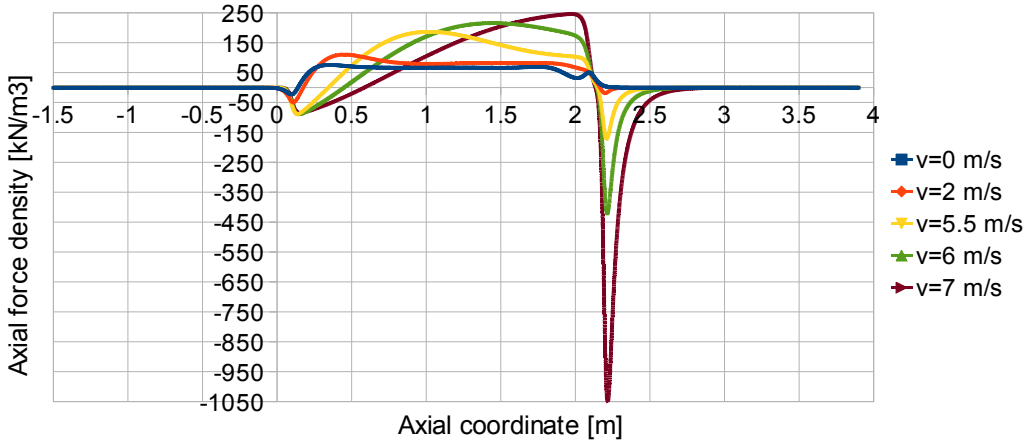

Fig. 5.31 Longitudinal profile of the axial force density for pump configuration 5 Hz, 2 poles at various sodium velocities

At low velocities, a higher number of poles, Fig. 5.30, or a very low frequency in configurations with two poles, Fig. 5.31, can ensure a plateau of constant force before pump outlet.

For the all three pump configurations it is observed that the module of the negative force density at the inlet increases as the velocity increase from zero to velocity corresponding to the maximum force of the Force – Velocity characteristic, namely for the velocities of the ascendant branch. As the sodium velocity belonging to the descendant branch increases the inlet effect does not consist anymore in increasing the module of the negative force density, but in extending the length along the pump of negative force action. Instead, at the outlet, any increase of the sodium velocity implies an important increase of the negative force.

From the point of view of longitudinal force stabilization, the least favorable cases are the 20 Hz, 2 poles pump, Fig. 5.29, and the 5 Hz, 2 poles which in addition to have similar behavior regarding the force stabilization, the outlet negative force density at any sodium velocity is extremely high.

The understanding related the force distribution in the three pump variants given in Fig. 5.28 is enriched by presentation of the radial profile of the axial force density along a radial path situated at the middle of the pump, Figs. 5.32 – 5.34. The electromagnetic design combined with the geometrical structure determines a non-uniform distribution of the force with respect to the channel thickness. For any pump configuration and sodium velocity, the axial force density is higher near the interior wall than near the exterior wall. The blue curve corresponds to null velocity, and the blue curve to a velocity between zero and velocity corresponding to maximum force. The yellow curve corresponds to the velocity at maximum force from the Force-Velocity characteristic and the other two curves correspond to velocities belonging to the descendant branch.

Figs. 5.32 – 5.34 reflect at the scale of local quantities the characteristics Force – Velocity presented in Fig. 5.10. The increase of the value of the axial force density integral along the ascendant branch is reflected by the increasing mean value of the blue, red and yellow curves. The decrease of the force along the descendant branch is evidenced by the mean value of the other two curves that decreases between the yellow curve and blue curve.

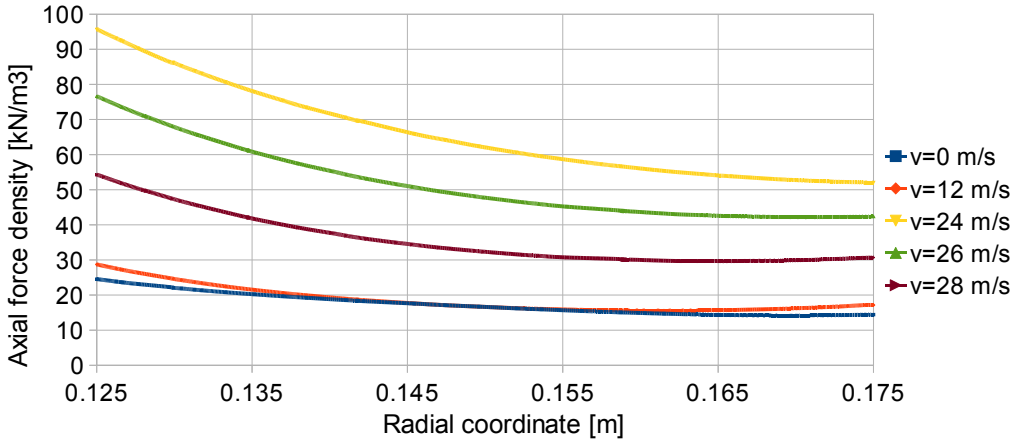

Fig. 5.32 Radial profile of the axial force density for pump configuration 20 Hz, 2 poles at various sodium velocities

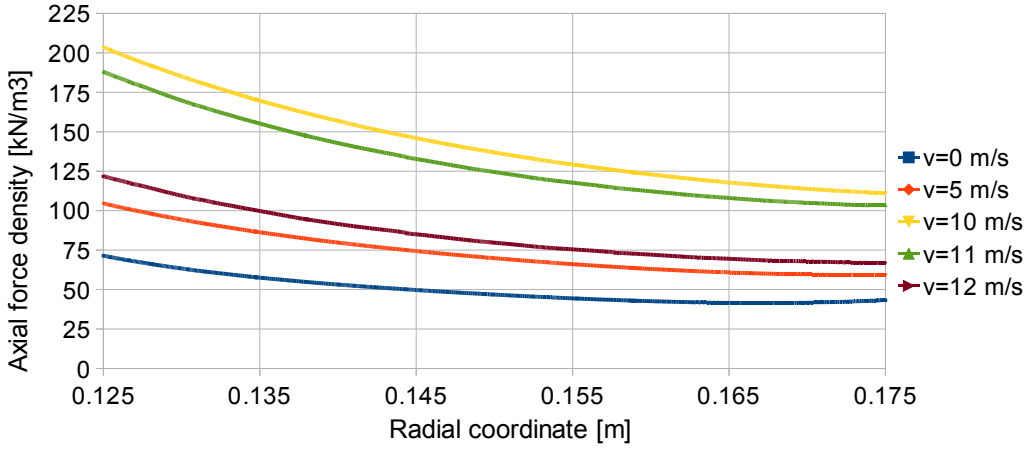

Fig. 5.33 Radial profile of the axial force density for pump configuration 20 Hz, 6 poles at various sodium velocities

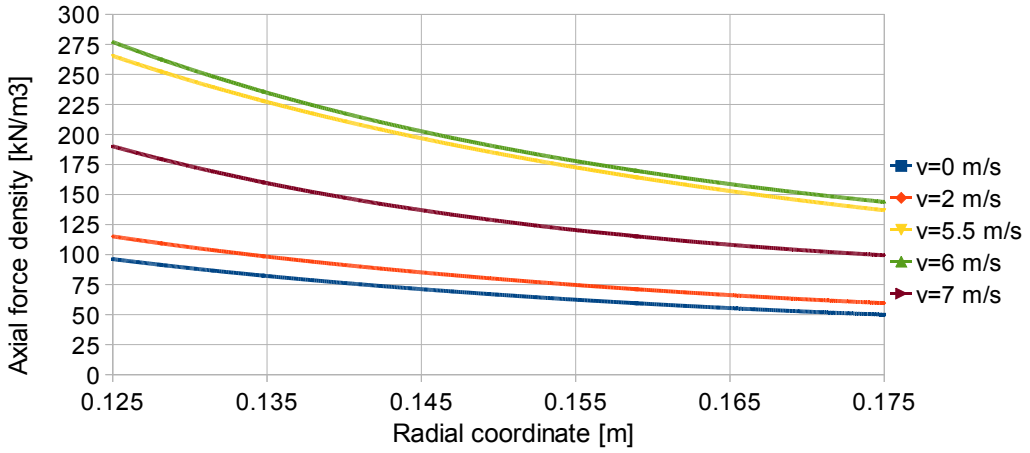

Fig. 5.34 Radial profile of the axial force density for pump configuration 5 Hz, 2 poles at various sodium velocities

5.2 Startup, steady state operation and dynamic behavior of double sided ALIP

Paragraphs 5.2.1 and 5.2.2 present detailed investigations of the 20 Hz, 6 poles version of the PEMDYN pump, based on 2D axisymmetric, respectively 3D models.

Paragraph 5.2.1 presents results of the coupling field – circuit - translating motion finite element models in order to characterize the pump startup, steady operating regime and the dynamic stability at sudden jump loads.

Fig. 5.35 presents the entire computation domain and a zoom of the geometry which is characterized by the following dimensions: magnetic yokes length 2220 mm, pole pitch of the six poles 330 mm, magnetic yokes width 67.2 mm, mean value of the channel diameter 265.5 mm, thickness of the annular channel 52.4 mm, thickness of the metallic walls 3 mm, slot height 35 mm and slot width 46.4 mm.

The physical properties considered are: sodium resistivity, $\rho_{Na} = 0.13511 \cdot 10^{-6}$ Ωm, metallic walls resistivity, $\rho_{Steel} = 0.7 \cdot 10^{-6}$ Ωm, sodium and walls relative permeability, $\mu_r = \mu/\mu_0 = 1$, relative permeability of the nonconductive linear magnetic yokes μ_r=1000.

The instantaneous values of the two current sources per inductor in the circuit model of the pump, Fig. 5.37, are:

$$i_{A\_i}(t) = \sqrt{2}\, I \sin \omega t\ ,\ \ i_{B\_i}(t) = \sqrt{2}\, I \sin (\omega t - 2\pi/3) \qquad (5.2)$$

$$i_{A\_e}(t) = \sqrt{2}\, I \sin \omega t\ ,\ \ i_{B\_e}(t) = \sqrt{2}\, I \sin (\omega t - 2\pi/3) \qquad (5.3)$$

where I = 2430 A is the rms value of the current related to each inductor slot. Taking into account the value of the slot pitch 330 / 6 = 55 mm, the RMS value of the current sheet equivalent to each inductor winding is 2430 / 55 = 44.812 A/mm.

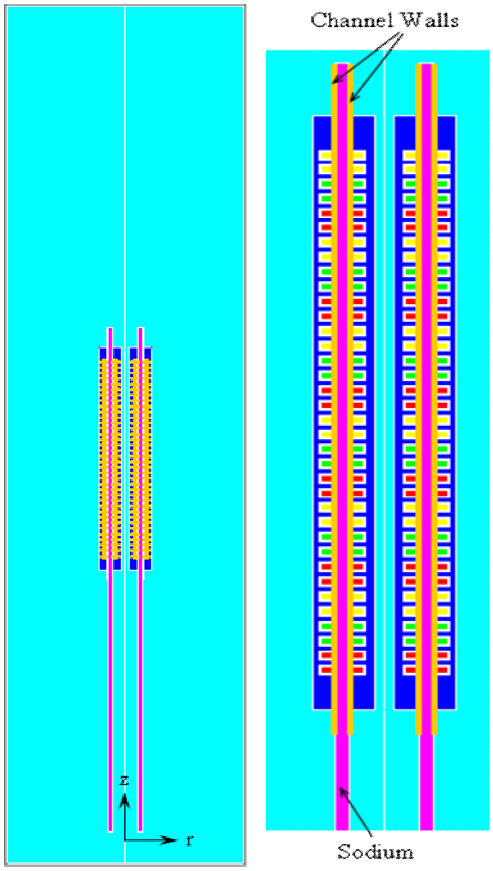

a) b)

Fig. 5.35 Full geometry and zoom of the computation domain

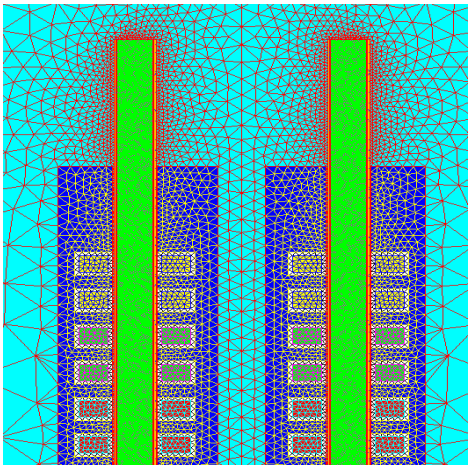

Fig. 5. 36 Meshing of the finite element computation domain (zoom)

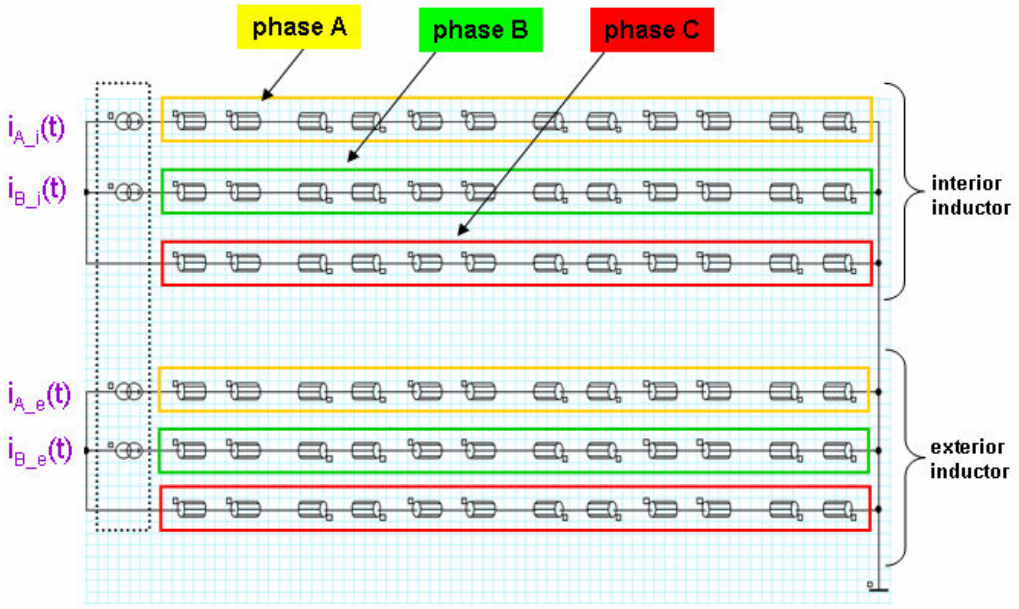

Fig. 5.37 Circuit model of the PEMDYN 20 Hz, 6 poles double sided pump

The mathematical model of the electromagnetic field – circuit – translation model used in this paragraph is similar with the one presented in paragraph 4.2 with distinction that the velocity v is an unknown satisfying the motion equation:

$$m(dv/dt) = F_{elmg} - F_{load} \tag{5.4}$$

where m is the mass of the sodium region in motion, F_{elmg} is the axial component of the Laplace force generated by the electromagnetic field in the sodium region, F_{load} is the load force of the pump and t is the variable time. A model of the pump load proportional with the square of sodium flowrate was considered, respectively:

$$F_{load} = k_l \cdot v^2 \tag{5.5}$$

The initial condition related the unknown velocity is $v(0) = 0$. The value $v^{(k)}$ of the sodium region at the time step t_k allows the computation of the displacement $v^{(k)} \cdot \Delta t$ of this mobile region along the Oz axis, respectively of the new position of the sodium region in the computation domain for the next time step $t_{k+1} = t_k + \Delta t$.

5.2.1 Pump transient startup

Figs. 5.38 – 5.43 present results related the transient of the pump startup when the load dependence on the speed v of the sodium is expressed by the formula $F_{load} = 20v^2$.

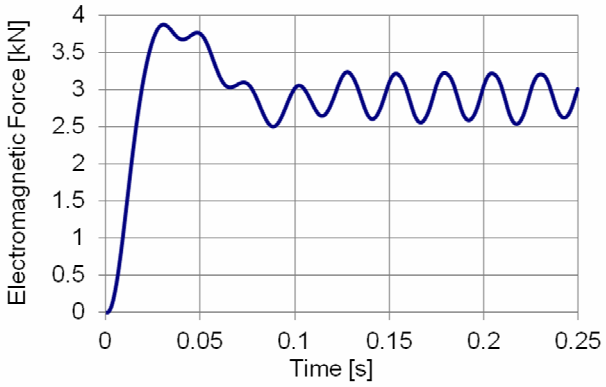

Fig. 5.38 Time variation of electromagnetic force acting on the sodium region

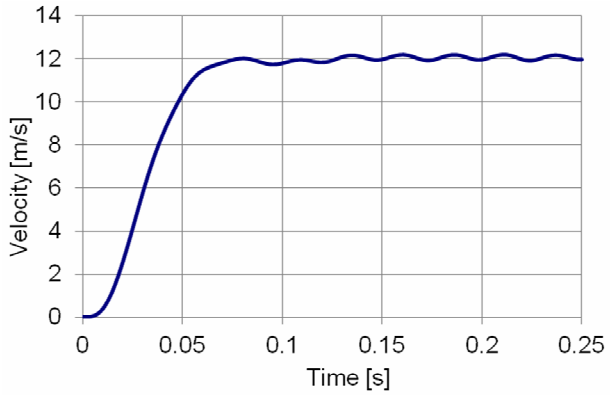

Fig. 5.39 Time variation of sodium region speed

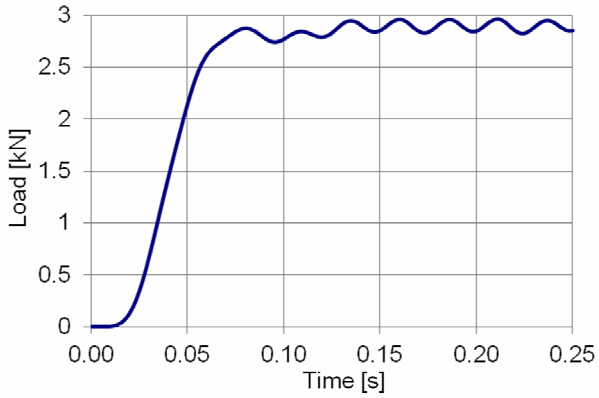

Fig. 5.40 Time variation of pump load, 20 v^2

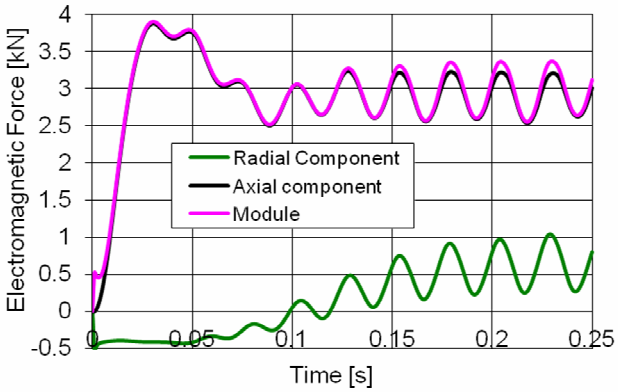

Fig. 5.41 Time variation of components and module of the Laplace force

One can observe that when the steady state pump operation is reached, the mean value of electromagnetic force time variation, Fig. 5.38, 2.87 kN, is equal with the mean value of the load force, Fig. 5.40.

The mean value of the speed characterizing the sodium block pumping is 12.03 m/s, Fig. 5.39. Fig. 5.41 presents the variation in time of the two components and of the module of the Laplace force. From the variations in time of the Joule power in the sodium region, Fig. 5.42 and in the channel walls, Fig. 5.43, it results the mean values of the two global quantities, P_{sodium} = 29.9 kW and P_{walls} = 24.4 kW.

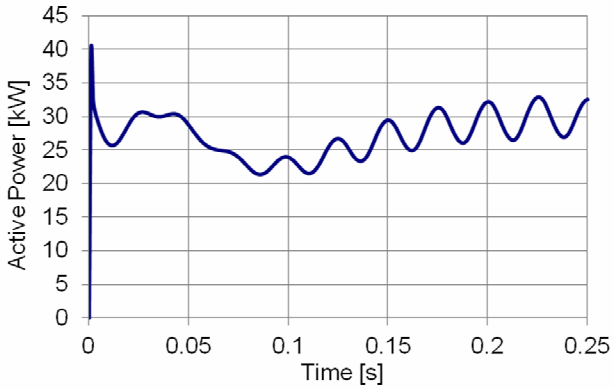

Fig. 5. 42 Variation in time of the active power induced in the sodium region

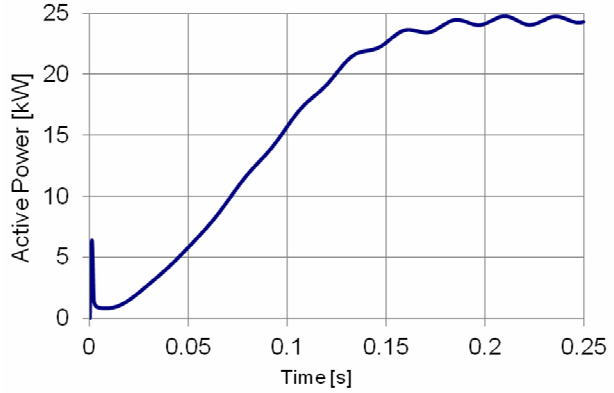

Fig. 5.43 Variation in time of the active power in the channel walls

Figs. 5.44 – 5.47 present the significant electromagnetic field quantities in the steady state regime for the time step 0.23 s, when the instantaneous value of sodium region speed is 12.02 m/s. The magnetic field lines that indicate the six poles of the pump are presented in Fig. 5.44. The color maps of the magnetic flux density in different regions of the computation domain are presented in Fig. 5.45. Fig. 5.46 presents the map of the induced current density in the sodium region.

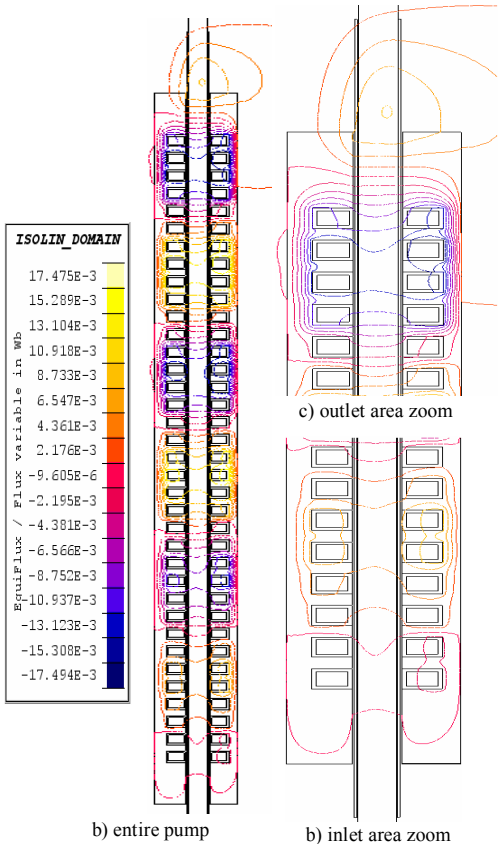

b) entire pump c) outlet area zoom b) inlet area zoom

Fig. 5.44 Magnetic field lines

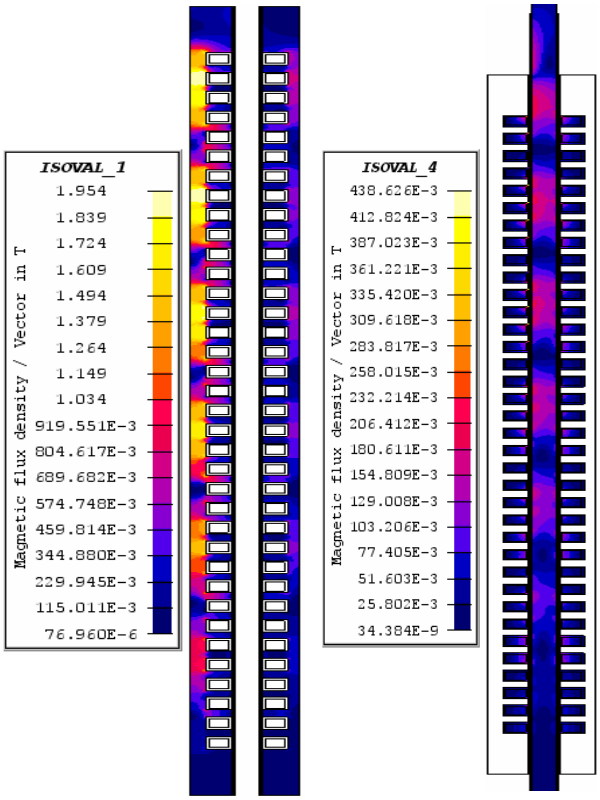

a) in the magnetic cores b) in the airgap and slots

Fig. 5.45 Maps of the magnetic flux density

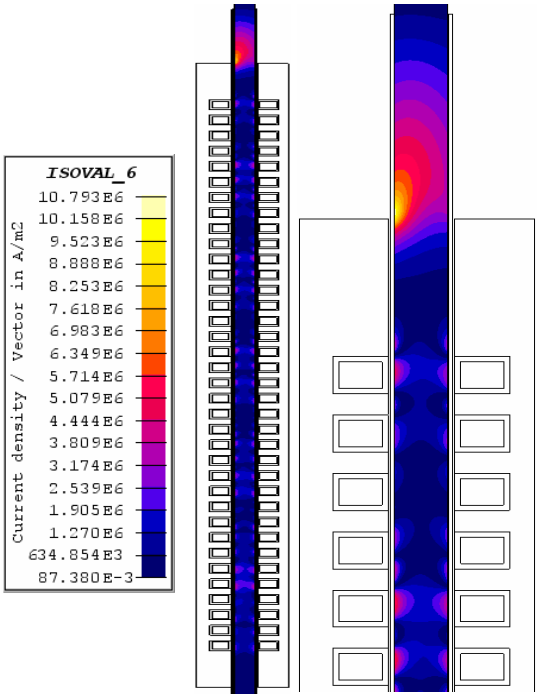

a) whole sodium region b) outlet area zoom

Fig. 5.46 Maps of the induced current density in the sodium

The interaction between the important value of the current density at the pump outlet, near the magnetic yoke end, Fig. 5.46, and the no negligible magnetic field in this area, Fig. 5.45b), Fig. 5.44c), has as result an important outlet breaking effect, Fig. 5.48, of the electromagnetic field in this area of the channel pump.

Fig. 5.47 shows the map of the induced current density in different sections of the channel metallic walls. The effects of the field entrainment are revealed at the inlet region, where the induced currents are significantly lower than at the outlet region. The length of this region of low induced currents is about one sixth of the total pump length.

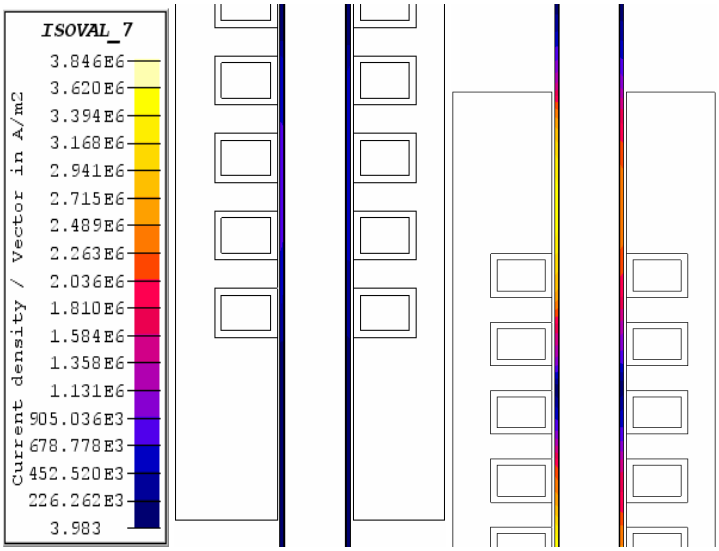

a) inlet area zoom b) outlet area zoom

Fig. 5.47 Maps of the current density in the channel walls

The axial component of electromagnetic force volume density along an axial path in the middle of the sodium region is presented in Fig. 5.48. It shows the non-uniformity along the channel of the local pumping effect, the effect of the slot-tooth alternation and the important braking effect at the outlet.

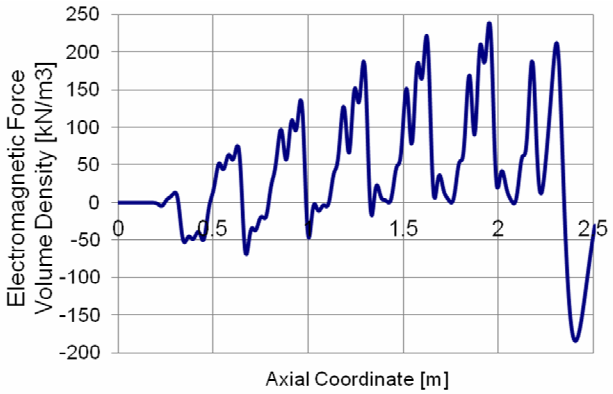

Fig. 5.48 Axial component of the electromagnetic force volume density along a path in the middle of the pumping channel

Solving successive numerical applications for different values of the parameter k_1, (5.5), curves representing variation of the electromagnetic force and velocity in time of type presented in Fig. 5.38 and 5.39 are obtained. Based on the mean values in time of the two quantities, the Electromagnetic Force – Velocity characteristic of the PEMDYN 20 Hz, 6 poles pump was determined, Fig. 5.49. The maximum force is 5.5 kN and corresponds to sodium velocity 10.5 m/s. The velocity corresponding to null force is 12.7 m/s. The point of abscise zero presented in magenta is the value of the synchronous velocity 13.3 m/s. The shielding effect of the metallic walls and the braking forces at inlet and outlet explain why the force is null at a lower velocity than the synchronous velocity.

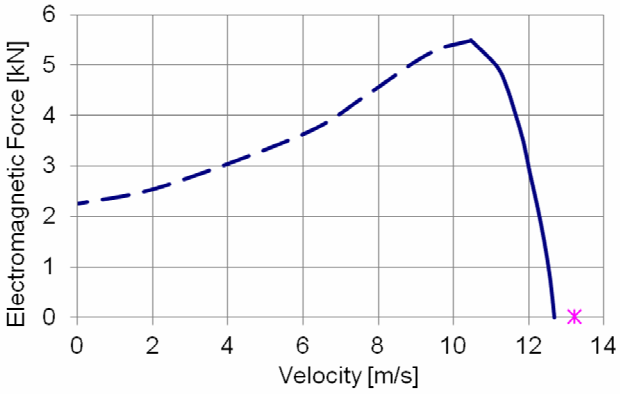

Fig. 5.49 Electromagnetic Force – Velocity characteristic of the PEMDYN 20 Hz, 6 poles pump

The electromagnetic pressure is calculated as the ratio of electromagnetic force and the area of annular surface of the cross section of the sodium region. The flow rate is calculated as the product between the sodium velocity and the mentioned surface area. The dependence between Electromagnetic Pressure and Flowrate represents another way of expressing the Force–Velocity pump characteristic.

Fig. 5.50 presents the Electromagnetic Pressure–Flowrate characteristic of the PEMDYN 20 Hz, 6 poles pump. The maximum electromagnetic pressure is 1.46 bar and corresponds to the flowrate 0.39 m^3/s.

The characteristic curves are split in an ascendant and a descendant branch by the point of maximum force defined by 5.5 kN and 10.5 m/s, respectively by the point of maximum pressure defined by 1.46 bar and 0.39 m^3/s.

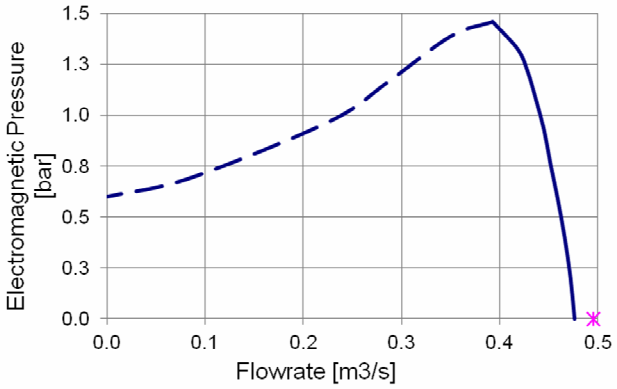

Fig. 5.50 Electromagnetic Pressure – Flowrate characteristic of the PEMDYN 20 Hz, 6 poles pump

The pump efficiency defined as the ratio between the electromechanical power and the sum of electromechanical power and Joule power in coils, sodium region and channel walls, is presented in Fig. 5.51 and 5.52 as function of velocity, respectively of flowrate.

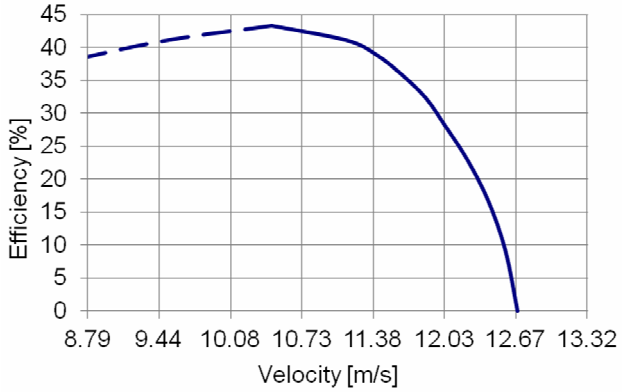

Fig. 5.51 Efficiency characteristic of PEMDYN 20 Hz, 6 poles pump as function of velocity

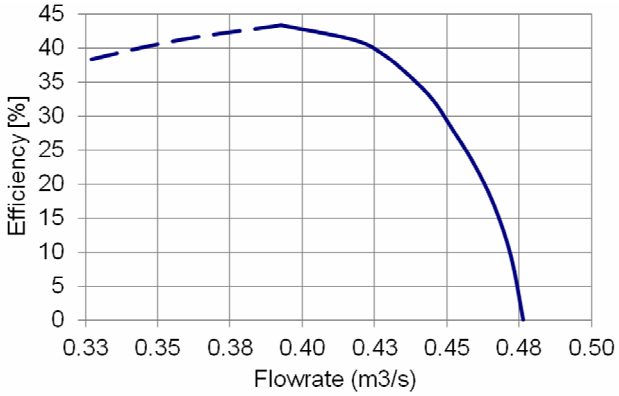

Fig. 5.51 Efficiency characteristic of PEMDYN 20 Hz, 6 poles pump as function of flowrate

The maximum efficiency of the pump 43.3% corresponds to the sodium region mean velocity 10.5 m/s, respectively to the flowrate value 0.39 m^3/s.

5.2.2 Dynamic answer of the pump for sudden load increase, [154]

In the hydrodynamic circuit of an electromagnetic pump some dynamic regimes can intervene by accident or due to different needs related the cooling process of the sodium fast reactor. The dynamic regimes studied in this paragraph refer to sudden changes of sodium flow rates that translate into pressure shocks in the pump circuit. The counter-pressures developed during these regimes are considered in the block pumping hypothesis by the term F_{load} in (5.4). Thus, this section gives information about the pump behavior at sudden load increase when: a) the operation point of the pump belongs to the descendant branch of the Force – Velocity characteristic, Fig. 5.49, and b) the operation point belongs to the ascendant branch of the characteristic.

A) Dynamic answer for the operation point on the descendant branch

Fig. 5.52 shows how starting from null velocity and null load, the pump reaches after approximately 0.15 s steady operation regime with the mean value in time of the load, 2.87 kN, respectively the mean velocity 12.03 m/s.

At the moment 0.166 s the pump load suddenly increases at the value 4 kN. After a new transient regime a new steady state pump operation, characterized by the mean value 4 kN of the electromagnetic force, Fig. 5.53 and the mean value of the sodium region speed 11.61 m/s, Fig. 5.54, is established.

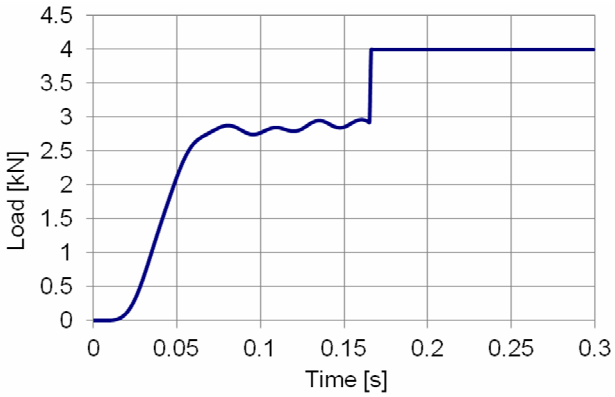

Fig. 5.52 Load jump at 4 kN at the moment 0.166 s

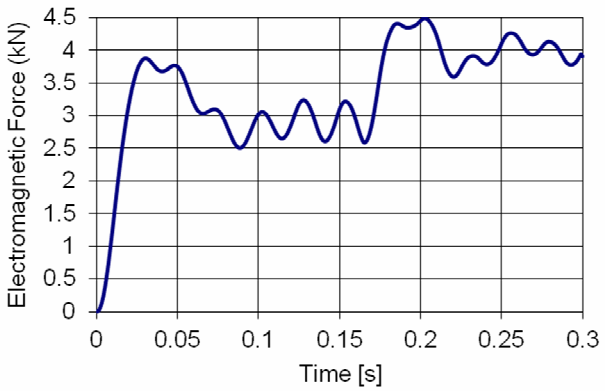

Fig. 5.53 Transient regime of the electromagnetic force for load jump at 4 kN

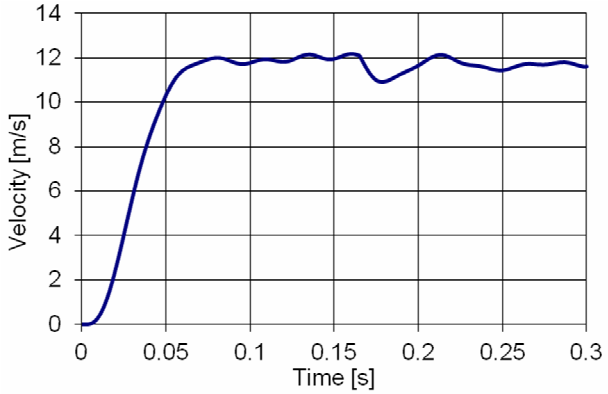

Fig. 5.54 Transient regime of sodium region velocity for load jump at 4 kN

If instead 4 kN, the sudden load is 6 kN, Fig. 5.55, higher than the maximum of the electromagnetic force, 5.5 kN, Fig. 5.49, the pump is not able to enter from the previous steady regime characterized by the mean value in time of the load, 2.87 kN, into another steady regime. The mean value, toward which the generated force tends, Fig. 5.56, is lower then the one required by the new load.

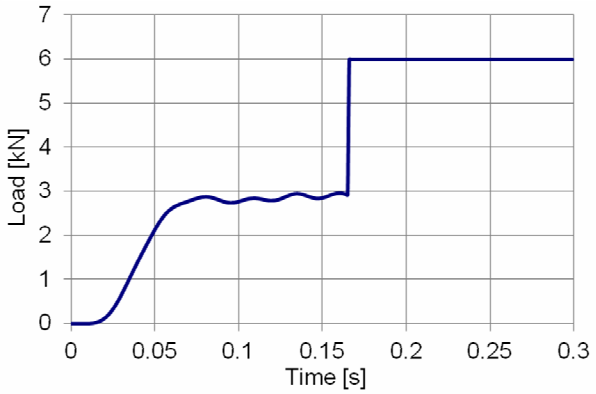

Fig. 5.55 Load jump at 6 kN at the moment 0.166 s

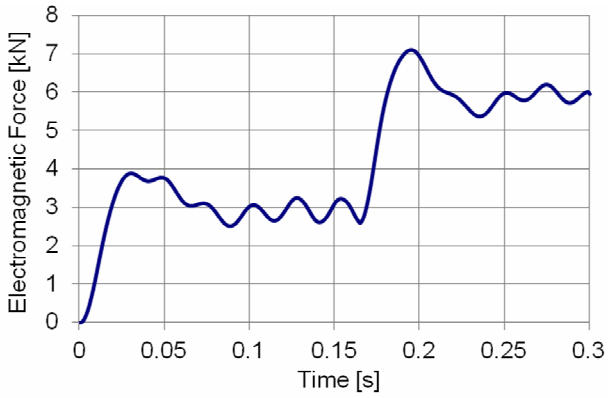

Fig. 5.56 Transient regime of the electromagnetic force for load jump at 6 kN

Fig. 5.57 shows a descending tendency of the mean velocity. The speed will be null, respectively the pump will stop after a certain time.

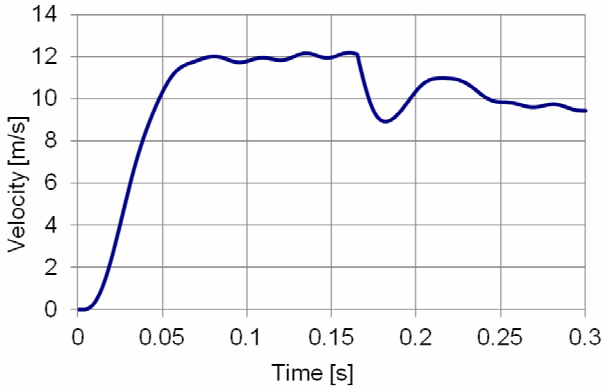

Fig. 5.57 Transient regime of sodium region velocity for load jump at 6 kN

B) Dynamic answer for the operation point on the ascendant branch

Fig. 5.58 shows that for the load model $F_{load} = 100\ v^2$ the pump reaches a steady operation regime characterized by the mean value in time 3.67 kN of the electromagnetic force and of the load, respectively 6.05 m/s of the velocity.

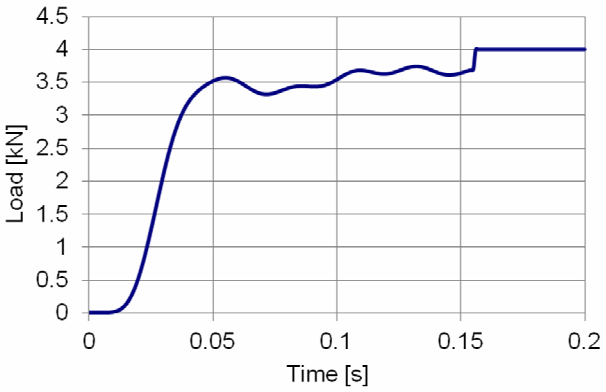

Fig. 5.58 Load jump at the moment 0.166 s

At the moment 0.166 s the pump load suddenly increases at 4 kN, a value lower than the maximum electromagnetic force 5.5 kN, Fig. 5.49. The evolution in time of the electromagnetic force, Fig. 5.59, shows that the pump is not able to compensate the load increase, so that the mean sodium velocity, Fig. 5.60, will rapidly decrease to zero.

It is demonstrated by similar applications that for any operation point belonging to the ascendant branch of the Electromagnetic Pressure-Flowrate characteristic, Fig. 5.49, for no matter how small the load jump is, the pump is not able to ensure a new steady operating regime. For this reason, any operating point on this branch represents an unsteady operating point.

If the characteristic parameters force and velocity of a given pump operation regime belong to the descendant branch, for any jump of load lower than the maximum electromagnetic force, the pump will ensure a new steady regime. For this reason, any point on the descendant branch represents a steady operating point.

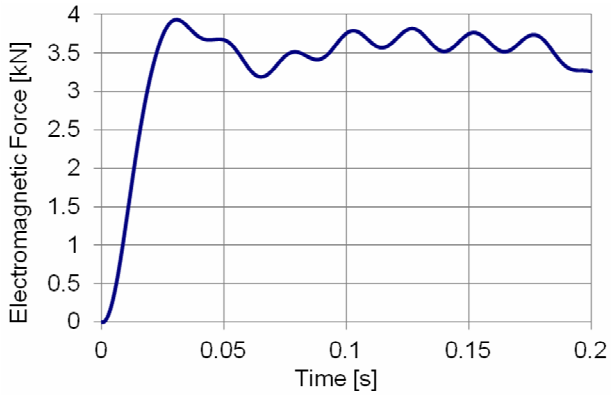

Fig. 5.59 Time variation of electromagnetic force

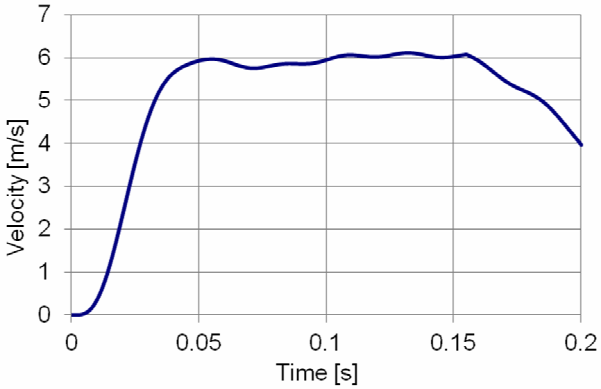

Fig. 5.60 Time variation of sodium region speed

5.3. Three-dimensional structure of the electromagnetic field in single sided ALIP, [155]

This paragraph deals with the electromagnetic field non-uniformity along the azimuth of the sodium region, time variation of the electromagnetic pumping force and evaluation of the braking effects caused by the negative forces at the inlet and outlet caused by the sudden entering and exiting the electromagnetic field.

The models used in this section are the 3D equivalent of the models used in paragraph 5.2, with the following mentions:

- The interior inductor is replaced, Fig. 5.35, with a cylindrical magnetic core of 43 mm width, Fig. 5.61;
- The walls of the annular channel are considered nonconductive and nonmagnetic;
- There are eight magnetic cores belonging to the one side inductor; the distance between two neighboring cores is subject of parametric study;
- The slot cross section area is 35 mm x 41.4 mm.

The other geometrical dimensions, rms current per slot, frequency, physical proprieties and finite element approach are similar with those in 5.2. A view of the 3D model is given in Fig. 5.61.

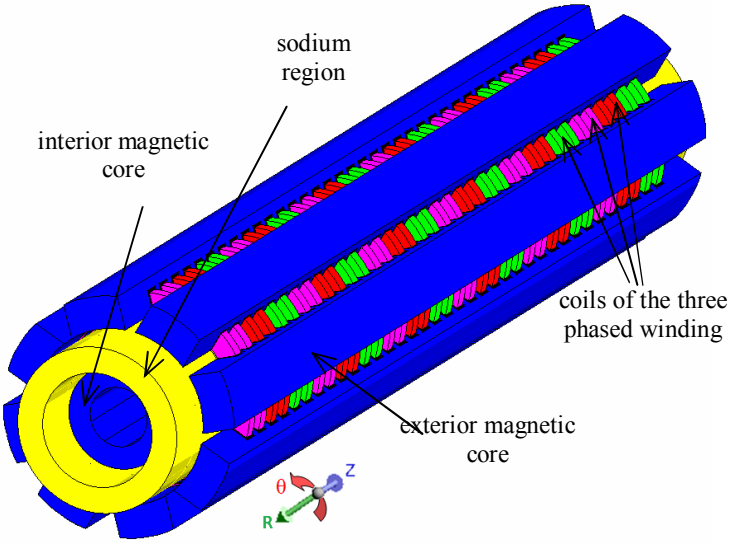

Fig. 5.61 Schematic structure of the ALIP

The geometrical symmetries of the device and the cyclic periodicity property of the electromagnetic quantities allows the reduction of the computation domain one eight of the full device, delimited by the symmetry planes of two neighboring magnetic cores, Fig. 5.62.

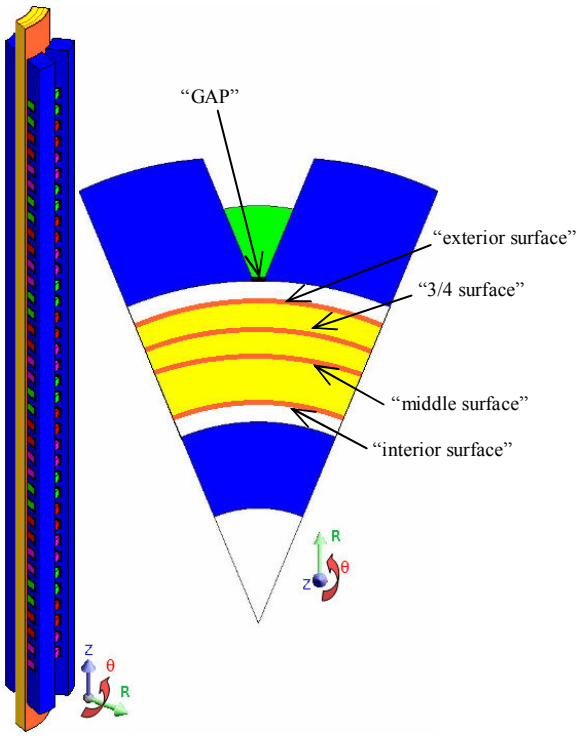

Fig. 5.62 3D and magnified top view of the reduced computation domain

The results of paragraph 5.3.1 are obtained with finite element models of type frequency domain analysis and the results presented in paragraph 5.3.2 are obtained with models of type time domain analysis coupled with translation motion.

5.3.1 Study of the azimuth non-uniformities of the electromagnetic field

The discontinuity of the magnetic cores along the azimuth direction put the question of the existence of non-uniformities with respect to the electromagnetic field and the associated quantities, such as induced currents and electromagnetic forces. The interest of such endeavor comes from the presumably effect that the non-uniformities of the field could have on the sodium flow instabilities and apparition of 3D flow. Thus, the *electromagnetic study* aims to give insight on topics as existence, favoring factors and effects on global electromagnetic quantities.

The azimuth non-uniformities are studied for several distances between cores. It is defined the parameter GAP as the straight line distance between two successive edges of two neighboring magnetic cores. Thus there are studied configurations with gaps of 20, 15, 10, 5, 0 mm, cases abbreviated as GAP 20, GAP 15, GAP 10, GAP 5 and GAP 0.

Figs. 5.63 – 5.67 represent the dependence on the longitudinal and azimuth coordinates of the longitudinal component of the electromagnetic force density with respect to the curved plane at the outer extremity of the sodium region, indicated in Fig. 5.62.

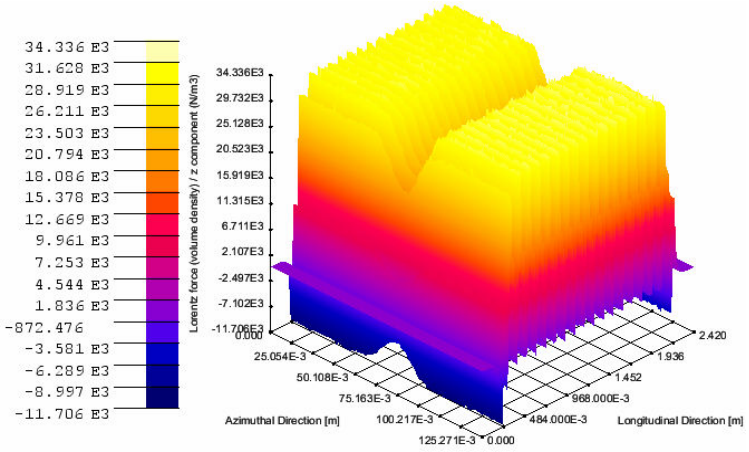

Fig. 5.63 Longitudinal force density on exterior surface, function of longitudinal and azimuth coordinates, GAP 20

It can be observed that along the sodium periphery in azimuth direction, the longitudinal force density is not uniform, namely it decreases in the gap between cores. This effect is more pronounced when the gap between cores increases. The decrease of the force density along the azimuth in the symmetry plane between cores, expressed as percentage from maximum value is 29.8%, 22.1%, 13.9%, 6% and 1% for the values of the gap 20, 15, 10, 5, 0 mm.

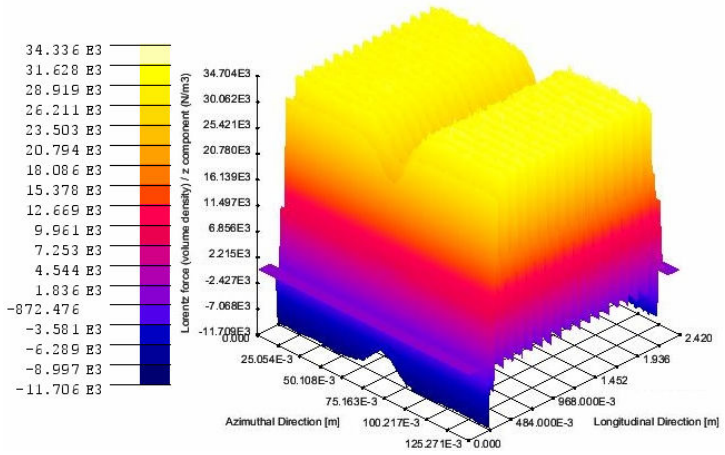

Fig. 5.64 Longitudinal force density on exterior surface, function of longitudinal and azimuth coordinates, GAP 15

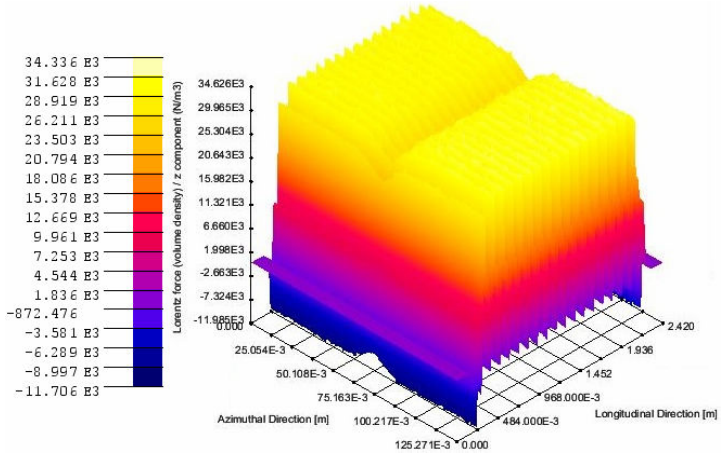

Fig. 5.65 Longitudinal force density on exterior surface, function of longitudinal and azimuth coordinates, GAP 10

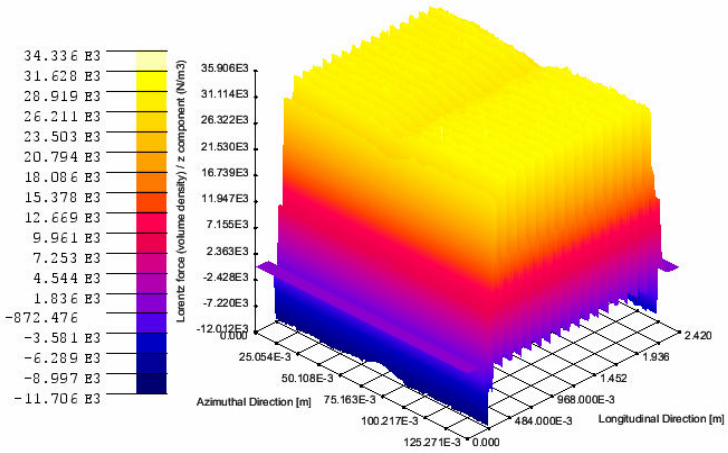

Fig. 5.66 Longitudinal force density on exterior surface, function of longitudinal and azimuth coordinates, GAP 5

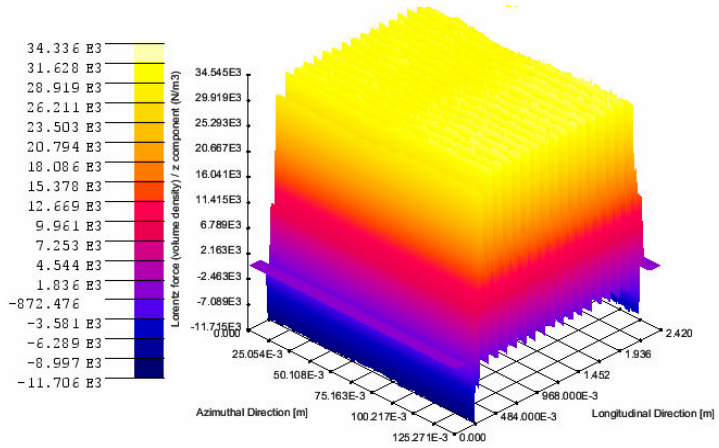

Fig. 5.67 Longitudinal force density on exterior surface, function of longitudinal and azimuth coordinates, GAP 0

In order to present the changes that the electromagnetic field structure suffers locally for two extreme values of the GAP, field quantities of interest are presented in color maps on the exterior surface of the sodium region zoomed at the middle of the pump.

Fig. 5.67 presents the color map of the current density, azimuth component. It can be seen that the current density is quasi independent of the GAP value.

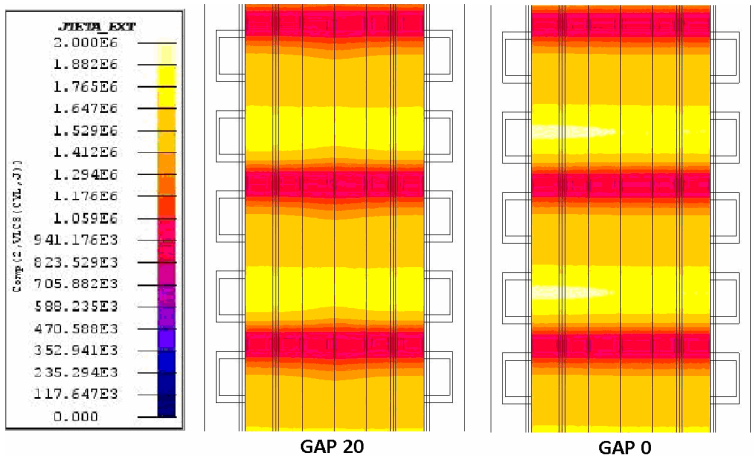

Fig. 5.67 Current density, azimuth component on the exterior sodium surface, middle of the pump, two extreme values of the GAP

Fig. 5.68 presents the color map of the magnetic flux density, radial component, which along the azimuth has decay, maximum in the symmetry plane of two neighboring magnetic cores. The magnetic flux density is most affected when the gap between cores is 20 mm.

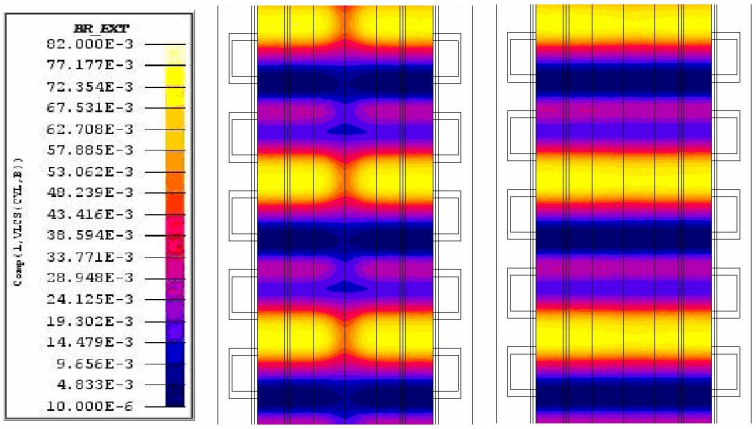

Fig. 5.68 Magnetic flux density, radial component on the exterior sodium surface, middle of the pump, two extreme values of the GAP

The longitudinal component of the electromagnetic force density has the expression

$$f_z = \frac{1}{2}\mathrm{Re}\,al\left\{\underline{J}_r\underline{B}_\theta^* - \underline{J}_\theta\underline{B}_r^*\right\} \tag{5.6}$$

where $\underline{J}_r$ and $\underline{J}_\theta$ are the complex images of the radial, respectively azimuthal components of the current density vector. $\underline{B}_r^*$ and $\underline{B}_\theta^*$ are the conjugate of the complex images of the radial, respectively azimuthal component of the magnetic flux density vector.

Fig. 5.69 presents the longitudinal force density. The decrease of the force is maximal in the symmetry plane between cores and has the largest azimuth extension for the GAP 20. Still, for the relatively small gap of 5 mm it is not to be neglected the decrease of 6%.

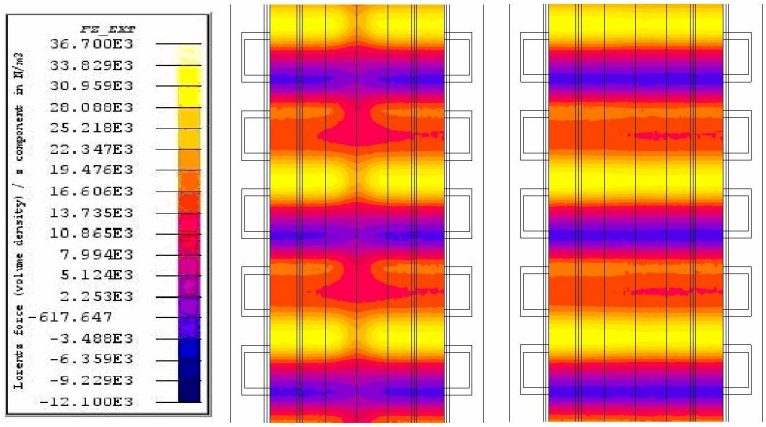

Fig. 5.69 Electromagnetic force density, longitudinal component on the exterior sodium surface, middle of the pump, two extreme values of the GAP

Until now it has been presented the influence that the distance between cores has on the electromagnetic field at the "exterior surface" of the sodium region. In order to study the intensity of the non-uniformity along the thickness of the sodium region, three other surfaces are defined, Fig. 5.62: "interior surface" at the interior extremity of the sodium region, "middle surface" at the middle of the channel and "3/4 surface" in the middle between "middle surface" and "exterior surface". Figs. 5.70 - 5.72 represent the longitudinal force density dependence of azimuth and

longitudinal coordinates with respect to the mentioned surfaces for the GAP 20 configuration.

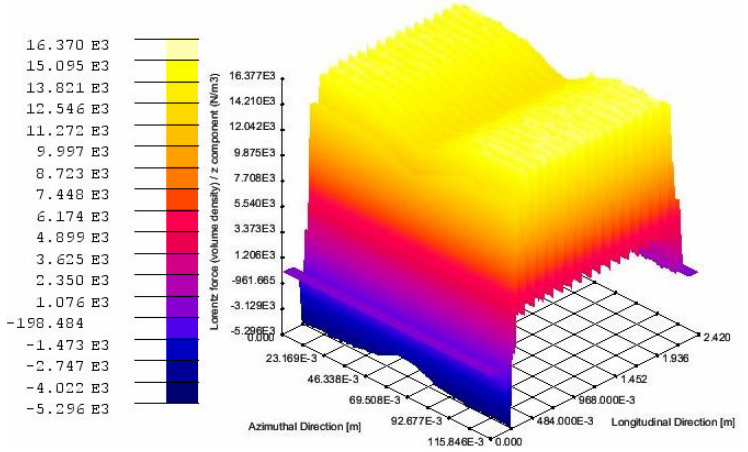

Fig. 5.70 Longitudinal force density on 3/4 surface, function of longitudinal and azimuth coordinates, GAP 20

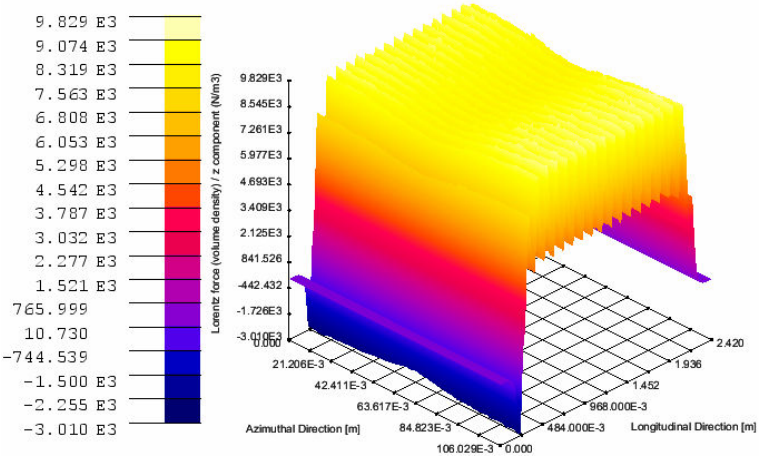

Fig. 5.71 Longitudinal force density on middle surface, function of longitudinal and azimuth coordinates, GAP 20

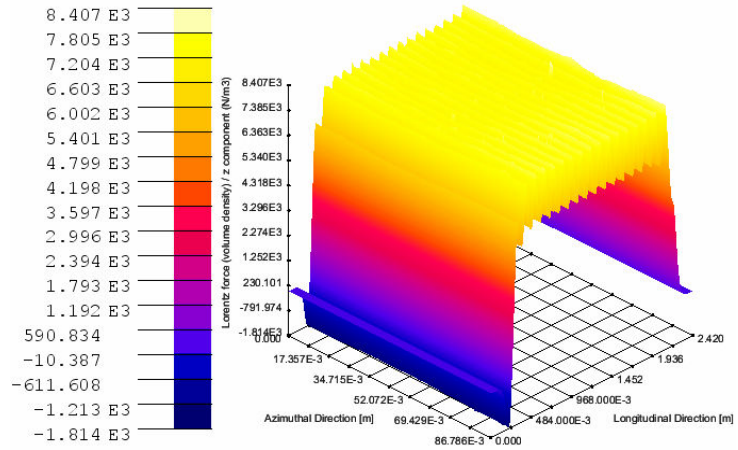

Fig. 5.72 Longitudinal force density on interior surface, function of longitudinal and azimuth coordinates, GAP 20

With respect to the non-uniformity propagation in the radial direction it can be said that from exterior to interior the decrease of the force density as a percentage of maximum value is 29.8%, 15.22%, 5.5% and practically null at the interior face. The

mean values of the curves in Figs. 5.63, 5.70 – 5.72 show the general decreasing of the axial force density along the channel thickness from exterior towards interior surface.

Figs. 5.73 and 5.74 present the radial component of the force density function of longitudinal and azimuth coordinates with respect to the exterior and the middle surface.

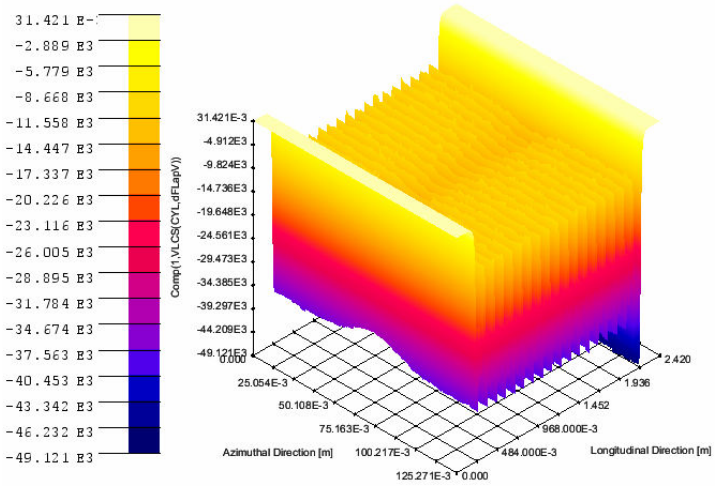

Fig. 5.73 Radial force density on exterior surface, function of longitudinal and azimuth coordinates, GAP 20

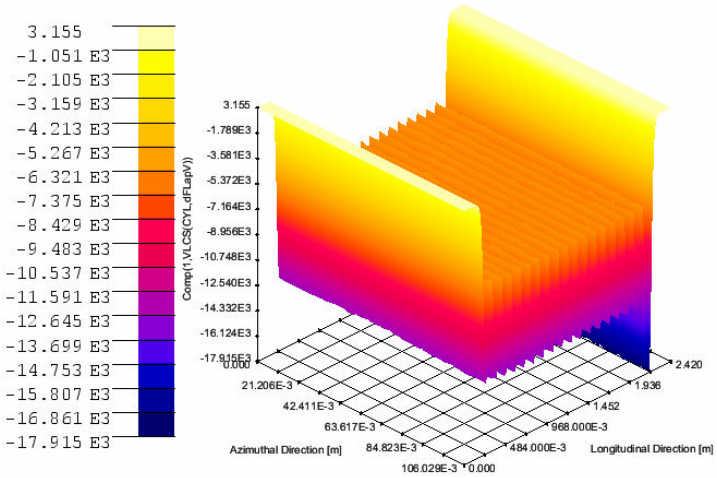

Fig. 5.74 Radial force density on the middle surface, function of longitudinal and azimuth coordinates, GAP 20

The negative values indicate the orientation of the radial forces towards the pump axis. It can be observed at the exterior surface the module of the radial forces is even higher than the forces oriented along the Oz axis. The radial forces decrease towards the middle of the sodium thickness, Fig. 5.74, and become insignificant at the interior surface. Fig. 5.73 indicates that the radial forces are also influenced by the gap between magnetic corers.

In order to quantify the influence of different distances between cores on various global quantities, the longitudinal force and the Joule power developed in sodium have been calculated in each case, Table VII. The two quantities decrease as the GAP increases and the decrease rate is presented in Fig. 5.75.

TABLE VII
EFFECTS OF THE AZIMUTH NON-UNIFORMITY ON GLOBAL QUANTITIES

	Longitudinal force [kN]	Sodium Joule power [kW]
GAP 0	0.693	6.293
GAP 5	0.686	6.216
GAP 10	0.681	6.158
GAP 15	0.675	6.089
GAP 20	0.668	6.004

Compared to GAP 0 configurations, in the GAP 20 configuration the longitudinal force is 3.72% lower and the sodium Joule power is 4.60% lower.

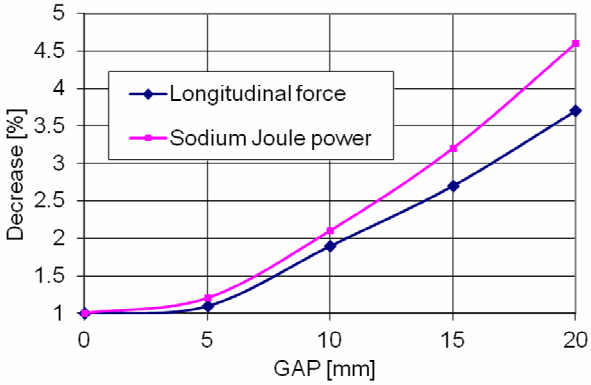

Fig. 5.75 Decrease rate of the force and Joule power when the gap between cores increases

5.3.2 Time and space variations of force and ends effects analysis

The results presented in this paragraph are based on coupled circuit - electromagnetic field - motion models solved with the step by step in time domain method. Thus, the position of the sodium region inside the computation domain is changing between two consecutive time steps due to the imposed sodium velocity as in paragraph 4.2.

Fig. 5.76 presents the answer of the pump in terms of variation in time of longitudinal component of the electromagnetic force. Because the solving method implemented in the software requires the passage through the transient regime and the interest is focused exclusively on the permanent regime, the time step is so managed to minimize computation time.

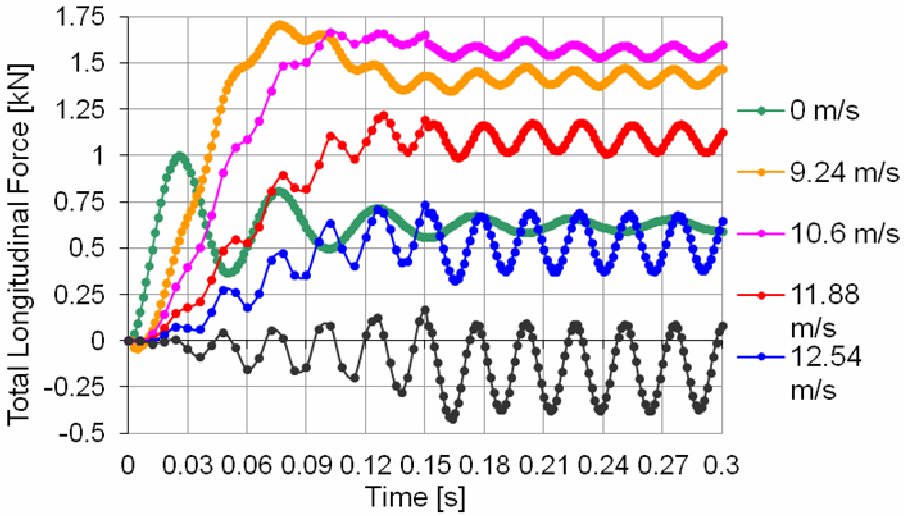

Fig. 5.76 Time variation of the longitudinal force

The value of the time step is chosen by the following strategy for most of the curves in Fig. 3.1: in the interval [0 - 0.12] s, 0.006 s, in the interval (0.12 – 0.15] s, 0.003 s and in the interval (0.15 – 0.3] s the time step is 0.0015 s. A characteristic fact for such devices is that the force frequency is twice the supply frequency, Fig. 5.76.

Fig. 5.77 presents some of the important points on the pump characteristic curve Force – Velocity on the basis of mean values of total longitudinal force in permanent regime. In nominal regime, the pump works on the descendant branch of the curve, namely in the range 10.6 m/s to approximately 13 m/s. In case of sudden load increase when the pump is operating at imposed load, the pump has the capacity to reach a new permanent regime if the new load is not exceeding the maximum available force, in this case, 1.56 kN at 10.6 m/s (paragraph 5.2.2).

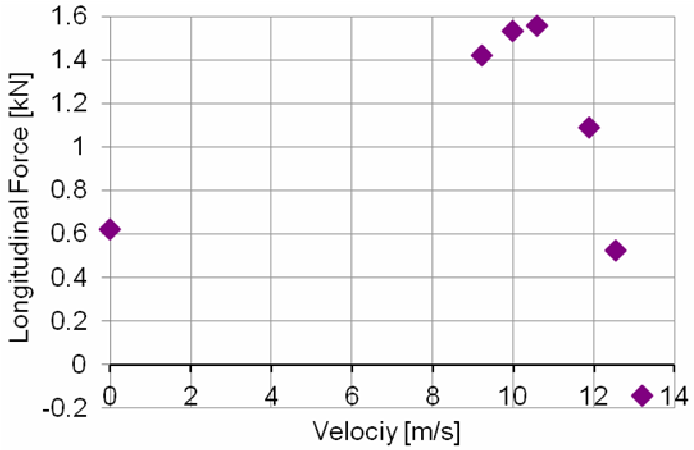

Fig. 5.77 Force – Velocity characteristic of PEMDYN 20 Hz, 6 poles according to the 3D model

In order to study the space oscillations and inlet-outlet braking effects it is defined a longitudinal path on the exterior surface of the sodium region, in the symmetry plane between two magnetic cores, Fig. 5.78. The curves in Figs. 5.79 – 3.8 represent the longitudinal component of the force density mediated on a force time period, along the presented path for no movement, 9.24 m/s, 10.6 m/s, 11.88 m/s, 12.54 m/s and 13.2 m/s that corresponds to the slips 1, 0.3, 0.2, 0.1, 0.05, 0.

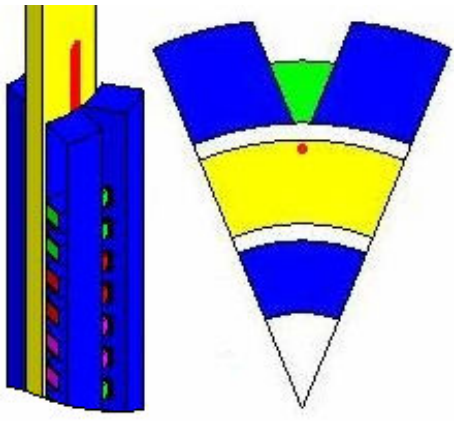

Fig. 5.78 Definition of longitudinal path in the symmetry plane between magnetic cores

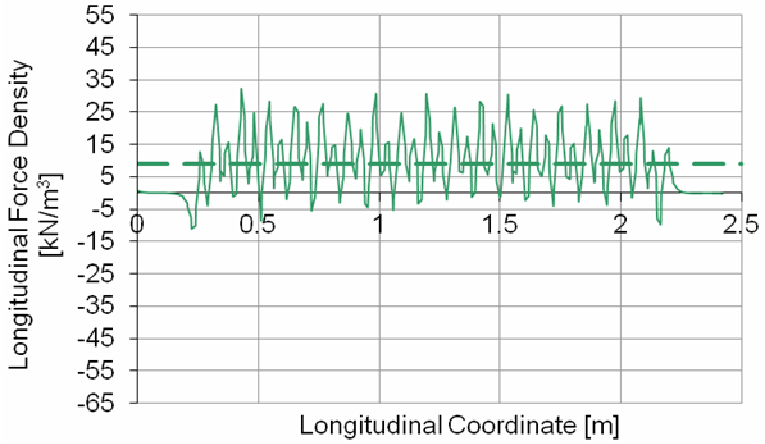

Fig. 5.79 Longitudinal force density along longitudinal path mediated on a force time period, sodium velocity 0 m/s

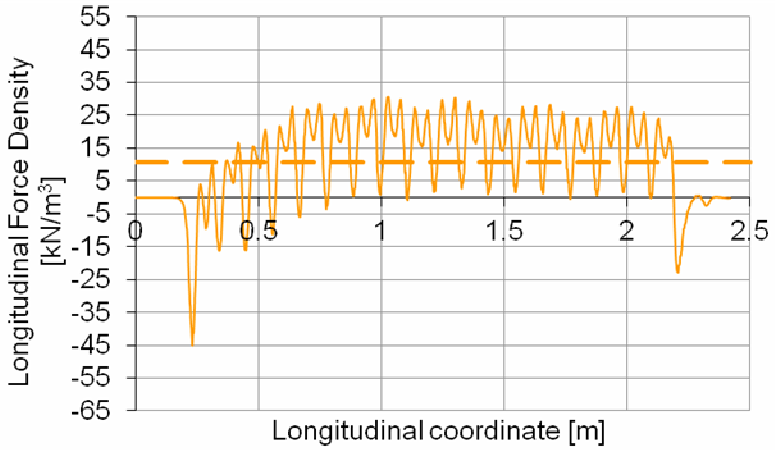

Fig. 5.80 Longitudinal force density along longitudinal path mediated on a force time period, sodium velocity 9.24 m/s

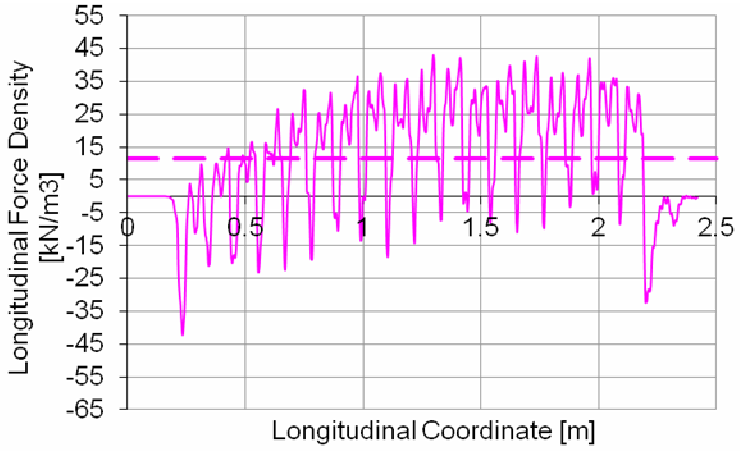

Fig. 5.81 Longitudinal force density along longitudinal path mediated on a force time period, sodium velocity 10.6 m/s

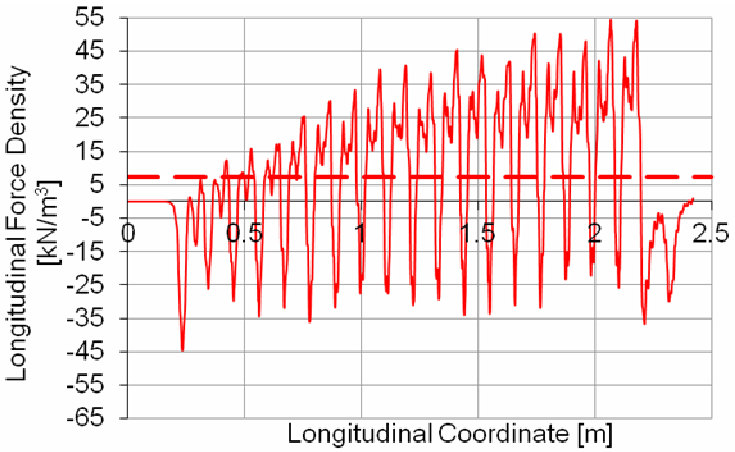

Fig. 5.82 Longitudinal force density along longitudinal path mediated on a force time period, sodium velocity 11.88 m/s

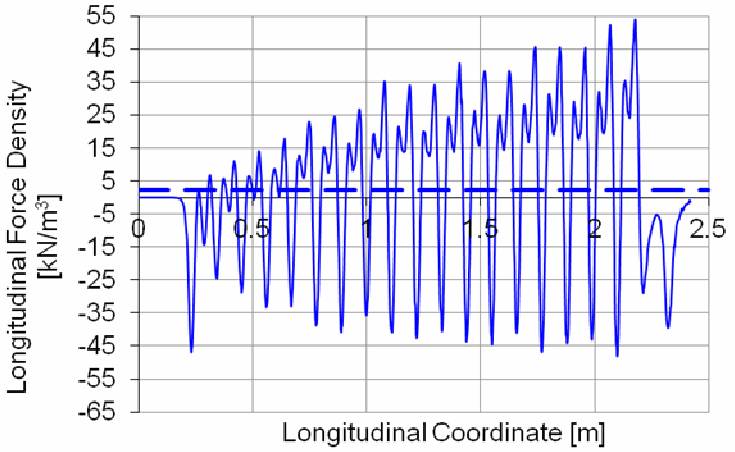

Fig. 5.83 Longitudinal force density along longitudinal path mediated on a force time period, sodium velocity 12.54 m/s

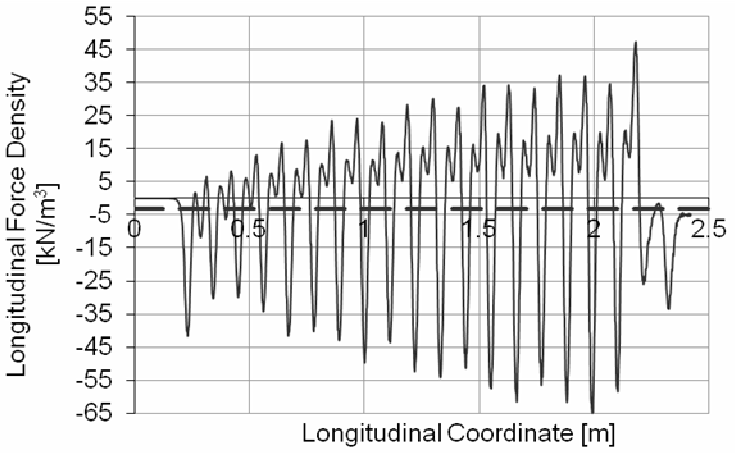

Fig. 5.84 Longitudinal force density along longitudinal path mediated on a force time period, sodium velocity 13.2 m/s

Table VIII is a synthesis of the most important results with respect to the above images. The stabilization distance refers to the length from the pump inlet necessary for the mean curve to reach a quasi-constant value. This length increases

with the sodium speed and for the velocities close to synchronous velocity the stabilization becomes impossible along the given pump length.

TABLE VIII
MAIN CHARACTERISTICS OF THE SPATIAL AND TIME OSCILLATIONS

Sodium mean speed [m/s]	Curve mean value [kN/m^3]	Stabilization distance [m]	Braking force percentage of mean curve [%]		Percent max deviation from mean value [%]	Longitudinal force [kN]
			inlet	outlet		
0	8.91	0.30	14.7	8.7	143.9	0.624
9.24	10.81	0.55	316.4	110.9	82.2	1.423
10.6	11.52	0.87	267.3	178.9	173.8	1.560
11.88	7.26	1.30	508.0	403.5	547.6	1.090
12.54	2.27	no	1916.8	1619.7	2105.5	0.524
13.2	-3.22	no	1143.4	903.7	1814.2	-0.142

The stabilization distance is preserved for any longitudinal path located at different radial coordinates with the mention that the oscillations around the mean curve decrease when the path is situated closer to the inner surface. The forth column presents the values of the inlet and outlet negative force density peaks as percentage of the curve mean value. In the next column is given the difference between the curve mean value and maximum peak as a percentage of the curve mean value.

On the basis of the total longitudinal force corresponding to synchronous speed 13.2 m/s it is possible to quantify the global braking effect. For example at the pump startup, the total negative force is 22% of the mean force developed in steady state, because 0.1424 kN represents 22% of 0.624 kN. At 10.6 m/s which corresponds to maximum force the braking effect is 9%. Consequently in any nominal regime found on the descendant branch of the characteristic curve, the global braking effect due to the negative forces at inlet and outlet is in the range of 9% - 100% from total longitudinal force, Fig. 5.85.

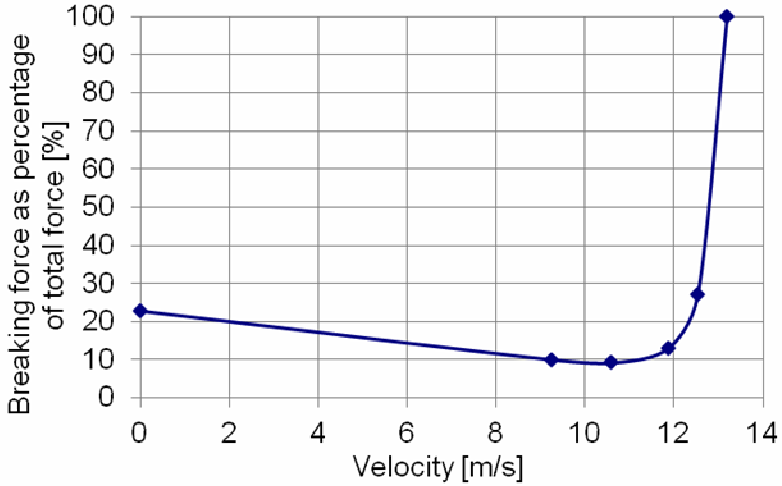

Fig. 5.85 Braking force quantification

The paragraph highlights the effects of the azimuth discontinuity of the magnetic cores over the spatial structure of the electromagnetic quantities inside the sodium channel of Annular Linear Induction Pumps. These effects exist even for

adjacent magnetic cores and they are becoming more and more important as the distance between cores increases. Adding this to the alternation of positive and negative forces along the Oz axis and the important radial oriented forces, it is possible to encounter flow instabilities and vortices even at small velocities.

It is presented the important decrease of the longitudinal forces from the sodium surface closed to the active face of the inductor towards the inner magnetic core. A double sided inductor can be a solution for pump performance improvement.
The post processing of the 3D transient magnetic models gives a good insight about the braking effect of the negative forces when entering and exiting the electromagnetic field as a fraction of the generated pumping force. The spatial variation of the force density for various sodium velocities and the slope of the descendant branch of the characteristic curve provides with important information about possible nominal operating points and overload capacity of the pump.

CONCLUSIONS

Based on electromagnetic models, this chapter treats the operation of large size electromagnetic pumps.

The first paragraph is a study on the optimum supply parameters frequency – number of poles for a given ALIP geometry. Families of Force – Velocity characteristic were presented for various numbers of poles and supply frequencies. For a given number of poles the maximum force decreases with the increase of the frequency and for a given frequency it is an optimal number of poles from the point of view of maximum force. The highest efficiency is obtained with configuration 20 Hz, 6 poles, configuration called further in the thesis PEMDYN.

Due to negative forces developed at pump inlet and outlet and due to shielding effect of the metallic walls, the force is zero at sodium velocities smaller than the synchronous velocity.

The effect of electromagnetic field entrainment beyond the pump outlet is specific to pumps with small number of poles and it increases with the sodium velocity. The most important consequence is the increase of the Joule power and the increase of the forces opposing the fluid flow.

The second paragraph treats the startup, steady state operation and dynamic behavior of the PEMDYN pump. In the presented calculation conditions, the maximum efficiency of the PEMDYN pump is 43% and corresponds to a flow rate of 0.39 m^3/s or sodium velocity 10.5 m/s.

It is demonstrated for any ALIP that a sudden increase of the load without surpassing the maximum pumping force, leads to a new stable operating regime of the pump only if the sodium velocity belongs to the descending branch of the Force – Velocity characteristic. If the pump is operating at a sodium velocity corresponding to the ascendant branch, any sudden load increase determines the pump to stop. Consequently it can be said that the descending branch is a “stable branch” and the ascendant is an “unstable branch”.

The last paragraph of the chapter presents a study of the three-dimensional structure of the electromagnetic field in the single sided version of the PEMDYN.

The study of the 3D model confirms the existence of azimuth non-uniformities of the electromagnetic field in the symmetry axis between any two adjacent magnetic cores. These non-uniformities are characterized by a decay of the field in this axis and the decay is fades in radial direction but it exists even beyond the middle of the channel. The non-uniformity increases as the distance between cores increases. Comparing the total force and Joule power in sodium in the cases of no gap between

cores and 20 mm gap between cores, the decrease of the two quantities is 3.7%, respectively 4.6%.

In any nominal regime characterized by the couple force - velocity found on the descendant branch of the characteristic curve, the global braking effect due to the negative forces at inlet and outlet is in the range of 9% - 100% from total generated longitudinal force, 9% at sodium velocity 10.5 m/s and 100% around synchronism.

Chapter 6: Magnetohydrodynamic interaction in sodium PEMDYN pump

The mutual influence exercised by the electromagnetic phenomena on the sodium flow and by the sodium flow on the electromagnetic quantities is only in part taken into consideration in the block–pumping hypothesis. Calculating the dependence between the force generated by an ALIP and the sodium mean velocity in the block – pumping hypothesis is a simplified approach to studying the influence of the hydrodynamic quantity velocity on an electromagnetic force. The drawback of this method is that the hydrodynamic quantities are not taken into account and consequently local quantities of both types, such as velocity profile, densities of magnetic flux, electrical current, electromagnetic force and hydrodynamic losses are not accurately described [156].

In this chapter the magnetohydrodynamic interaction is studied taking into account both phenomena, namely the study is made by means of coupled models electromagnetism - hydrodynamics. The chapter aims to give information about the intimately behavior of the 20 Hz, 6 poles configuration of the PEMDYN pump with respect to the MHD interaction. For simplicity the pump will be called only PEMDYN. Some quantities are compared with the values obtained through block – pumping hypothesis in order to highlight the advantages of the *magnetohydrodynamic models*.

Many works regarding the magnetohydrodynamic interaction, turbulence, Hartmann boundary layer are of great help in the study of electromagnetic pumps [157]-[168].

The principal steps in realizing a coupled model are the same as in the case of a standard numerical model: geometry, mesh, physical properties and sources. There are two possibilities of realizing a coupled model: a) using a dedicated software for each type of physical phenomenon involved – in this case in each software are defined the elements specified before and quantities are transported between software by a supervisor program; b) using a multiphysic software capable of solving by itself coupled problems. In this chapter both methods are used. The first part of the chapter studies the MHD coupling based on laminar model of the sodium flow and uses a multiphysic software, namely the coupled problem electromagnetism – fluid flow is solved using a single finite element software. The second part of the chapter represents a *MHD study* of the sodium flow in the ALIP based on turbulent model of the flow and using two independent software, one for electromagnetism and one for hydrodynamic.

The two parts of the chapter refer to the same pump geometrical shape and dimensions. The 2D axisymmetric finite element model is presented in Fig. 6.1. The interior and exterior three phase inductors are modeled by two cylindrical current sheets as in paragraph 5.1. The axial extension of the pumping channel over the magnetic yokes is 2000 mm, namely the distance between INLET and PUMP_INLET is equal with the distance between PUMP_OUTLET and OUTLET and equal with 2000 mm. All the other dimensions are given in paragraph 5.1.The inner and outer current sheets, with respect to the annular channel, belonging to the simplified inductor, are defined by the traveling wave of the line current $J_s(z,t) = J_0\cos(\omega t-kz)$ along the axial coordinate z. The frequency of the wave is $f = \omega/2\pi$, $J_0 = 64.48$ A/mm is the amplitude of the current sheet wave and $k = 2\pi/\lambda$, where the wave length $\lambda = 2\tau$ is the double of the pole pitch length, τ.

The material properties are: sodium resistivity, $\rho_{Na} = 1/\sigma_{Na} = 0.13511 \cdot 10^{-6}\,\Omega m$, sodium relative permeability, $\mu_{rNa} = \mu/\mu_0 = 1$, relative permeability of the nonconductive magnetic yokes $\mu_{r\_mgcore} = 1000$, channel walls (stainless steel) resistivity, $\rho_{Steel} = 1/\sigma_{Steel} = 0.565 \cdot 10^{-6}\ \Omega m$. The dynamic viscosity of the liquid sodium is $\eta_{Na} = 4.568 \cdot 10^{-4}$ Pa·s, the sodium mass density is $d_{Na} = 903.56\ kg/m^3$.

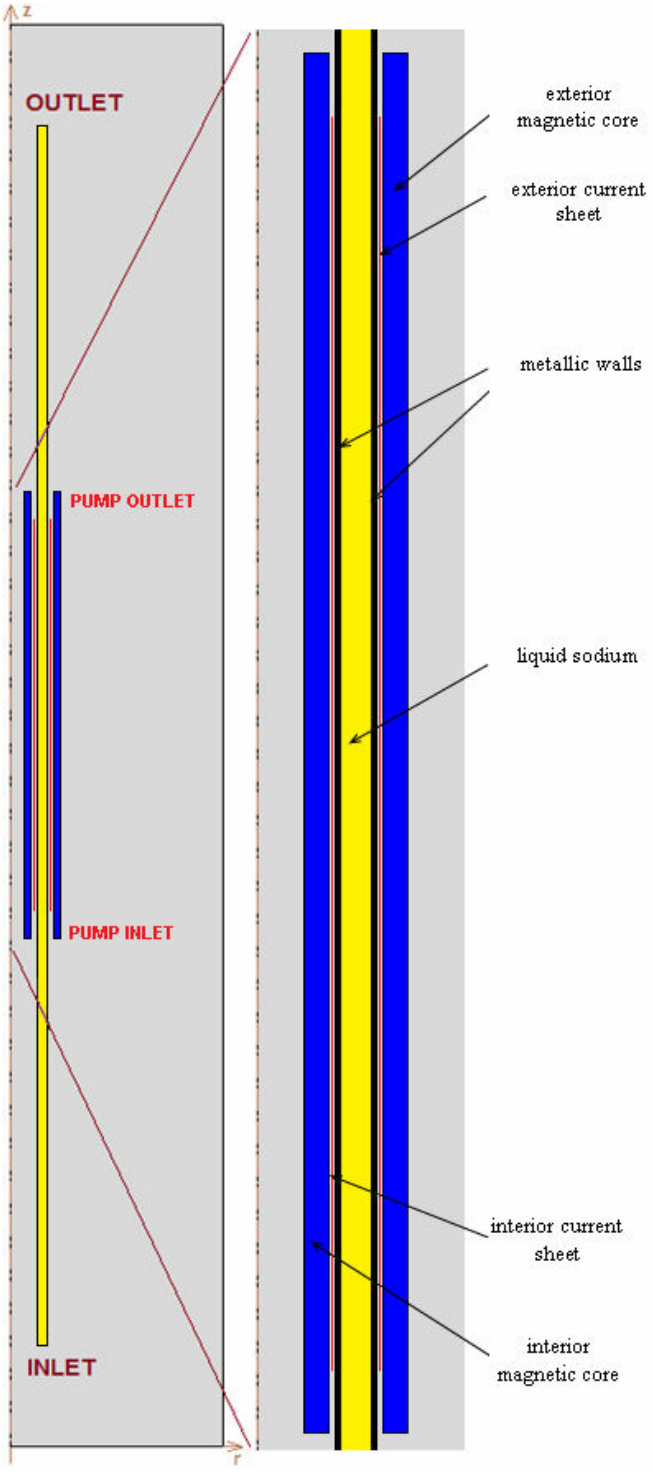

Fig. 6.1 Axisymmetric structure of the ALIP

The flow conditions are differently prescribed in the two paragraph of the chapter. In paragraph 6.1, where single multiphysic software is used for the coupling, the software allows to set as condition at the INLET line, a null pressure at a position with 1000 mm before the INLET even if that line does not belong to the computation domain. At OUTLET, the pressure is prescribed by a parameter. Changing the value of the parameter, namely of the pressure difference between the two ends of the domain, different flow rates are obtained.

In paragraph 6.2, where the flow is studied in different software than the electromagnetic problem, the flow conditions are: at INLET imposed uniform velocity radial profile and at OUTLET, conservation of mass condition. Applying different values for the sodium mean velocity, various pressure differences are obtained. Relative to the formulation used in paragraph 6.1, this is an indirect formulation.

In both problems the channel walls have standard wall condition with null velocity in the points adjacent to the wall.

The following paragraph is a synthesis of most important parameters that should give some preliminary analytic information about the type of sodium flow in the pump.

a) **Pole pith length**, $\tau = 0.333$ m
b) **Wave length**, $\lambda = 2\tau = 0.666$ m
c) **Wave number**, $k = \pi/\tau = 2\pi/\lambda = 9.43$ m^{-1}
d) **Channel thickness**, e = 0.05 m
e) **Synchronous velocity**, $U_s = \lambda f = 2\tau f = 2 \cdot 0.33 \cdot 20 = 13.2 \ m/s$
f) **Reynolds number:**

$$\mathrm{Re} = \frac{d\boldsymbol{v}D_H}{\eta} = \frac{\boldsymbol{v}D_H}{\nu} = \frac{QD_H}{\nu A}, \tag{6.1}$$

where D_H is the hydraulic diameter [m], Q is the volumetric flowrate [m^3/s], A is the pipe cross sectional area [m^2], **v** is the mean velocity [m/s].

For shapes such as squares, rectangular or annular ducts where the height and width are comparable, the characteristic dimension for internal flow situations is taken to be the hydraulic diameter, D_H, defined as:

$$D_H = \frac{4A}{P}, \tag{6.2}$$

where P is the wetted perimeter.

The wetted perimeter for a channel is the total perimeter of all channel walls that are in contact with the flow. For a circular pipe, the hydraulic diameter is exactly equal to the inside pipe diameter.
For an annular duct, the hydraulic diameter can be shown algebraically to reduce to:

$$D_{H,annulus} = D_o - D_i, \tag{6.3}$$

where D_o is the inside diameter of the outside pipe and D_i is the outside diameter of the inside pipe.

$$\mathrm{Re} = \frac{d\boldsymbol{v}D_H}{\eta} = \frac{903.56 \cdot \boldsymbol{v} \cdot 0.1}{4.57 \cdot 10^{-4}} = 197715.5 \cdot \boldsymbol{v} \tag{6.4}$$

Reynolds for a typical velocity of the sodium through pipe, 10 m/s, is:

$$\mathrm{Re}_{10m/s} = 1977155 \cong 2 \cdot 10^6 \tag{6.5}$$

g) **Reynolds magnetic number**

$$\mathrm{Re}m = \frac{\mu_0 \sigma_{Na} \omega}{k^2} = \frac{4\pi 10^{-7} \cdot 7.4 \cdot 10^6 \cdot 2\pi 20}{(9.43)^2} = 13.14 \tag{6.6}$$

h) **Hartmann layer thickness**

$$\delta_{Ha} = \frac{1}{B_0}\sqrt{\frac{\eta_{Na}}{\sigma_{Na}}} = \frac{1}{0.13}\sqrt{\frac{4.57 \cdot 10^{-4}}{7.4 \cdot 10^6}} = 60.45 \cdot 10^{-6} m = 0.0645 mm, \tag{6.7}$$

where B_0 is the mean value of the magnetic flux density in the sodium.

i) **Hartmann number:**

$$Ha = \frac{e}{\delta_{Ha}} = \frac{0.05}{60.45 \cdot 10^{-6}} = 827.13 \tag{6.8}$$

j) **Penetration depth of the electromagnetic field:**

$$\delta_B = \sqrt{\frac{2}{\mu_0 \sigma_{Na} \omega}} = \sqrt{\frac{2}{4\pi 10^{-7} \cdot 7.4 \cdot 10^6 \cdot 2\pi 20}} = 41.4\ mm \tag{6.9}$$

k) **Interaction parameter:**

The interaction parameter, N, expresses a ratio between characteristic time scales of fluid convection and action of the electromagnetic forces.

$$N = \frac{\sigma_{Na} B_0^2}{d_{Na}} \cdot \frac{L}{\boldsymbol{v}} \tag{6.10}$$

There are two possibilities to interpret the characteristic length L:

If the pump length is considered the characteristic length,

$$N = \frac{7.4 \cdot 10^6 \cdot (0.13)^2}{903.56} \cdot \frac{2}{\boldsymbol{v}} = \frac{276.82}{\boldsymbol{v}} \tag{6.11}$$

$$N_{10m/s} = 27.7 \tag{6.12}$$

If the pump length is considered the hydraulic diameter,

$$N = \frac{\sigma_{Na} B_0^2}{d_{Na}} \cdot \frac{D_H}{\boldsymbol{v}} = \frac{7.4 \cdot 10^6 \cdot (0.13)^2}{903.56} \cdot \frac{0.1}{\boldsymbol{v}} = \frac{13.84}{\boldsymbol{v}} \tag{6.13}$$

$$N_{10m/s} = 1.4 \tag{6.14}$$

As this number increases it means that the time scale of the electromagnetic quantities is higher than the time scale of the quantities related to the flow, namely the electromagnetic phenomena have variations in time much more rapid than the variation of the flow quantities, such as velocity.

l) **Place of Reynolds number in Navier – Stokes equation**

It is resumed the Navier – Stokes equation (2.56) for incompressible flows:

$$d\left(\frac{\partial \boldsymbol{v}}{\partial t} + \boldsymbol{v} \cdot \nabla \boldsymbol{v}\right) = -\nabla p + \eta \nabla^2 \boldsymbol{v} + \boldsymbol{f} \tag{6.15}$$

The right side terms in the equation have the units of force per unit volume and the left side terms are acceleration times a density. Each term is thus dependent on quantities of the flow. The non-dimensional form of the equation supposes a form which does not depend directly on the physical sizes. One possible way to obtain a non-dimensional equation is to multiply the whole equation by the following factor, which has inverse measurement unit of the base equation, $\frac{L}{d\boldsymbol{V}^2}$, where L is the characteristic length, d is the fluid mass density and **v** is the fluid mean velocity.

If the following notations are made

$\boldsymbol{v}' = \frac{\boldsymbol{v}}{\boldsymbol{V}}$; $p' = p\frac{1}{d\boldsymbol{V}^2}$; $\boldsymbol{f}' = \boldsymbol{f}\frac{L}{d\boldsymbol{V}^2}$; $\frac{\partial}{\partial t'} = \frac{L}{\boldsymbol{V}}\frac{\partial}{\partial t}$; $\nabla' = L\nabla$, the Navier – Stokes equation without can be write:

$$\frac{\partial \boldsymbol{v}'}{\partial t'} + \boldsymbol{v}' \cdot \nabla' \boldsymbol{v}' = -\nabla' p' + \frac{\eta}{dL\boldsymbol{V}} \nabla'^2 \boldsymbol{v}' + \boldsymbol{f}', \tag{6.16}$$

where the term $\frac{\eta}{dLV} = \frac{1}{\mathrm{Re}}$.

For the ease of reading, the apostrophes are abandoned and the equation becomes:

$$\frac{\partial \boldsymbol{v}}{\partial t} + \boldsymbol{v} \cdot \nabla \boldsymbol{v} = -\nabla p + \frac{1}{Re} \nabla^2 \boldsymbol{v} + \boldsymbol{f} \tag{6.17}$$

It can be remarked in (6.18) that as Re → ∞, the viscous term vanishes. Thus, flows characterized by high Reynolds numbers are approximately inviscid in the bulk region.

For flow in a pipe, experimental observations show that laminar flow occurs when Re < 2300 and turbulent flow occurs when Re > 4000. In the interval between 2300 and 4000, laminar and turbulent flows are possible and are called "transition flows", depending on other factors, such as pipe roughness and flow uniformity. This empirical dividing between laminar and turbulent flows can be applied to flows through annular channel with enough accuracy.

Considering the calculated value of the Re number for the PEMDYN pump it is expected to have turbulent flow for any mean velocity of sodium and especially for the velocities of the descending branch of the Force – Velocity characteristic.

The value of the Hartmann number, (6.9), indicates that the electromagnetic forces are much higher than the viscous forces.

Since the convection direction is axial, a more suitable formula for the interaction parameter is (6.12). In this case it can be observed that for any value of the sodium mean velocity the time scale of the variations in time of velocity is much lower than the time scale of variations in time of the electromagnetic force. In other words it can be said that there is no time for each variation in time of the force to determine a variation in the velocity field. Thus, the coupled models in this chapter have the following structure. The electromagnetic problem is solved in the frequency domain; the results of such calculation are implicitly time averaged. The hydrodynamic problem is solved in the time domain; the results of such calculation characterize the flow at a specific moment of time. The interchange of results between the two problems is made at each time step of the governing solving scenario in time domain. Namely the Navier – Stokes equation is solved for the current velocity distribution and for the previous distribution of the electromagnetic force, Fig. 6.2. The loop is continued until a certain convergence criterion is reached. The convergence criterion used in paragraph 6.1 is the implicit criterion of COMSOL, namely the solving algorithm is set for result accuracy of three digits. The convergence criterion used in paragraph 6.2 is presented later.

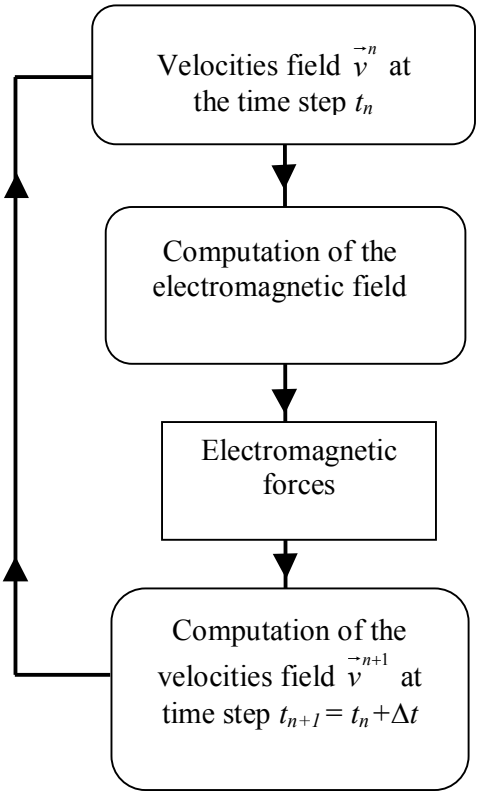

Fig. 6.2 Algorithm of the coupled problem

6.1 MHD coupling using the laminar flow model in the hydrodynamic problem

The laminar to turbulent transition occurs when the Reynolds number increases. Besides that, if the density of the fluid increases, respectively the viscosity of the fluid decreases, the laminar to turbulent transition takes place. This leads to the possibility of using a scheme where for an expected turbulent flow, a laminar flow numerical model with increased fluid viscosity can be used. Thus, the approach in this paragraph in the study of the MHD flow is based on the mentioned approximation with a fictive sodium viscosity increased 1000 times, $\eta_{Na\_fictive} = 4.568 \cdot 10^{-1}$ Pa·s. In this case the Hartmann layer and the Hartmann number have the values:

$$\delta_{Ha\_fictive} = \frac{1}{B_0}\sqrt{\frac{\eta_{Na\_fictive}}{\sigma_{Na}}} = \frac{1}{0.13}\sqrt{\frac{0.457}{7.4 \cdot 10^6}} = 0.00191m = 1.91mm \qquad (6.18)$$

$$Ha_{fictive} = \frac{e}{\delta_{Ha\_fictive}} = \frac{0.05}{0.00191} = 26.15 \qquad (6.19)$$

The mesh of the sodium channel is mapped. In radial direction it is an arithmetic sequence distribution of 20 elements with the element ratio 0.1. The first element near the wall has a width of 0.333 mm and the element in the middle is approximately 5 mm. In the axial direction there are 1000 elements uniform distributed, which means that the height of any element is 6 mm.

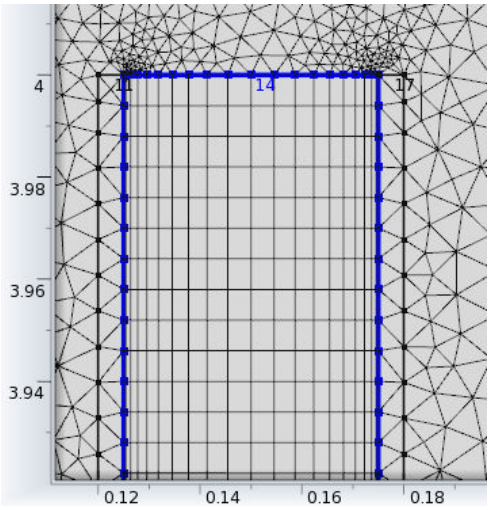

Fig. 6.3 Mapped mesh of the channel of PEMDYN (PUMP_OUTLET zoom)

Several applications have been solved for various values of the pressure difference between the two ends of the hydrodynamic computation domain. Thus, the dependence between the hydrodynamic pressure generated by the pump and the sodium flow rate was calculated. It is used the expression *hydrodynamic pressure* in order to make a distinction of *electromagnetic pressure* terminology, used in the previous chapter. The hydrodynamic pressure generated by the pump refers to the pressure difference calculated between the pump inlet and pump outlet, Fig. 6.1, namely between the two ends of the magnetic yoke.

One of the most important effects of the magnetohydrodynamic interaction of the sodium flow through the annular channel of the PEMDYN pump in the presence of the electromagnetic field are called *Hartmann effects* and they refer to modifications of the velocity profile due to the electromagnetic field and modifications of the force

density radial distribution due to sodium velocity. These modifications consist in flattening of the velocity profile and an important non-uniformity of the force density radial profile between walls and channel middle. Namely as the sodium flow rate increases, or the magnetic flux density increases, the bulk region of the velocity profile becomes more flat and the value of the electromagnetic force in the Hartmann layer becomes much higher than in the middle of the channel.

These effects are highlighted in Figs. 6.4 and 6.5 where the field quantities are presented for the sodium mean velocity 11.7m/s. Fig. 6.4 presents in colors and arrows the velocity magnitude in the entire channel and in successive zooms in order to see more clear the central region of the pump. It can be observed that along the pump channel there is a transition of the velocity profile towards a Hartmann velocity profile.

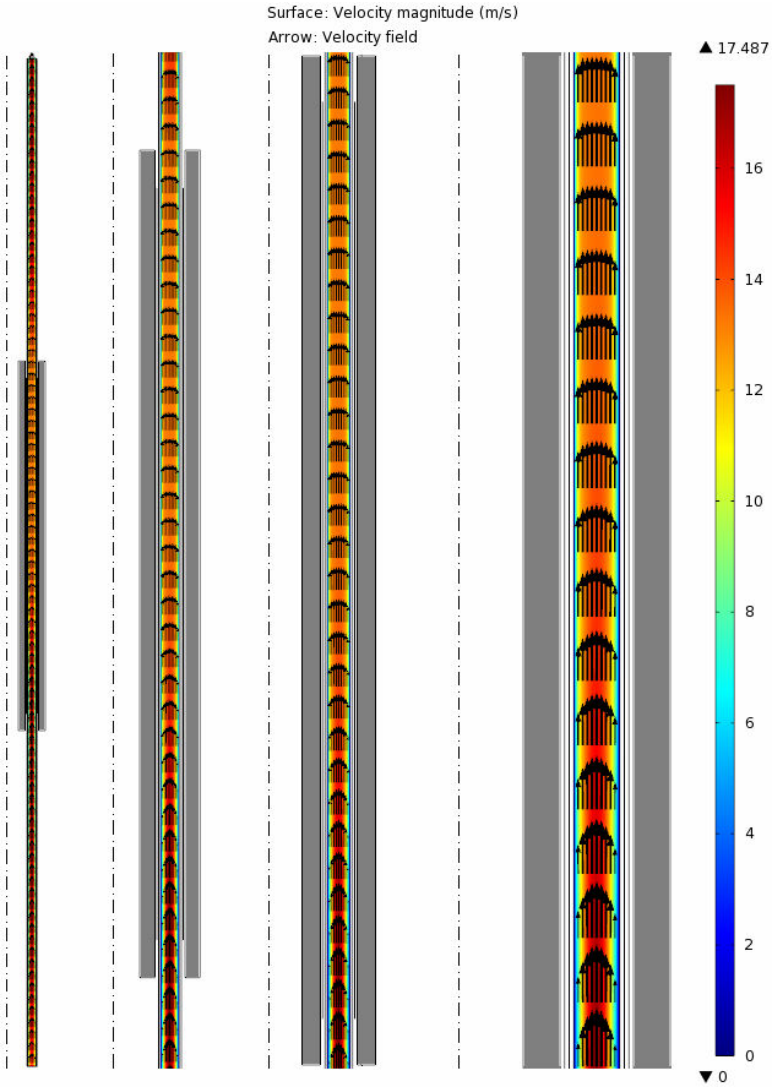

Fig.6.4 Hartmann profile set up along the pump, sodium mean velocity 11.7 m/s

Fig. 6.5 presents in colors and arrows the electromagnetic force density in a zoomed region in the pump for the sodium mean velocity 11.7 m/s. It can be observed that near the walls the force density is six orders of magnitude higher than in the bulk region. In this case it can be said that the electromagnetic field at sodium speeds close

to the synchronous velocity has an effect of expulsion towards the walls of the electromagnetic force.

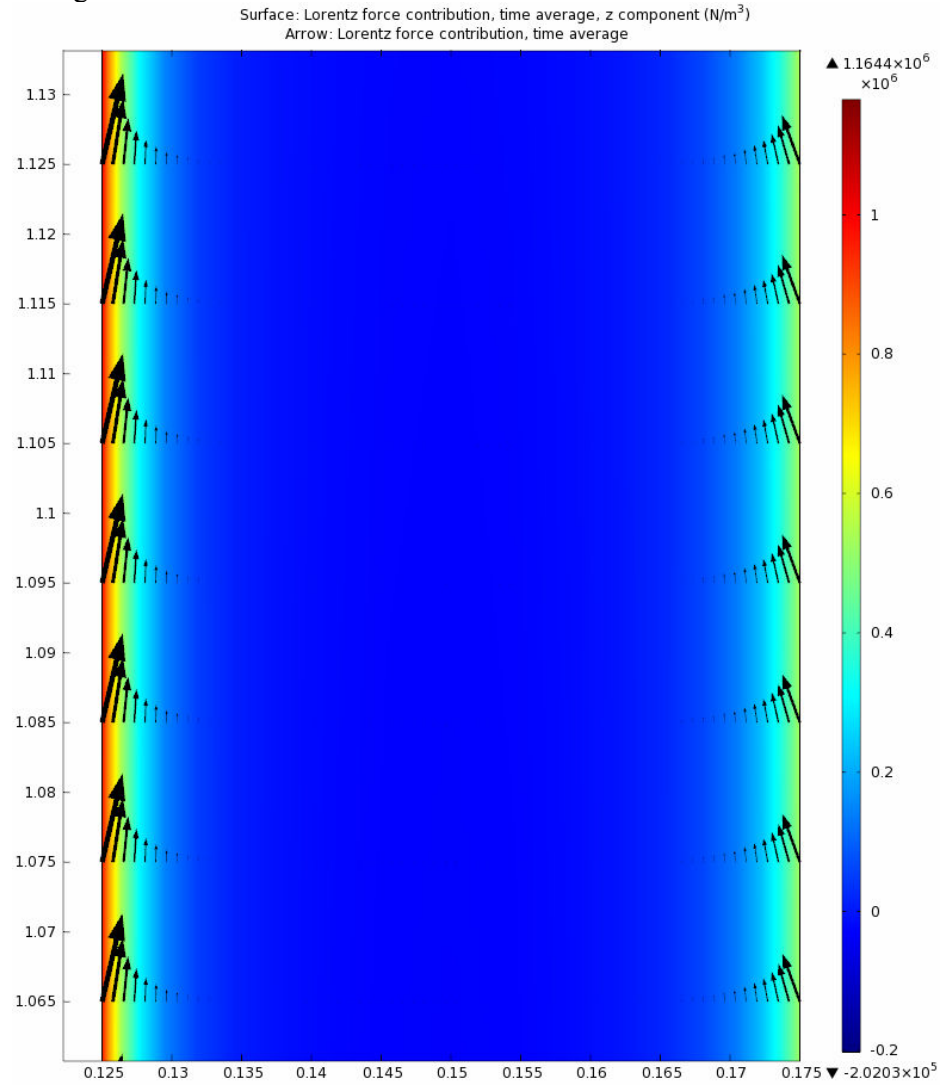

Fig. 6.5 Electromagnetic force density in the middle of the pump, sodium mean velocity 11.7 m/s

Figs. 6.7 and 6.8 present the evolution of the velocity and force radial profiles along the pump as another solution to show the effects highlighted in Figs. 6.4, 6.5. Fig. 6.6 presents six radial paths along which the force density and velocity are plotted. It can be observed, Fig. 6.7, the velocity profile flattening and the very high values of the force density near the walls relative to the force in the bulk region which close to zero, Fig. 6.8. The force profile corresponding to path 6 show that in the bulk region, the force is negative and only in the regions close to the walls the force is positive due to the longitudinal ends braking effect.

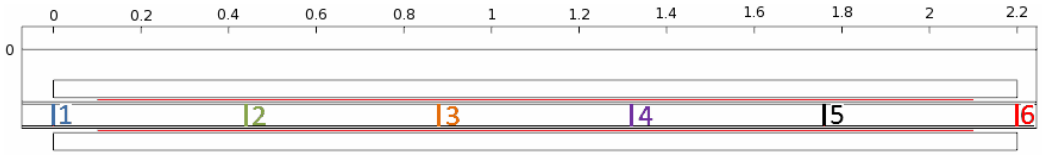

Fig. 6.6 Radial paths along the PEMDYN pump

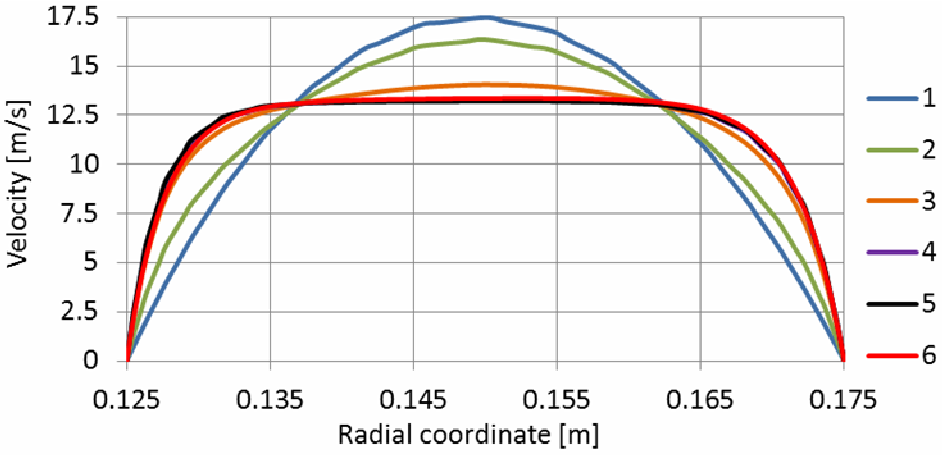

Fig. 6.7 Velocity profiles along the pump, sodium mean velocity 11.7 m/s

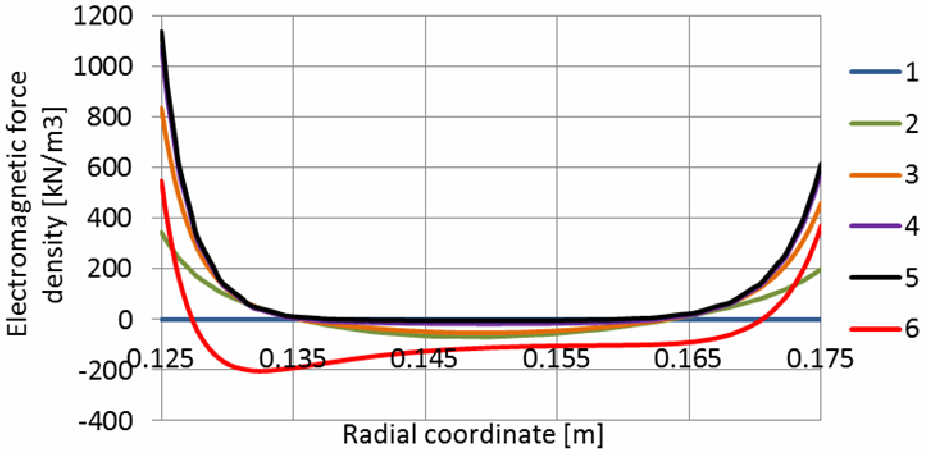

Fig. 6.8 Electromagnetic force density profiles along the pump, sodium mean velocity 11.7 m/s

The Hydrodynamic pressure – Mean velocity characteristic of the PEMDYN pump obtained based on a laminar flow model is presented in Fig. 6.9. It contains only the most important part, namely the descending branch.

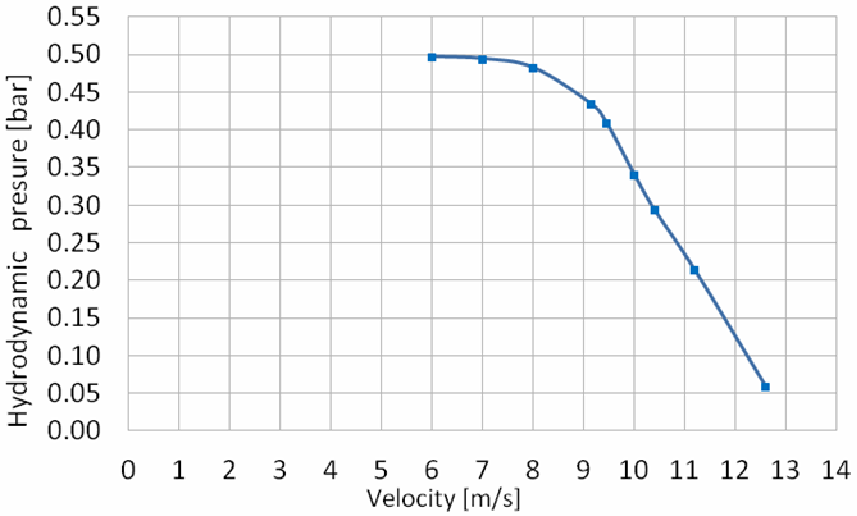

Fig. 6.9 Pressure – Velocity characteristic of PEMDYN, laminar flow model

The second half of paragraph 6.1 represents a verification of the results. The coupled model that uses two software and is detailed in paragraph 6.2 was used to double check the results obtained. The coupling realized with only one software is called *COMSOL – COMSOL coupling*, after the name of the software used, and the coupled realized with two software is called *COMSOL – FLUENT coupling* after the names of the software used, COMSOL for electromagnetism and FLUENT for hydrodynamics. The COMSOL – FLUENT model uses a laminar flow model and the fictive sodium dynamic viscosity increased one thousands times.

The comparison is made in three aspects: characteristic curve, global quantities, and force profiles at various longitudinal coordinates of the pump.

Fig. 6.10 presents the Hydrodynamic pressure – Velocity characteristic of the PEMDYN pump based on laminar flow model, obtained with the two coupling methods. It can be said that for the common portion, both computation methods give similar results and validates each other. From the characteristic it was chosen the mean velocity 8 m/s to do some detailed comparisons. Table IX presents the differences between models in terms of global quantities (force and pressure) and a local quantity (maximum axial velocity of the computation domain). The differences found can be considered as reference differences between COMSOL – COMSOL and COMSOL – FLUENT couplings for any sodium velocity on the descendent branch.

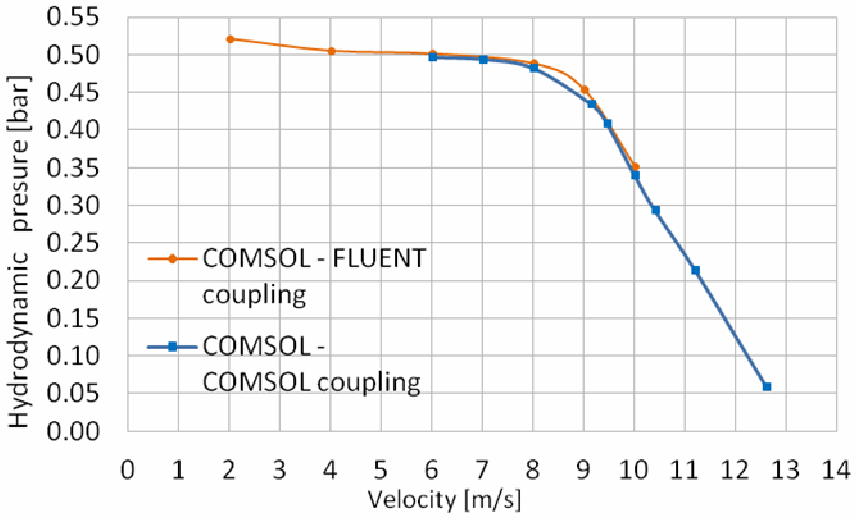

Fig. 6.10 Hydrodynamic pressure – Velocity characteristic of PEMDYN obtained by COMSOL-COMSOL and COMSOL-FLUENT coupling variants, laminar flow model

Table IX Comparison between coupled models of the PEMDYN pump

	comsol-comsol	**comsol-fluent**
Total axial force [kN]	5.298	5.224
Electromagnetic pressure [bar]	1.125	1.109
Hydrodtnamic pressure [bar]	0.4612	0.4897
Maximum axial velocity in a point of the computation domain [m/s]	12.18	11.88

In order to do the comparison with respect to the force density radial profile, in Fig. 6.11 are presented some radial paths. Their name represents the distance from the pump inlet until the place marked their name.

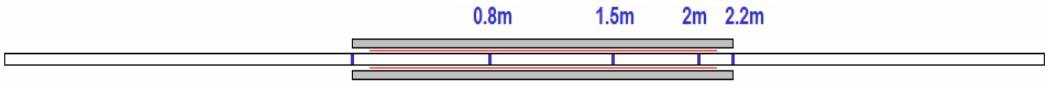

Fig. 6.11 Radial path along the computation domain

Figs. 6.12 – 6.15 present the axial force density profile at various radial path along the pump, for the mean sodium velocity 8 m/s. The radial coordinate r = 0.125 m corresponds to the interior wall and the radial coordinate r = 0.175 m corresponds to the exterior wall. In general, the most important differences are near the walls.

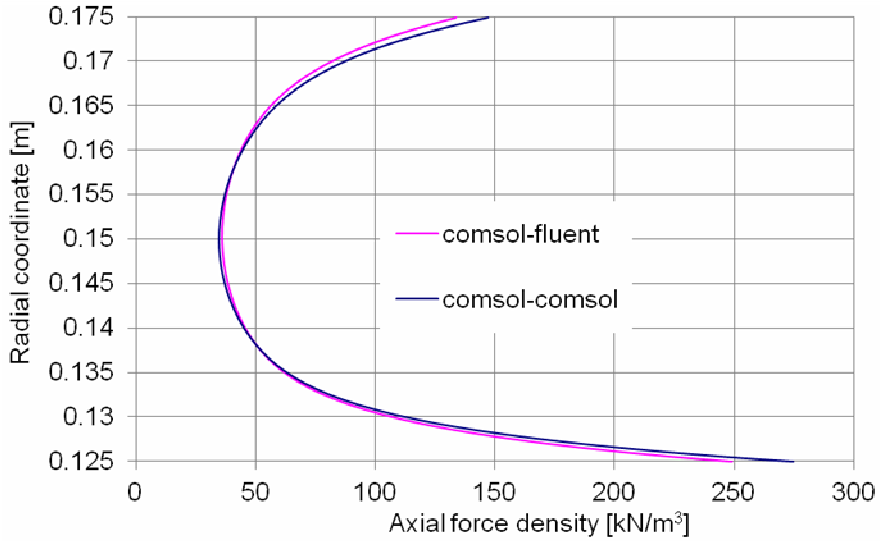

Fig. 6.12 Comparison between COMSOL-COMSOL and COMSOL-FLUENT coupled models, laminar flow model, sodium mean velocity 8 m/s, regarding the force profile at radial path *0.8m*

At radial path 0.8m, Fig. 6.12, the force density percent difference between COMSOL-COMSOL and COMSOL-FLUENT at interior wall is 9.31 %. The force density percent difference at exterior wall is 9.17 %.

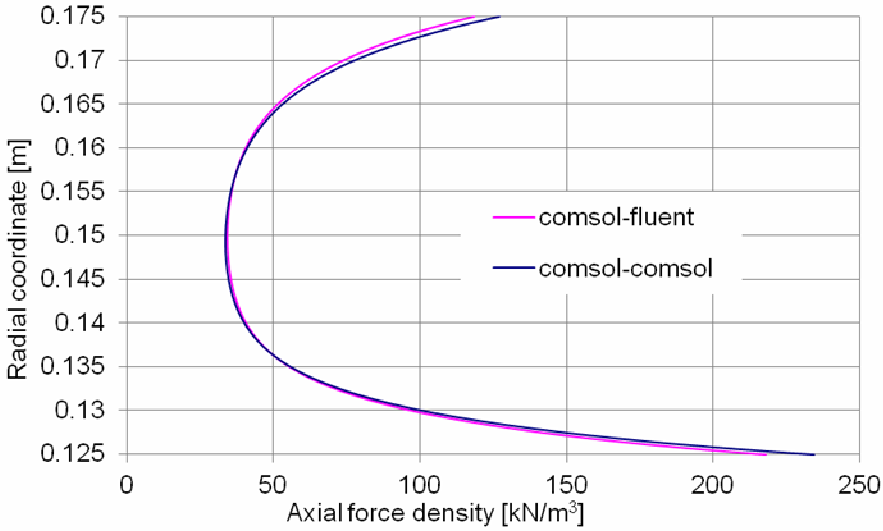

Fig. 6.13 Comparison between COMSOL-COMSOL and COMSOL-FLUENT coupled models, laminar flow model, sodium mean velocity 8 m/s, regarding the force profile at radial path *1.5m*

At 1.5 m from pump inlet, namely at radial path *1.5m*, Fig. 6.13 the force density percent difference at interior wall is 6.97 % and at exterior wall 6.75 %.

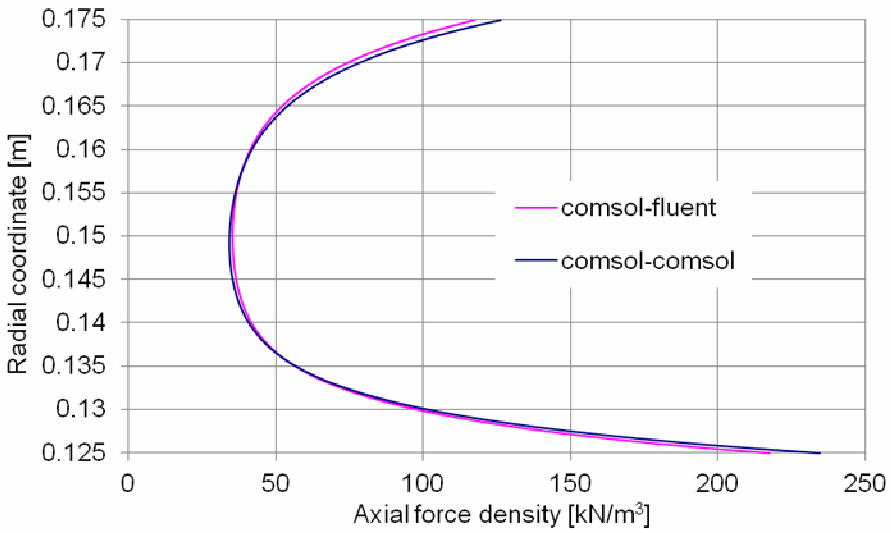

Fig. 6.14 Comparison between COMSOL-COMSOL and COMSOL-FLUENT coupled models, laminar flow model, sodium mean velocity 8 m/s, regarding the force profile at radial path *2m*

At 2 m from pump inlet, the force density percent difference at interior wall is 7.37 % and at exterior wall 7.13 %.

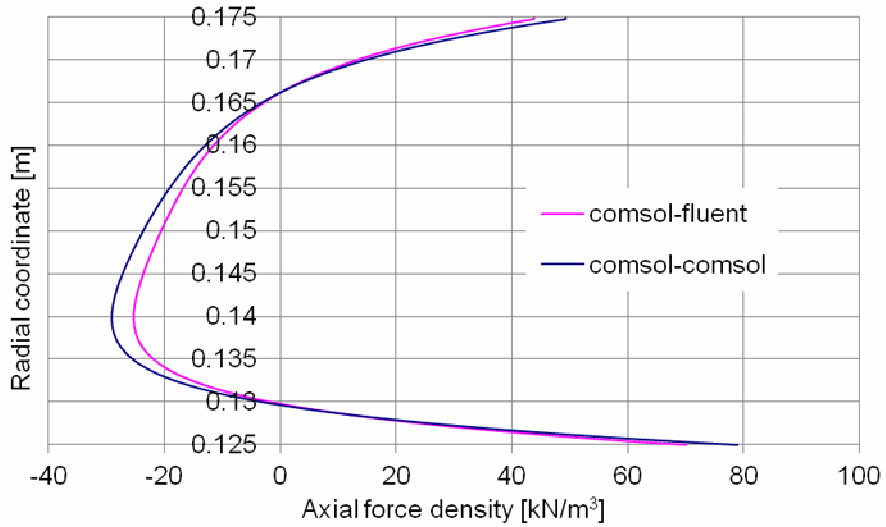

Fig. 6.15 Comparison between COMSOL-COMSOL and COMSOL-FLUENT coupled models, laminar flow model, sodium mean velocity 8 m/s, regarding the force profile at radial path *2.2m*

For path 2.2 m, the force density percent difference at interior wall is 11.30 % and at exterior wall 11.21 %. The maximum difference is 12.98 and corresponds to the radial coordinate 0.1396 mm.

The conclusion of this paragraph is that the global parameters and local quantities of the PEMDYN pump are obtained with similar precisions with both coupled models, COMSOL – COMSOL and COMSOL – FLUENT.

6.2 MHD coupling using the turbulent flow model in the hydrodynamic problem

In the MHD study presented in this paragraph it is used the RNG k-ε turbulent model of the flow. The MHD coupling is made using two professional software: COMSOL for the electromagnetic problem and FLUENT for the flow problem. The paragraph presents the differences between the results of the coupled model using the laminar flow model, namely a fictive value of the viscosity and the results of the coupled model that considers a dedicated turbulent flow model and the real sodium viscosity. Some of the relevant results are presented in parallel with results obtained in the block – pumping hypothesis. The representative quantities of the MHD flow are characterized for low and high velocities.

6.2.1 RNG k- ε model

Turbulence modeling means constructing and using a model to predict the effects of turbulence. The *k-ε* model is one of the most common turbulence models. It is a two equation model, which means that it includes two transport equations to represent the turbulent properties of the flow. This allows the two equation model to consider the convection and diffusion of the turbulent energy. The two transported variables are: the turbulent kinetic energy, k that determines the energy in the turbulence, and the turbulent dissipation rate, ε which determines the scale of the turbulence.

The *RNG k-ε* model was developed by Yakhot et al., [169] to renormalise the Navier-Stokes equations, to account for the effects of smaller scales motion. The RNG-based k-ε turbulence model is derived from the instantaneous Navier-Stokes equations, using a mathematical technique called "renormalization group" (RNG) methods. The analytical derivation results in a model with constants different from those in the standard k-ε model, and additional terms and functions in the transport equations for k and ε. In the standard k-ε model the eddy viscosity is determined from a single turbulence length scale, so the calculated turbulent diffusion is that which occurs only at the specified scale, whereas in reality all scales of motion will contribute to the turbulent diffusion. The RNG k-ε model is similar in form to the standard k-ε model, but includes the following refinements:

- The RNG model has an additional term in its ε equation that improves the accuracy for rapidly forced flows.
- The effect of swirl on turbulence is included in the RNG model, enhancing accuracy for swirling flows.
- The RNG theory provides an analytical formula for turbulent Prandtl numbers, while the standard k-ε model uses user-specified, constant values.
- While the standard k-ε model is a high-Reynolds-number model, the RNG theory provides an analytically-derived differential formula for effective viscosity that accounts for low-Reynolds-number effects. Effective use of this feature does, however, depend on an appropriate treatment of the near-wall region.

These features make the RNG k-ε model more accurate and reliable for a wider class of flows than the standard k-ε model.

The transport equations for the RNG k-ε model are:

$$\frac{\partial}{\partial t}(dk) + div(dk\mathbf{v}) = div(a_k \eta_{eff} grad\, k) + G_k + G_b - d\varepsilon - Y_M + S_k \qquad (6.20)$$

$$\frac{\partial}{\partial t}(d\varepsilon)+div(d\varepsilon \boldsymbol{v})=div(a_\varepsilon \eta_{eff}\, grad\, \varepsilon)+C_{1\varepsilon}\frac{\varepsilon}{k}(G_k+C_{3\varepsilon}G_b)-C_{2\varepsilon}d\frac{\varepsilon^2}{k}-R_\varepsilon+S_\varepsilon \quad (6.21)$$

where:

- k and ε are the turbulent kinetic energy, respectively the turbulent dissipation rate
- d is the mass density
- $\boldsymbol{v}$ is the velocity
- G_k represents the generation of turbulence kinetic energy due to the mean velocity gradients
- G_b is the generation of turbulence kinetic energy due to buoyancy
- Y_M represents the contribution of the fluctuating dilatation in compressible turbulence to the overall dissipation rate
- S_k and S_ε are user defined source terms
- The quantities a_k and a_ε are the inverse effective Prandtl numbers for k, respectively for ε. These values are calculated using the following formula derived analytically by the RNG theory:

$$\left|\frac{a-1.3929}{a_0-1.3929}\right|^{0.6321}\left|\frac{a+2.3929}{a_0+2.3929}\right|^{0.3679}=\frac{\eta_{mol}}{\eta_{eff}} \quad (6.22)$$

where $a_0=1$ and η_{mol} is the molecular viscosity.

In the high Reynolds number limit, namely for $\frac{\eta_{mol}}{\eta_{eff}}\ll 1$, $a_k=a_\varepsilon\approx 1.393$.

- η_{eff} is the effective viscosity and is defined by the following relation

$$d\left(\frac{d^2k}{\sqrt{\varepsilon\eta}}\right)=1.72\frac{\hat{\nu}}{\sqrt{\hat{\nu}^2-1+C_\nu}}d\hat{\nu} \quad (6.23)$$

where $\hat{\nu}=\frac{\eta_{eff}}{\eta_{mol}}$ and $C_\nu\approx 100$

Equation (6.24) is integrated to obtain an accurate description of how the effective turbulent transport varies with the effective Reynolds number, allowing the model to better handle low Reynolds number and near-wall flows.

In the high-Reynolds-number limit, equation (6.24) gives

$$\eta_t=dC_\eta\frac{k^2}{\varepsilon} \quad (6.24)$$

where $C_\eta=0.0845$, derived using RNG theory. This value is very close to the empirically determined value of 0.09 used in the standard k- ε model.

- R_ε represents the term that makes the main difference between the RNG and standard k-ε model:

$$R_\varepsilon=\frac{C_\eta d n^3(1-n/n_0)}{1+\beta n^3}\frac{\varepsilon^2}{k} \quad (6.25)$$

where $n\equiv\frac{S_k}{\varepsilon}$, $n_0=4.38$, $\beta=0.012$

This term makes the RNG model more responsive to the effects of rapid strain and of streamline curvature than the standard k-ε model, which explains the superior performance of the RNG model for certain classes of flows.

- The constants $C_{1\varepsilon}$ and $C_{2\varepsilon}$ have values derived analytically by the RNG theory. These values, used by default in ANSYS FLUENT are $C_{1\varepsilon}=1.42$ and $C_{2\varepsilon}=1.68$.

6.2.2 The coupling

The electromagnetic problem has the same sources, properties, conditions and it is solved as presented in paragraph 6.1. The mesh of the channel in the electromagnetic problem, Fig. 6.16, is mapped. It contains 2000 equal cells in the axial direction and 80 cells in the radial direction. The height of every finite element is 3 mm. The dimension of the cells in radial direction is progressive and symmetric distributed with respect to the middle of the channel. The first element near the wall is 0.1345 mm, and the largest, in the middle is 1 mm.

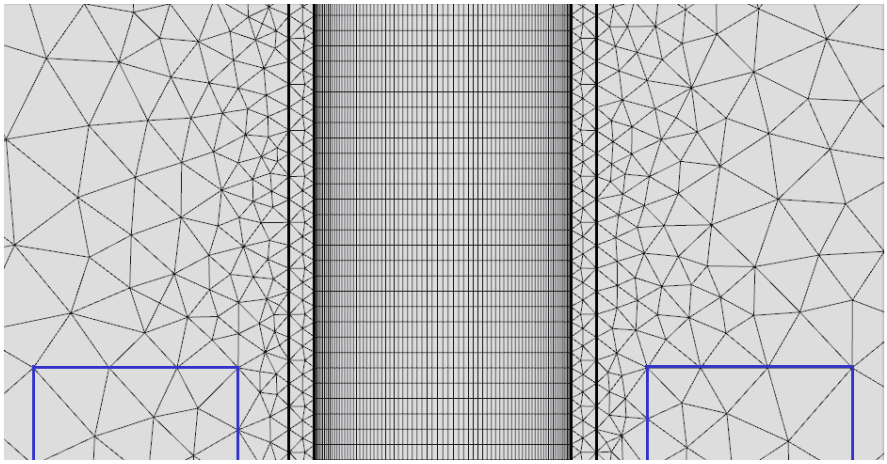

Fig. 6.16 Finite element network used in the electromagnetic problem (zoom)

The computation domain of the flow problem, Fig. 6.17, solved in time domain, consists only in the interior of the channel through which the sodium is flowing. The domain boundary conditions are: at INLET imposed uniform velocity profile, at OUTLET conservation of mass condition and null velocity at the walls. The mesh of the hydrodynamic problem is mapped, with 2000 cells in the axial direction, which gives a 3 mm length for any cell. In radial direction the mesh is symmetric with respect to the middle of the channel. There are 80 elements, with the smallest near the wall having 0.2 mm height and the largest, in the middle, 1.4 mm.

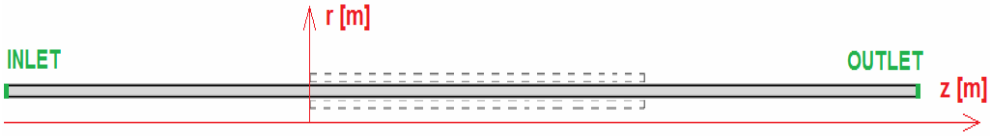

Fig. 6.17 Computation domain in FLUENT

The solution of the coupled study is taken care by an iterative process of separately solving the two problems and, by turns, updating each one. The scheme presented in Fig. 6.2 is valid for the solving process used in this paragraph with the mention that the "Computation of the electromagnetic field" is made in COMSOL and the "Computation of the velocities field $\vec{u}^{n+1}$ at time step $t_{n+1} = t_n + \Delta t$" is made in FLUENT.

The computation of the Maxwell's equation in the frequency domain provides with the distribution of the electromagnetic axial and radial forces densities in the channel.

Importation of the forces field in the FLUENT domain consists in two steps:
a) preparing the interpolation file in order to pass from a vertical orientation of the Oz axis as COMSOL requires, to an horizontal position required by FLUENT,
b) interpolating the values of the axial and radial force density associated to the nodes of the finite element network of the electromagnetic problem to the cell centers of the mesh of the hydrodynamic problem.

The time step used in the hydrodynamic problem is 0.1 s. The updating of the velocities field or forces field is made after each time step.

The calculation of the Navier-Stokes equation provides with the velocities field corresponding to the current time step or current iteration. The velocities field is interpolated back to the field domain of the electromagnetic problem, where the Lorentz term of the Ohm law is updated.

The time depending process, described in Fig. 6.2 is repeated until the convergence criterion is reached. The convergence criterion consists in fulfilling simultaneously the following four aspects with respect to the results corresponding to time steps t_n and t_{n+1}:

- identical three significant figures for the *integral of the axial volume density* of the electromagnetic force
- identical three significant figures regarding the maximum of the *kinetic energy* found anywhere in the domain
- identical three significant figures regarding the maximum of the *axial velocity* found anywhere in the domain
- identical *velocity profile* at the pump outlet

The convergence for the low velocities is fast and the few oscillations of the total force or any other quantity with respect to the stabilized value are insignificant. Figs. 6.18 and 6.19 present the convergence evolution for two sodium velocities found at extremities of the descendant branch of the Pressure – Velocity characteristic, namely 10 and 12.5 m/s.

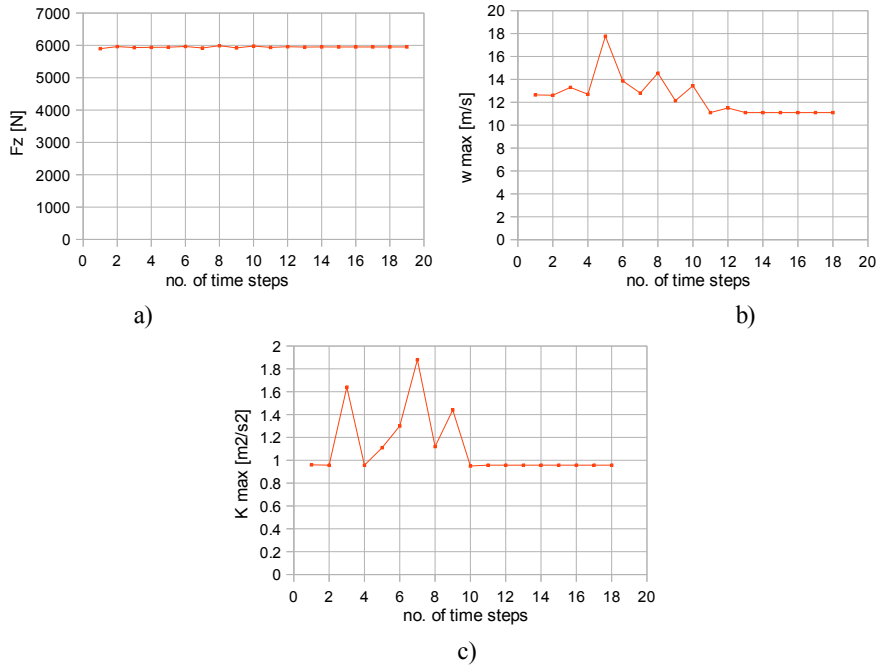

Fig. 6.18 Convergence progress for the mean velocity 10 m/s: a) Total axial force, b) Maximum axial velocity in any point of the domain, d) Maximum kinetic energy in any point of the domain

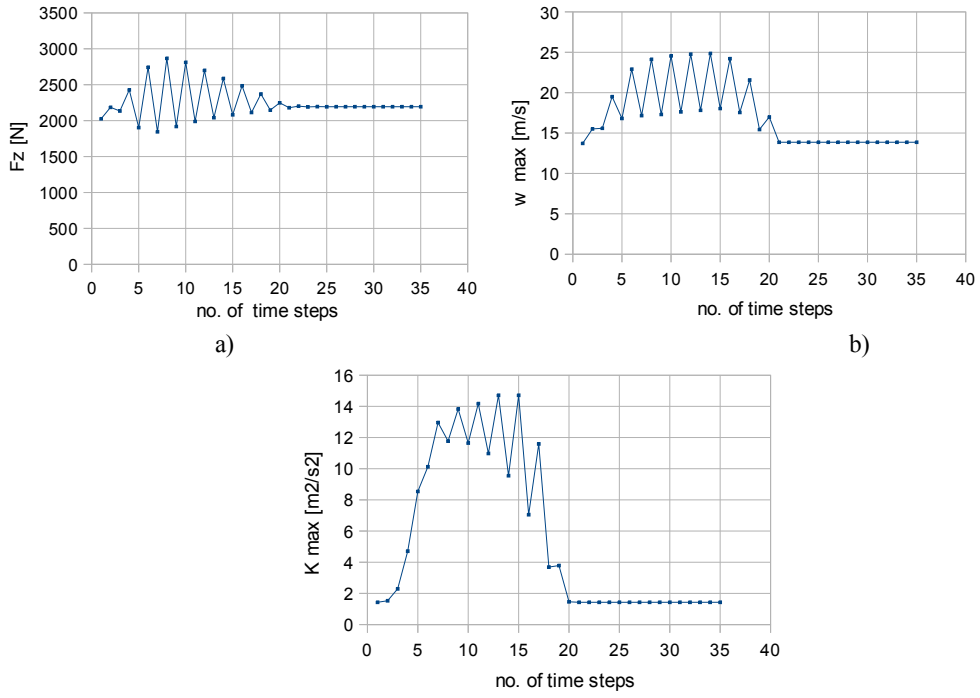

Fig. 6.19 Convergence progress for the mean velocity 12.5 m/s: a) Total axial force, b) Maximum axial velocity in any point of the domain, c) Maximum kinetic energy in any point of the domain

Analyzing the evolution of convergence at different sodium mean velocities in terms of total axial force, it is observed that the maximum amplitude of the oscillations with respect to the stabilized value is considerable increasing as the sodium velocity increases. In the two limit cases, 10 m/s and 12.5 m/s, the ratio between the amplitude of the maximum oscillation and the stabilized value of the total axial force, is 7.3% for 10 m/s and 46.6% for 12.5 m/s. The same ratio for the maximum axial velocity in a point gives 8.2% for 10 m/s and 51.5% for 12.5 m/s and for the maximum kinetic energy in a point it gives 517% for 10 m/s sodium velocity and 556% for 12.5 m/s sodium velocity.

For the sodium mean velocities 10 m/s and 12.5 m/s and two different places along the channel, Figs 6.20 – 6.27 present the force and velocity profiles for two successive time steps corresponding to the highest oscillation amplitude of the axial force and the profile corresponding to the stabilized solution.

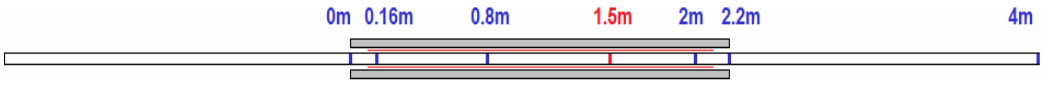

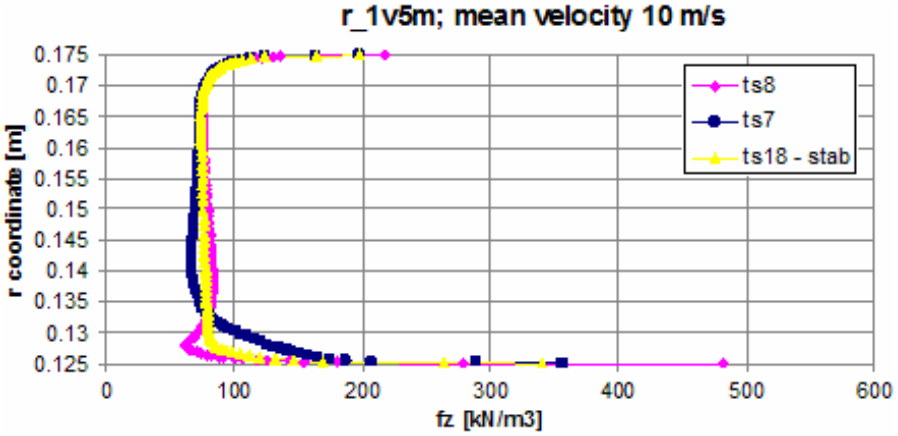

Fig. 6.20 Force profile at radial path "1.5m" for sodium mean velocity 10 m/s at three different time steps: ts7 and ts8 are two successive time steps during the iterative solving and starting with the 18th time step, respectively ts18, the force profile is stabilized

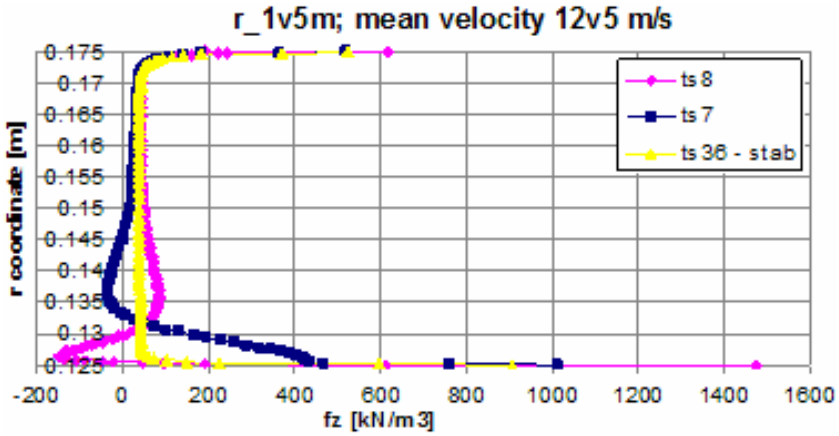

Fig. 6.21 Force profile at radial path "1.5m" for sodium mean velocity 12.5 m/s at three different time steps: ts7 and ts8 are two successive time steps during the iterative solving and starting with the 36th time step, respectively ts36, the force profile is stabilized

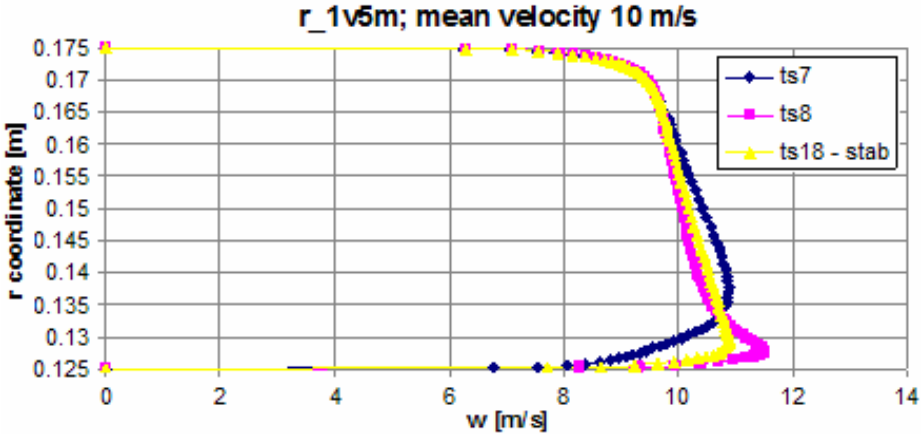

Fig. 6.22 Velocity profile at radial path "1.5m" for sodium mean velocity 10 m/s at three different time steps: ts7 and ts8 are two successive time steps during the iterative solving and starting with the 18th time step, respectively ts18, the velocity profile is stabilized

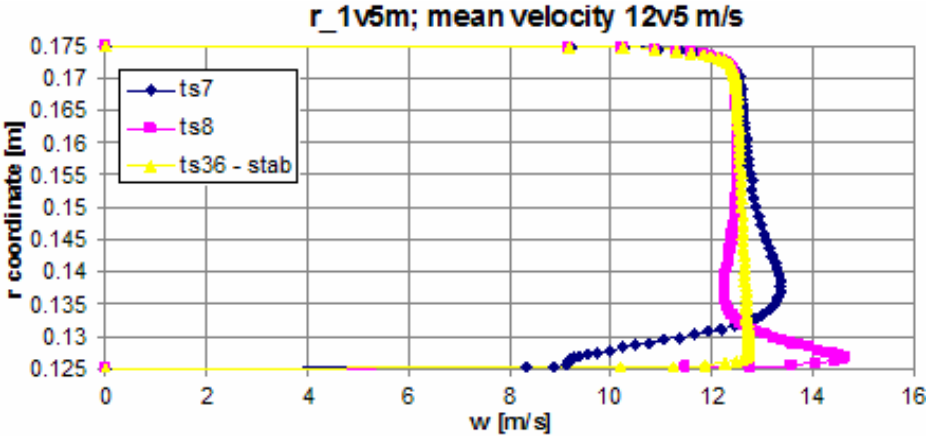

Fig. 6.23 Velocity profile at radial path "1.5m" for sodium mean velocity 12.5 m/s at three different time steps: ts7 and ts8 are two successive time steps during the iterative solving and starting with the 36th time step, respectively ts36, the velocity profile is stabilized

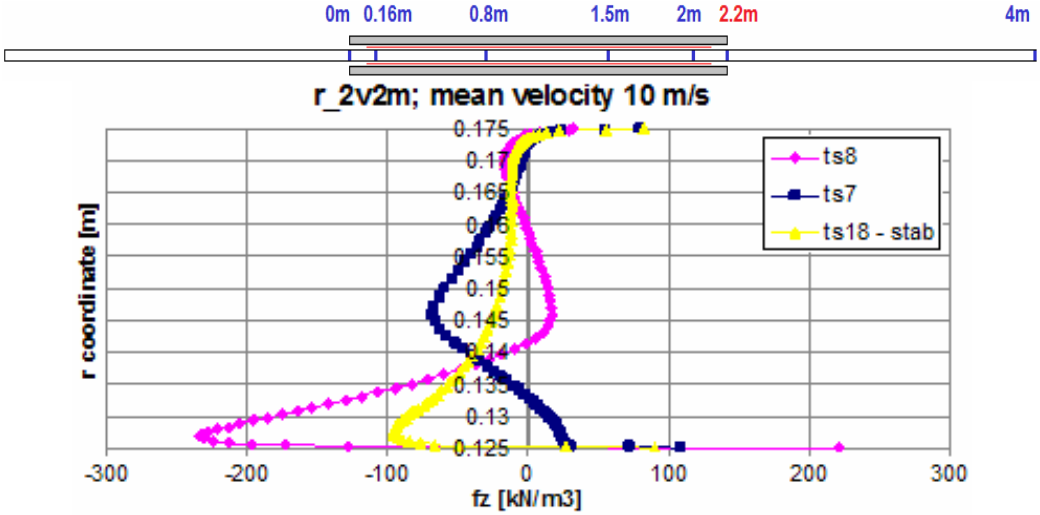

Fig. 6.24 Force profile at radial path "2.2m" for sodium mean velocity 10 m/s at three different time steps: ts7 and ts8 are two successive time steps during the iterative solving and starting with the 18th time step, respectively ts18, the force profile is stabilized

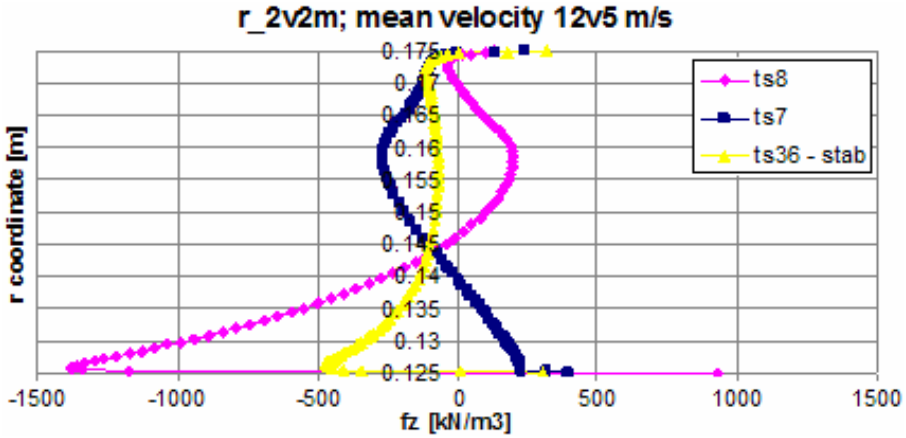

Fig. 6.25 Force profile at radial path "2.2m" for sodium mean velocity 12.5 m/s at three different time steps: ts7 and ts8 are two successive time steps during the iterative solving and starting with the 36th time step, respectively ts36, the force profile is stabilized

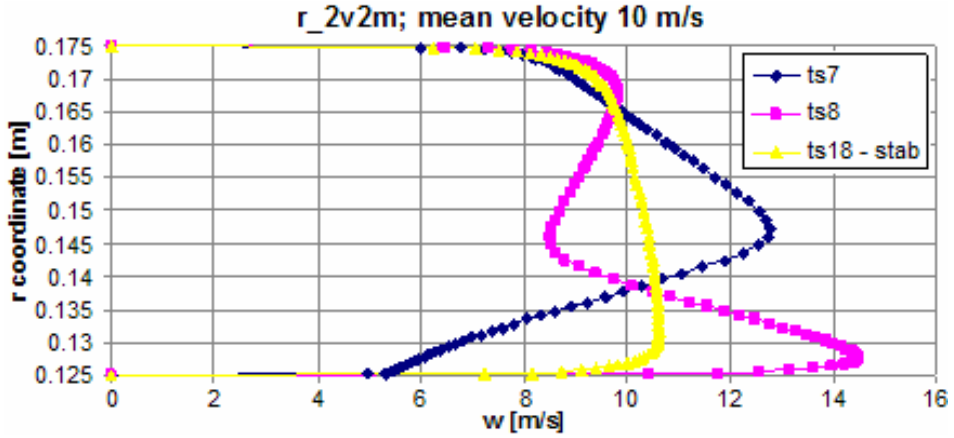

Fig. 6.26 Velocity profile at radial path "2.2m" for sodium mean velocity 10 m/s at three different time steps: ts7 and ts8 are two successive time steps during the iterative solving and starting with the 18th time step, respectively ts18, the velocity profile is stabilized

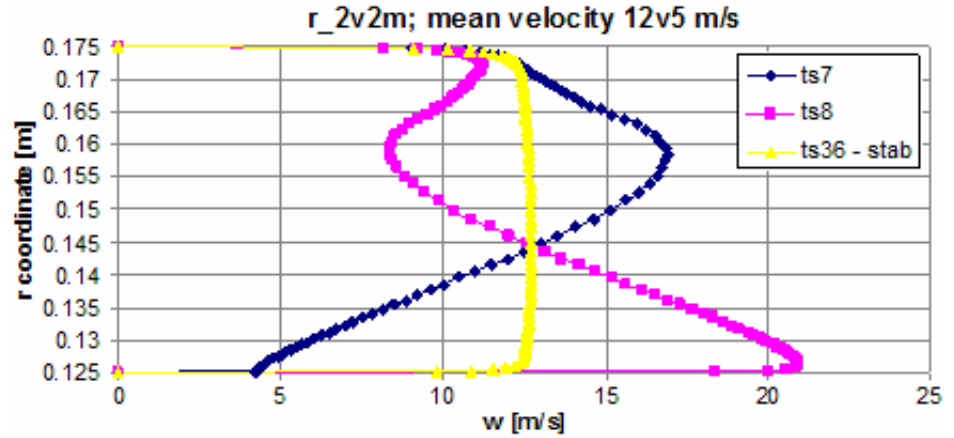

Fig. 6.27 Velocity profiles at radial path "2.2m" for sodium mean velocity 12.5 m/s at three different time steps: ts7 and ts8 are two successive time steps during the iterative solving and starting with the 36th time step, respectively ts36, the velocity profile is stabilized

Some observation can be made with respect to the variation with time step of the velocity and force profiles:

- whenever the velocity is higher than the synchronous velocity (13.32 m/s) the corresponding force profile contains portions of negative forces
- the amplitudes of the oscillations with respect to the stabilized force or velocity profile increase with the sodium flowrate and with the proximity of the pump outlet, due to the fact that ending effects are more and more important as the sodium velocity increases.
- The stabilized force profile at the pump outlet, namely radial path "2.2m", contains negative portions for high velocities due to the exiting the magnetic field, but force profiles at radial path "1.5m" with negative portions indicate that the presence of points with local velocity higher than the synchronous speed could be introduced by the imposed velocity condition.

6.2.3 Hydrodynamic pressure – Velocity characteristic

The red curve "COMSOL-FLUENT-turbulent" in Fig. 6.28 represents the Hydrodynamic pressure – Velocity characteristic of PEMDYN pump build with coupled model based on RNG k-ε turbulent model. It was obtained by solving the iterative process presented in Fig. 6.2 for different imposed velocities. The black curve "P_elmg_block-pumping" represents the dependence of the electromagnetic pressure on sodium velocity computed in the block – pumping hypothesis. The other two curves are the same representations as in Fig. 6.10 and are given for comparison purposes.

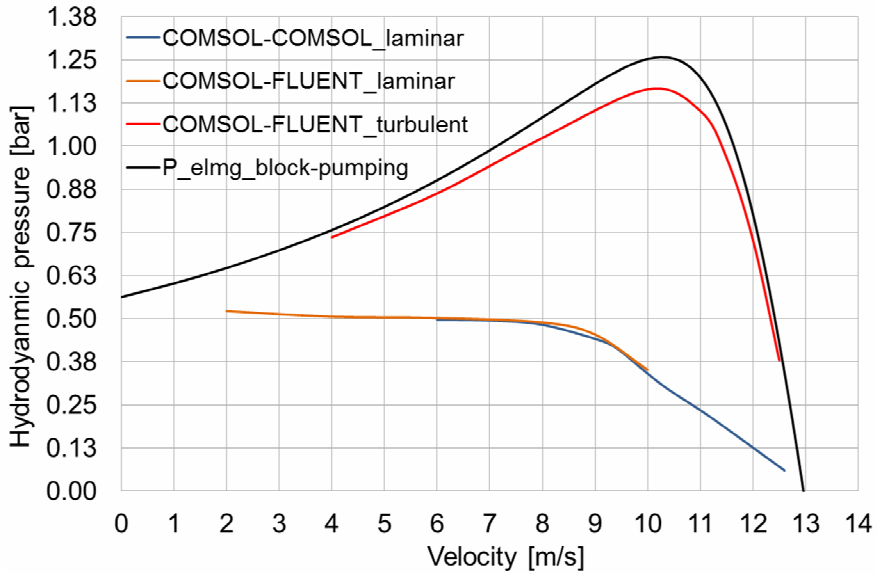

Fig. 6.28 Hydrodynamic pressure – Velocity characteristic of PEMDYN obtained by COMSOL-FLUENT coupling, k-ε turbulent flow model

The curves "COMSOL-FLUENT-turbulent" and "P_elmg_block-pumping" show the differences between the characteristic obtained using a simple *electromagnetic model* with motion and the characteristic obtained with a *MHD model*. The importance of obtaining the characteristic with an adequate MHD coupled model consists in determination with a better accuracy of the pump maximum pressure at any sodium velocity. The difference between the curves "P_elmg_block-pumping" and "COMSOL-FLUENT_turbulent" is due to the fact that the second takes into account the hydrodynamic losses due to viscous forces, and therefore it is closer to physical reality.

Taking into consideration the two curves obtained by MHD coupling based on laminar flow model with fictive value of the dynamic viscosity and the "COMSOL-FLUENT-turbulent" curve, it is obvious that the scheme with fictive viscosity 1000 times higher than the real molecular sodium viscosity gives acceptable results only for very low velocities or velocities very close to synchronous velocity. As it can be seen in (6.24) and (6.25), the effective viscosity is function of turbulent kinetic energy k and of turbulence dissipation rate ε, which both depend on velocity. Thus for the remained velocity range another value for the ration between fictive dynamic viscosity and real dynamic viscosity should be chosen. Due to the fact that this ratio is a priori unknown, the Hydrodynamic pressure – Velocity characteristic based on turbulent flow model is clearly superior to that based on laminar model when a wider range of velocities is taken into account.

The relative difference defined as the division by 100 of the algebraic difference between the values of the "COMSOL-FLUENT-turbulent" and "P_elmg_block-pumping" curves is given in Fig. 6.29.

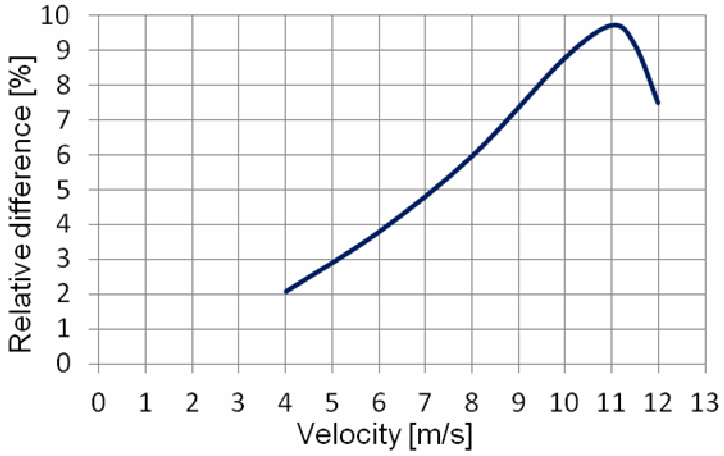

Fig. 6.29 Relative difference between "COMSOL-FLUENT-turbulent" and "P_elmg_block-pumping"

6.2.4 Longitudinal effects and MHD interaction

At local scale, the MHD interaction is expressed by variations of electromagnetic and hydrodynamic quantities under the influence of the sodium velocity and of the electromagnetic field. These effects are present along the pump length and also along the radial direction. This paragraph presents the variation of significant quantities of the MHD flow along the pump length.

For representations along the pump, there are defined three longitudinal paths called INT, EXT, MIDDLE, Fig. 6.30, where

- INT represents the boundary between sodium and channel wall near the Oz axis of the pump,
- EXT represents the boundary between sodium and channel wall near the radial extremity of the channel and
- MIDDLE represents a longitudinal path through the middle of the sodium channel

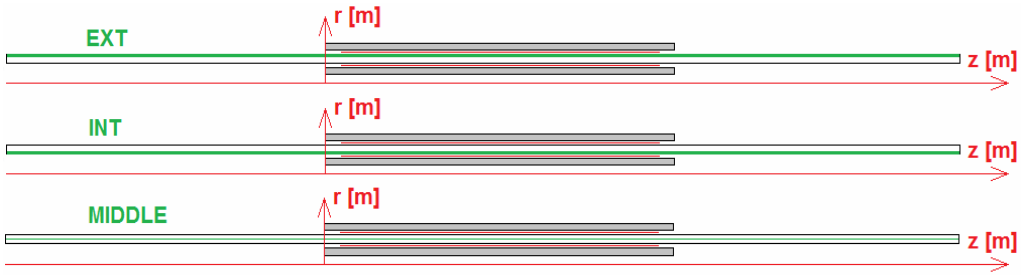

Fig. 6.30 Three longitudinal paths: INT and EXT at the boundary between sodium and the walls, and MIDDLE in the middle of the sodium

Some figures represent comparisons between results obtained with the block – pumping hypothesis and with the coupled COMSOL-FLUENT-turbulent model. The legend code for these figures is the following: "BLOC" refers to the block – pumping hypothesis and "MHD" refers to COMSOL-FLUENT-turbulent model. The two words might be accompanied by velocity expressions, which refer to sodium mean velocity.

A) Magnetic flux density

Fig. 6.31 presents the distribution of the radial component of magnetic flux density along the MIDDLE path for sodium mean velocity 10 m/s and null velocity taken from block-pumping calculation. Fig. 6.32 presents the distribution of the modulus of the magnetic flux density along the middle path for sodium mean velocity 10 m/s and null velocity. These figures are representative for the allure of the longitudinal variation of the magnetic flux density. If the two quantities would be plotted along the INT and EXT longitudinal paths, small differences with respect tot the values in Figs. 6.31 and 6.32 would be found. More about the radial variation of the magnetic flux density is presented in section 6.2.4.

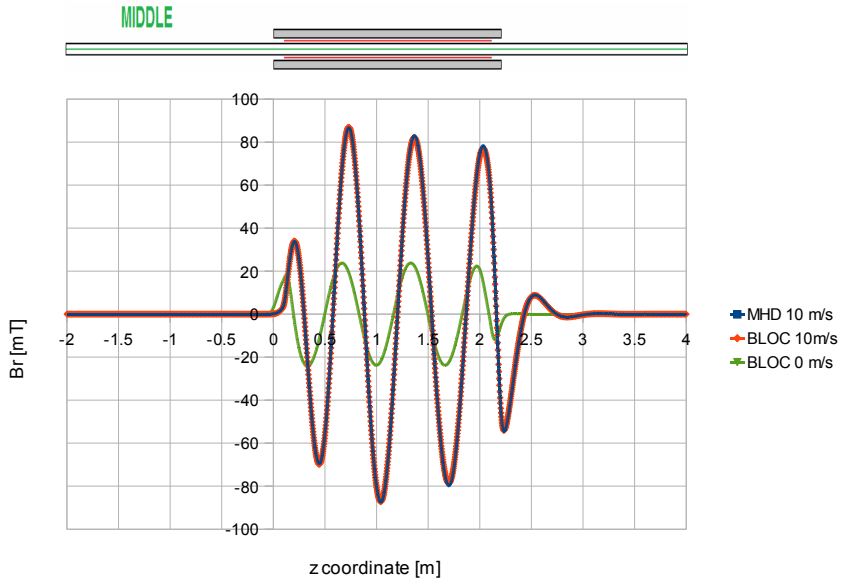

Fig. 6.31 Radial component of the magnetic flux density (phase shift 0 degrees) for null velocity and for 10 m/s in MHD and BLOC cases, along the MIDDLE longitudinal path

The value of the magnetic flux density is increasing with the increase of the sodium velocity. The space variations of the radial component of the magnetic flux density along the pump are due to the fact that the magnetic flux density changes the polarity between two adjacent poles and is maxim in the pole axis. The first positive peak and the last two peaks (negative and positive) reflect the longitudinal ends effect due to the important variation of electromagnetic field at pump inlet and pump outlet.

The longitudinal non-uniformity of the magnetic flux density module distribution, Fig. 6.32, increases as the sodium velocity increases.

It can be observed that the longitudinal profile of the magnetic flux density very similar for both methods of calculation, block – pumping and MHD coupling.

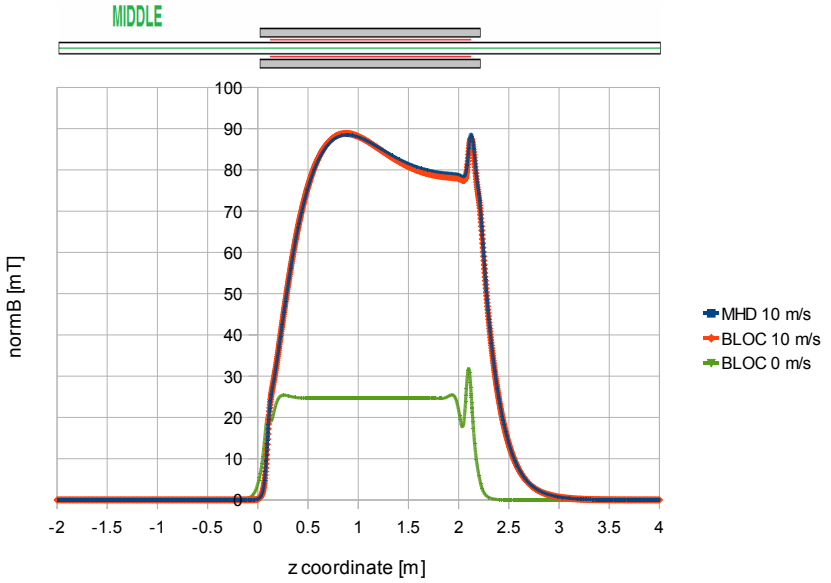

Fig. 6.32 Modulus of the magnetic flux density for null velocity and for 10 m/s in MHD and BLOC cases, along the MIDDLE longitudinal path

B) Longitudinal profile of axial force density

The longitudinal profile of the axial component of the force density along the MIDDLE path is presented in Fig. 6.33, obtained with the MHD coupling and in Fig. 6.34, obtained in block – pumping hypothesis, for representative velocities of the Pressure – Velocity characteristic. The curve for 4 m/s is representative for the behavior at low velocities and the other curves are corresponding to important velocities of the descending branch of the characteristic.

The two figures highlight some particularities about the dependence of the longitudinal force density profile on sodium mean velocity with respect to the ends effects and force uniformity along the pump. It can be observed that for low velocities the negative force at inlet and outlet are small and along the pump there is a large region of constant force. The increase of velocity amplifies the negative force at inlet and outlet and determines important non-uniformities of the force density along the pump. For velocities close to the synchronous velocity there is no constant region. The increase of velocity in the range corresponding to the descendant branch of the characteristic curve tends to have different effects at pump inlet, respectively at pump outlet. At inlet the effects consists rather in a prolongation of the negative forces towards the pump outlet than in an increase of the negative forces. Instead, at the outlet, any increase of velocity generates an increase of the negative force.

Comparing Figs. 6.33 and 6.34 it can be observed that the results of the two computation hypothesis, MHD coupling and block – pumping, are close with regard to the values of the force density along the MIDDLE path. Yet, the MHD coupled model better evaluates the length of propagation of the negative forces at pump inlet.

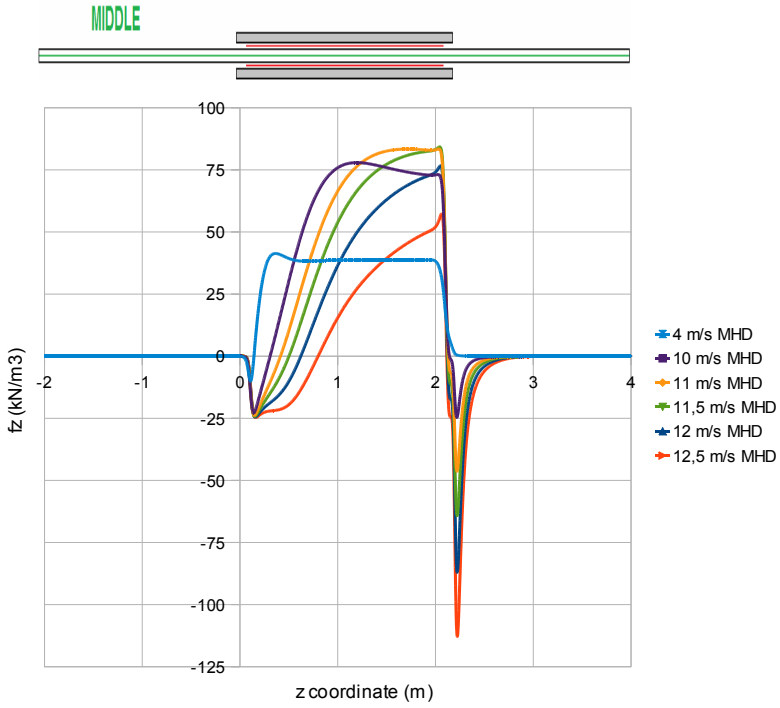

Fig. 6.33 Axial force density along the MIDDLE longitudinal path for different mean velocities, in case of MHD model

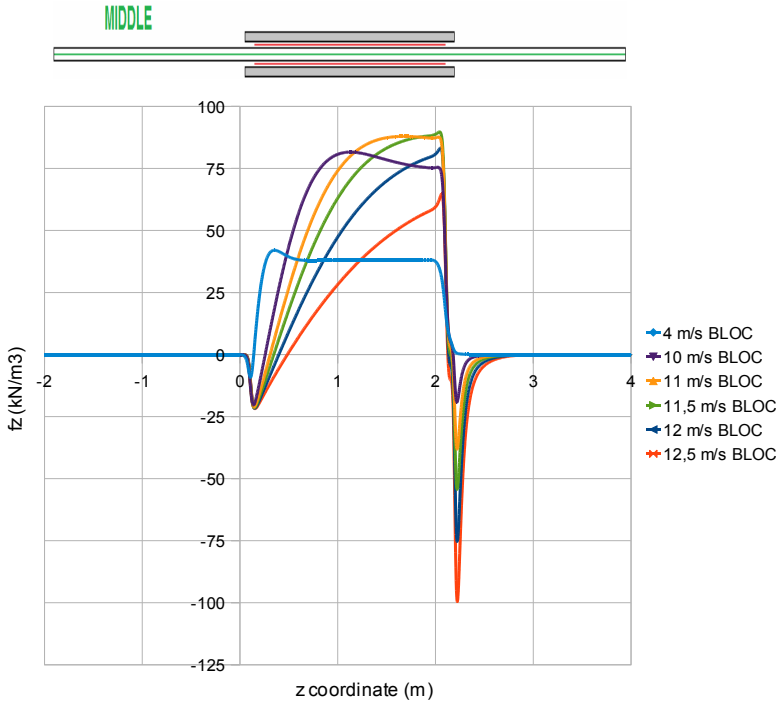

Fig. 6.34 Axial force density along the MIDDLE longitudinal path for different mean velocities, in case of BLOC

C) Hydrodyanamic pressure drop

The hydrodynamic pressure drop along the channel is not a function of the radial coordinate. Consequently it could be represented on any longitudinal path

inside the sodium channel. Fig. 6.35 presents the pressure drop along the MIDDLE longitudinal path.

For the velocities corresponding to ascendant branch of the pump characteristic, namely from null velocity to around 10 m/s, the pressure difference between pump outlet and pump inlet increases. As the velocity increases over 10 m/s, the pressure generated by the pump, decreases.

The negative forces at pump inlet produce a region of depression that can extend even until one meter from pump inlet for the very high velocities and contributes to the decrease of the pump efficiency.

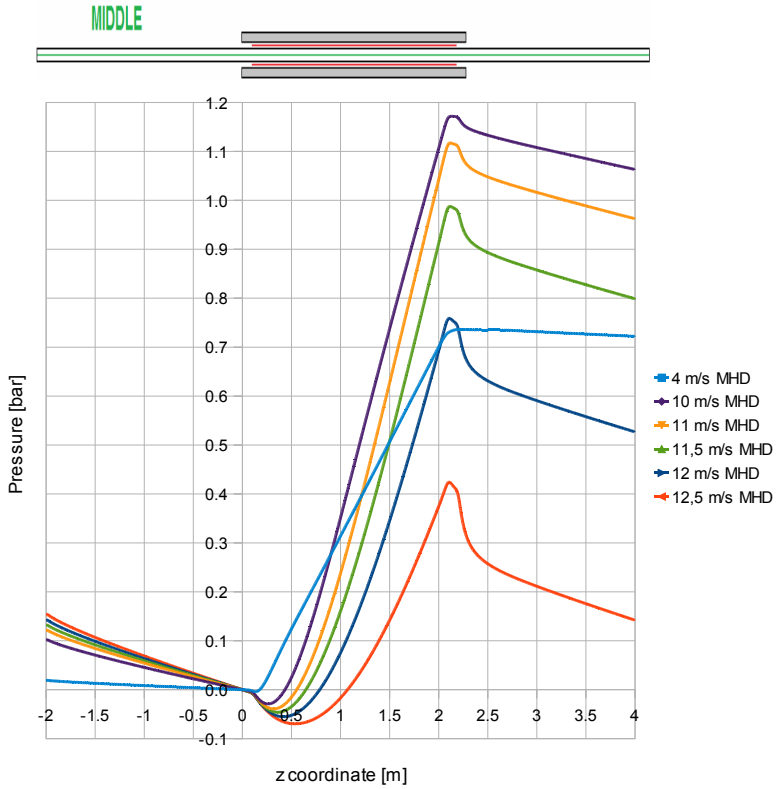

Fig. 6.35 Pressure drop along the computation domain for different velocities, MHD model

6.2.5 Radial effects of the MHD interaction

Fig. 6.36 represents the longitudinal profile of the axial force density for sodium mean velocity 10 m/s, computed in MHD coupling and bloc – pumping hypothesis, and for null velocity. In the region between z = 1 m and z = 2 m the quantity is quasi-constant and the mean value of the axial force density with respect to the pump length defined by the two coordinates is found at z = 1.5 m.

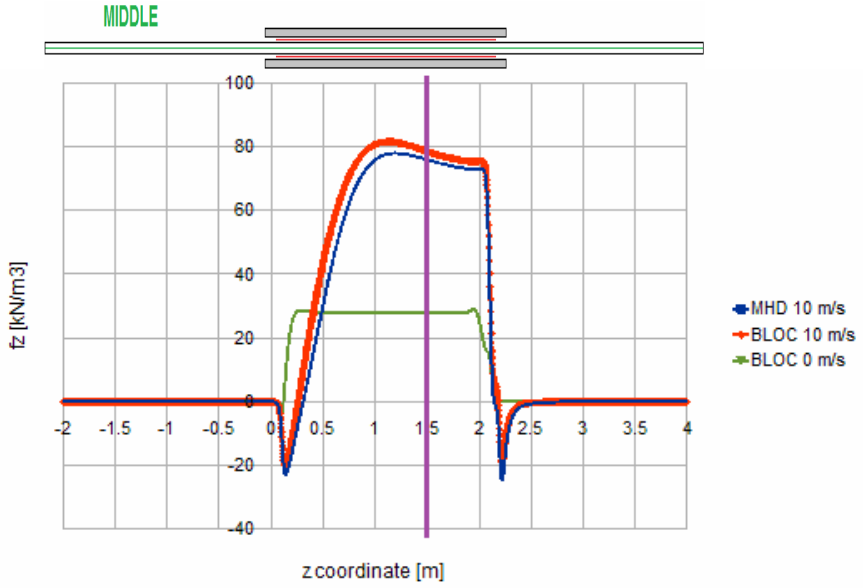

Fig. 6.36 Axial force density for null velocity and for 10 m/s in MHD and BLOC cases, along the MIDDLE longitudinal path

Thus, the behavior in radial direction of various quantities significant for the MHD flow are studied using representations along a radial path of axial coordinate z = 1.5 m, indicated in red in Fig. 6.37.

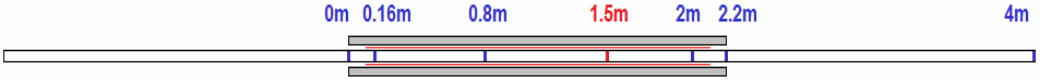

Fig. 6.37 Radial path at z coordinate 1.5m

A) Radial profile of magnetic flux density module

Fig. 6.38 presents the radial variation of the magnetic flux density module for various sodium velocities. The curves are presented for both hypothesis of computation and it can be seen that for any given velocity, the curves corresponding to the two methods are very close. This fact and the comments on Figs. 6.31 and 6.32 show that the magnetic flux density is equally well approximated by the two methods.

Regarding the influence of sodium velocity on the radial profile of magnetic flux density, Fig. 6.38 shows that as the velocity increases the decay of the magnetic flux density in the middle of the channel softens and the difference between the values at the two walls is increasing. Comparing the mean values of the curves corresponding to 4 m/s (firsts from bottom to top) with the mean values of the curves corresponding to 12.5 m/s (lasts from bottom to top), it is concluded that the global effect of velocity increase is the increase of the magnetic flux density in the sodium.

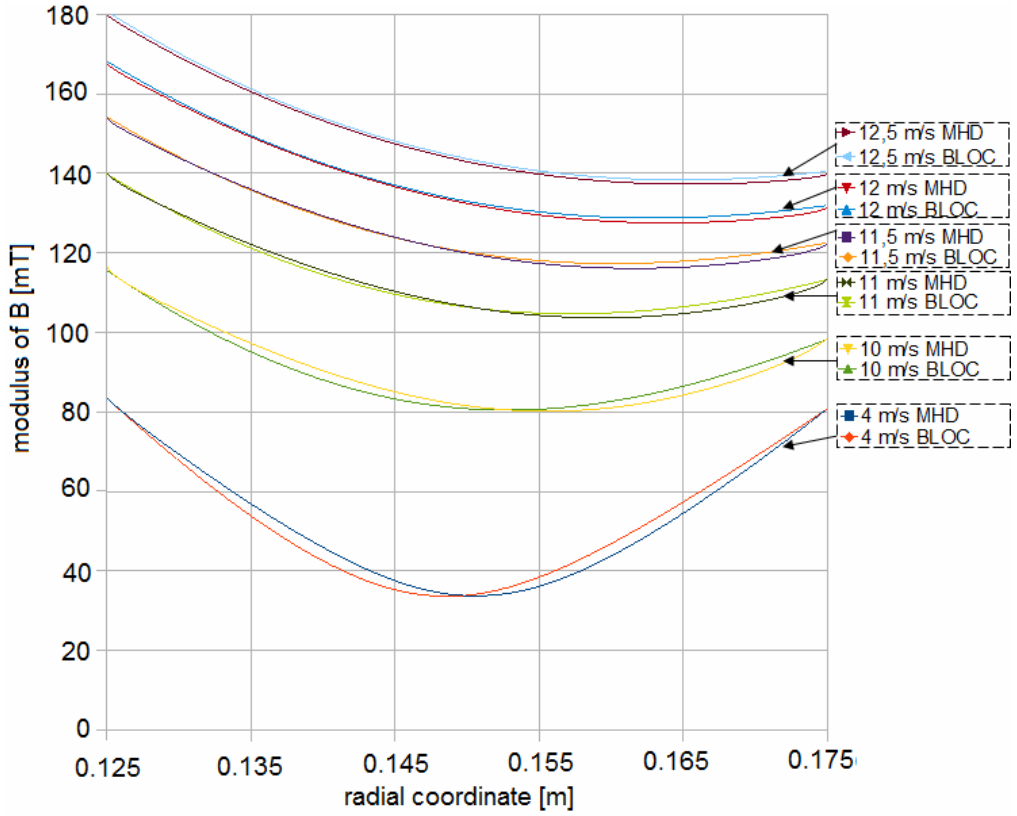

Fig. 6.38 Profile of the magnetic flux density at radial path "1.5m" for the mean velocities 4, 10, 11, 11.5, 12, 12.5 m/s, MHD and BLOC model

B) Radial profile of current density module

Fig. 6.39 presents the modulus of the current density induced in sodium, for various values of the sodium mean velocity. Fig. 6.40 represents a zoom close to the interior wall, namely the zoom represents the radial distribution of the current density on the first 1.45 millimeters of the radial path, starting from the interior wall.

The MHD interaction is very well illustrated by the radial profile of current density. The flow of sodium in magnetic field determines an important non-uniform distribution of the current density in the radial direction of the channel. The values of the current density are very high near the walls, in the boundary layer and much smaller in the bulk region. The ratio between two values increases as the velocity increases. Even if in the bulk region the current density is not null, through an accepted abuse of language, this effect is also known as expulsion to the walls of the currents.

In Fig. 6.39 the order of the curves (from top to bottom) in the bulk region is the same as the order of sodium velocity increase, namely the sodium velocity increase determines the decrease of the current density in the bulk region.

Fig. 6.40 shows that the top to bottom order of the curves is inversed near the wall with respect to the order in the bulk region. In other words, the sodium velocity increase determines the increase of the current density in the boundary layer. The ratio between the near-wall value and bulk-mean values of current density is 25 for 12.5 m/s and 6 for 4 m/s.

Such a disposal of the current density determines a similar distribution of the force density in the channel. These two aspects can be noticed only by using the MHD coupled model.

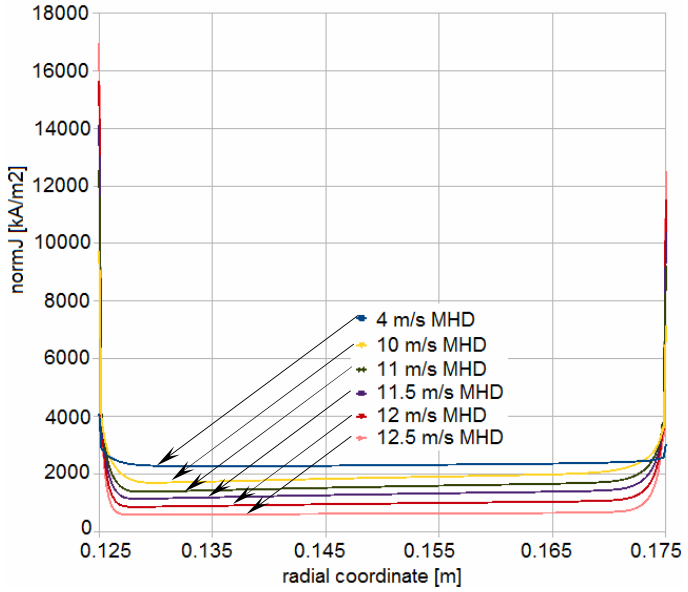

Fig. 6.39 Profile of the norm of the current density at radial path "1.5m" for the mean velocities 4, 10, 11, 11.5, 12, 12.5 m/s, MHD model

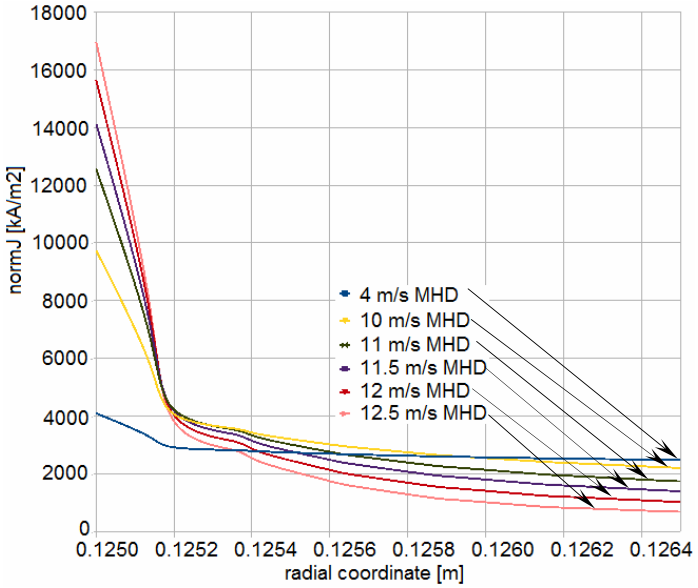

Fig. 6.40 Profile of the norm of the current density at radial path "1.5m" for the mean velocities 4, 10, 11, 11.5, 12, 12.5 m/s, MHD model (zoom)

Fig. 6.41 presents the radial profile of the induced current density both in the metallic walls and in the sodium channel. The current density along the walls thickness is also not uniform. It decays from the interface between sodium and metallic walls towards the walls limits. The increase of velocity determines an increase of the current density in the metallic walls.

The fact that from the total electromagnetic power developed by the pump double inductor a part is found in the form of Joule power in the metallic walls, constitutes losses with respect to the objective of sodium pumping caused by the metallic walls and is called the shielding effect of the walls.

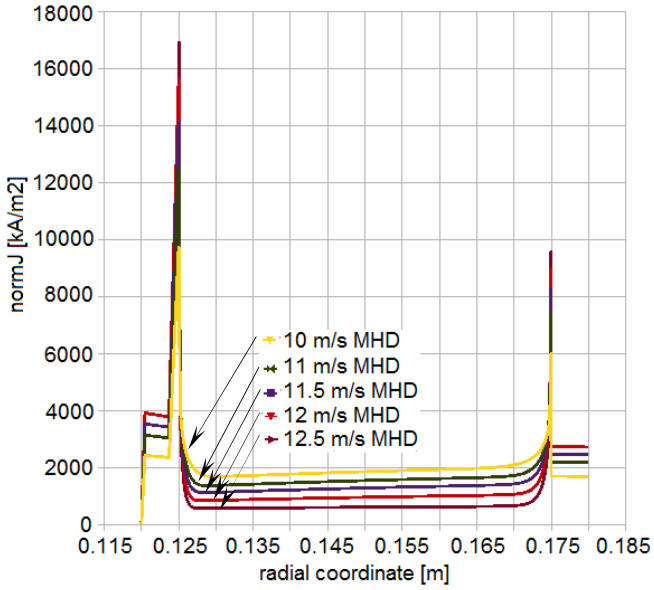

Fig. 6.41 Profile of the norm of the current density at radial path "1.5m" including the metallic walls, for the mean velocities 10, 11, 11.5, 12, 12.5 m/s, MHD model

C) Radial profile of axial force density

The axial force density along the radial path "1.5m" is presented in Fig. 6.42a). A zoom of the profile along the first millimeter of the radial path starting with the interior wall is presented in Fig. 6.42b).

In the boundary layer the force density increases as the velocity increases. In the bulk region it can be seen that the force density has an important decay with respect to the values near the walls. The ratio between the two values is 30 in the case of 12.5 m/s sodium velocity.

Table X presents the values of the Hartmann layer thickness, the layer next to the walls that delimits the very high forces with respect to the forces in the bulk region of the channel. The thickness of the Hartmann layer is calculated with expression (6.8) where B_0 is considered as the mean value of the magnetic flux density module in the sodium channel.

The thickness of the layer in which the force density decreases from maximum, next to the wall, to the quasi-constant value along the bulk region of the channel, is 3 to 4 times larger than the Hartmann layer, namely in the range 0.2 mm - 0.33 mm for the velocity range 4 m/s – 12.5 m/s.

Table X. Hartmann layer thickness for different sodium means velocity

Mean velocity	B_0	Hartmann layer thickness
m/s	mT	mm
4	66.06	0.1189
10	98.35	0.0798
11	120	0.0654
11.5	132.13	0.0594
12	143.87	0.0546
12.5	154.55	0.0508

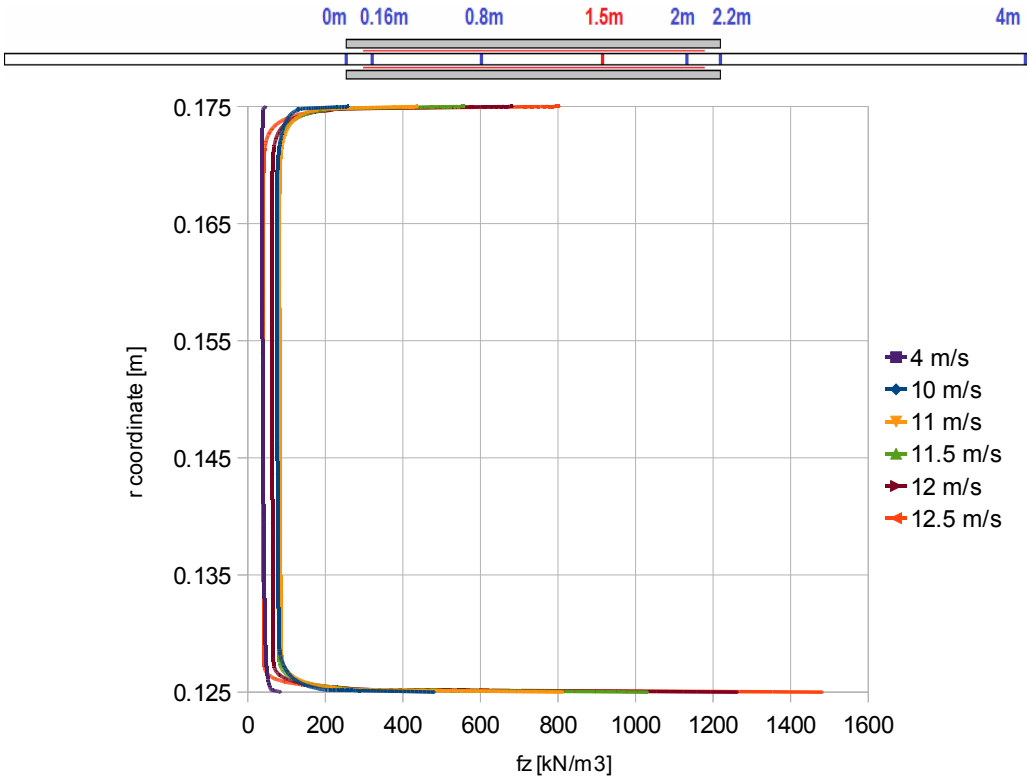

a)

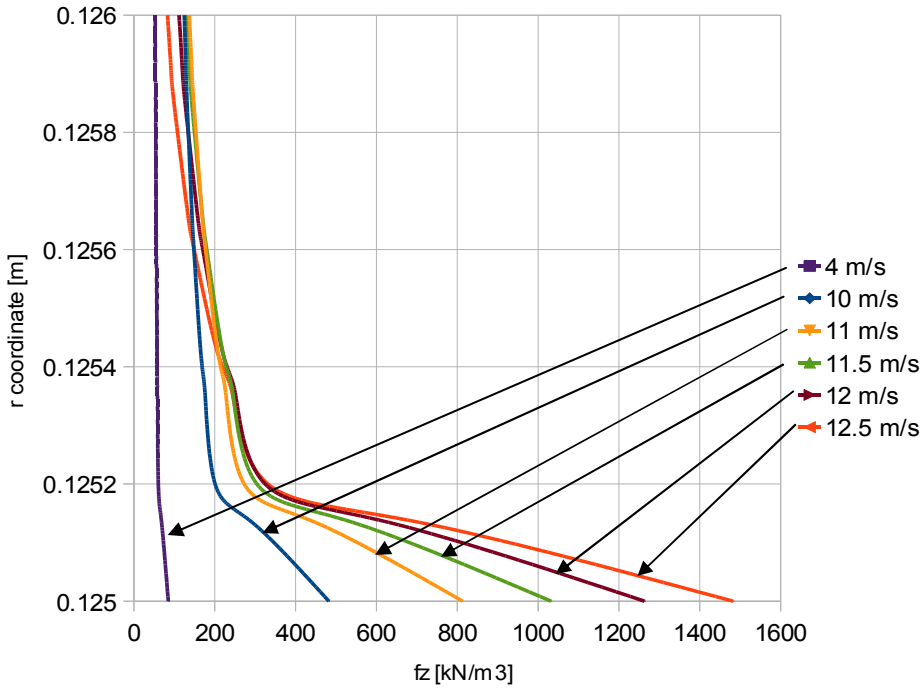

Fig. 6.42 Axial force density profiles at radial path "1.5m" for the MHD model
a) entire channel width, b) zoom close to the INTERIOR wall

The radial profiles of the axial force density at radial path "1.5m" resulting form applications solved in the bloc – pumping hypothesis show the strong expulsion of currents and forces to the walls. This expulsion being a result of the flow in

magnetic field, by default it can not result out of a purely electromagnetic calculation. Fig. 6.43 presents for various sodium velocities the radial profile of the axial force density in block –pumping hypothesis.

The inclination of the curves is in the greatest extent due to the electromagnetic structure of the pump with double-sided inductor that generates higher currents and forces near the interior wall of the channel than at the exterior wall.

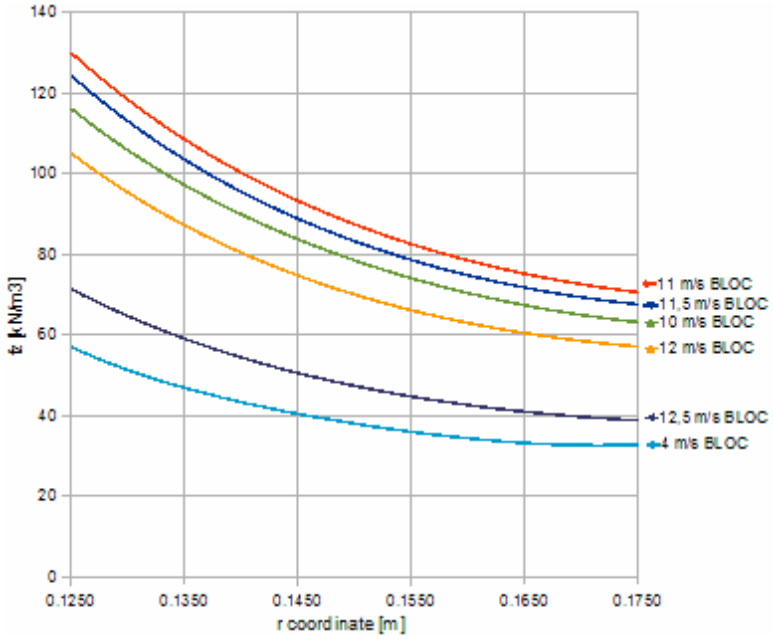

Fig. 6.43 Axial force density profiles at radial path "1.5m" for the BLOC model

The comparison between radial profiles of axial force density corresponding to the two computation hypothesis block – pumping and MHD coupling are more clearly presented in Figs. 6.44-6.45 for the sodium velocities 4 and 10 m/s.

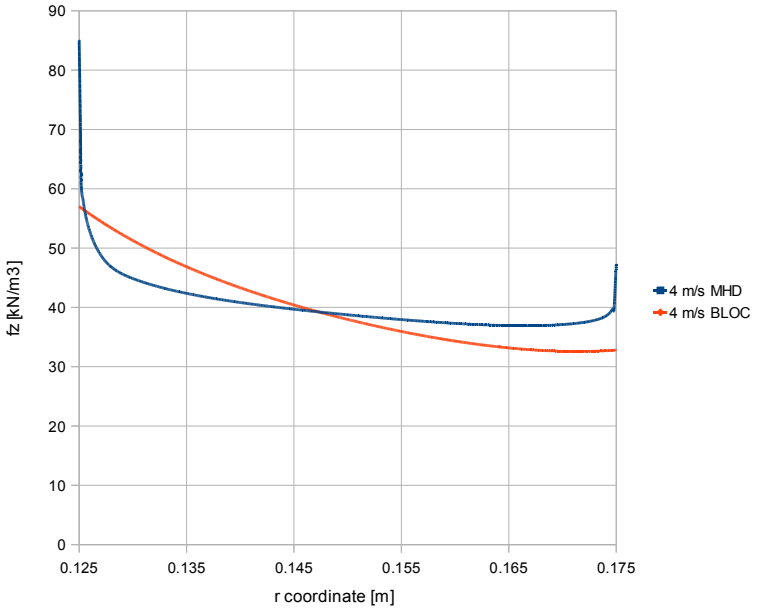

Fig. 6.44 Comparison between the axial force profiles at mean velocity 4 m/s given by the MHD and BLOC models

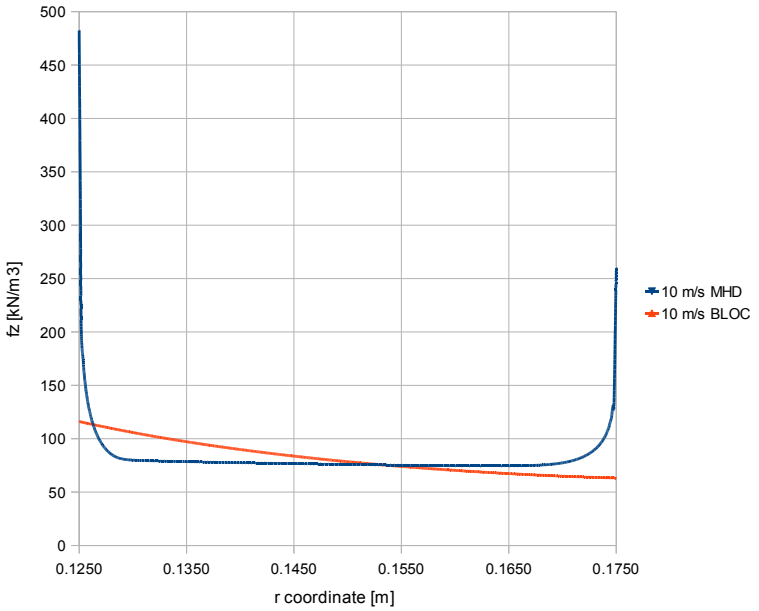

Fig. 6.45 Comparison between the axial force profiles at mean velocity 10 m/s given by the MHD and BLOC models

The axial force density is integrated along the radial path for three cases, Figs. 6.47-6.49, for the sodium velocities 4 m/s, 10 m/s and 12.5 m/s – MHD coupling and block–pumping hypotheses, the values of the line integrals of axial force density along radial paths located at various longitudinal coordinates along the pump. The principal longitudinal coordinates used in the figures are given in Fig. 6.46.

In order to choose some radial paths in the most important places along the channel, the representation of the axial force density along the middle longitudinal path is used, Fig. 6.46. The chosen radial paths are called “0m”, “0.16m”, “0.8m”, “1.5m”, “2m”, “2.2m” and “4m” and these names correspond also with the axial coordinate of the radial path.

- at “0m” represents the inlet of the pump; more or less the place where the sodium enters in the electromagnetic field
- at “0.16” is the place where for all high flow rates we observe the maximum negative force with respect to the pump inlet
- at “0.8m” is the place from where for any flow rate the breaking entry effect is ended
- at “1.5m” there is an intermediary position; for some flow rates it can be approximated with the stabilized force
- at “2m” represents a place very close to exiting the magnetic field
- at “2.2m” is the homolog of “0m”, place of maximum breaking effect with respect to the pump outlet
- at “4m” is the furthest position available in the computation domain to check the recovering of the turbulent flow profile.

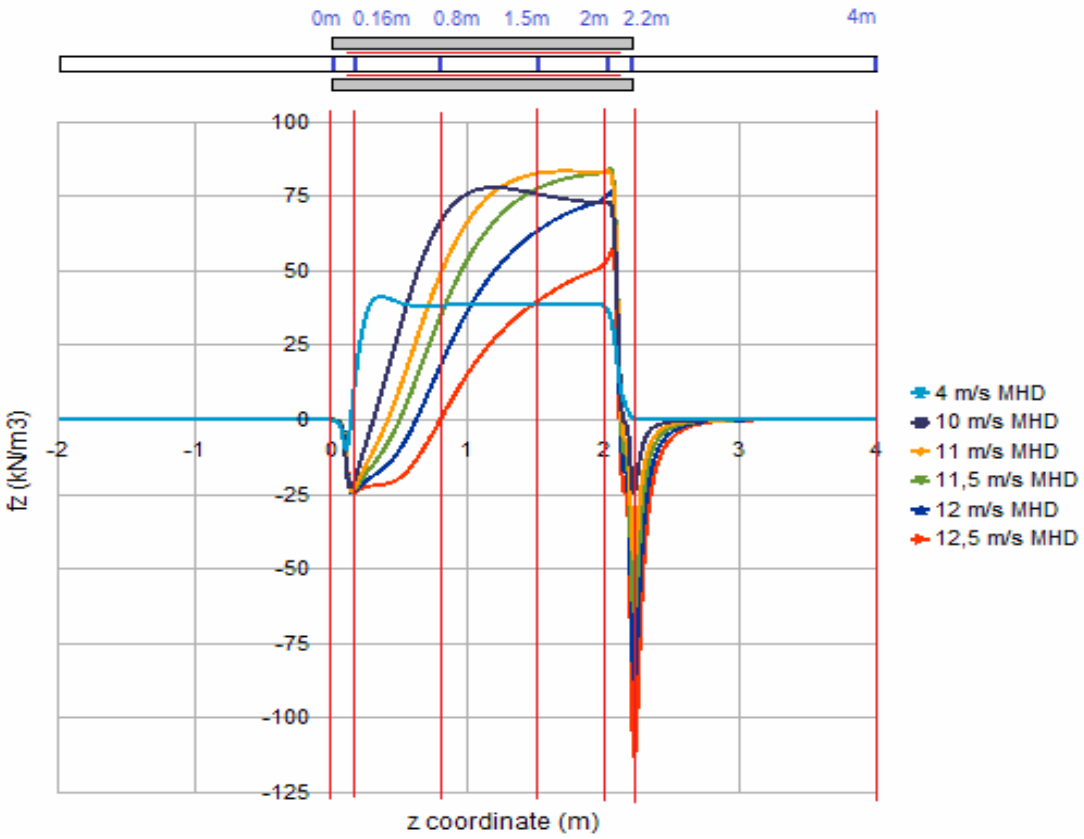

Fig. 6.46 Choosing the most significant radial path to describe the flow

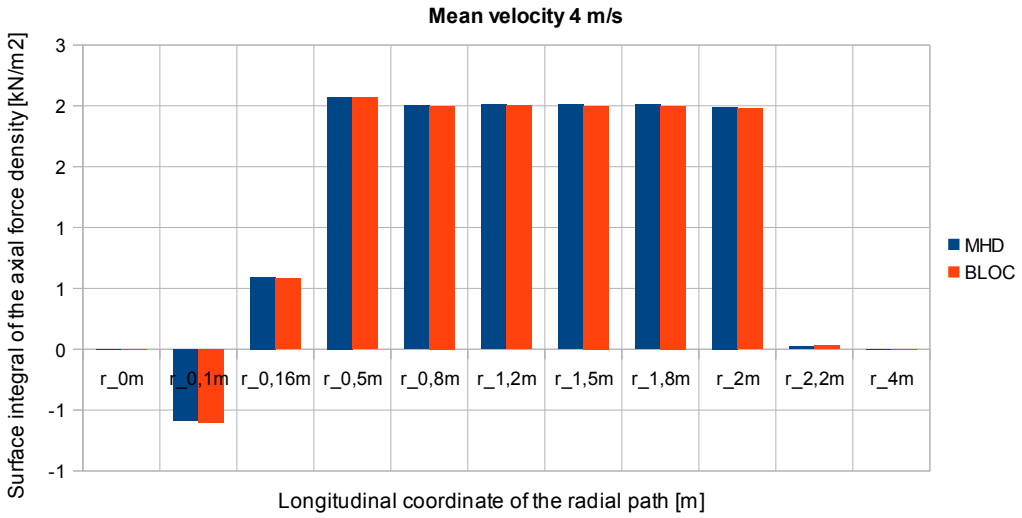

Fig. 6.47 Surface integral of the axial force density at different radial paths in BLOC_PUMPING and MHD coupling hypotheses for sodium mean velocity 4 m/s

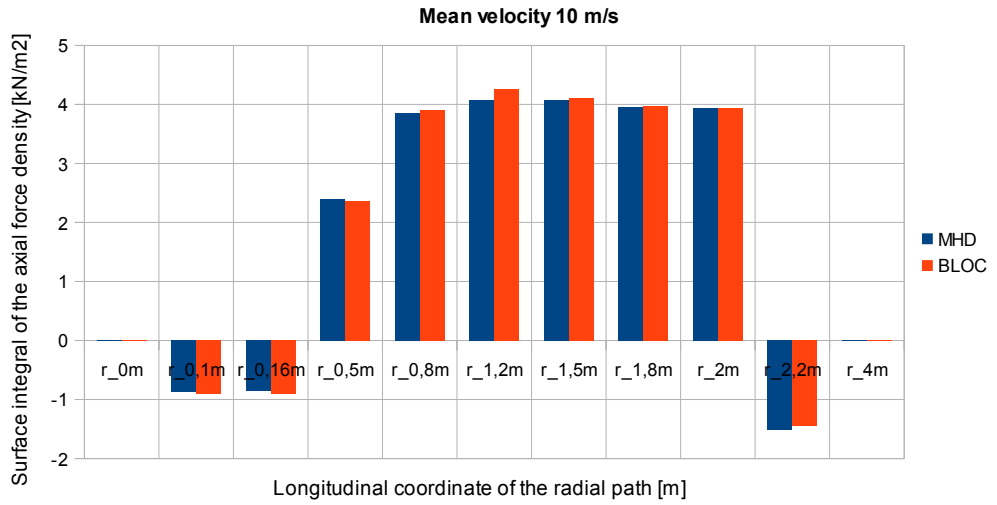

Fig. 6.48 Surface integral of the axial force density at different radial paths in BLOC_PUMPING and MHD coupling hypotheses for sodium mean velocity 10 m/s

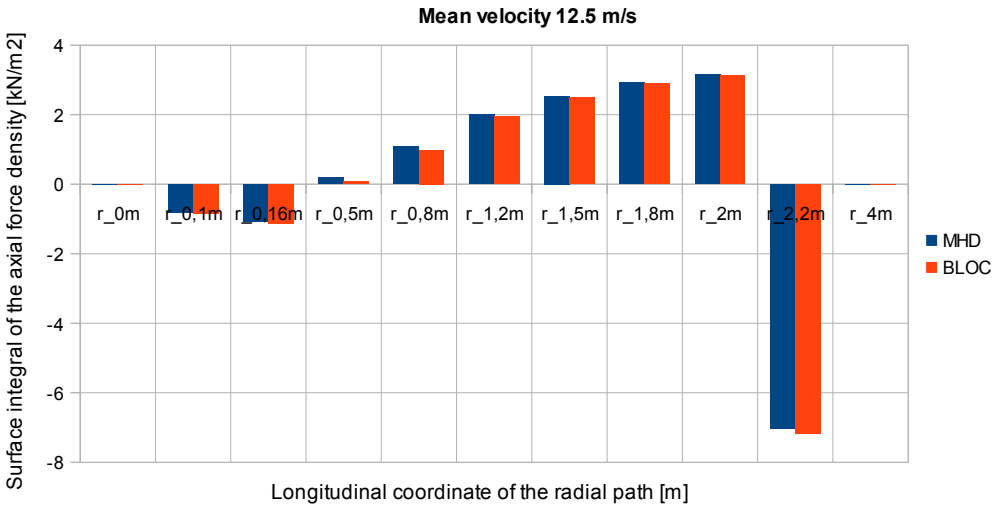

Fig. 6.49 Surface integral of the axial force density at different radial paths in BLOC_PUMPING and MHD coupling hypotheses for sodium mean velocity 12.5 m/s

As it is observed, the integral values of the axial force density calculated in both hypotheses are close for any radial path and for any velocity. This fact leads to the conclusion that the two hypotheses have similar accuracies with respect to the global quantity electromagnetic force. The conclusion is confirmed by Fig. 6.50 which represents the electromagnetic pressure, respectively the volume integral of the electromagnetic force density divided to the area of the flow section, corresponding to block – pumping assumption – red curve and to MHD coupling hypothesis – blue curve. Fig. 6.50 contains also the dependence of the hydrodynamic pressure on sodium velocity. This curve is a hydrodynamic result of the MHD coupled model and show that the pumping capacities are well enough approximated only by the coupled model that takes into account the hydrodynamic losses.

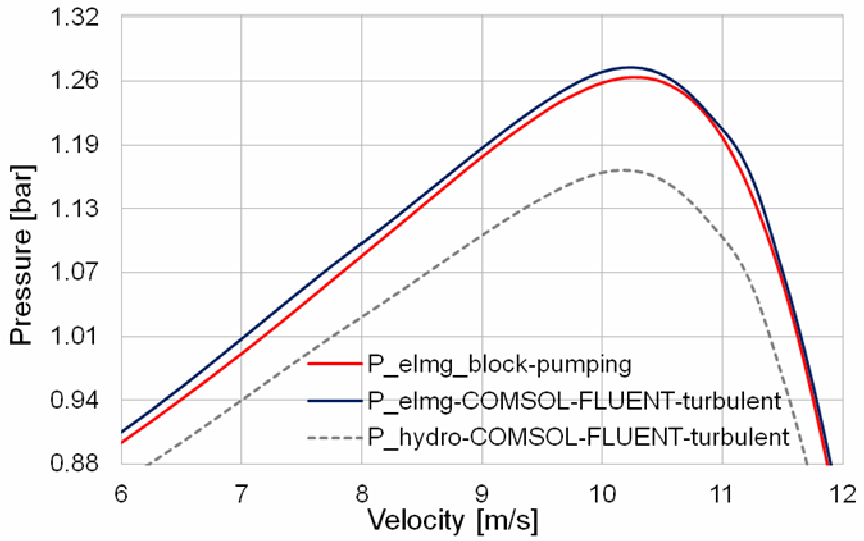

Fig. 6.50 Approximations of the Pressure – Velocity characteristic of PEMDYN obtained by coupled COMSOL-FLUENT turbulent model and block-pumping hypothesis

Figs. 6.42a) and 6.42b) present the force density profile at radial path "1.5m". Force profiles corresponding to other radial paths and sodium velocities are given in Figs. 6.51 – 6.54. Figs. 6.51a) and 6.54a) present the force profiles at the pump inlet and outlet. It can be observed that at both ends that the negative force increase as the sodium velocity increases. The negative forces are much higher at the inlet than at the outlet. The maximum negative force at radial path "2.2m" at 12.5 m/s is 20 times higher than the maximum negative force corresponding to the radial path "0.16m" at the same sodium velocity. Also it can be observed that at very low sodium velocities the force profiles are positive on the entire radial path situated anywhere along the pump.

Figs. 6.52, 6.53 and 6.42 which express the variation of the force profile along the pump for various sodium velocities, show that the non-uniformity of the force radial distribution, namely the Hartmann effect of expulsion of the force towards the walls, is increasing in two situations: as the liquid travels between inlet and outlet for a given sodium velocity and as the sodium velocity increases.

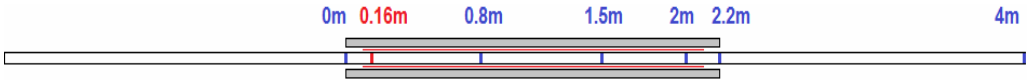

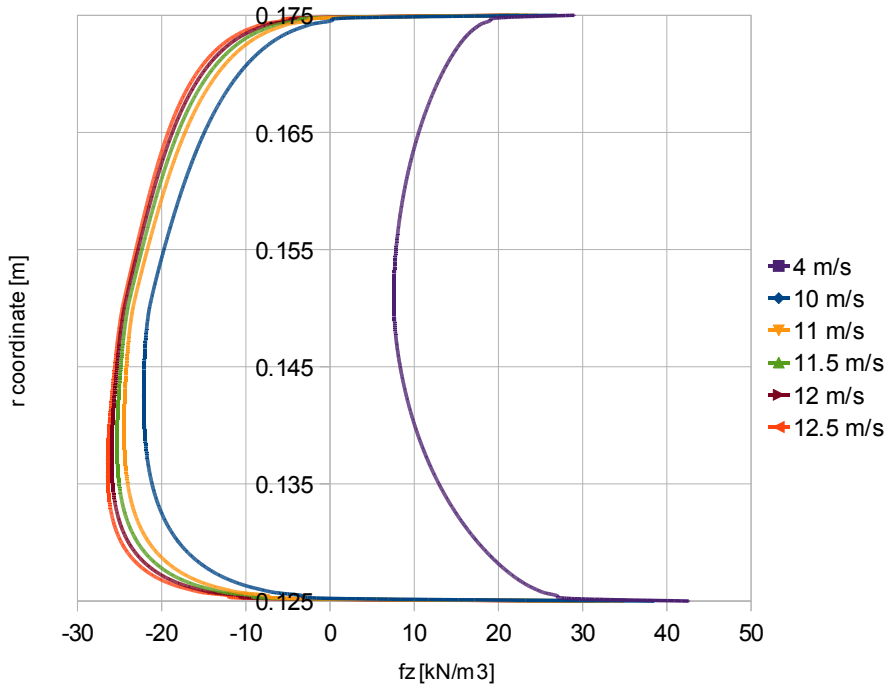

a)

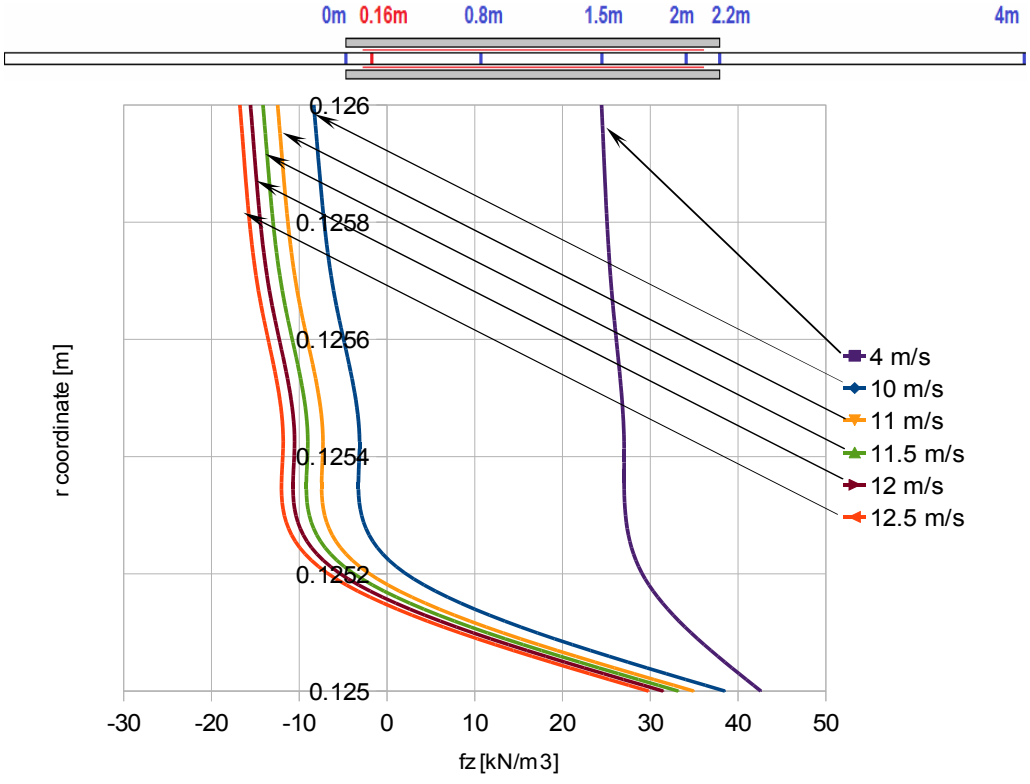

b)

Fig. 6.51 Axial force density profile at radial path "0.16m" for different flows, a) entire channel width, b) zoom near the interior wall

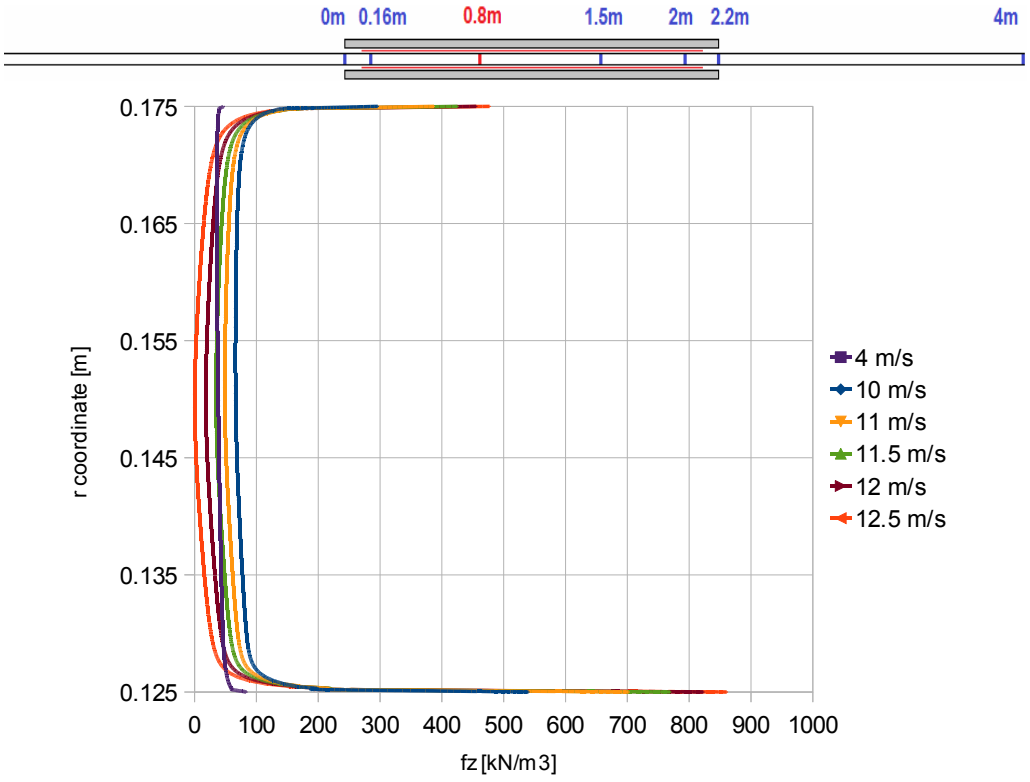

a)

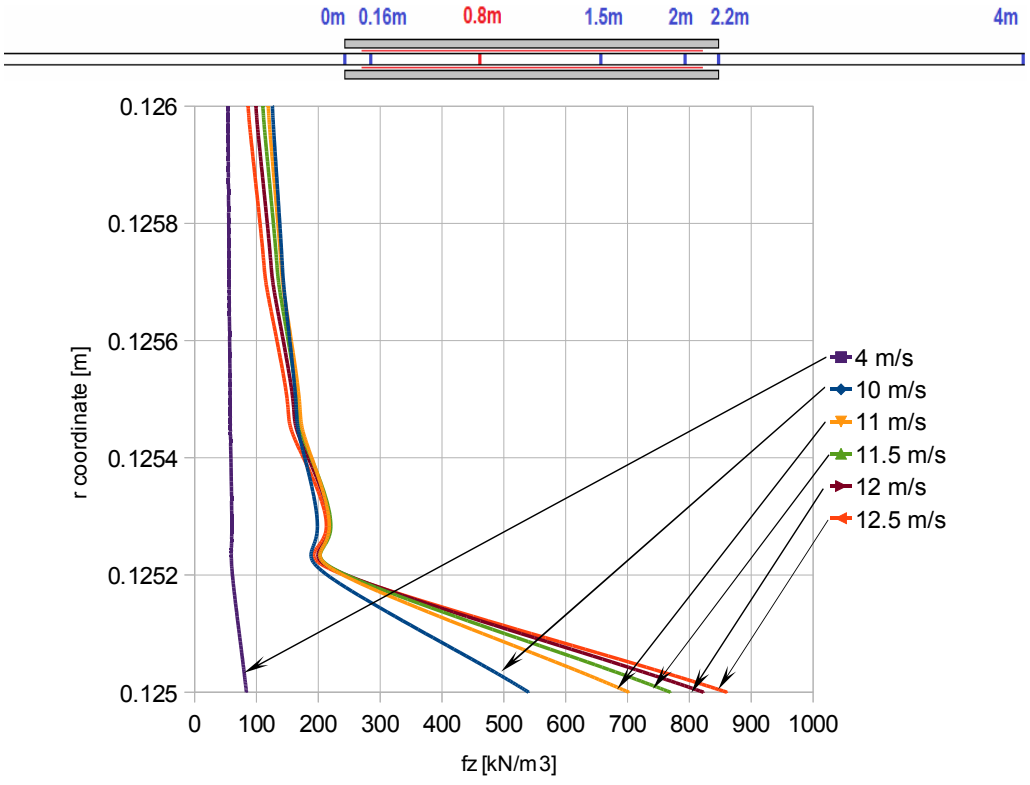

b)

Fig. 6.52b) Axial force density profile at radial path "0.8m" for different flows, MHD model; a) entire channel width, b) zoom near the interior wall

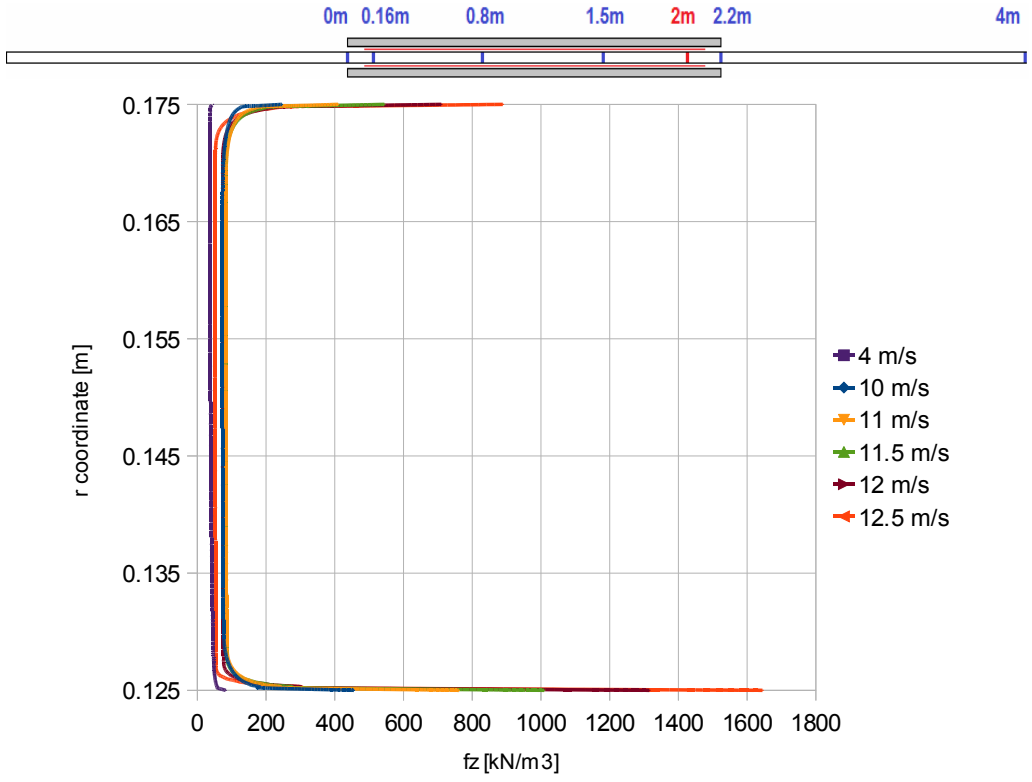

a)

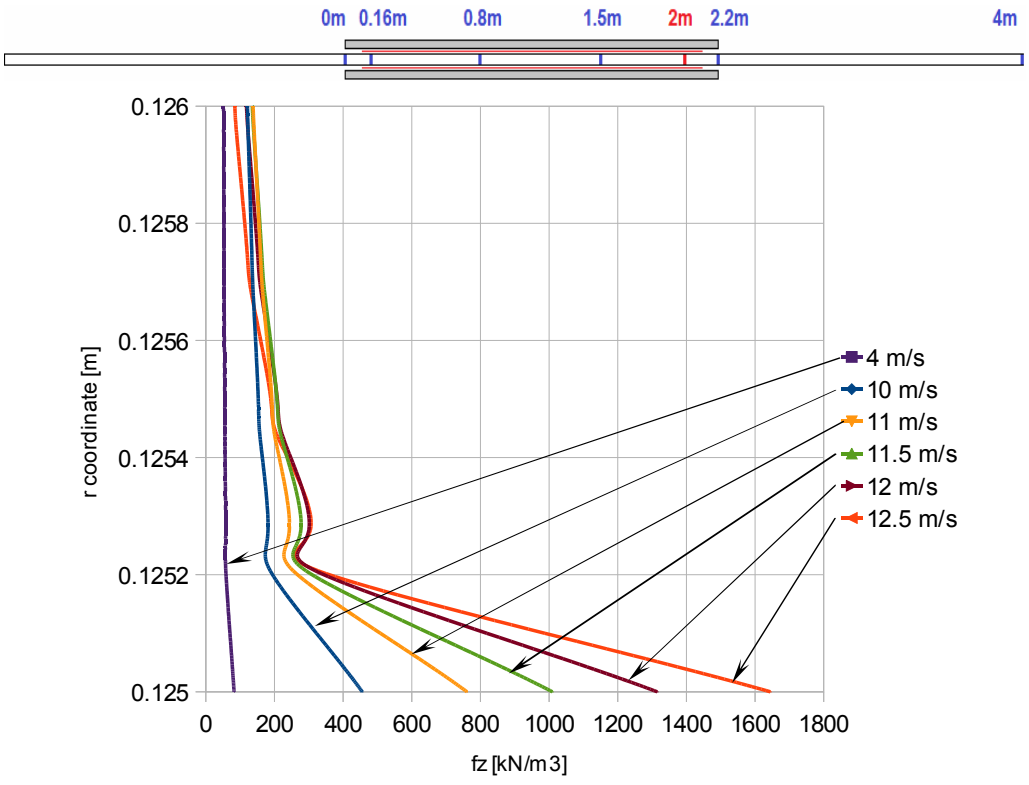

b)

Fig. 6.53 Axial force density profile at radial path "2m" for different flows, MHD model, a) entire channel width, b) zoom near the interior wall

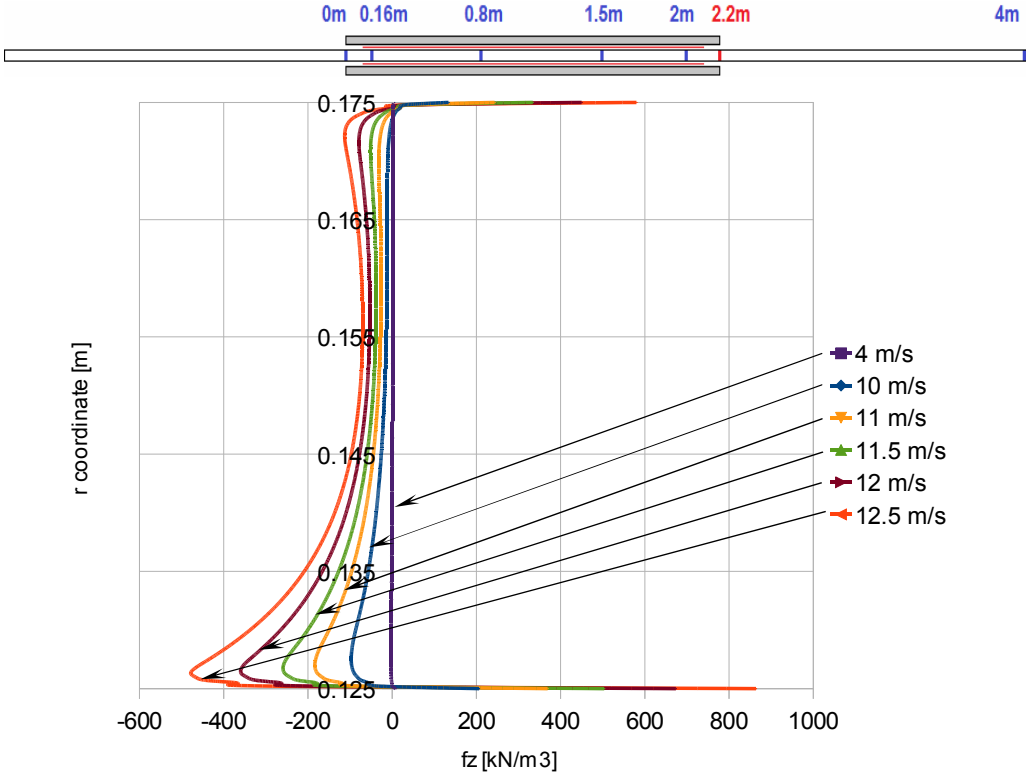

a)

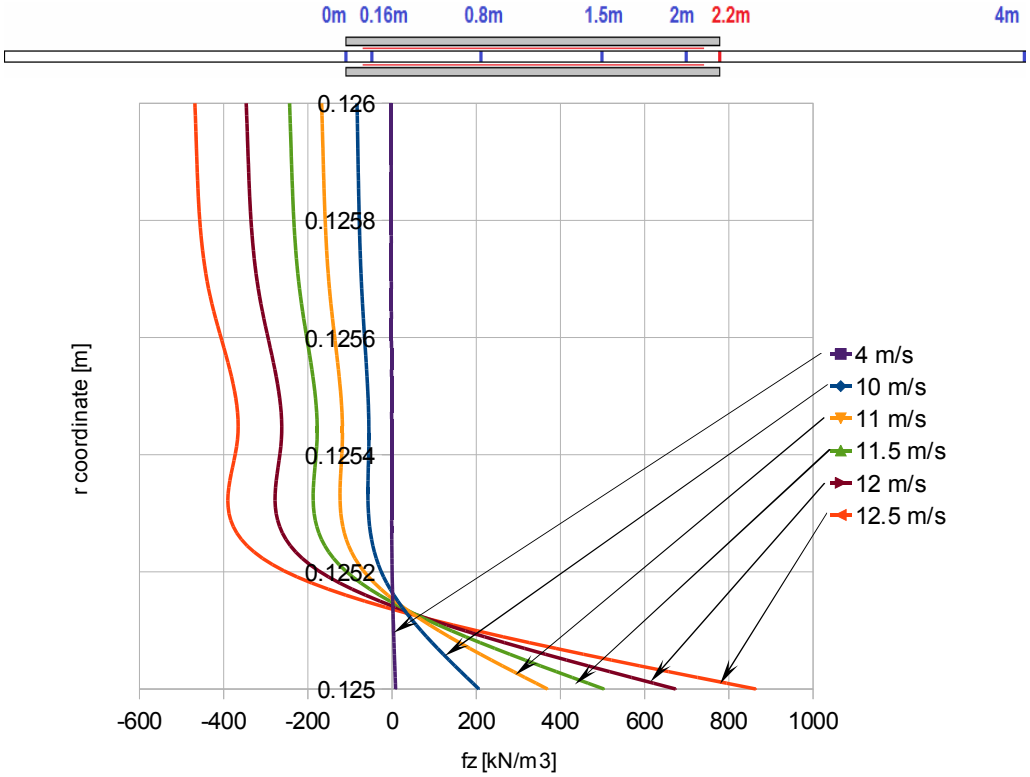

b)

Fig. 6.54 Axial force density profile at radial path "2.2m" for different flows, MHD model, a) entire channel width, b) zoom near the interior wall

D) Radial profile of velocity

Figs. 6.55 – 6.59 present the variation of the velocity profile at different radial paths along the pump for various sodium velocities. Fig. 6.55 presents the velocity profiles at radial path "0.16m", where the profiles corresponding to high sodium velocities are slightly modified from a standard turbulent profile. Yet, the velocity profile for 4 m/s is more affected by the negative forces.

It is observed that under the influence of the electromagnetic field the profile is flattening both at low and high sodium mean velocities. Another aspect to mention is that the tilting effect of the unequal force density near the two walls is gradually diminished as the sodium velocity increases.

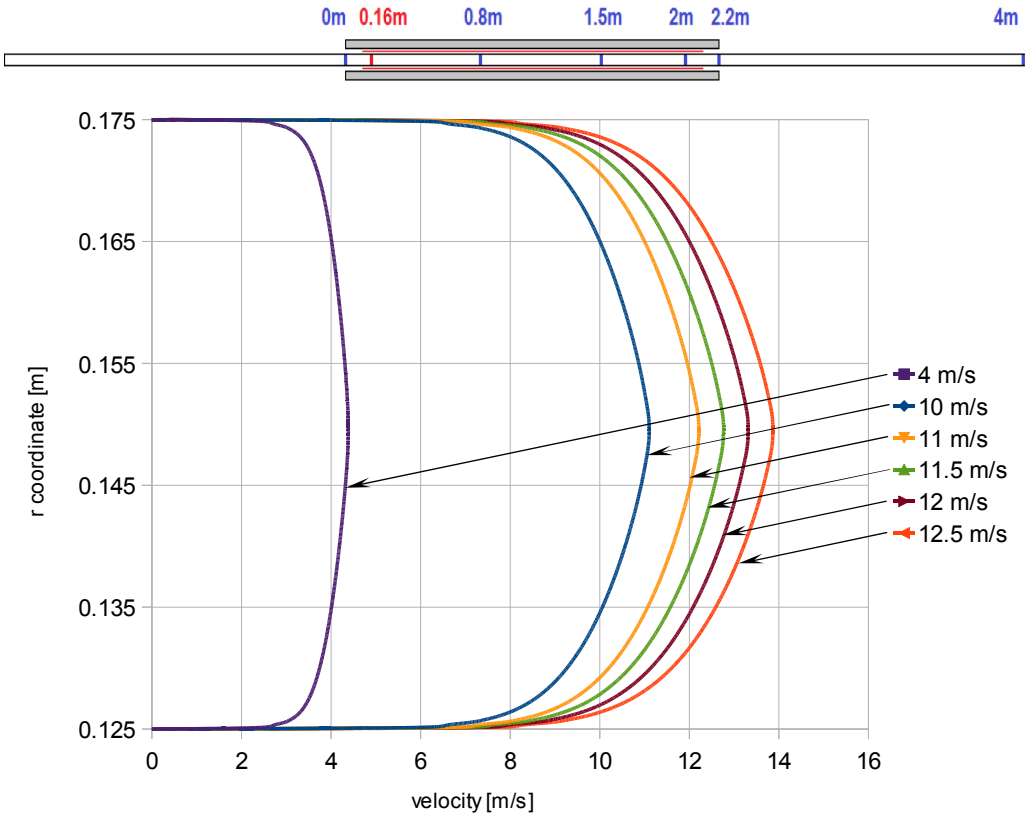

Fig. 6.55 Velocity profiles at radial path "0.16m" at different flows, MHD model

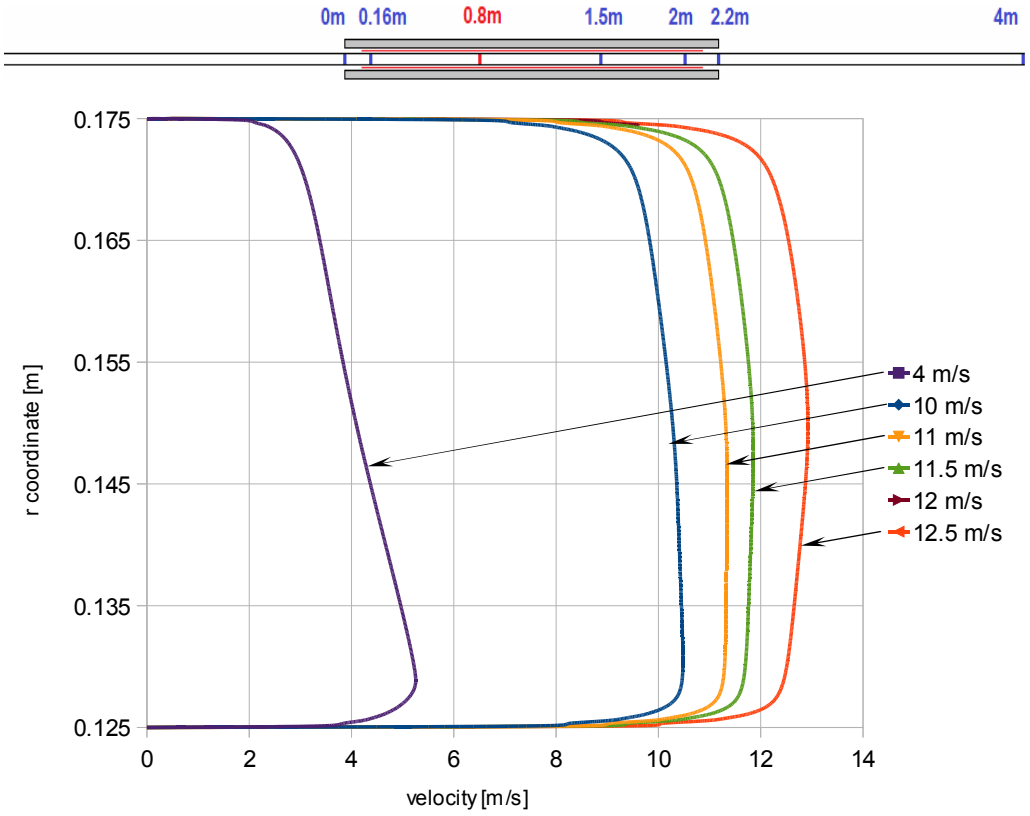

Fig. 6.56 Velocity profiles at radial path "0.8m" at different flows, MHD model

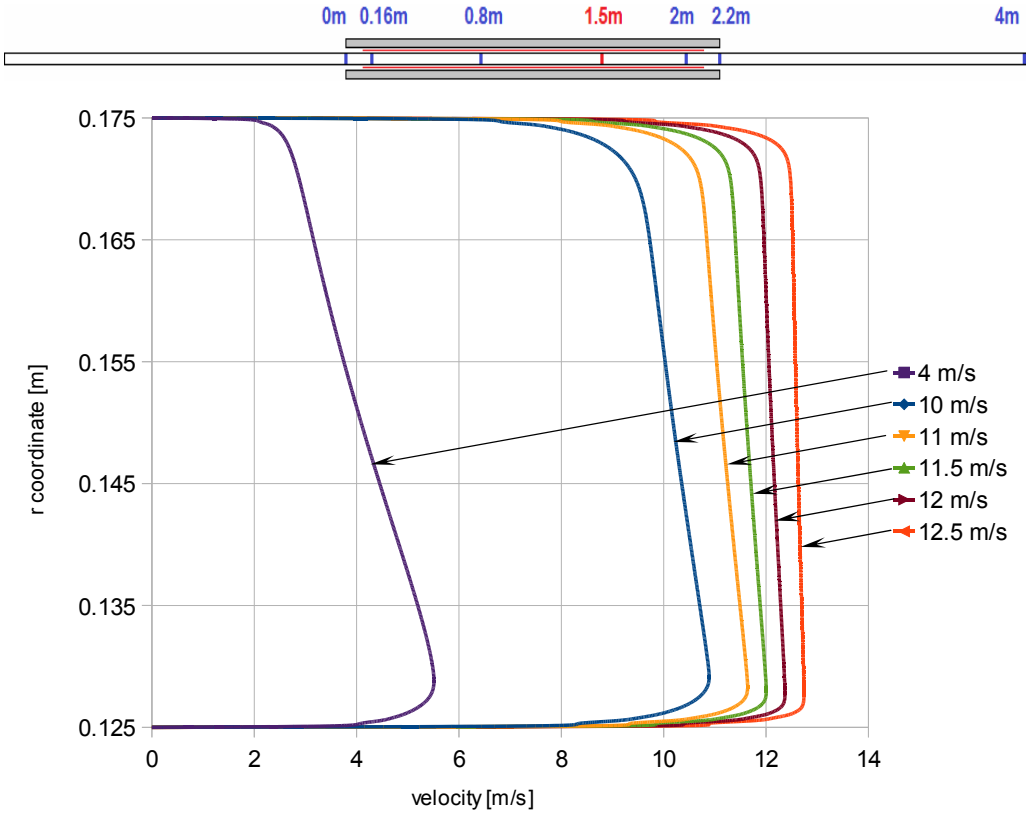

Fig. 6.57 Velocity profiles at radial path "1.5m" at different flows, MHD model

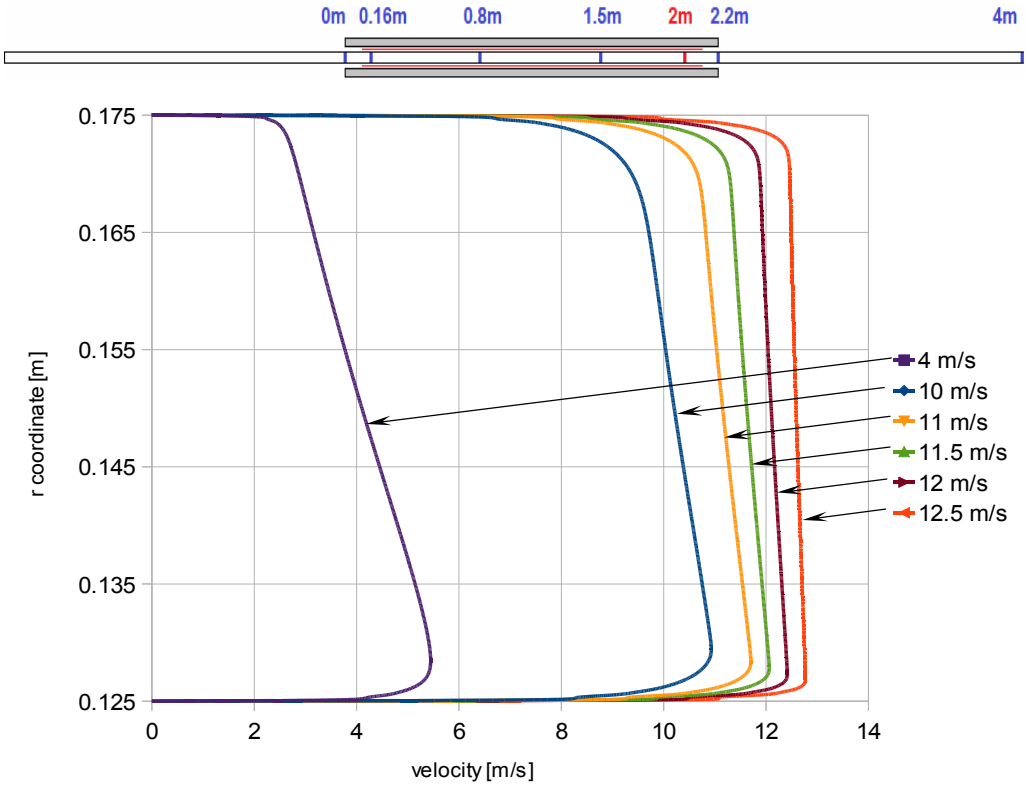

Fig. 6.58 Velocity profiles at radial path "2m" at different flows, MHD model

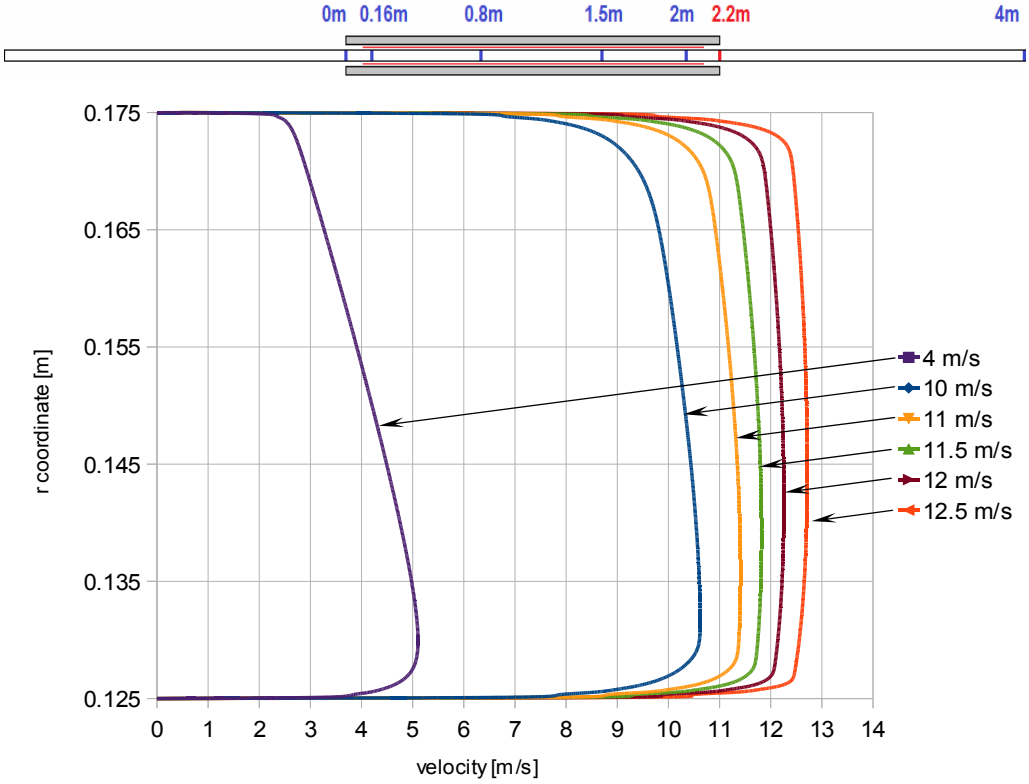

Fig. 6.59 Velocity profiles at radial path "2.2m" at different flows, MHD model

6.2.6 Comparative characterization of the MHD interaction with respect to two very different sodium velocities

The results presented in paragraphs 6.2.3 and 6.2.4 are focused on describing the effects of the MHD interaction developed along the longitudinal and radial directions. This paragraph is a detailed comparison of the pump behavior at low and high sodium velocities. For this purpose, various field quantities are presented for two very different velocities, 4 m/s and 11 m/s. Thus, this study can have practical and theoretical interests: it characterizes the internal behavior of the pump when the sodium happens to flow with low velocities, respectively velocities belonging to the ascendant branch and draws a parallel with respect to the intensity of the MHD interaction in the two cases.

A) Color map of axial velocity

Figs. 6.60 and 6.61 present the axial velocity field distribution in the cases of low, respectively high sodium velocity. The two graphic representations verify the velocity profiles given in Figs. 6.55 - 6.59. If it is to refer only to the bulk region of the channel, namely to exclude the two limit layers, it is observed that at high sodium velocities the velocity profile is quasi-uniform in comparison with the profile at low sodium velocities as a result of a more intense MHD interaction due to high velocities.

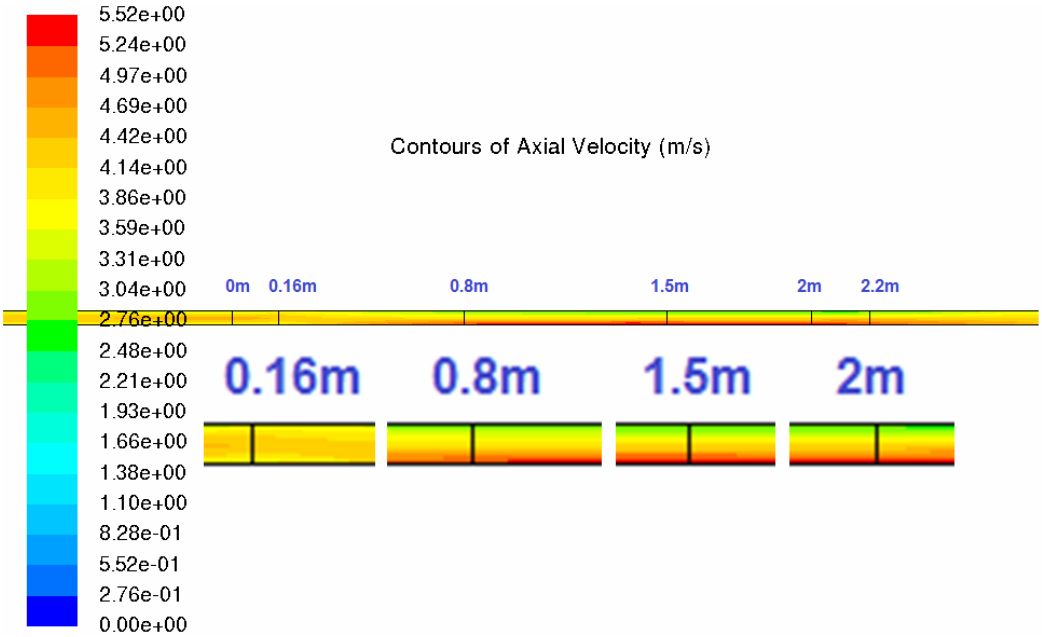

Fig. 6.60 The velocity field for sodium velocity 4m/s

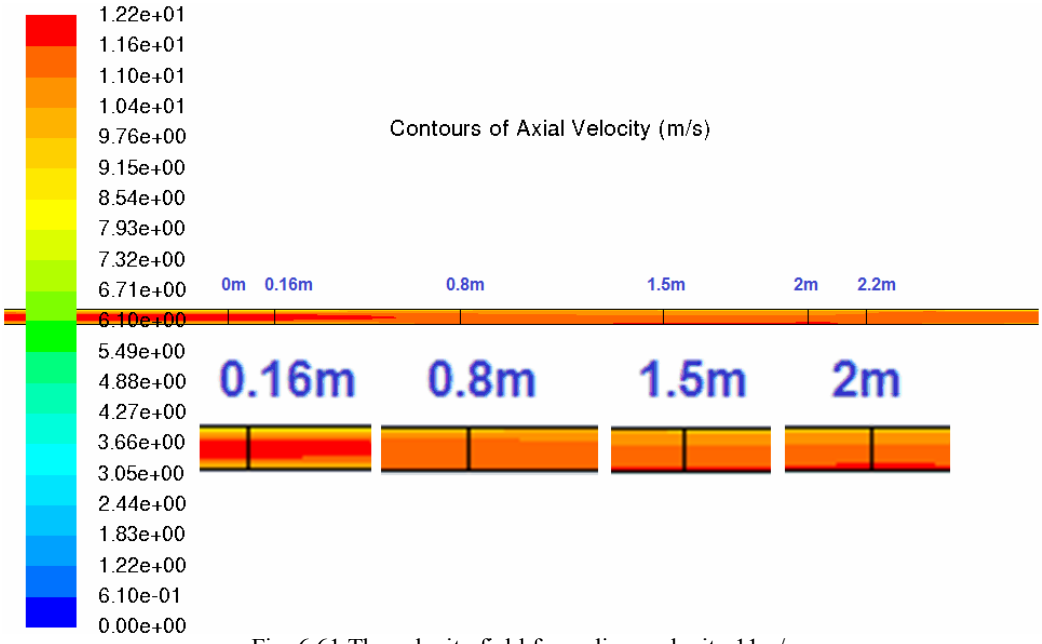

Fig. 6.61 The velocity field for sodium velocity 11m/s

B) Velocity profile variation along the channel

The variations of the velocity profile along the channel for the two cases of low and high sodium velocity are given in Figs. 6.62 and 6.63. The two representations are images for the intensity and effects of MHD interaction, separately in the two cases.

Fig. 6.62a) shows that the radical change of the velocity profile is occurring between paths “0.16m” and “0.8m”. Thus it can be said that the at sodium velocity 4 m/s the Hartmann profile is established approximately after 0.8 m from pump inlet. The velocity profile corresponding to radial path “4m” is similar to that corresponding to “0m”. This means that to recover the standard turbulent profile after the pump outlet it is needed a distance of approximately 2 m. This fact is valid for high sodium velocities also.

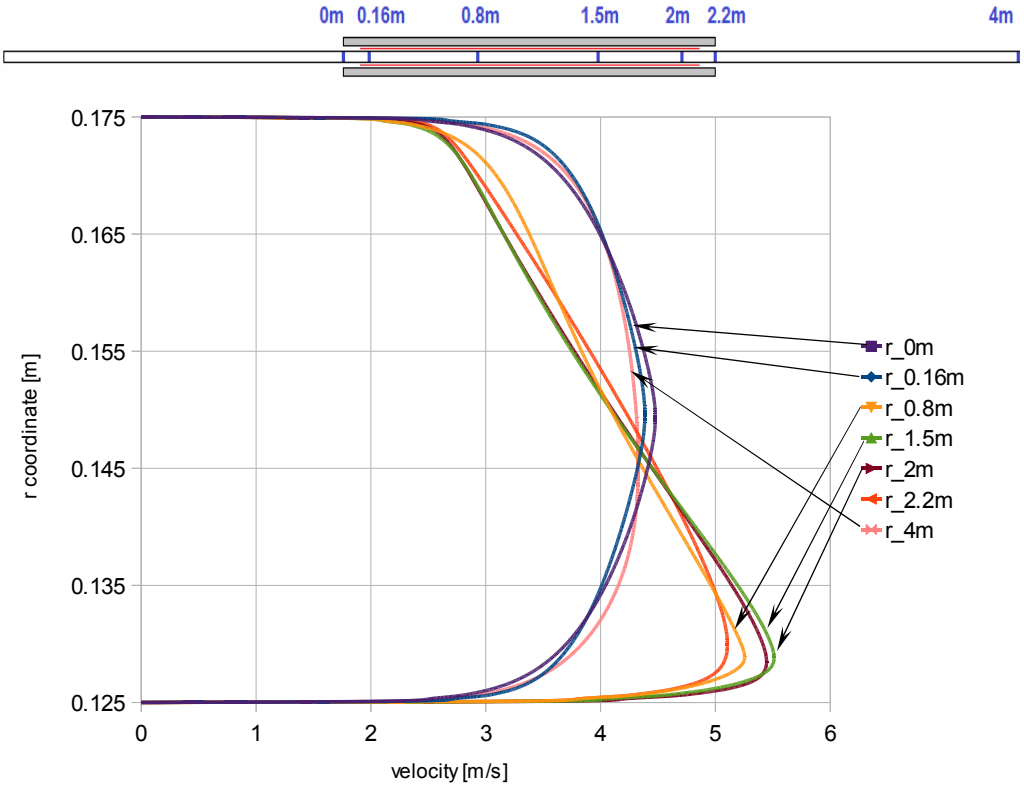

a)

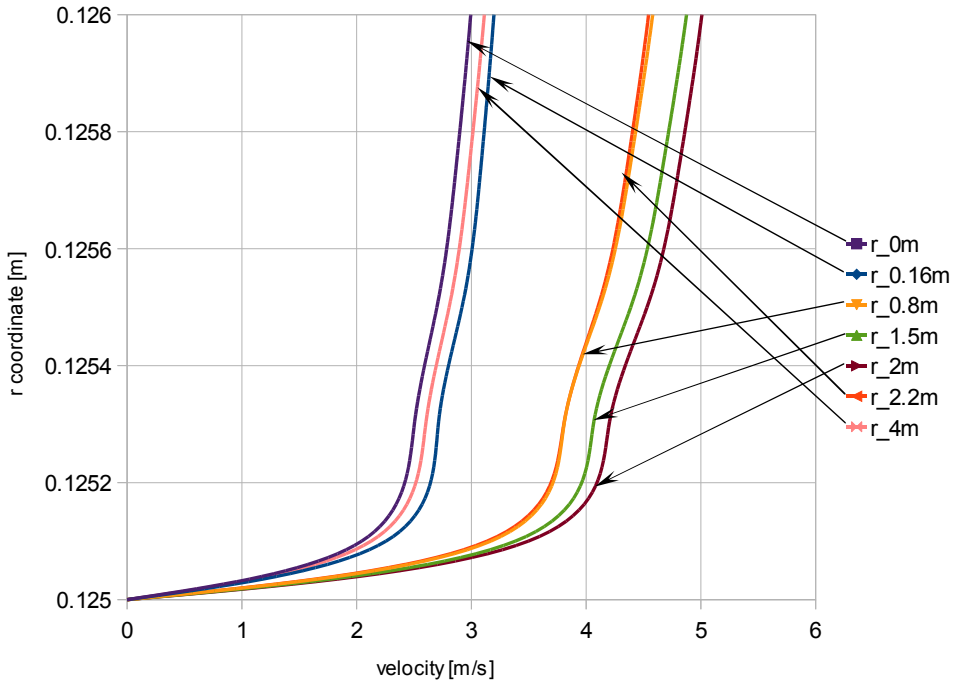

b)

Fig. 6.62 Velocity profiles at different radial paths along the pump, sodium velocity 4 m/s, a) entire channel width, b) zoom near the interior wall

The major difference between cases with low and high sodium velocity with respect to velocity profile variation along the pump consists in the inclination of the flat region of the profile, Fig. 6.63.

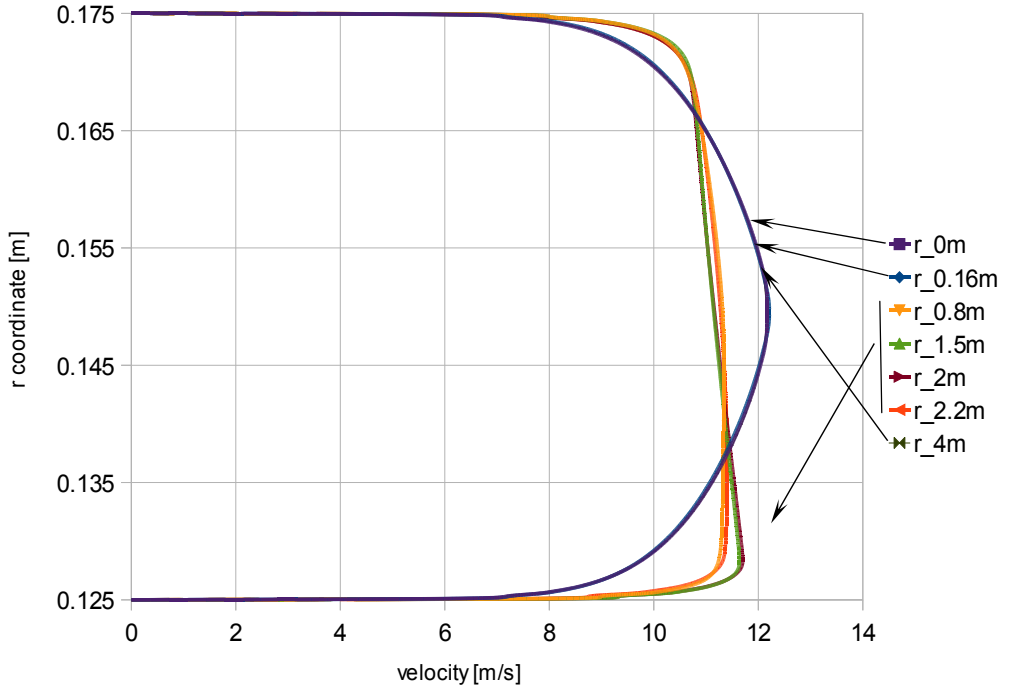

a)

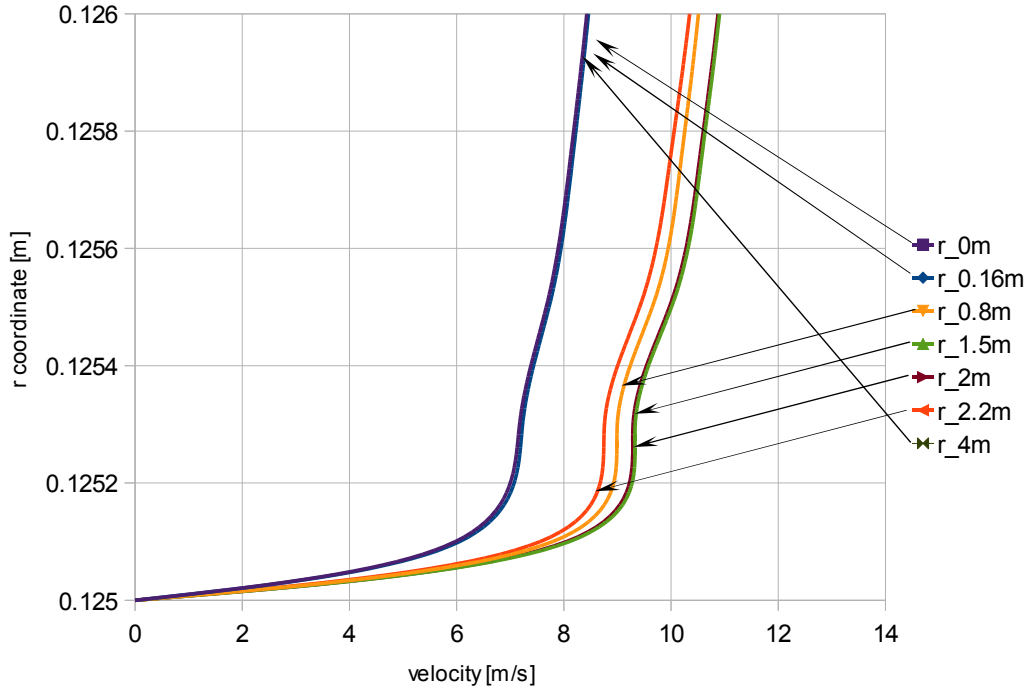

b)

Fig. 6.63 Velocity profiles at different radial paths along the pump, sodium velocity 11m/s, a) entire channel width, b) zoom near the interior wall

C) Force profile evolution along the channel

Figs. 6.64 and 6.65 present the variation of the force profile along the pump specific to low sodium velocities, respectively high sodium velocities. At sodium velocity 4 m/s it can be observed that at pump inlet, respectively path "0m" the force is null, the integral force increases along the pump and at the outlet the integral value is again close to zero.

For sodium velocity 11 m/s, Fig. 6.65, it can be observed that from inlet until path "0.16m" the force profile is negative and then it becomes positive until the pump outlet.

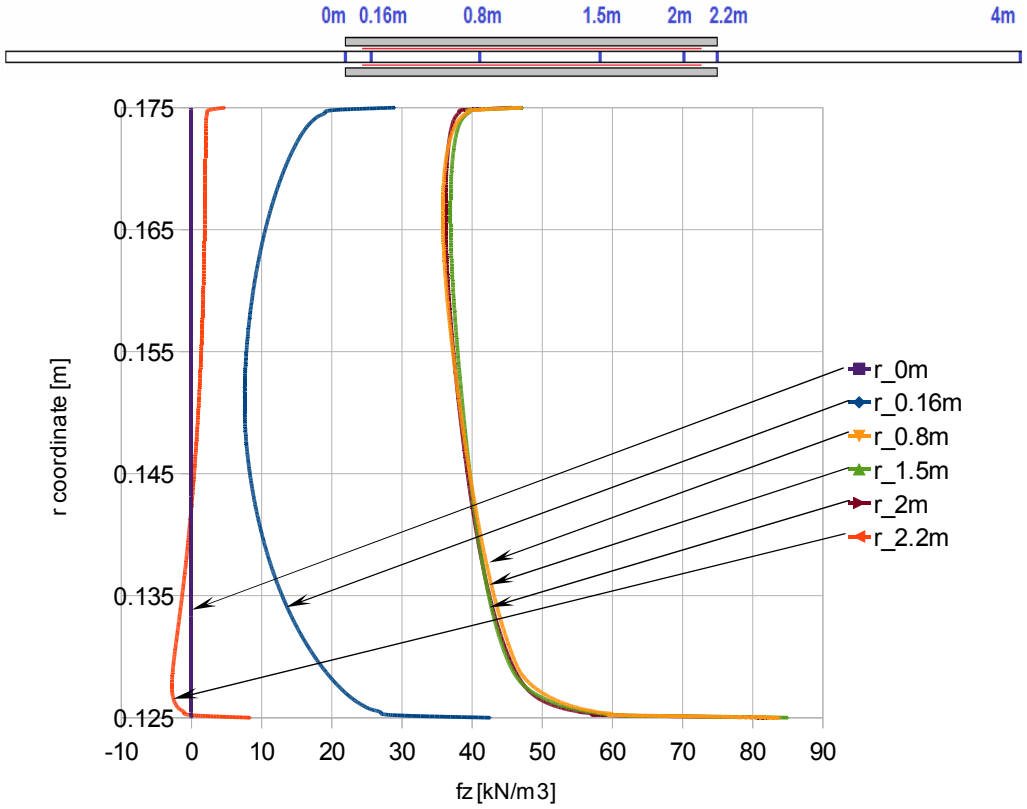

Fig. 6.64 a) Force profiles at different radial paths along the channel, sodium velocity 4 m/s

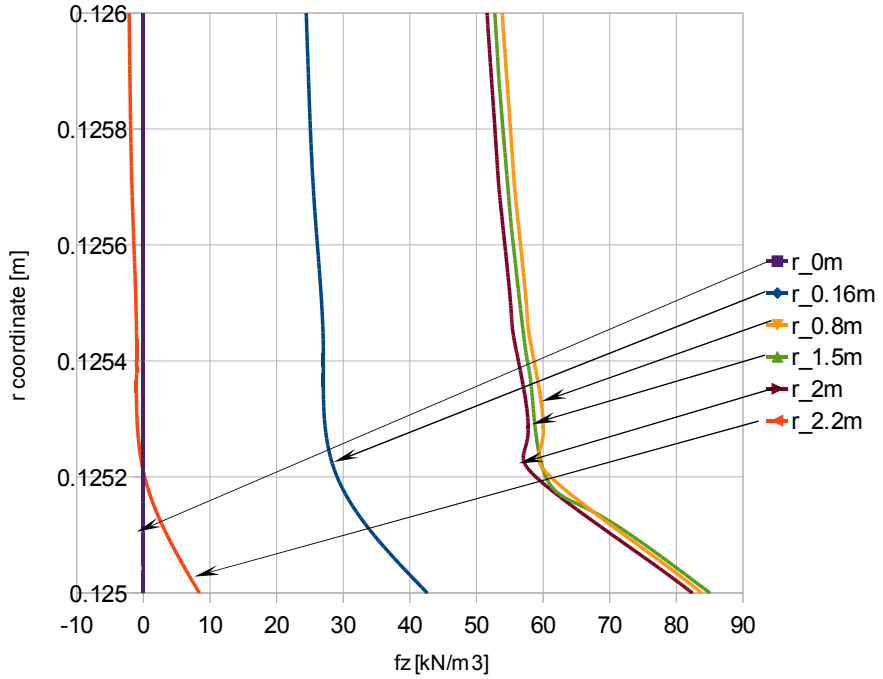

Fig. 6.64 b) Force profiles at different radial paths along the channel, sodium velocity 4 m/s – zoom near the interior wall

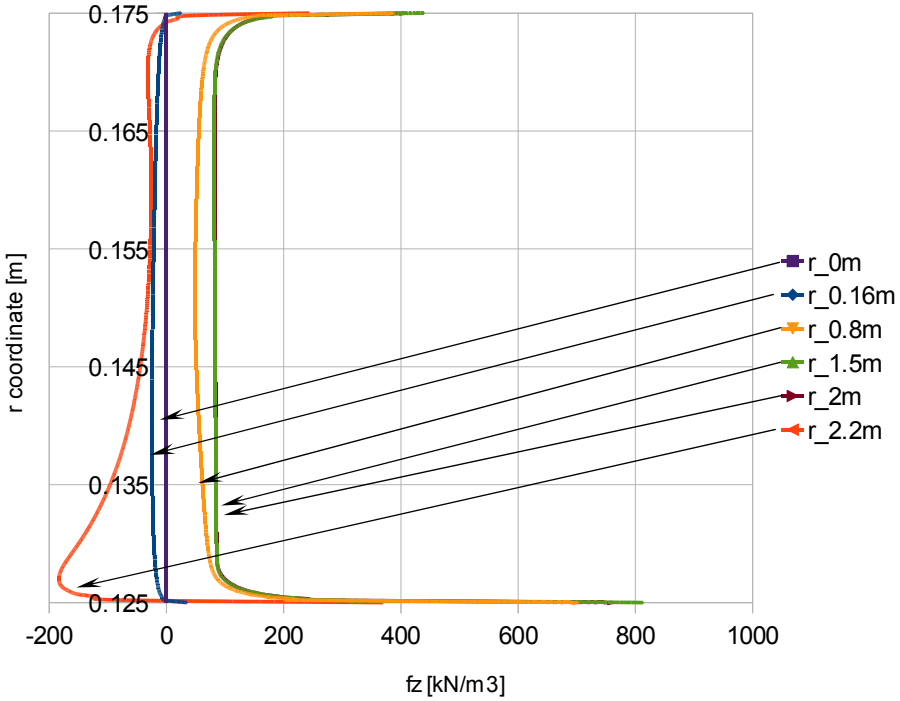

Fig. 6.65 a) Force profiles at different radial paths along the channel, sodium velocity 11m/s

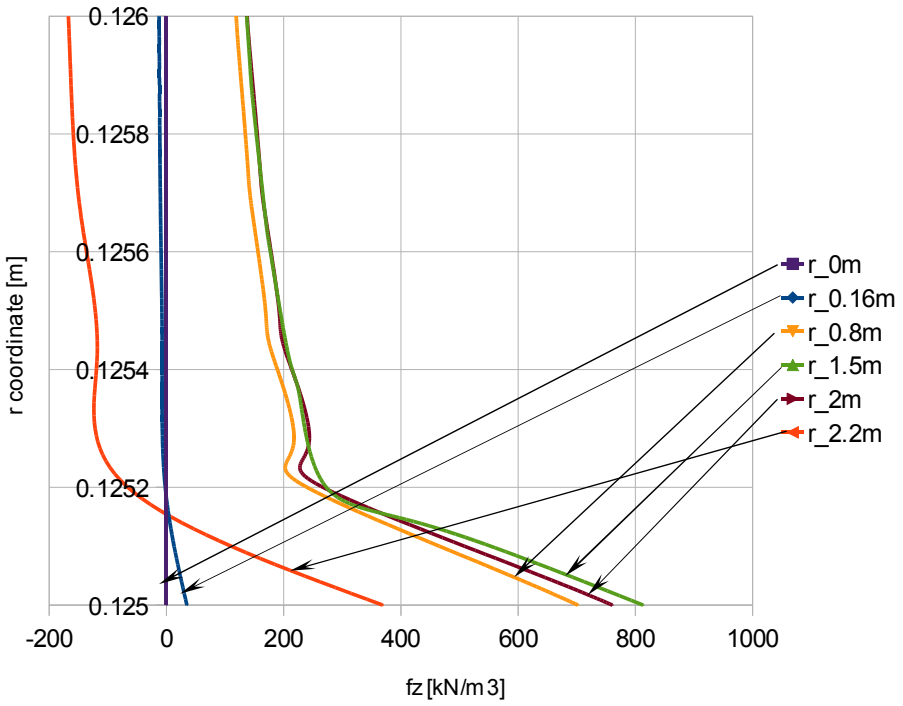

Fig. 6.65 b) Force profiles at different radial paths along the channel, sodium velocity 11m/s – zoom near the interior wall

D) Color maps of magnetic flux density and arrows of the axial force density

Fig. 6.66 presents the magnetic flux density in the sodium channel and in the magnetic cores of the pump for sodium velocity 4 m/s, respectively 11 m/s. It can be observed the increase of the magnetic flux density in the sodium channel together with the tendency of flattening of the radial profile of the magnetic flux density when the sodium velocity increases. This representation completes the information given in Fig. 6.38.

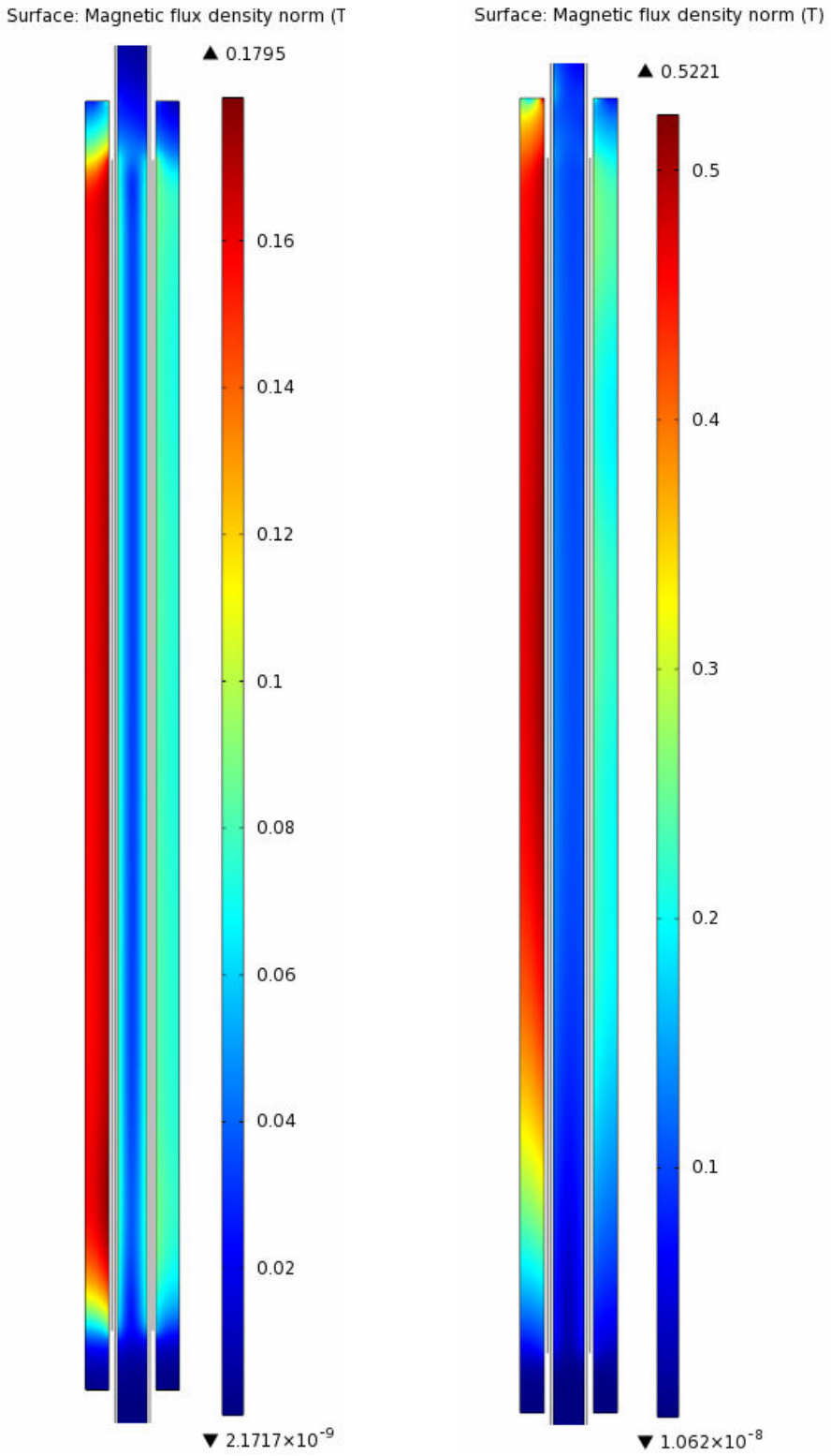

a) b)

Fig. 6.66 Map of magnetic flux density module in colors, magnetic field lines in contours, and axial electromagnetic force in arrows for sodium velocity a) 4 m/s and b) 11 m/s

Another important result of the variation of the MHD interaction intensity due to sodium velocity consists in differences with respect to the magnetic flux density in

the magnetic cores. Fig. 6.66 shows that even if the magnetic cores are immobile, the traveling electromagnetic field produces a magnetic flux density approximately three times larger when the sodium velocity is 11 m/s than at sodium velocity 4 m/s.

E) Magnetic flux density, magnetic vector potential and electromagnetic force vectors at pump inlet and outlet

Figs. 6.67 and 6.68 present in colors the magnetic flux density, with contours the magnetic vector potential and with arrows the axial force density at pump inlet, respectively pump outlet for the two representative sodium velocities.

Because at high sodium velocities there is a large discrepancy with regards to the force distribution between pump inlet region and pump outlet region and also in radial direction, the zooms at the pump outlet and at the pump inlet are in different scales. The zoom at the pump inlet, Fig. 6.67 is in a different scale than that at the pump outlet, Fig. 6.68.

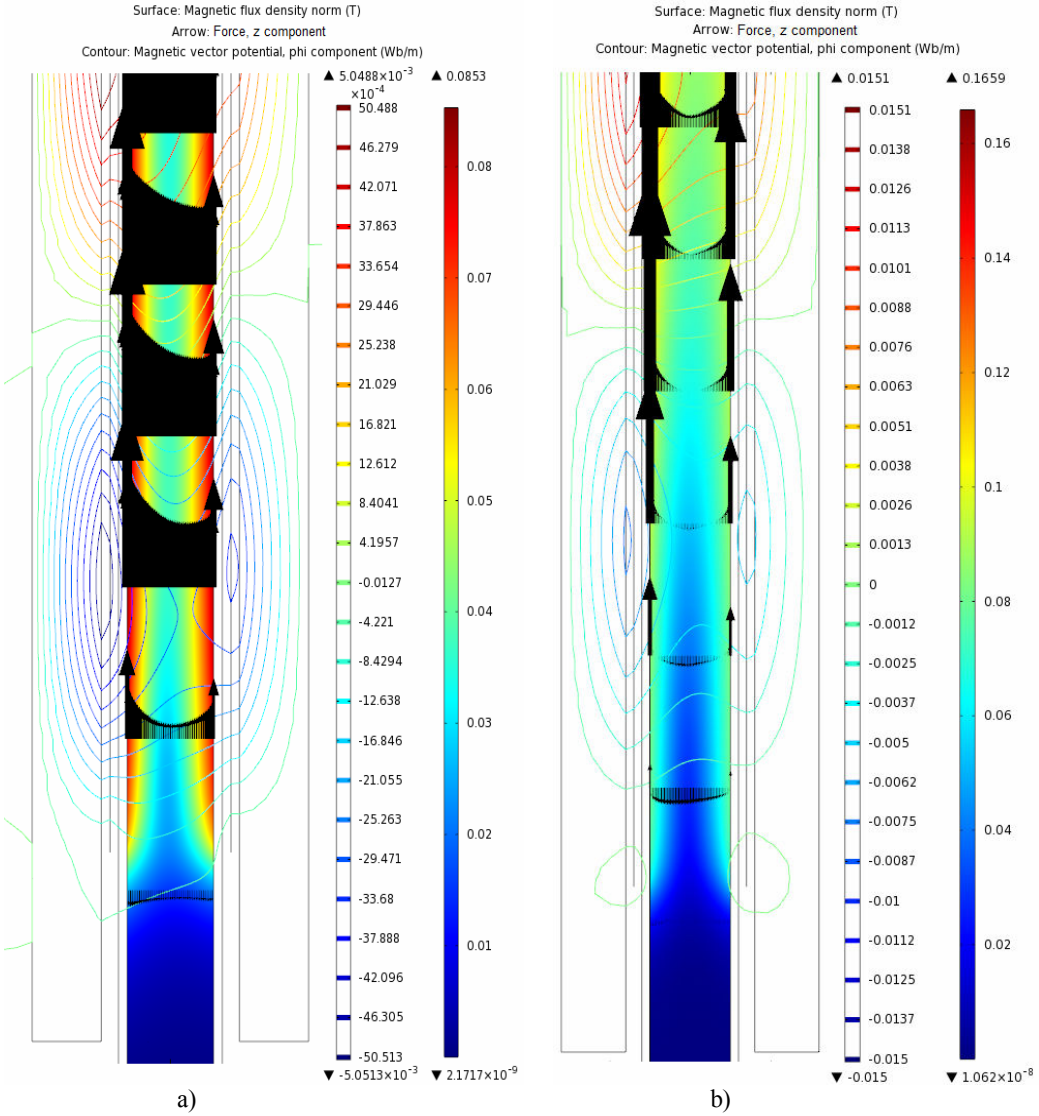

a) b)

Fig. 6.67 Map of magnetic flux density module in colors, magnetic field lines in contours, and axial electromagnetic force in arrows for sodium velocity a) 4 m/s and b) 11 m/s – zoom at the pump inlet

Fig. 6.67 highlights the inlet effects produced at low and high sodium velocities. In conformity with to the information provided by Fig. 6.51, it can be observed that at high velocities the negative forces are higher and in addition, Fig. 6.67 shows that the negative forces are extended along a greater distance towards the outlet.

Fig. 6.68 puts in parallel the MHD interaction effects at the pump outlet for the two sodium velocities. The arrows of the axial force density show that the radial non-uniformity is increasing at higher velocities and the comparison between Figs. 6.68b) and 6.67b) show that the non-uniformity is increasing along the pump.

Another important fact highlighted by the magnetic flux density color map and electromagnetic field lines is the effect of entrainment of the electromagnetic field by the electroconductive fluid in motion. The distance of the entrainment beyond the pump outlet is proportional with the sodium velocity.

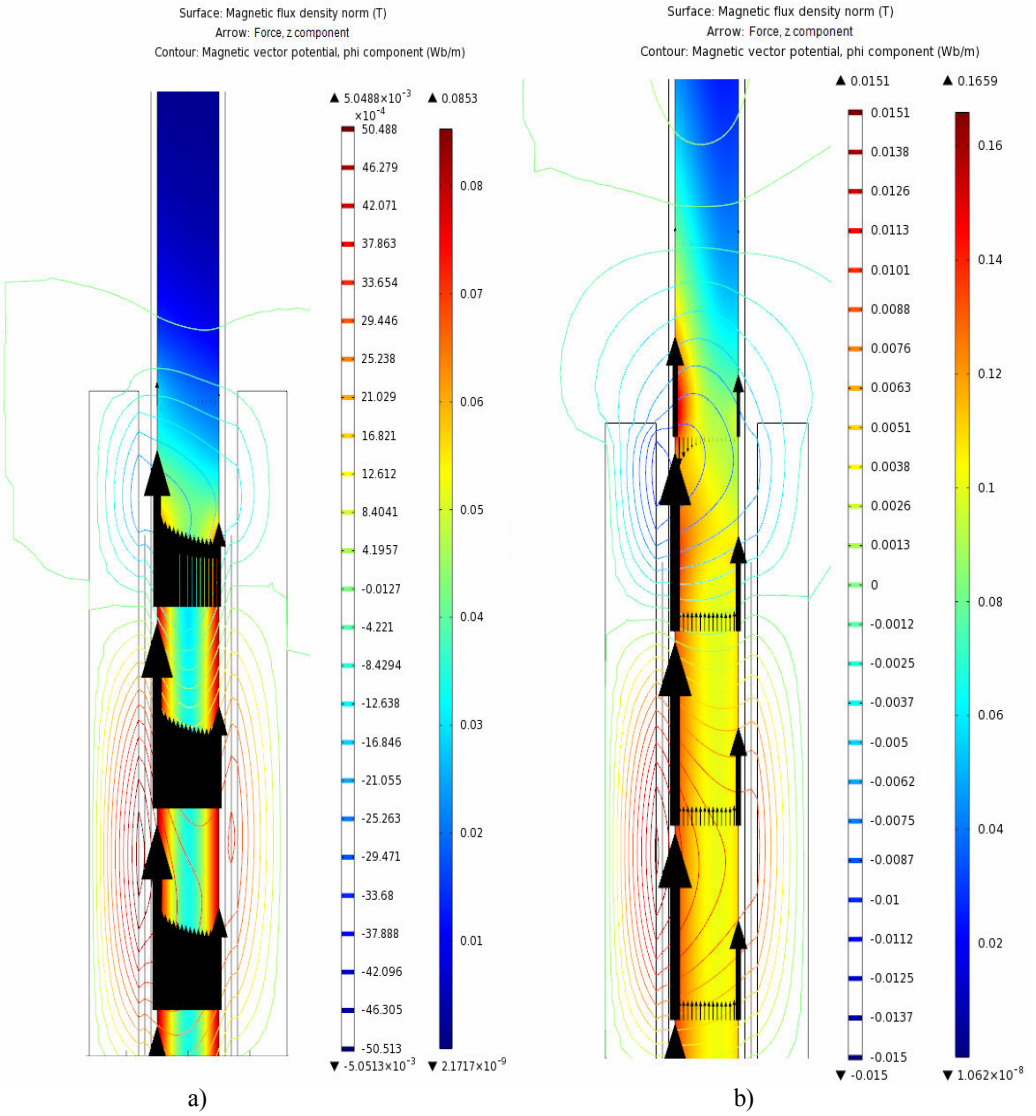

a) b)

Fig. 6.68 Map of magnetic flux density module in colors, magnetic field lines in contours, and axial electromagnetic force in arrows for sodium velocity a) 4 m/s and b) 11 m/s – zoom at the pump outlet

Because the pumping effect is realized by the axial oriented electromagnetic force, more often throughout the thesis in representations and calculations it is used

the axial electromagnetic force density. Fig. 6.69 gives an insight about the real orientation of the modulus of the electromagnetic force density. It results that the radial force density has important values and effects with respect to orientation of the forces that generate motion, respectively that oppose the motion.

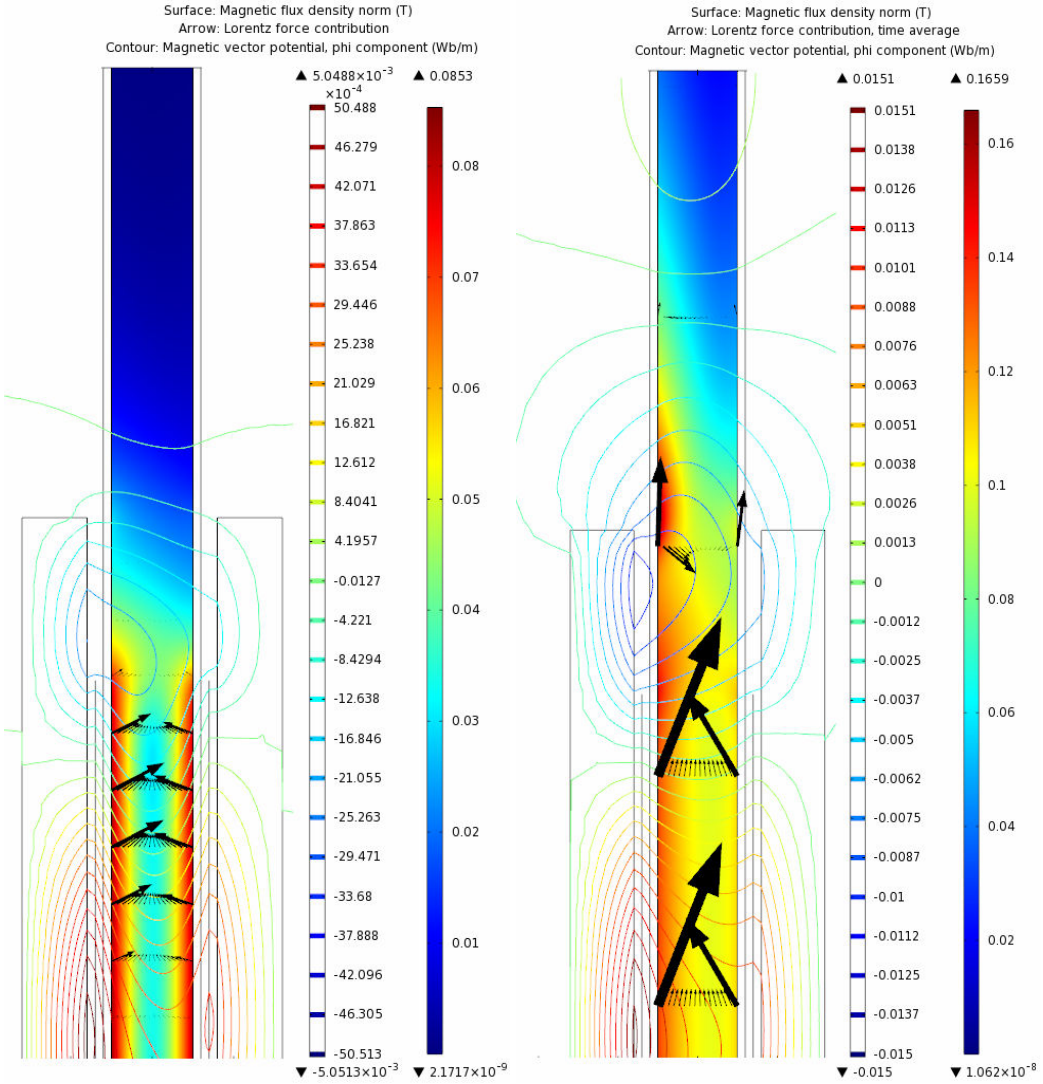

a) b)

Fig. 6.69 Map of magnetic flux density module in colors, magnetic field lines in contours, and electromagnetic force module in arrows for sodium velocity a) 4 m/s, b) 11m/s – zoom at the pump outlet

F) Color maps of turbulent viscosity

As shown in (6.25), the turbulent viscosity is function of the turbulent kinetic energy, respectively velocity and turbulent dissipation rate. Figs. 6.70 and 6.71 present the distribution of the turbulent viscosity in the sodium flow. As the sodium velocity increases the turbulent viscosity decreases. The ratio between maximum value of the turbulent viscosity and the dynamic viscosity of sodium is 4137.4 at 4 m/s and 1488.6 at 11 m/s. The mean value of the turbulent viscosity at 11 m/s, Fig. 6.71, is approximately 0.37 Pa·s or 0.37 kg/(m·s), which is comparable with the fictive value used in the MHD coupled model with laminar flow model in paragraph 6.1.

In other words, the fictive dynamic viscosity used in the laminar model, one thousand times larger than the real dynamic viscosity, is close to the mean value of the turbulent viscosity found as a result of the turbulent flow model for sodium velocity 11 m/s. This explains why the chosen fictive viscosity can not be used for the entire range of the characteristic curve, Fig. 6.28. If it is preferred the usage of a laminar flow model for solving the coupled problem, it is mandatory to adjust the fictive viscosity for each interval of sodium velocity.

It can be observed that as the sodium velocity increases the turbulence is moving from the outlet region towards the pump inlet.

The values of the hydrodynamic pressure in Fig. 6.28 corresponding to laminar model are approaching those of the curve corresponding to the turbulent model only for sodium velocities close to synchronous velocity because the mean value of the turbulent viscosity is approaching the fictive dynamic viscosity chosen in the laminar model only at very high sodium velocities.

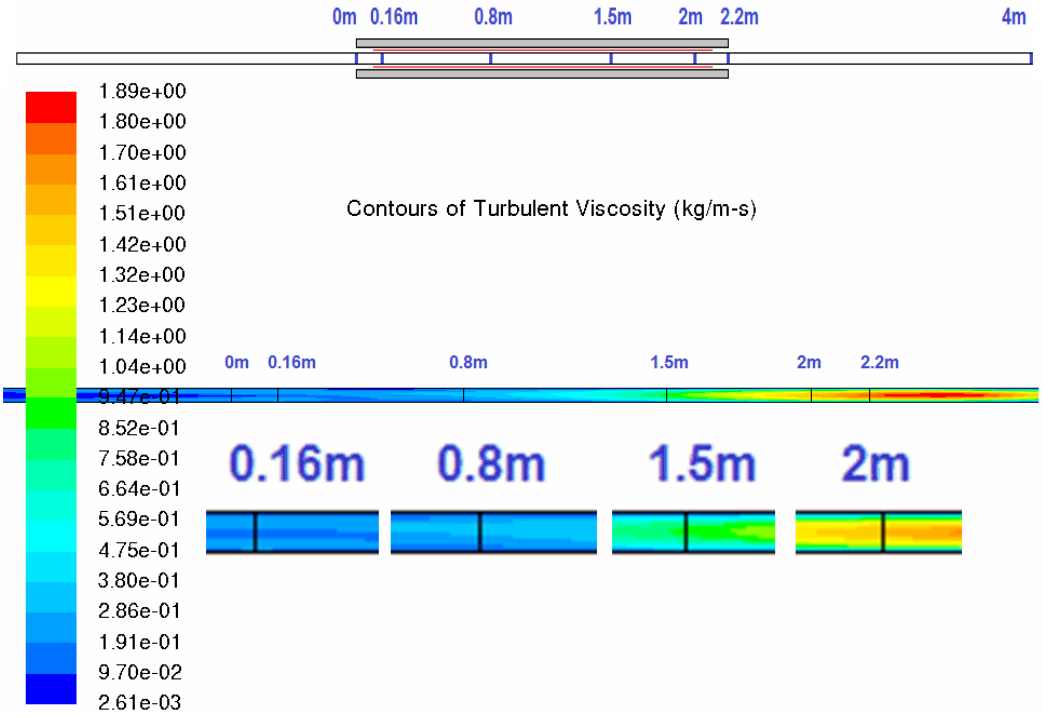

Fig. 6.70 Turbulent viscosity map in the computation domain; sodium velocity 4 m/s

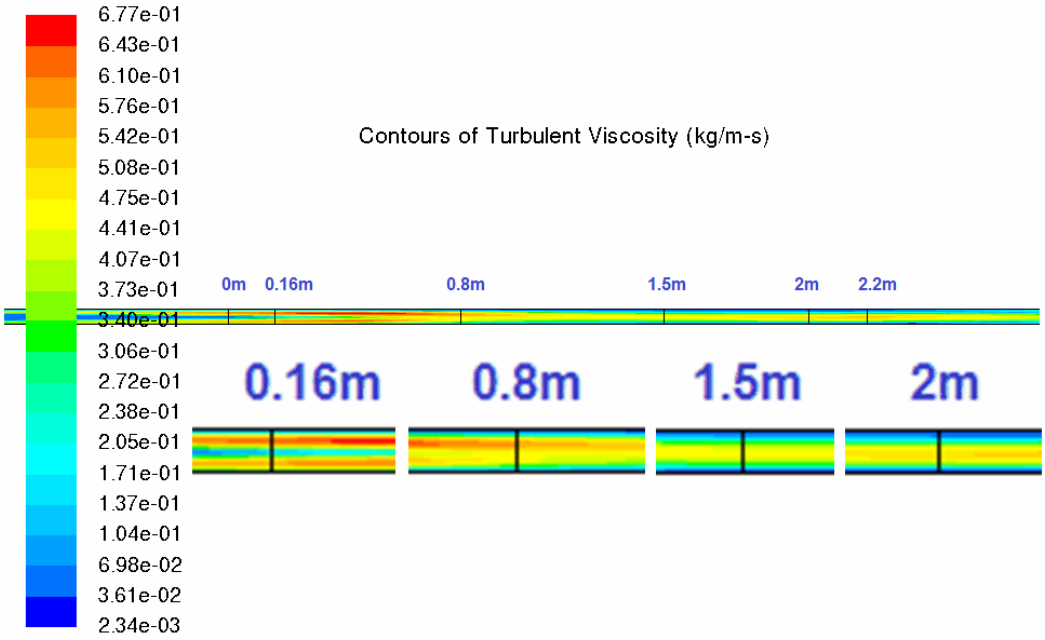

Fig. 6.71 Turbulent viscosity map in the computation domain; sodium velocity 11m/s

G) Color maps of turbulent kinetic energy

Figs. 6.72 and 6.73 present the turbulent kinetic energy for the two representative sodium velocities.

Figs. 6.74 and 6.75 present the longitudinal profile of the turbulent kinetic energy along three longitudinal paths. Path "MIDDLE" passes through the center of the channel, path "QUARTER_INT" passes along the middle distance between path "MIDDLE" and channel's interior wall. Paths "LONGIT_r0.1189" and "LONGIT_r0.0654" represent longitudinal paths, close to the interior wall of radial coordinates equal with the Hartmann layer correspondent to sodium velocity 4 m/s, respectively 11 m/s, Table X.

When correlating Fig. 6.72 with 6.74 and Fig. 6.73 with 6.75 it reveals that for low velocities the turbulent kinetic energy is higher along the channel center line than in the Hartmann layer and for high sodium speeds the maximum turbulent energy is generated along the longitudinal path describing the Hartmann Layer height.

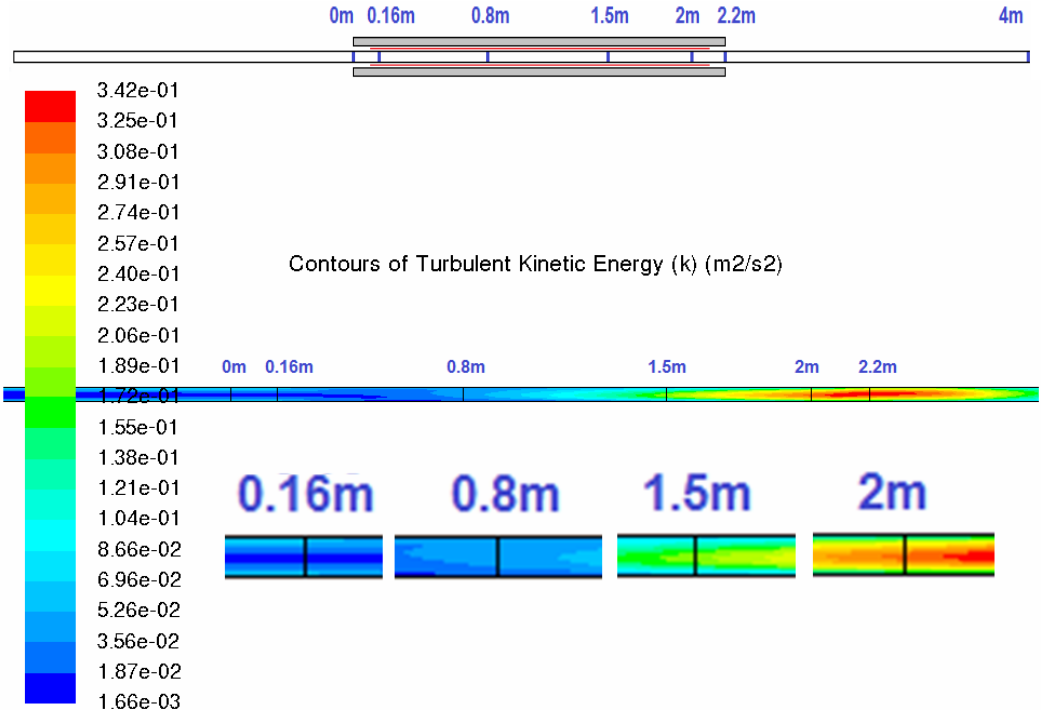

Fig. 6.72 Turbulent kinetic energy map in the computation domain; sodium velocity 4 m/s

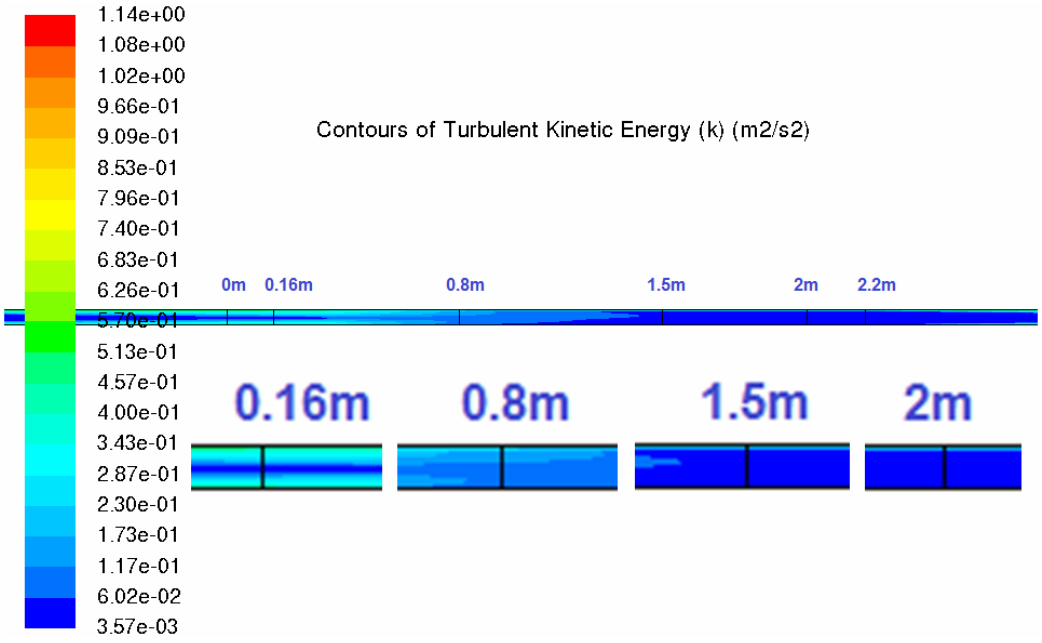

Fig. 6.73 Turbulent kinetic energy map in the computation domain; sodium velocity 11m/s

H) Longitudinal profile of kinetic energy along three longitudinal paths

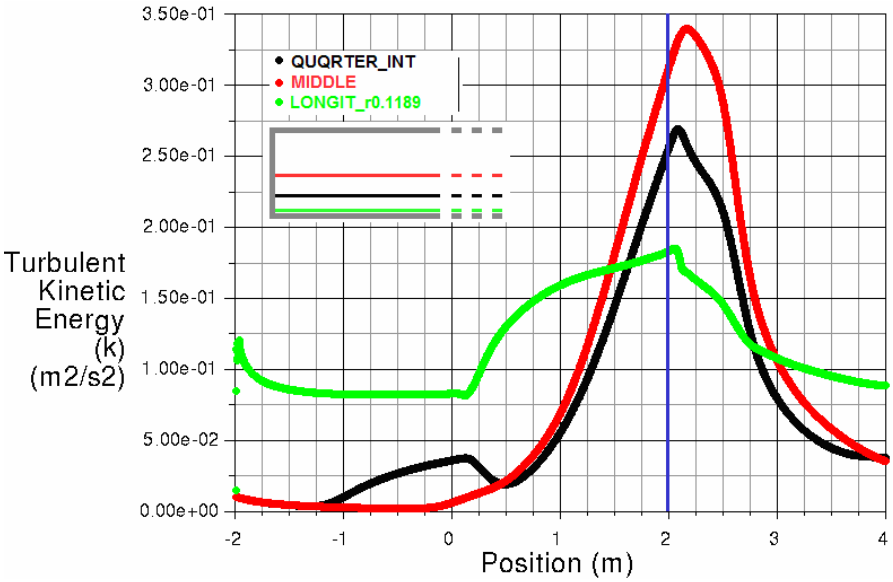

Fig. 6.74 Turbulent kinetic energy along three longitudinal paths, sodium velocity 4m/s

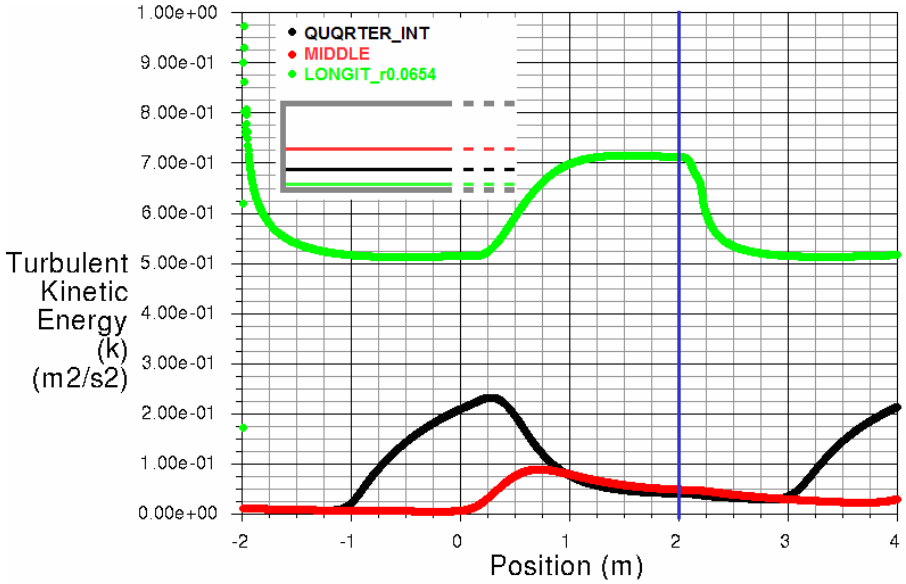

Fig. 6.75 Turbulent kinetic energy along three longitudinal paths, sodium velocity 11m/s

6.2.7 Efficiency calculation

This paragraph presents information about the PEMDYN pump efficiency and its dependence on sodium velocity. In order to observe the differences regarding the efficiency calculation, between block-pumping hypothesis and MHD coupling with turbulent flow model, all the curves in this paragraph are presented in parallel for both calculation hypotheses.

Figs. 6.76 – 6.78 present the dependence on sodium velocity of the Joule power developed in sodium, metallic walls, respectively in both regions. In Fig. 6.76 it can be observed that after a monotonous decreasing, the Joule power starts to increase when sodium velocity increases more than 11.5 m/s. This is due to considerable increase of the induced currents and consequently Joule power in the

immediate region after pump outlet as an effect of the electromagnetic field entrainment exemplified in Fig. 6.68b).

Because the hydrodynamic losses, that are taken into account only in the MHD model, become more significant at very high sodium velocities and negatively influence the MHD interaction, the values of the Joule power calculated in MHD-coupling hypothesis are higher than those calculated in block-pumping, Fig. 6.76.

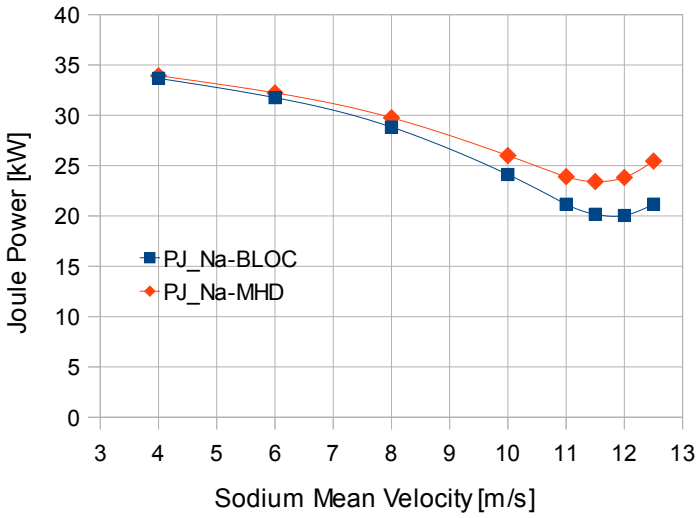

Fig.6.76 Dependence of Joule power generated in sodium on sodium velocity in block-pumping and MHD-coupling hypotheses

The Joule power developed in the metallic walls of the channel has the same exponential variation with sodium velocity in both hypotheses, namely it increases monotonically.

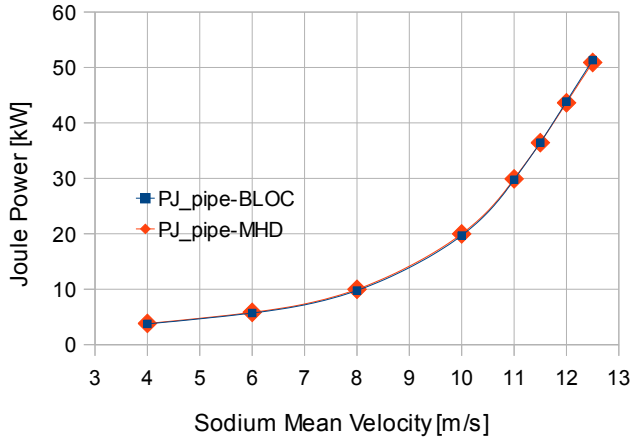

Fig. 6.77 Dependence of Joule power generated in the channel metallic walls on sodium velocity in block-pumping and MHD-coupling hypotheses

Fig. 6.78 gives the dependence on sodium velocity of the total Joule power induced in the walls and sodium.

The electromechanical power is calculated as the multiplication of the integral of the electromagnetic axial force volume density with the sodium mean velocity, Fig. 6.79.

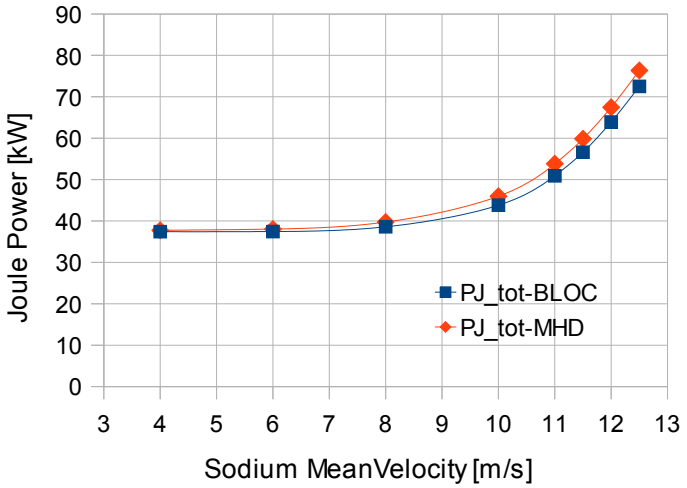

Fig. 6.78 Dependence of total Joule power generated in the channel metallic walls and sodium on sodium velocity in block-pumping and MHD-coupling hypotheses

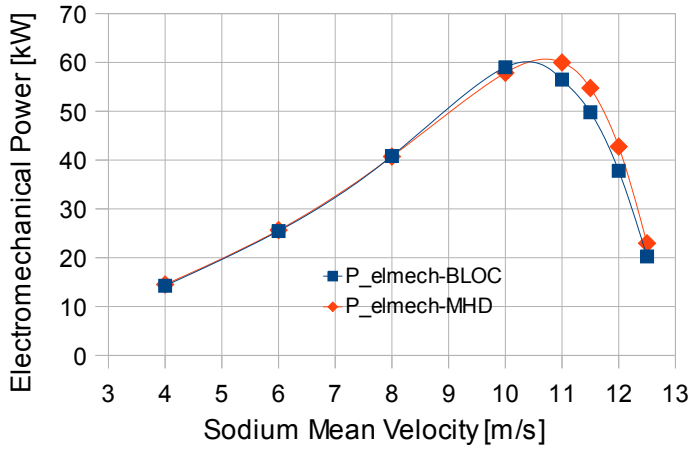

Fig. 6.79 Dependence of electromechanical power developed in sodium on sodium velocity in block-pumping and MHD-coupling hypotheses

The pump efficiency, Fig. 6.80, is calculated as the ratio between the electromechanical power and the sum of electromechanical power and total Joule power (in sodium and walls). The efficiency characteristics presented in Fig. 6.80 do not take into account the Joule power developed in the windings of the interior and exterior inductors. The maximum efficiency of the PEMDYN pump, according to the MHD-coupling hypothesis, is approximately 55% for sodium velocity 10 m/s. As the sodium velocity increases, the efficiency decreases until it becomes zero a little before the synchronous velocity, 13.2 m/s.

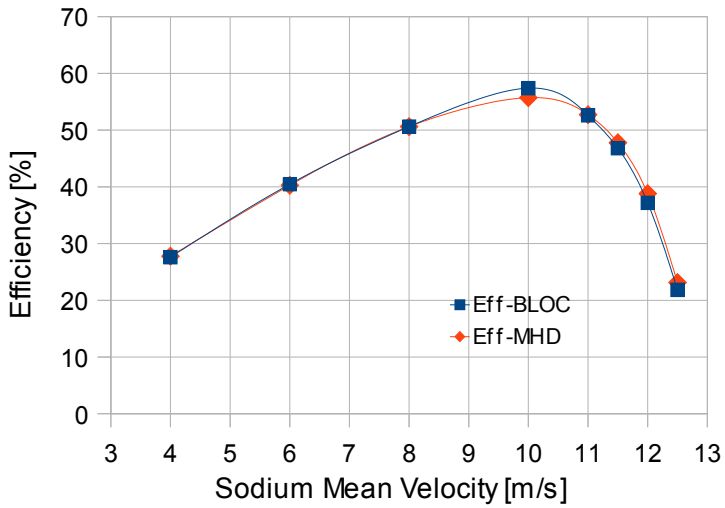

Fig. 6.80 Dependence of efficiency on sodium velocity in block-pumping and MHD-coupling hypotheses

6.2.8 Verification of the direct formulation of the hydrodynamic problem using the indirect formulation

In the paragraph 6.2.2 is specified the condition for the hydrodynamic problem, at INLET imposed uniform velocity profile and at OUTLET conservation of mass. This condition is equivalent with imposing the flow rate. The formulation of the problem with this condition is called direct formulation. In the direct formulation the sodium flow rate, respectively sodium mean velocity is known and the pressure is a result.

This paragraph is a verification of the direct formulation by the indirect formulation. The indirect formulation of the problem means to impose a pressure difference between the inlet and outlet of the hydrodynamic domain and to retrieve the flow rate, respectively sodium mean velocity as a result.

The verification was done the following way. First a problem in the indirect formulation was solved. Thus, when imposing a pressure difference at the two ends of the domain (P_{inlet} = 0.781 bar; P_{outlet} = 0.122 bar, corresponding to curve "11.5 m/s MHD" in Fig. 6.35) it was obtained:

- Sodium mean velocity,11.6346 m/s
- Pressure generated by the pump, 0.91084 bar
- Pressure difference between the two ends of the hydrodynamic flow, 0.59742 bar
- Volume integral of the axial force density, 4.77619 N
- Maximum axial velocity in a point of the domain, 12.8242 m/s
- Maximum kinetic energy in a point of the domain, 1.2241 m^2/s^2

After this, the solution was checked by solving a loop with imposed mean velocity 11.6346 m/s. The results are:

- Pressure generated by the pump, 0.9123 bar
- Pressure difference between the two ends of the hydrodynamic flow, 0.600052 bar
- Volume integral of the axial force density, 4.77619 N
- Maximum axial velocity in a point of the domain, 12.905 m/s
- Maximum kinetic energy in a point of the domain, 1.2560 m^2/s^2

The percent difference between the two sets of values is:

- Pressure generated by the pump, 0.16 %
- Pressure difference between the two ends of the hydrodynamic flow, 0.44 %
- Volume integral of the axial force density, 0.02056 %
- Maximum axial velocity in a point of the domain, 0.6256 %
- Maximum kinetic energy in a point of the domain, 2.54 %

It can be said that the indirect formulation that was used to obtain all the results of the paragraph 6.2 is approved by the test presented in this paragraph.

CONCLUSIONS

If in the previous chapters the sodium flow was simplifying modeled as a solid conductor in translation motion, this chapter is devoted to *MHD study*, namely to the bidirectional coupling of the hydrodynamic problem and the electromagnetic problem. The sodium flow is taken into account as the flow of a viscous fluid by the Navier-Stokes equation and the electromagnetic phenomena are governed by the Maxwell equations. The interaction occurs in accordance with the system of equations described in paragraph 2.4.

The first paragraph presents the MHD coupling using multiphysic software. Under certain assumptions, the flow, which according to the Reynolds number the flow is expected to be turbulent, is model with a laminar model. In these conditions, the characteristic curve of PEMDYN expressed as Pressure - Velocity was presented. The most significant result consists in presenting the flattening of the velocity profile at high sodium velocities as the sodium flows through the pump channel from inlet to outlet. The flat profile as result of the MHD interaction is called Hartmann profile. In the same time with the changes in the velocity profile, changes in the force radial profile occurs. As the velocity profile flattens, the force profile becomes more non-uniform in radial direction, namely, the force close to the walls increases along the channel. The result of the model was successful verified by a coupled model between two software dedicated to electromagnetism, respectively fluid dynamics.

The second paragraph is devoted to building the MHD coupled model using different software for the two physics with a turbulent k-ε model. The most significant conclusions regarding this paragraph are:

- Global convergence of the coupled problem is slower as the imposed sodium flow rate increases.
- The characteristic curve of the pump differs very much from the one calculated with the coupled model based on laminar flow model.
- The fundamental advantage of the MHD coupled model in opposition to a block-pumping model is highlighted by the
  - possibility to have the velocity profile at any longitudinal coordinate of the channel
  - accuracy of the force density profile and current density profile, namely the Hartmann profile of these quantities can be observed only with a coupled model
  - taking into account the hydrodynamic losses

  Otherwise, some global quantities like dependence on sodium velocity of the integral of the force density or total Joule power can be rapidly and with enough precision calculated in the block-pumping hypothesis.
- The Hartmann effect of velocity profile flattening depends on the sodium velocity and at constant velocity is more and more pronounced as the liquid sodium is closer to the pump outlet.

- For any sodium velocity, after 0.8 m from the pump inlet:
    - there are no more negative forces, namely the inlet effect is ended.
    - the Hartmann velocity profile is reached.
- The breaking effect of the negative forces at pump outlet is always much stronger than at inlet. The breaking effect at pump inlet produces a zone of depression that can extend to even 1m from inlet at very high sodium velocities.
- The entrainment of the magnetic field at the pump outlet is stronger with the increase of velocity and contributes to the breaking effect.
- Due to the unequal distribution of the current, respectively of forces between interior and exterior walls, the bulk part of the Hartmann profile is not perfectly vertical, but tilted towards the exterior boundary.
- Knowing the slope of the stable branch of the pumping characteristic of PEMDYN means knowing the reserve of maximum hydraulic overload, because the pump can self regulate at a sudden load shock only if the new load is lower than the maximum pressure indicated by the characteristic.
- The maximum efficiency of PEMDYN calculated in the assumptions of this paragraph is 60% at sodium velocity 10.5 m/s. The difference between this efficiency and the one calculated in paragraph 5.2 is due to the implications of the idealized double inductor with no slots used in paragraph 6.2.
- The rapid decay of the efficiency after 11 m/s is due to high induced currents in the metallic walls and low induced currents in the sodium bulk region, namely due to the increase of the Joule losses together with the decrease of the pumping effect.

Chapter 7: General conclusions and contributions

The general conclusions and contributions of the thesis in the study of electromagnetic pumping systems can be divided in two categories. First category is about results with technical character related to various specificities of electromagnetic pump operation. The second category is related to the methods and tool used in the study.

The presentation of the first category of contribution is organized as answers that the thesis gives to problems or difficulties that designing or exploitation of electromagnetic pump may raise. Thus the following paragraph is built as a succession of questions / topics and answers.

A. Possibility of electromagnetic pumping of molten salts.

The general answer as it may be concluded from third chapter is that with special designs that take into account the high electrical resistivity, at very low supply frequencies or in DC supply it is possible to pump by electromagnetic means. Anyways, due to the high Joule power generated, such devices are best suited to applications where the heating effect is considered benefic.

These conclusions are based on building an important number of 2D and 3D numerical models and on the analysis of the influence of various parameters as geometry, electrical resistivity, supply frequency and constructive variants.

B. What difficulties are expected in numerical modeling of Annular Linear Induction Pumps (ALIP)? What are most important phenomena that deserve important attention?

The various models of the small dimensions pump presented in the fourth chapter designed to give preliminary information about ALIP modeling and operation reveal the following:

- The complex geometrical structure and high number of nodes of the finite elements mesh imposes special consideration of the finite element study domain, especially for the 3D models. Thus, by taking into account the symmetries of the device and using the right periodicity conditions, the study domain can be reduced to a fraction of the full domain. This constitutes important advantages for improvement of precision and time of calculations.
- The existence of the interaction electromagnetic field – motion raises the question of taking into account the motion. The electromagnetic models that couples electromagnetic field, circuit and translation motion of solid conductors, namely block-pumping hypothesis, represent solutions that the thesis proposes as an acceptable solution when only some global quantities present interest. It was proved that on the basis of series of models that use a certain law for the sodium region velocity, the Force - Velocity characteristic can be built.
- The exploitation of the 2D and 3D models for high sodium velocities highlighted special phenomenon especially at the outlet region consisting in generation of intense electromagnetic field outside the pump, generally called ends effects with negative impact on the pump operation.
- Other important observations are related to oscillations in time of the generated force, radial and longitudinal variations of various quantities, and possible effects of the discontinuous disposal of the magnetic cores.

- All the conclusions resulted from numerical models building and exploitation, modeling techniques and special phenomena highlighted by treating the small size pump in the block-pumping hypothesis proved to be of high importance in the study of the large size PEMDYN pump.

C. Influence of the number of poles and supply frequency

The thesis provides extensive information with respect to the influence of the number of poles and supply frequency on the pumping characteristics in the case of an ALIP with given dimensions and electric supply limited by the cooling system reported to a slot dimensions. Actually, the study shows that for an ALIP of given length there is an optimal couple number of poles – supply frequency with respect to obtaining the maximum force possible.

D. Influence of metallic walls and ends effects

It is shown that the electrical properties of the walls of the channel of an ALIP are of considerable importance with respect to the pump operation characteristics. As the material of the walls is of lower and lower resistivity, the generated force acting on the sodium decreases and the Joule power developed in the walls increases. The example presented in paragraph 5.1.2 shows that the force may be reduced with 30 % only due to electroconductive walls. The generally called ends effects include two important aspects: generation of forces opposing to motion and developing of important Joule power outside the pump in the outlet vicinity due to the entrainment of the field. The thesis uses various approaches in paragraphs 5.1.4, 5.3.2 and 6.2 to present and quantify the ends effects and their dependences of sodium velocity.

E. Overload capacity of an ALIP

The operation regime of an ALIP in a hydrodynamic circuit is function not only of the pump supply parameters, but also of other circuit components that may increase or decrease the sodium flow rate, respectively sodium velocity. The thesis proposes in paragraph 5.2 a method for finding the overload capacity of an ALIP and presents the pump behavior for various sudden load jump as function of the position of the rated regime on the Force-Velocity Characteristic.

F. Azimuth discontinuity of the magnetic core

The conclusion of the thesis with respect to the discontinuity of the magnetic cores in azimuth direction in both constructive types of ALIP, namely with double inductor or only with an exterior inductor, is that it generates a azimuth non-uniformity of the electromagnetic field, but with minor influences over the pumping capacities. This conclusion is based on a parametric study of the electromagnetic field three-dimensional structure with the distance between adjacent cores as parameter.

G. What is the behavior of the generated force as function of time? How varies the force along the pump channel?

An important achievement of the thesis consists in presenting results about the time oscillations and spatial variation of the force. It was observed that the frequency of the force is always double the supply frequency and that the amplitude of the force increases as the sodium velocity increases.

The force distribution along the channel, paragraph 5.1.5, shows that at low sodium velocities the force has a stabilized region. As the sodium velocity increases, the force stops having a region of quasi-constant value and it is monotonous increasing from inlet to outlet. In addition, paragraph 5.3.2 highlights that the point to point variation of the force density is strongly affected by the tooth – slot alternation.

H. On the electromagnetic field – fluid dynamics coupling

In the chapter destined to the magnetohydrodynamic interaction through coupled models the thesis proposes two models that couple the electromagnetism and the fluid flow. The first was realized using multiphysic software and the second by coupling two different software by means of a simple supervisor.

There are presented the advantages of the coupled model with respect to the results accuracy in comparison with the block-pumping method. Only the coupled model can present the evolution of velocity, force and current densities towards Hartmann profiles. It also takes into account the hydrodynamic losses, the dependence of the turbulent viscosity distribution on sodium velocity.

Regarding the category of contributions related to methods and tools, the most important are:

I. Realization of the fully coupled model electromagnetism – fluid dynamics by coupling two software. Validation of the method by formulating and solving the indirect problem and by other multiphysic software.
J. Using strategies of relaxation for the variables that make the object of transfer between electromagnetic problem and fluid flow problem.
K. Adaptation of the mesh properties to the laminar, respectively laminar model
L. An important observation is that the laminar model of the flow can give satisfactory results if the imposed fictive value of the dynamic viscosity at a certain sodium velocity is equal with the integral value of the turbulent viscosity obtained as a result of the flow in turbulent model at the same sodium velocity. Once found the proportionality factor, that describe the relation between the integral of the turbulent viscosity at a certain sodium mean velocity and the value of fictive dynamic viscosity, for which the laminar model and the turbulent model are equivalent, the laminar model which requires less computation resources can be used for further studies.
M. Throughout the thesis the differences, respectively advantages and disadvantages of the 2D and 3D models, respectively of the block-pumping hypothesis and fully coupled model, are presented.
N. The thesis proves that numerical modeling is a modern and powerful tool that can relatively rapidly give results of every kind about operation in various regimes and optimization needs of devices long before prototype.

ANNEX

ELECTROMAGNETIC STIRRING OF ELECTROCONDUCTIVE LIQUIDS

A topic in close relation with electromagnetic pumping is the electromagnetic stirring. As the electromagnetic pumping, electromagnetic stirring is also based on the action of the electromagnetic forces and is used in various processes where homogenization of various electroconductive liquids is needed. In comparison with mechanical stirring, electromagnetic stirring presents the advantage of contactless generation of motion, consequently the advantage of a better reliability and efficiency. The benefits of the electromagnetic stirring in numerous metallurgical applications where extensively researched and continue to be studied and developed currently, [170]-[181].

This annex contains results of various studies on the subject of electromagnetic stirring of electroconductive liquids of high and low electrical conductivities. The division of the annex reflects the methods of electromagnetic field generation and fluid flow propagation direction. There are two types of stirring procedures investigated: induction stirring and conduction stirring.

Induction stirring is studied in paragraph A.1, "Traveling field induction stirring" and in paragraph A.3, "Rotating field induction stirring" with *MHD coupled models*. The resemblance between the two consists in generation of the electromagnetic forces through the induction phenomenon. The difference consists in the direction of propagation of the electromagnetic field, namely the flow direction. In paragraph A.1 the inductor produces a traveling electromagnetic field, in paragraph A.3 the electromagnetic field is rotational.

Paragraph A.2, "Conduction stirring" is an *electromagnetic study* and treats the stirring produced by the electromagnetic forces generated by the interaction between the currents injected in the bath by electrodes and the magnetic flux density produced by field coils located in the exterior of the bath.

A.1 Traveling field induction stirring

Subchapter A.1 presents a stirring device for liquid aluminum at 700 °C. Fig. A.1 presents the entire computation domain consisting of the aluminum bath and the inductor.

The inductor is placed at an angle of about 35° from the vertical and has the following dimensions: length 1170 mm, height 180 mm and width 360 mm. It has 12 slots of 30 mm x 71.6 mm cross-section each. The two pole inductor has a three phase winding of 2 slots per pole per phase. The peak value of the current density over a slot cross-section is 4 A/mm^2 at supply frequency 7 Hz. This means that the generated traveling magnetic field has the synchronous speed 8.2 m/s. The magnetic core is modeled by a material with linear relative permeability 1000.

The parallelepiped part of the aluminum bath is 1000 mm high, 2000 mm wide and 2000 mm long. At one of the faces, the bath extends with an inclined port with presumable double role: a) feeding the bath with material for stirring and b) siphon the melt out, [182]-[184]. The horizontal dimension of the port is 700 mm and the distance between inductor and port is 145 mm. The dynamic viscosity of liquid aluminum at 700 °C is 0.00289 Pa·s, the mass density 2315 kg/m^3 and the electrical resistivity is $2e^{-7}$ Ωm.

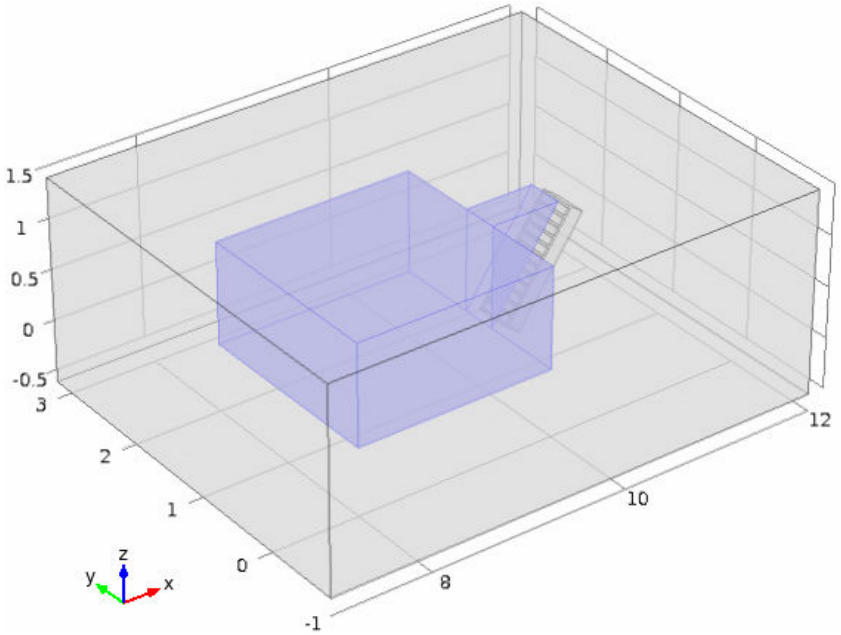

Fig. A.1 Computation domain of the aluminum bath

The double role of the port is related to the two directions that the generated traveling field can have by means of different connection of the inductor's phases. When the field direction is downwards, towards the bath bottom, the inductor plays the role of a stirrer because it generates motion which extends towards the bath's walls. When the field is traveling upwards the fluid in port will be entrained towards the port top. By gradually introducing a metallic plate parallel to the inclined wall of the port, a channel of relatively small cross section 360 mm x (50-100) mm is formed. In this case, the inductor plays the role of an electromagnetic pump for emptying the bath after the stirring process. Further is treated the stirring application based on coupled electromagnetic - hydrodynamic finite element models.

The following results are obtained for a turbulent k-ε model with 0.0289 Pa·s dynamic viscosity, using a stationary study. The relative tolerance of the model is 0.001. The boundary condition for all the walls of the hydrodynamic domain is standard wall functions.

Fig. A.2 presents the magnetic flux density in the bath with colors and arrows. The magnetic flux density is concentrated in the inclined area of the bath. The arrows highlight the two poles structure of the inductor. Fig. A.3 presents with colors and arrows the generated electromagnetic force density concentrated close to the active face of the inductor.

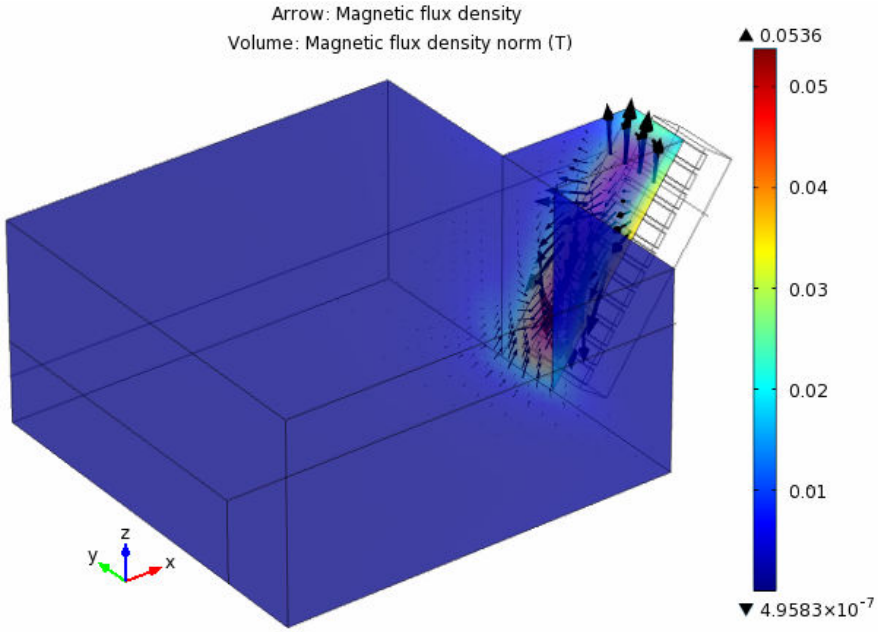

Fig. A.2 Magnetic flux density in the aluminum bath

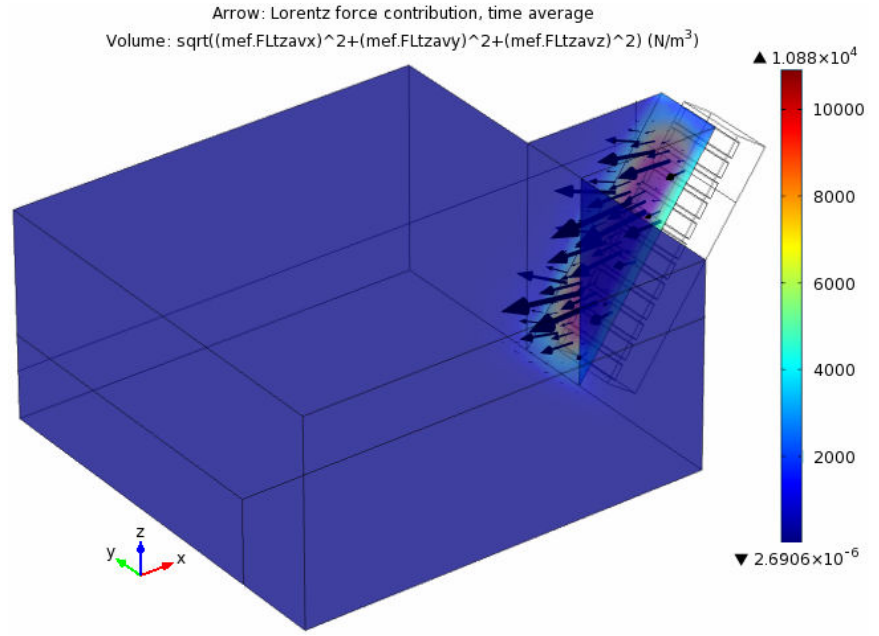

Fig. A.3 Electromagnetic force density in the aluminum bath

Figs. A.4 - A.6 give information about the fully developed steady flow in the bath. The liquid aluminum is entrained in a loop movement mainly in the xOz plane. The maximum speed is near the inclined wall, 1.4 m/s and close to the bottom, in the middle of the bath the speed is around 0.7 m/s, Fig. A.3. At the bath surface, the mean velocity is about 0.3 m/s. In other words the flow is occurring mainly close to the upper and bottom walls and there is a middle portion with low velocity - even null velocity - because as seen previous along the bath height a change of flow direction exists.

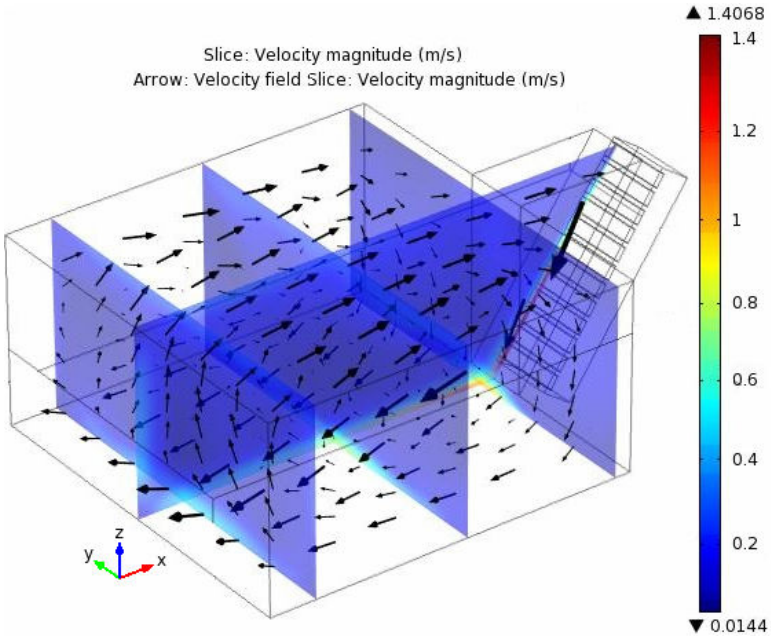

a) Velocity magnitude in colors and flow direction in arrows

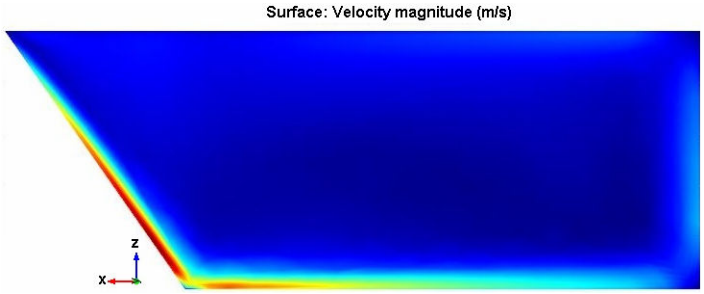

b) Velocity magnitude in the median zOx plane

Fig. A.3 Maximum velocity reached in the median plane

The existence of the very low velocity strip along the half height of the aluminum bath combined with the effects of the low velocities near the vertical walls can lead to unsatisfactory results regarding the homogeneity of the melt after the stirring process due to a weak agitation of the core region. From here two possible conclusions can be drawn. For a device with of the presented type there is an optimum height for which the core fluid region is entrained. For devices with important heights, an additional system for vertical stirring could be needed.

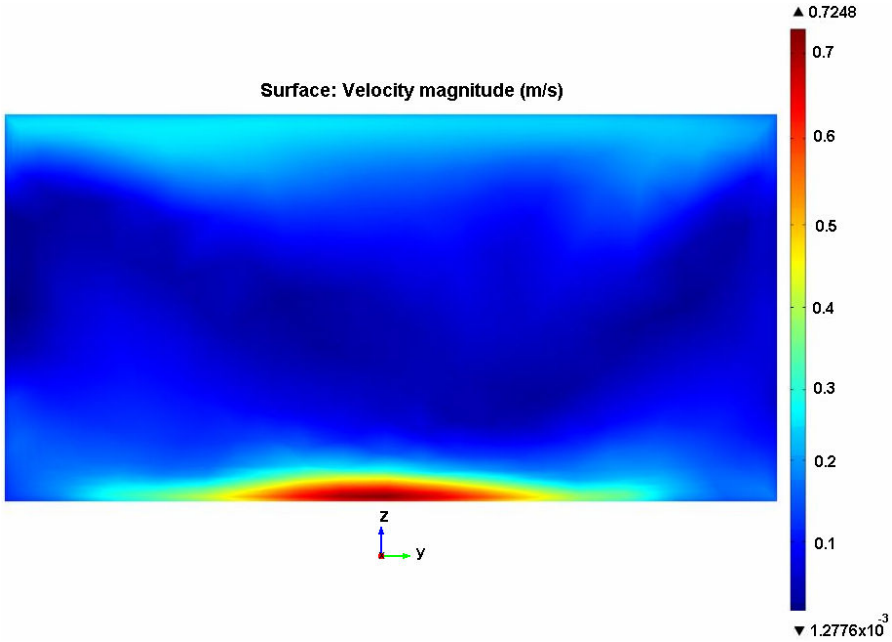

Fig. A.4 Velocity magnitude in the median transversal yOz plane

Fig. A.5 presents the Ox component of velocity along a vertical line in the middle of the bath. The two quasi-equal areas described by the curve and the abscissas axis highlights the passing through null velocity somewhere along the bath height and demonstrate the observance of the low of mass conservation.

Figs. A.6 – A.8 present the velocity magnitude along an Ox oriented line placed in the symmetry plane of the bath, at the surface, half-height and bottom. They present the velocity variation from the wall farthest from inductor towards the inductor. Comparing Figs. A.6 and A.8 one can see that the highest velocity is towards the inductor in the bottom plane and towards the opposing wall in the surface plane. Fig. A.7 presents more clearly the low velocity region at the bath half height. The increase of the velocity magnitude at the left and at the right of the graph shows the downward and upward flow at the two extremities of the xOz plane.

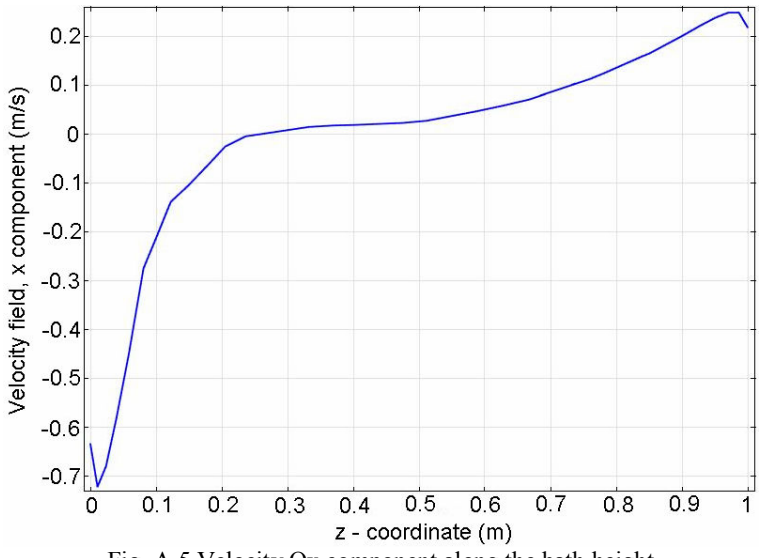

Fig. A.5 Velocity Ox component along the bath height

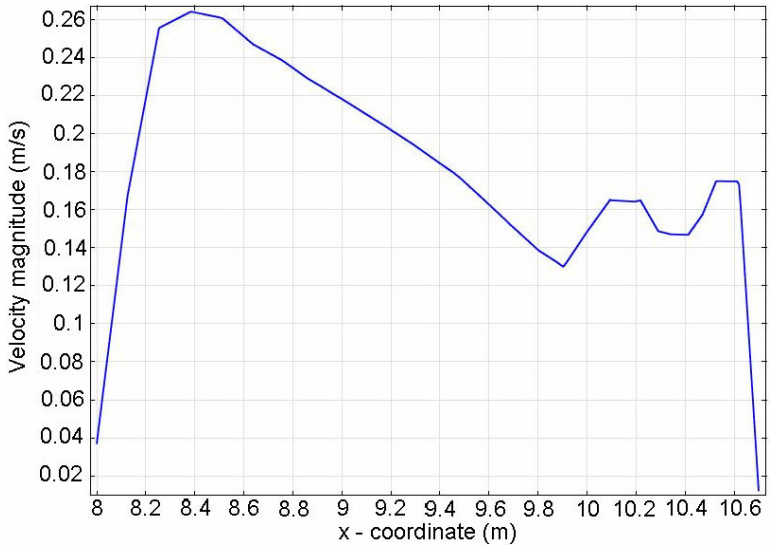

Fig. A.6 Velocity magnitude along the Ox (flow) direction at bath surface

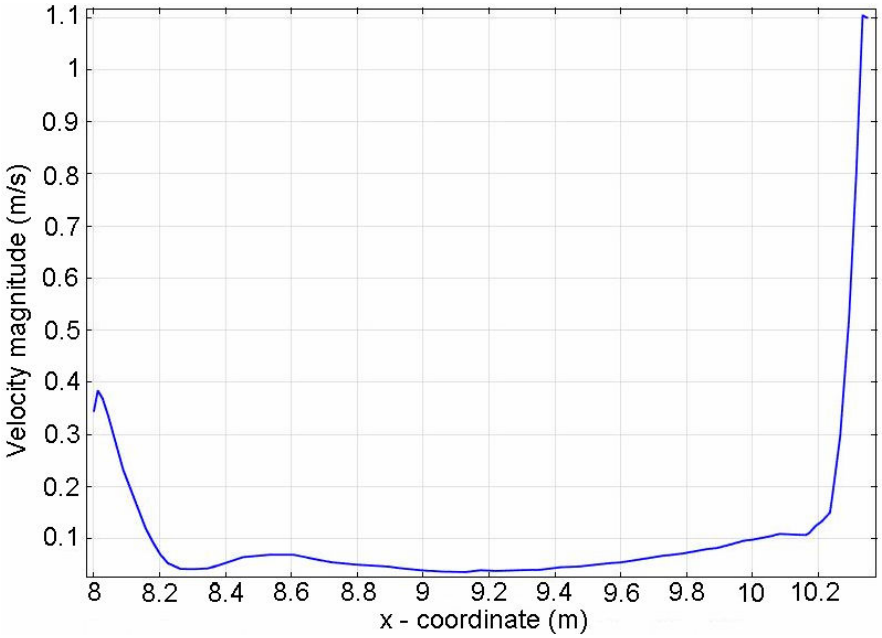

Fig. A.7 Velocity magnitude along the Ox (flow) direction at half height

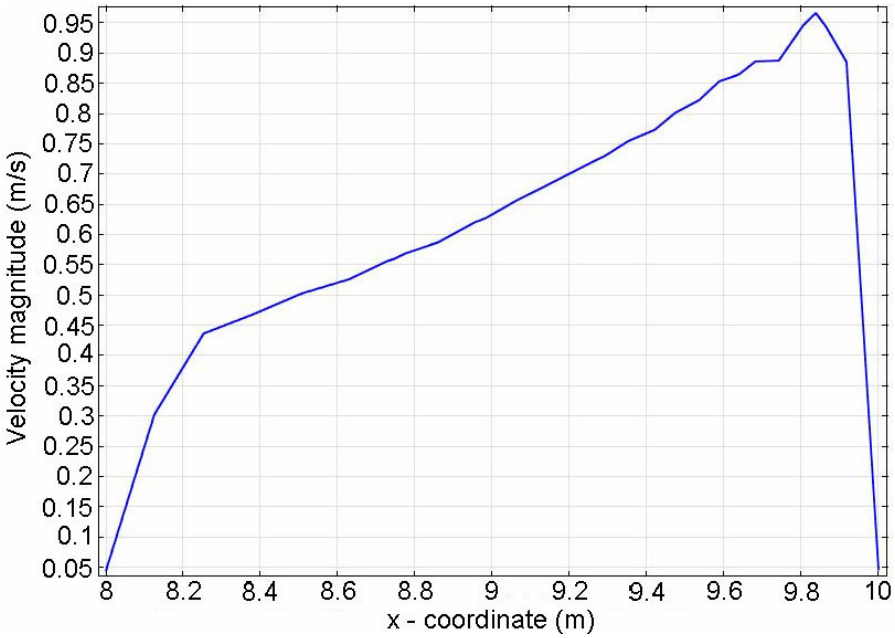

Fig. A.8 Velocity magnitude along the Ox (flow) direction at bath bottom

Fig. A.9 presents the streamlines which are a family of curves instantaneously tangent to the velocity vector of the flow. They show the direction a fluid element will travel in at any point in time.

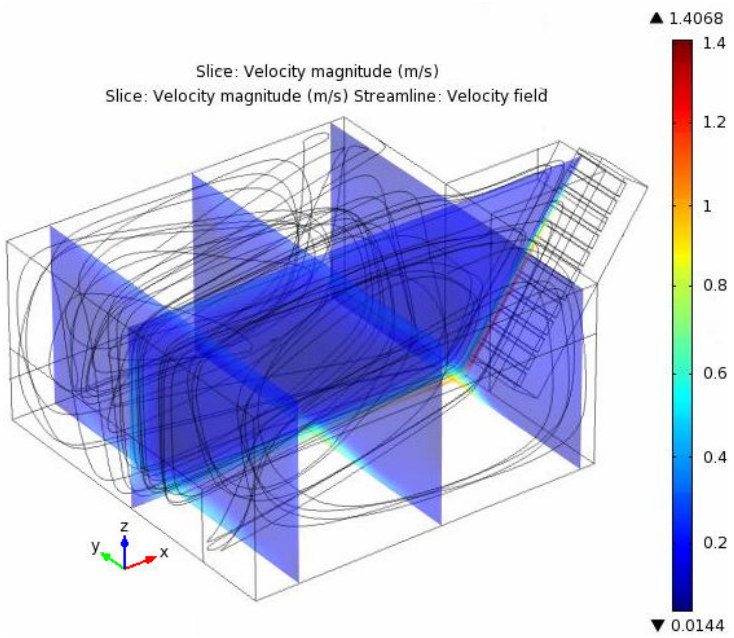

Fig. A.9 Streamlines of velocity in the aluminum bath

If it is separately integrated on the bath volume the three components of the volume force density, it is found: total force acting against the Ox direction Fx = 132.4 N, total force acting against the Oy direction Fy = 0.028 N and total force acting in the Oz direction Fz = 16.2 N. The total injected power in the liquid aluminum is Ptot = 5.13 kW.

The viscosity of a fluid is decreasing with the increase of the temperature. As the viscosity decreases, namely the fluidity increase, the friction between neighboring

parcels of fluid that are moving at different velocities becomes smaller and the fluid is more free to move under the action of the surrounding forces. The local or global temperature of aluminum in the bath can vary in time and/or space due to insufficient homogenization, new cast of aluminum of different temperature, different supply parameters etc. Fig. A.10 presents the variation of maximum velocity magnitude computed in any point of the domain with the dynamic viscosity. Any factor that determine a decrease of the viscosity is a factor of lowering the aluminum velocity, namely of lowering the stirring effect and finally a factor of efficiency decrease. The difference between the maximum velocities decreases as the correspondent dynamic viscosity decreases. This observation support the conclusion that for the real viscosity 0.00289 Pa·s, the maximum velocity is not far from 1.4 m/s. While the viscosity variation affects some of the hydrodynamic quantities, it doesn't affects the global quantities Fx, Fy, Fz, Ptot presented above which are quantities of electromagnetic nature.

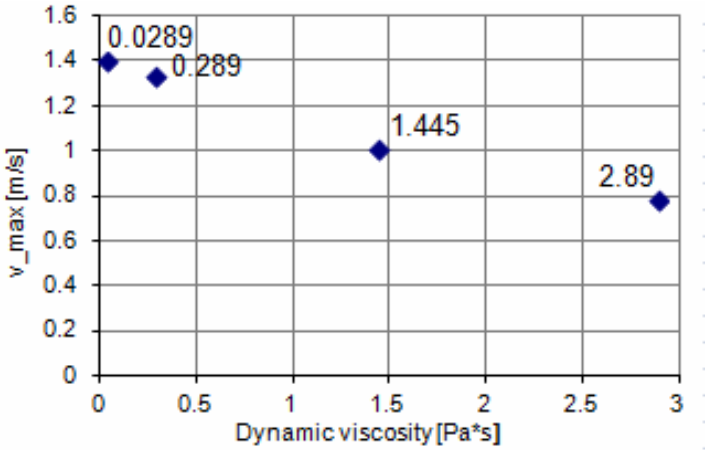

Fig. A.10 Maximum velocity dependence of dynamic viscosity

There are industrial applications when stirring of fluids much less electroconductive must be done through electromagnetic means due to safety reasons, maintenance reasons or to prevent the introduction of impurities, [185]-[188].

Molten glass at 1200 °C has dynamic viscosity around 50 Pa·s, mass density 2500 kg/m^3 and electrical resistivity 6.6e^{-2} Ωm, which is about 10^5 times higher than that of liquid aluminum.

If it is separately integrated on the bath volume the three components of the volume force density and compared to the case of aluminum stirring, it is found: total force acting against the Ox direction Fx = 45.7 N, namely 3 times lower, total force acting against the Oy direction Fy = 0.061 N, namely 2.17 times higher, and total force acting in the Oz direction Fz = 28.6 N, namely 1.7 times higher.

Figs. A.11 and A.12 present the magnetic flux density in the molten glass bath with arrows and colors. The maximum force density is almost half in comparison with the case of aluminum bath.

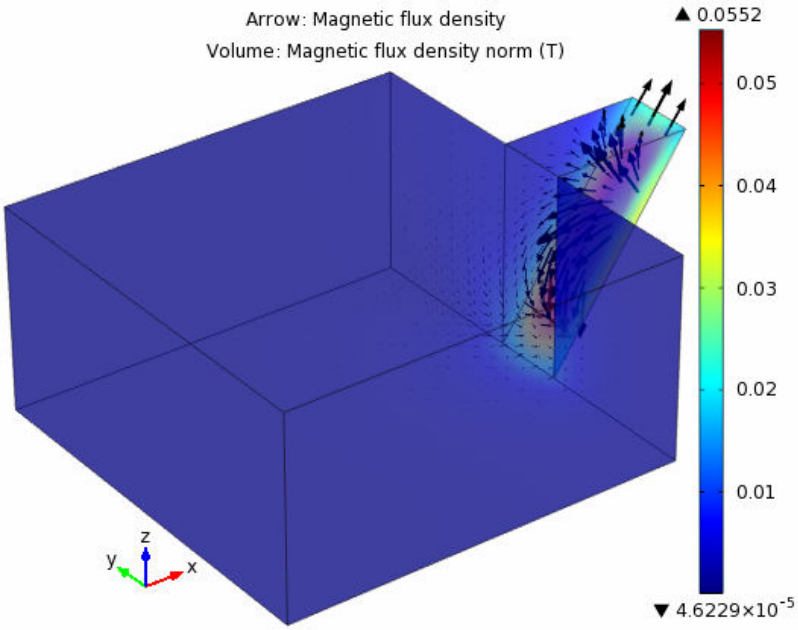

Fig. A.11 Magnetic flux density in the molten glass bath

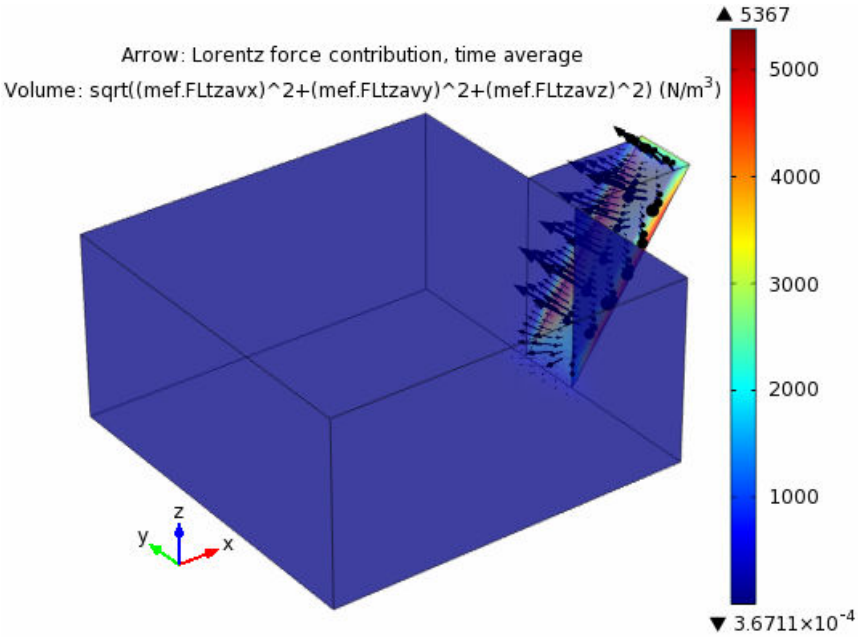

Fig. A.12 Electromagnetic force density in the molten glass bath

Fig. A.13 presents the velocity magnitude in colors and the flow direction in arrows. The maximum velocity is $5.4 \cdot 10^{-3}$ m/s, which is more then 250 times lower than the maximum velocity in the case of aluminum stirring. The result is expected to be so, taking into account the molten glass lower resistivity and higher viscosity in comparison with aluminum. Fig. A.14 shows the streamlines of velocity which give a complete understanding with respect to the differences between the two cases.

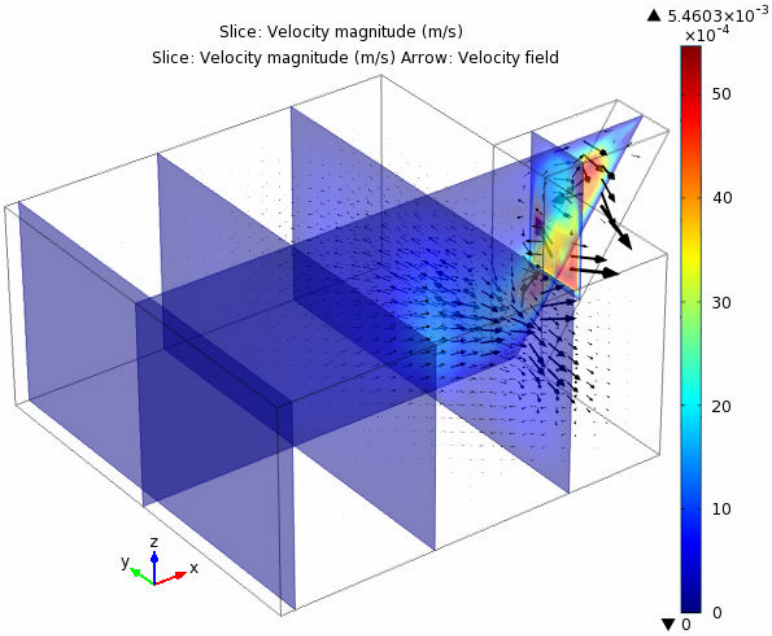

Fig. A.13 Velocity magnitude in colors and flow direction in arrows

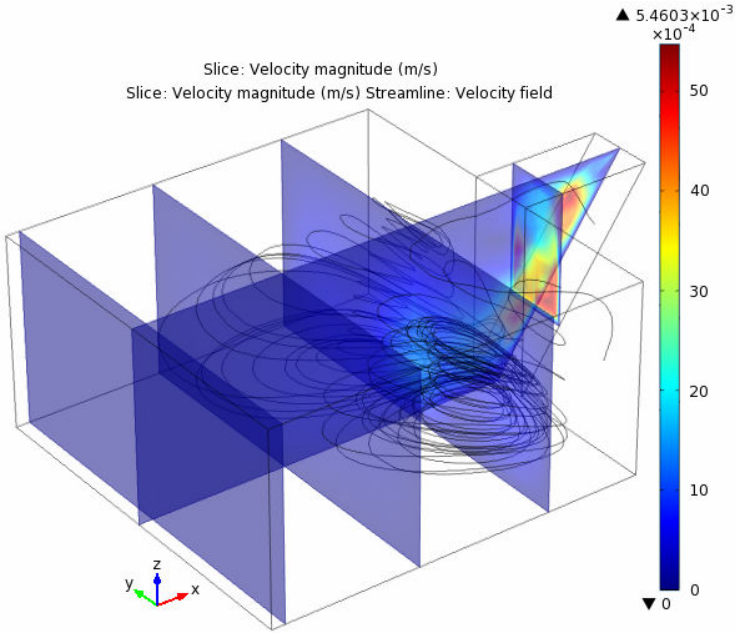

Fig. A.14 Streamlines of velocity in the molten glass bath

A.2 Conduction stirring

This paragraph is a study only from electromagnetic perspective of the possibility of electromagnetic stirring fluids of low electrical conductivity. The device is of cylindrical construction with two electrodes inside and two field coils of saddle type outside, Fig. A.15. It is called conduction stirrer because most of the current density in the molten glass is obtained by the current flow between the positive and negative electrode when they are connected to a voltage supply. The magnetic flux density is ensured by the two field coils. Such operation principle is valid with DC supply or low frequency AC supply.

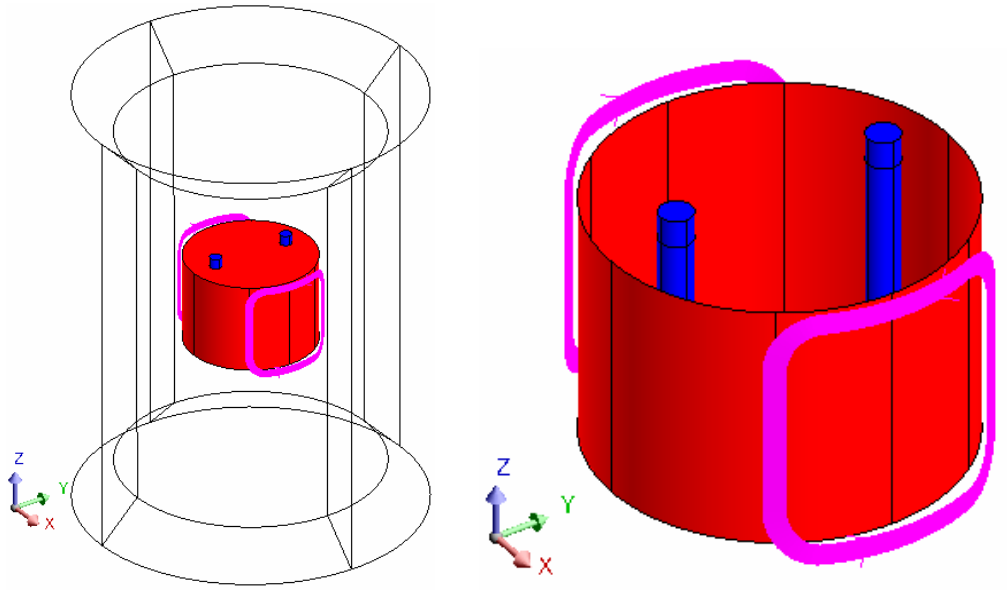

a) b)

Fig. A.15 a) Computation domain and b) detailed view of the conduction stirrer

The results refer to the following numerical application. The bath is 450 mm high and 650 mm in diameter. The two electrodes of 60 mm diameter are 400 mm high, distanced one from each other at 400 mm and the distance between bath bottom and electrodes is 100 mm. The distance between bath wall and the coil is 20 mm. The total current through the two coils is 100 kA and the voltage drop between the two electrodes is 100 V.

Being an electromagnetic calculation, the significant quantities are mainly forces and generated power. Only the electromagnetic aspect of this stirring type will be further analyzed. Even if the interest resides in studying the behavior of the molten glass under the generated electromagnetic forces, a parallel study is made with respect to the case of molten salt as a material subject to stirring and heating. The electrical resistivity of molten salt is $3.3 \cdot 10^{-3}$ Ωm, namely 20 times more conductive than the molten glass [185].

Figs. A.16 and A.17 present with arrows the magnetic flux density distribution. The structure and values are similar in the two cases due to the fact that both materials have not magnetic properties and the field in the bath is produced largely only by the two coils. Figs. A.18 and A.19 present the current density structure and orientation. The current flows between the two electrodes. The range of current density for the molten glass is $0 - 45 \cdot 10^3$ A/m^2 and for the molten salt, $0 - 250 \cdot 10^3$ A/m^2, due to the electrical conductivity difference. This affects also the magnitude of the generated force in the two cases. Figs. A.20 – A.24 present the electromagnetic force developed in the bath. The force is mainly directed along the Oz axis towards the bath bottom. The maximum local value of the force density in the molten glass is about 500 N/m^3 while in the molten salt is $10 \cdot 10^3$ N/m^3.

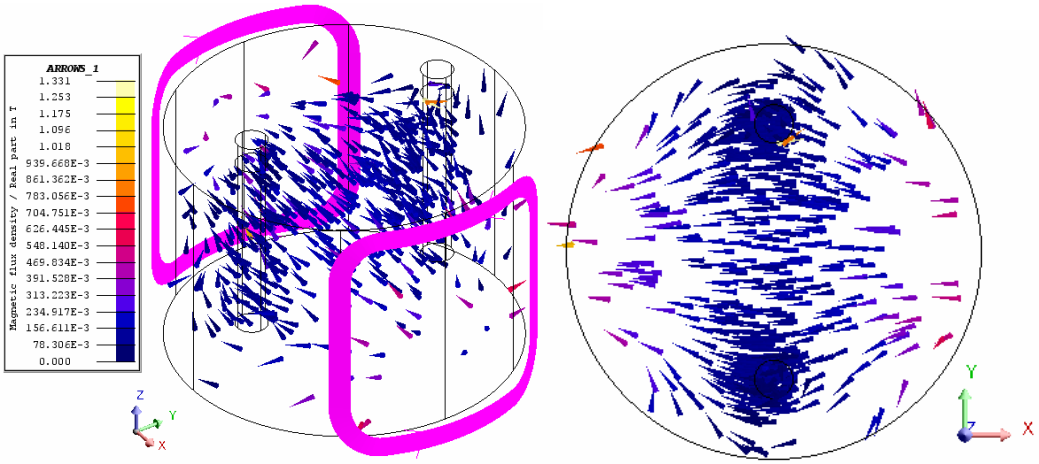

a) b)

Fig. A.16 Magnetic flux density (molten glass)

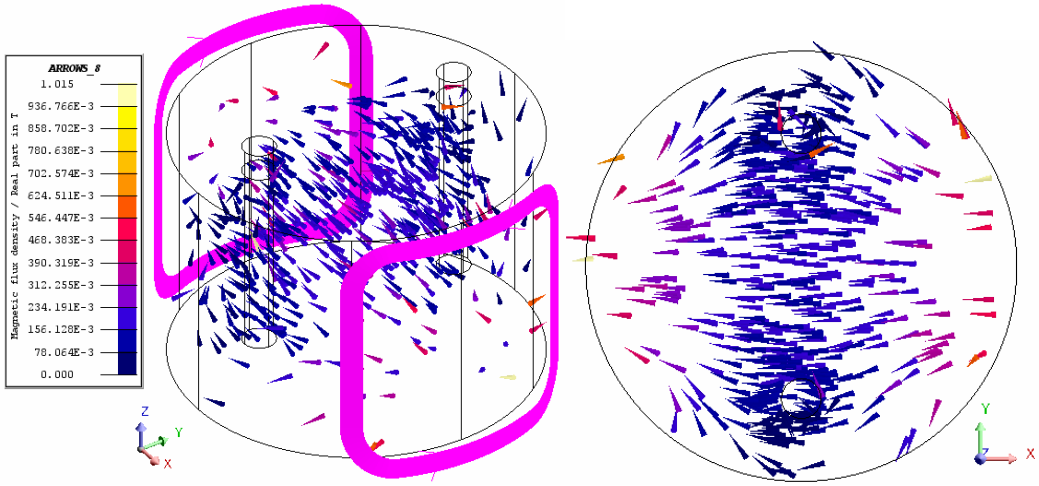

a) b)

Fig. A.17 Magnetic flux density (molten salt)

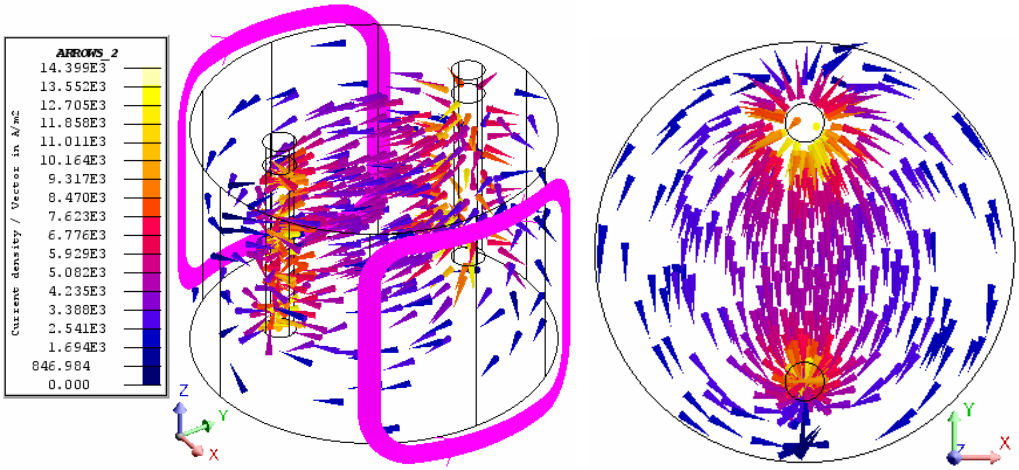

Fig. A.18 Current density in molten glass

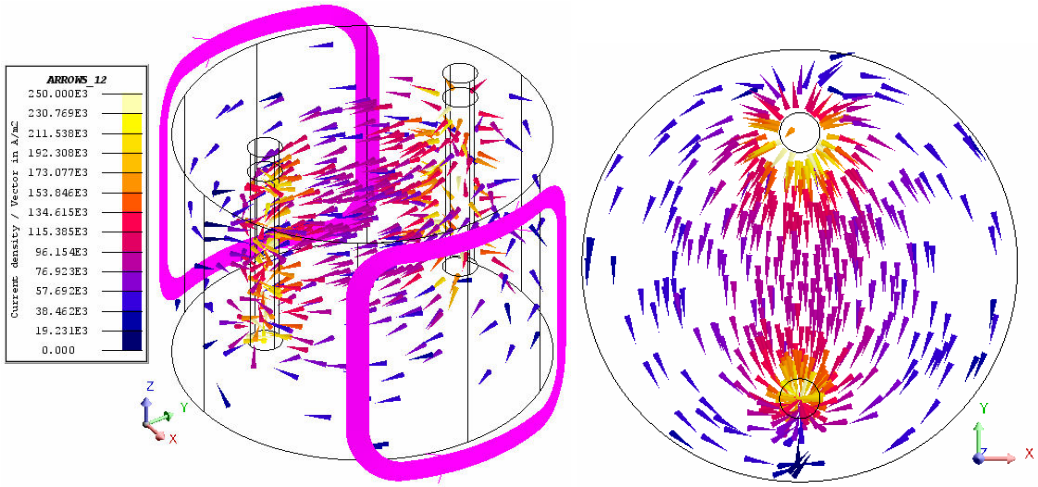

Fig. A.19 Current density in molten salt

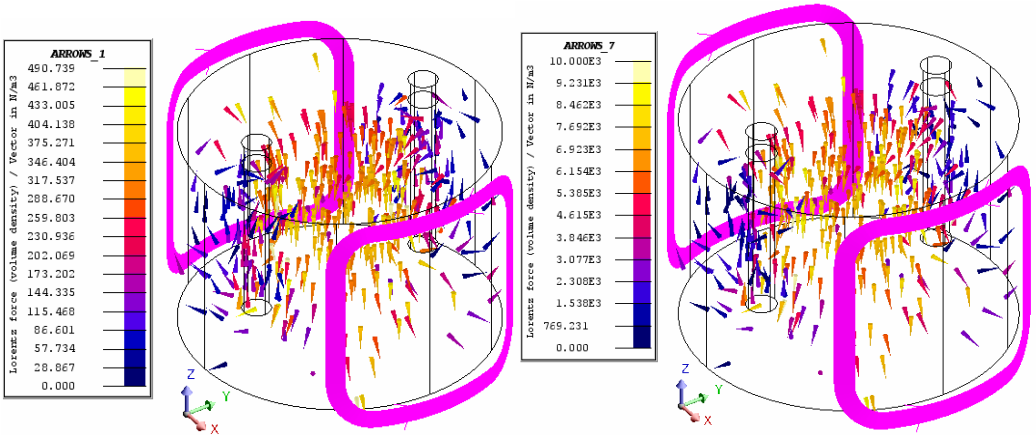

a) molten glass b) molten slat

Fig. A.20 Electromagnetic force density in a) molten glass and b) molten salt

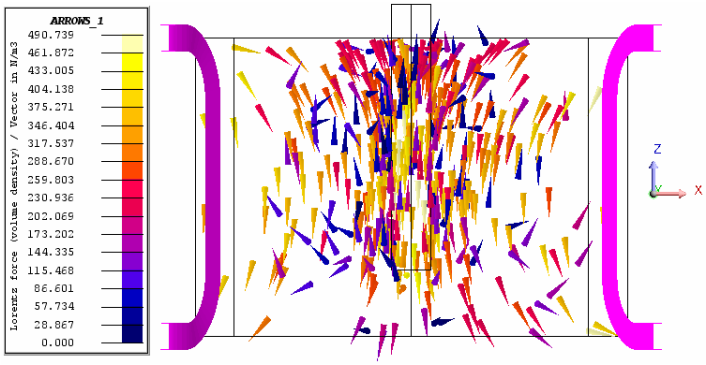

Fig. A.21 Electromagnetic force density in molten glass, lateral view 1

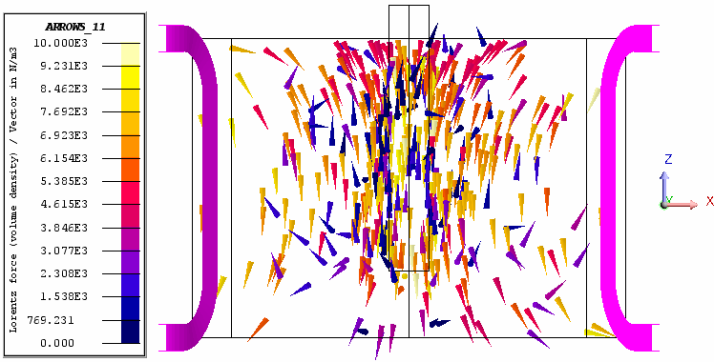

Fig. A.22 Electromagnetic force density in molten salt, lateral view 1

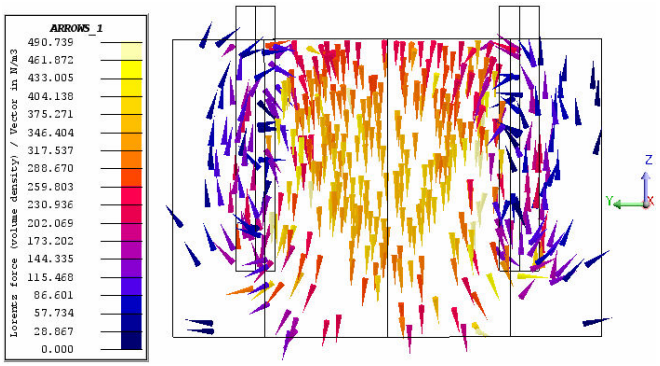

Fig. A.23 Electromagnetic force density in molten glass, lateral view 2

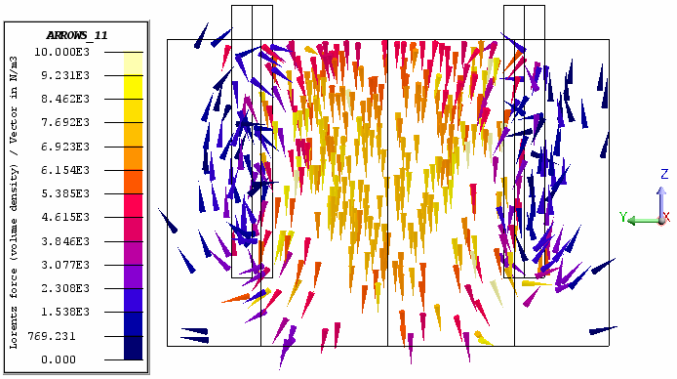

Fig. A.24 Electromagnetic force density in molten salt, lateral view 2

Beside the supply 100 V, 100 kA other combinations have been tested in order to study the behavior of the device and the impact over the stirring parameters. Table AI presents the supply parameters tested for molten salt and molten glass. For each material two sets of tests have been done, one for constant coil supply and second for constant voltage drop between electrodes while the other parameter was varied. Looking at Table AI some conclusions can be drawn.

The modulus of the total force is predominantly given by the Oz component and is acting against the axis direction towards the bottom of the bath. Taking into account the low values of the radial and azimuth components of the force it is expected the flow to be in vertical loops.

When the current through the field coils is kept constant, the volume integral of the magnetic flux density remains constant even if the electrodes voltage is modifying. This can represent an advantage over the induction-only systems, namely

the possibility of separately controlling the current density and the magnetic flux density.

When the electrodes voltage is kept constant and the coil current is varied, the magnetic energy and the magnetic flux density vary but the power injected in the bath is constant. So, there is the possibility to increase the entrainment force while the power is kept constant, since it is given mainly by the conduction current between the two electrodes.

For constant coil current, the force has a linear variation with the electrodes voltage and the power has a square variation with the electrodes voltage.

It is found that the ratio between the generated forces and powers in the cases of molten salt and molten glass is equal with the reverse of the ratio between electrical resistivities of molten salt and molten glass, as follows:

$$\frac{F_{molten\_salt}}{F_{molten\_glass}} = \frac{544.35\ N/m^3}{25.74\ N/m^3} \cong \frac{P_{molten\_salt}}{P_{molten\_glass}} = \frac{1154\ kW}{59.4\ kW} \cong \left(\frac{\rho_{molten\_salt}}{\rho_{molten\_plass}}\right)^{-1} = \left(\frac{0.0033\ \Omega m}{0.0667\ \Omega m}\right)^{-1}$$

Table AI

			integrals over the bath volume						
	Coil current [kA]	**ΔV_electrodes** [V]	**F_modulus** [N]	**F_{radial}** [N]	**$F_{azymuth}$** [N]	**F_z** [N]	**Joule power** [kW]	**Magnetic energy** [J]	**Mg flux dens** [mT]
Molten Salts rho = 0.0033 Ωm	100	10	50.93	1.77	-0.03	-50.93	11.54	2126.64	27.24
	100	20	102.63	3.54	-0.06	-102.63	46.15	2128.36	27.27
	100	100	544.35	17.52	-0.31	-544.35	1153.85	2144.60	27.54
	100	200	1166.67	34.56	-0.64	-1166.66	4615.39	2170.94	27.87
	10	100	89.52	1.53	-0.04	-89.52	1153.85	26.25	3.05
	25	100	165.32	4.20	-0.09	-165.32	1153.85	140.24	7.13
	50	100	291.67	8.64	-0.16	-291.66	1153.85	542.73	13.64
	100	100	544.35	17.52	-0.31	-544.35	1153.85	2144.60	27.54
	150	100	797.04	26.40	-0.46	-797.03	1153.85	4808.92	41.14
	200	100	1049.73	35.28	-0.61	-1049.71	1153.85	8535.75	54.74
Molten Glass rho = 0.066 Ωm	100	10	2.56	0.09	0.00	-2.56	0.59	2125.06	27.21
	100	20	5.13	0.17	0.00	-5.13	2.38	2125.14	27.21
	100	100	25.74	0.87	-0.02	-25.74	59.41	2125.82	27.22
	100	200	51.69	1.74	-0.03	-51.69	237.64	2126.67	27.24
	10	100	2.66	0.09	0.00	-2.66	59.41	21.34	2.73
	25	100	6.51	0.22	0.00	-6.51	59.41	133.03	6.82
	50	100	12.92	0.43	-0.01	-12.92	59.41	531.67	13.62
	100	100	25.74	0.87	-0.02	-25.74	59.41	2125.82	27.22
	150	100	38.56	1.31	-0.02	-38.56	59.41	4782.45	40.82
	200	100	51.39	1.74	-0.03	-51.38	59.41	8501.58	54.43

A.3 Rotating field induction stirring

This paragraph represents another system of electromagnetic stirring of electroconductive fluids in cylindrical baths. The results presented in this paragraph are corresponding to a magnetohydrodynamic analysis.

Fig. A.25 is a top view of the device that consists of cylindrical molten glass bath, eight vertical metallic segments representing an eight phase supply equivalent to a squirrel cage of an asynchronous motor and an exterior magnetic yoke. The bath is 620 mm in diameter and 450 mm high. The thickness of the magnetic yoke is 200 mm and the thickness of the winding is 40 mm. The total current through each coil is 120 kA and the supply frequency is 1 kHz. The eight phase inductor generates a rotating electromagnetic field.

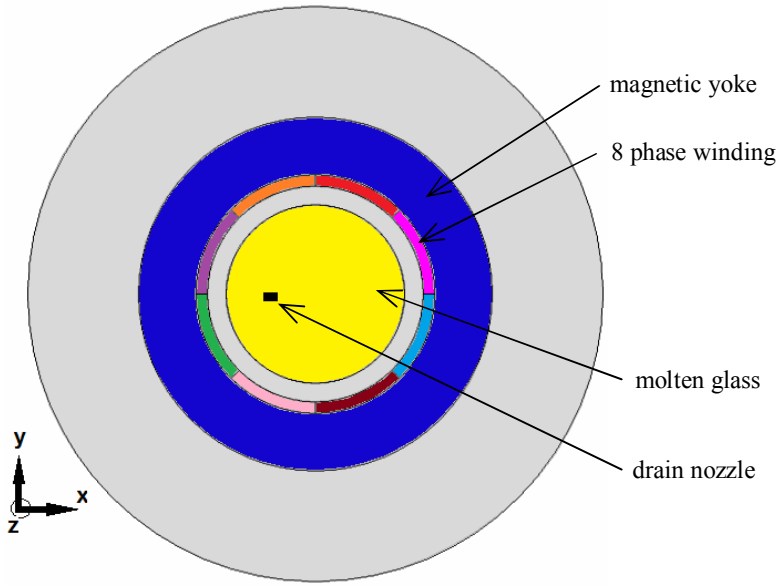

Fig. A.25 Induction stirring and heating device for molten glass

For the flow problem it was used a laminar model with standard null velocity at the wall and it was solved in the time domain with adjustable time step. The electromagnetic problem was solved in the frequency domain and the up-date with the force density in the hydrodynamic problem and with the velocity field in the electromagnetic problem was done at each time step.

Fig. A.26 presents the magnetic flux density in the entire computation domain. The magnetic flux density is maximum in the magnetic core and quasi-constant in the molten glass bath, which is around 0.9 T. Fig. A.28 gives the magnetic flux density in the molten glass region. It can be observed a very small azimuth non-uniformity of the electromagnetic field in the proximity of the segments.

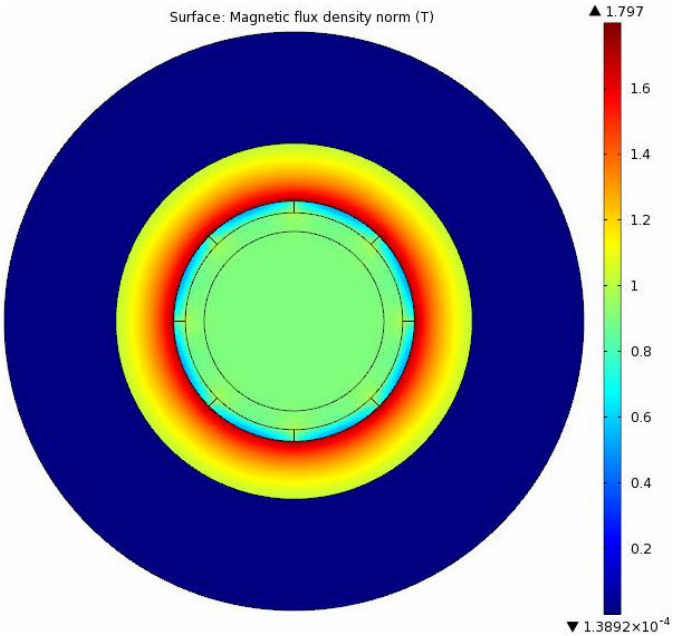

Fig. A.26 Magnetic flux density over entire computation domain

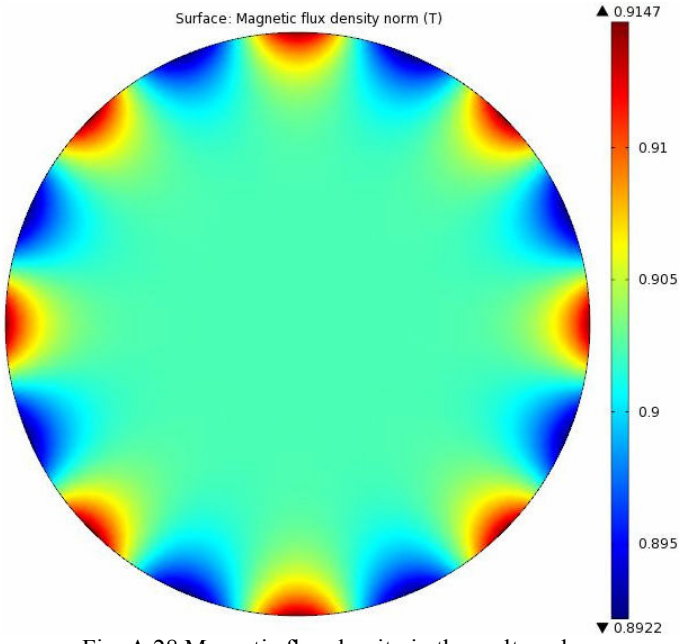

Fig. A.28 Magnetic flux density in the molten glass

Fig. A.29 presents the module of the current density induced in the molten glass. The magnitude of the generated force density is showed in Fig. A.30 with colors and the direction with arrows. Due to the decrease of the term **v** x **B** in the Ohm's law in the region close to the wall, due to the diminishing of the velocity in the limit layer, the force is also decreasing close to the wall.

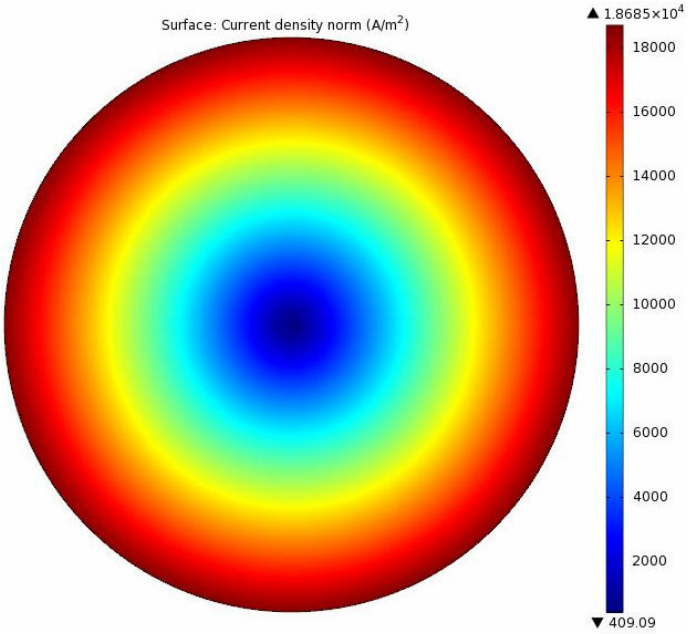

Fig. A.29 Module of current density in the molten glass

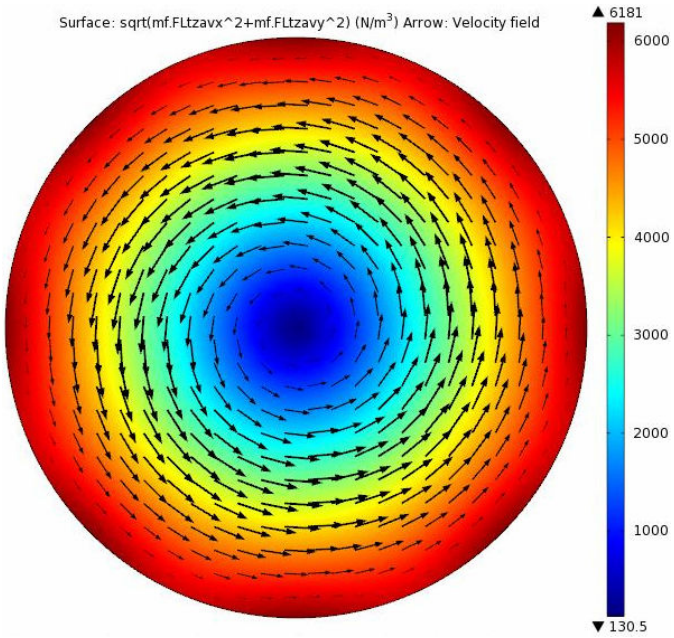

Fig. A.30 Volume force density in the molten glass

Fig. A.31 presents the orientation and magnitude of the velocity. The flow is circular, as the field propagation direction and the maximum velocity is 0.55 m/s.

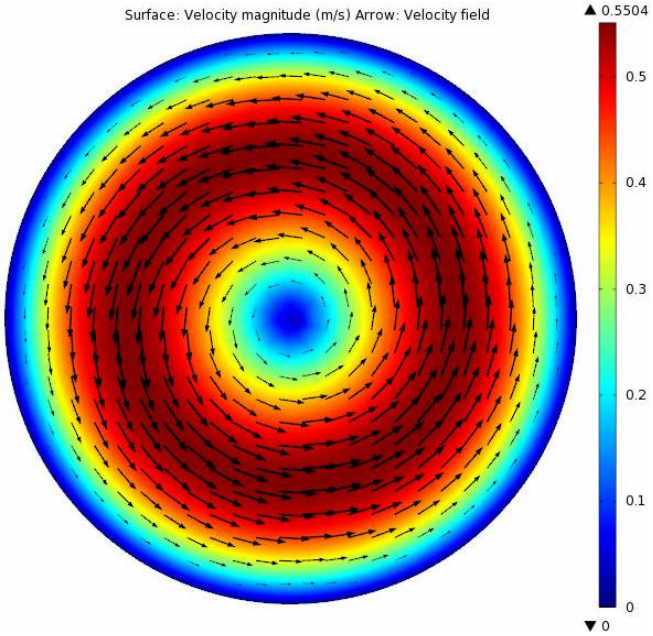

Fig. A.31 Velocity field represented in colors and arrows

The influence of the supply parameters current and frequency on electromagnetic and hydrodynamic quantities is given in Table AII. The various supply combinations give an insight over the contribution of each parameter to the maximum speed obtained, power, or the stirring torque generated by the azimuthally oriented force.

Table AII

Current	**Frequency**	**P_glass**	**B_glass_max**	**U_max**	**Flow rate**	**U_mean**	**Torque**
[kA]	[kHz]	[kW]	[T]	[m/s]	[dm^3/s]	[m/s]	[Nm]
120	1.00	785.8	0.915	0.550	49.7	0.356	126.97
120	0.50	196.5	0.915	0.275	24.8	0.178	63.48
60	1.00	196.5	0.457	0.137	12.4	0.089	31.75
240	0.25	164.7	1.660	0.461	41.6	0.298	106.00

The velocity, the flow rate and the torque are doubling and the magnetic flux density remains constant when the frequency is doubled. When the current is doubled the first group of quantities increases four times and the magnetic flux density increases two times. The power responds similar in both situation of doubling frequency or current.

The last two lines analyses a combined action of the two parameters. By doubling the current and decreasing two times the frequency it is possible to double all the other quantities and keeping the power constant. By doubling the current and decreasing four times the frequency, the power is decreased almost five times, magnetic flux density is increased 1.8 times and the other quantities have a small decrease of 1.2 times. Thus, in order to have an important decrease of power and only a small loss of velocity such strategy can be useful.

The influences of the supply parameters over the velocity profiles are presented in the following three pictures. Fig. A.32 presents the velocity profiles along the diameter for the supply parameters that respect the invariant product between supply current and frequency. Although keeping the product constant can

have the effect of keeping the generated power in the same range, the separate influence of frequency and current is important for the local structure of the velocity profile.

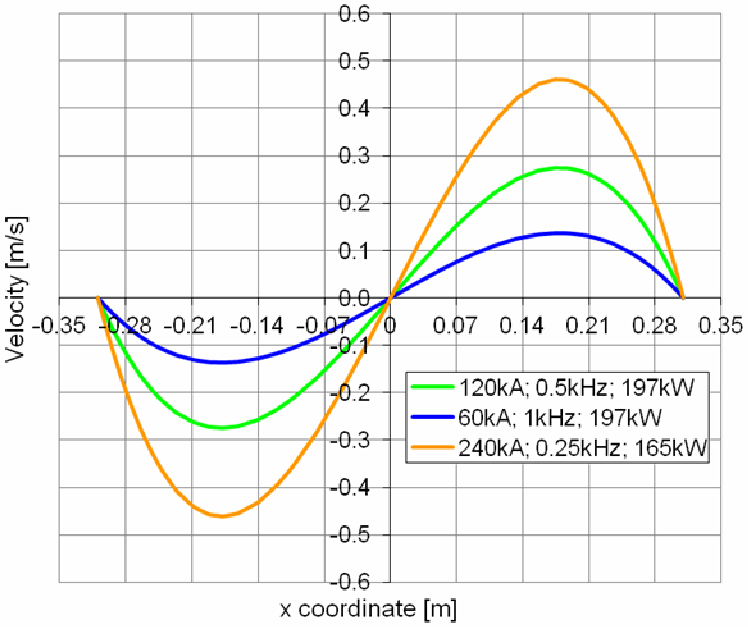

Fig. A.32 Velocity profiles along diameter for constant product (current x frequency)

Fig. A.33 highlights the influence of the supply current on the velocity profile, respectively on the mean velocity. Doubling the current has the effect of four times increase of the maximum velocity and of the power. The influence of frequency over the velocity profiles is given in Fig. A.34.

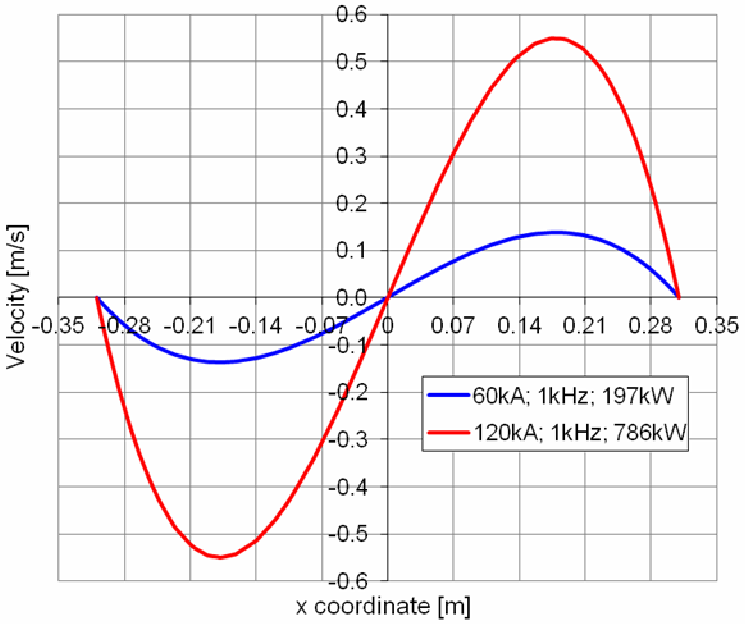

Fig. A.33 Velocity profiles along diameter for current influence

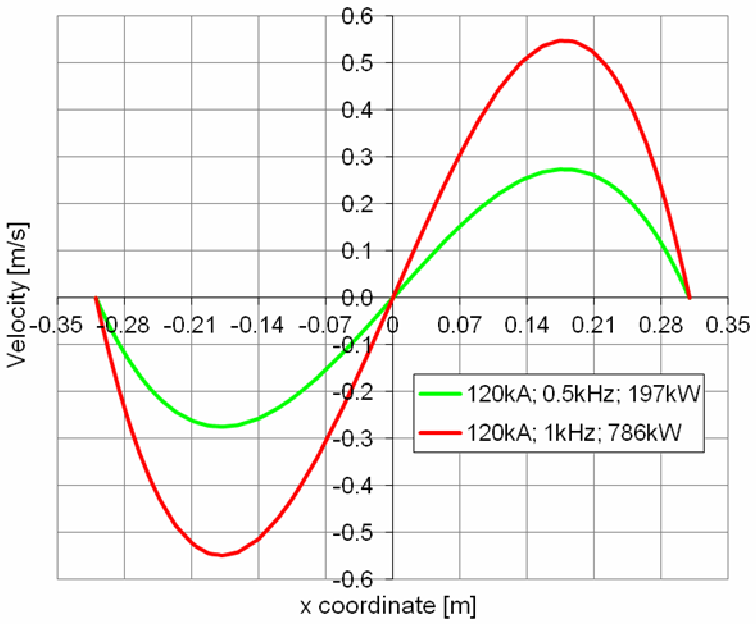

Fig. A.34 Velocity profiles along diameter for frequency influence

The combined influence of the current and frequency aver the velocity profile is given in Fig. A.35. Namely this figure shows the correspondent velocity profile for each line of Table AII.

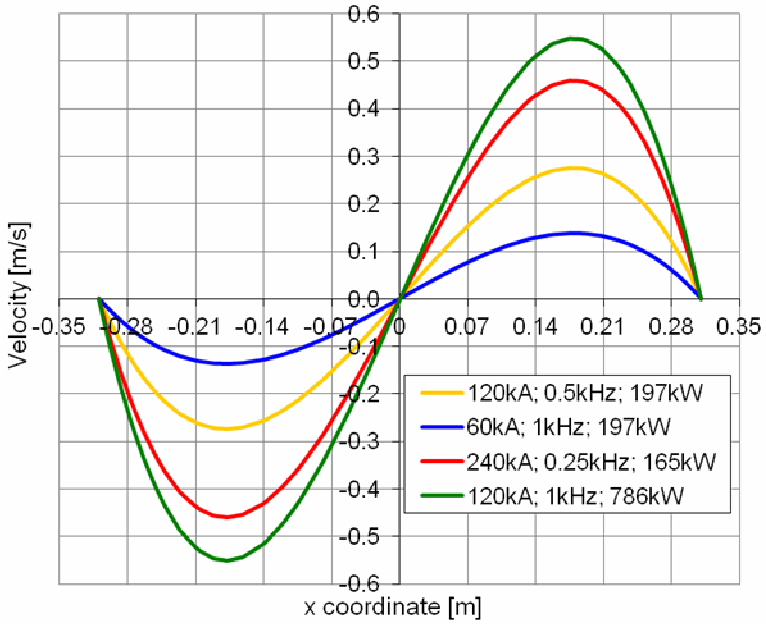

Fig. A.35 Velocity profiles along diameter for frequency and current influence

Some variation of viscosity may intervene during overheat or cooling. This can have in impact on the flow. Fig. A.36 presents a study of the dynamic viscosity influence on the velocity profile, in the case of 120 kA, 1 kHz supply conditions. As expected, a decrease of viscosity determines an increase of the velocity.

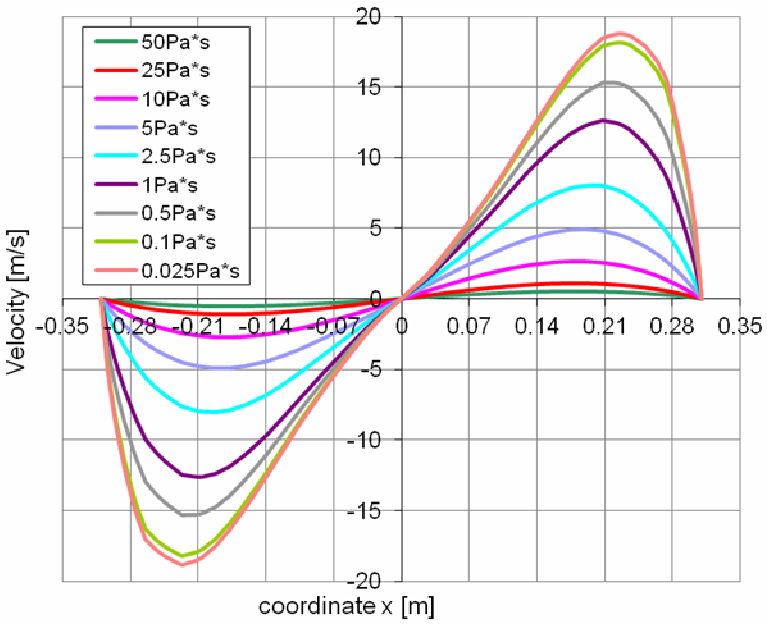

Fig. A.36 Influence of viscosity over velocity profiles

CONCLUSIONS

This annex treated a very close subject to electromagnetic pumping, respectively electromagnetic stirring. The study contains three variants of electromagnetic stirring and offers parallel information about the dependence of each stirring type capacity on the conductivity and viscosity of various electroconductive liquids.

As a concept, the traveling field induction stirring is very much related to the Flat Linear Induction Pump presented in paragraph 3.1.5. The stirring devices built on this basis present the advantage of using the inductor for double role, to stir and to empty the furnace bath.

The structure of the conduction stirring devices is related to the conduction pump presented in paragraph 3.2.2. It is based on two independent sources, namely two electrodes immersed in the bath mainly for the electric current generation in the liquid and field coils for electromagnetic field. This type of stirring presents the advantage that for a certain range of generated forces various combinations of values of the two supply sources can provide situations with predominant stirring effect or situations where not only the stirring effect is present but also an important heating through Joule effect.

The device presented in the last paragraph generates a rotating field through electromagnetic induction. The concept is similar to a squirrel cage of an induction machine. The main advantage of such structure is that if in the phase prior to stirring the material is solid, the inductor can be used firstly for melting and after for stirring with out making appeal to two working phases or two different machines.

Each stirring type has its advantages and disadvantages and choosing one or another is a matter of specific needs that take into account the industry type, exploitation conditions, nature of the electroconductive fluid, etc. For any type, the generated force for stirring and the maximum velocity are functions of fluid resistivity, supply parameters and bath dimensions.

BIBLIOGRAPHY

[1] *M. S. Tillack, N. B. Morley*, Magnetohydrodynamics, McGraw Hill, 14th Edition, 1998.

[2] *S. Asai*, Recent development and prospect of electromagnetic processing of materials, Science and Technology of Advanced Materials, Volume 1, Issue 4, December 2000, pp. 191-200.

[3] *A. Gailitis, O. Lielausis, E. Platacis, G. Gerbeth, F. Stefani*, The riga dynamo experiment, Surveys in Geophysics 24: 247-167, 2003.

[4] https://en.wikipedia.org/wiki/Dynamo_theory.

[5] *A. Gailitis, G. Gerbeth, T. Gundrum, O. Lielausis, E. Platacis, F. Stefani*, History and results of the Riga dynamo experiments, Elsevier Science, July 2008.

[6] *W. Elsasser*, On the origin of the Earth's magnetic field, Phys Rev 55:489-498, 1939.

[7] *W. Elsasser*, Hydromagnetism. I. a review, Am J Phys 23:590-609, 1955.

[8] *W. Elsasser*, Hydromagnetism. II. a review, Am J Phys 24:85-110, 1955.

[9] *W. Elsasser*, The hydromagnetic equations, Phys Rev 79:183, 1950.

[10] *W. Elsasser*, Induction effects in terrestrial magnetism. Part II. The secular variation, Phys Rev 70:202-212, 1946.

[11] *E. C. Bullard, H. Gellman*, Homogeneous dynamos and terrestrial magnetism, Philos Trans R Soc Lond A247:213-278.

[12] *U. Müller, R. Stieglitz*, The Geodynamo: models and supporting experiments, Forschungszentrum Karlsruhe GmbH, Karlsruhe, 2003.

[13] *V. Courtillot, J. L. Le Mouel*, Time variations of the Earth's magnetic field: from daily to secular, Ann. Rev. Earth Planet. Sci. pp. 389-476, 1988.

[14] *J. Hartmann*, Hg-Dynamics I. Theory of the laminar flow of an electrically conductive liquid in a homogeneous magnetic field, Det Kgl Danske Vid Sels Mat-Fys Medd XV(6):1-27, 1937.

[15] *J. Hartmann, F. Lazarus*, Hg-Dynamics II. Experimental investigations on the flow of mercury in a homogeneous magnetic field. Det Kgl Danske Vid Sels Mat-Fys Medd XV(7):1-45, 1937.

[16] *H. Alfvén*, Existence of electromagnetic-hydrodynamic waves, Nature 150:405-406, 1942.

[17] *H. Alfvén*, On the existence of electromagnetic-hydrodynamic waves, Arkiv F Mat Astron Fys 29B(2):1-7, 1943.

[18] *T. G. Cowling*, The magnetic field of sunspots, Mon Not R Astr Soc 94:39-48, 1933.

[19] *T. E. Markusic, K. A. Polzin, A. Dehoyos*, Electromagnetic pump for conductive-propellant feed systems, Proceedings of the 29th International Electric Propulsion conference, Princeton University, November 2005.

[20] *Z. Kulenović*, Stress concentration in an element of ship's electromagnetic pump, Proceedings of the 47th International Sympsoum ELMAR, Croatia, June 2005.

[21] *H. Araseki*, Method for measuring discharge quantity of electromagnetic pump – European Patent, date of publication 30.03.2011.

[22] *E. M. Borges, F. A. Braz Filho, L. N. Guimarães*, Liquid metal flow control by DC electromagnetic pumps, Engenharia Térmica (Thermal Engineering), Vol. 9, No. 01 e 02, pp. 47-54, December 2010.

[23] *T. J. Lutz, R. E. Nygren, T. J. Tanaka, J. M. McDonald, F. J. Bauer, K. P. Troncosa, M. A. Ulrickson*, Measurements of lithium flow with an EM flow meter in LIMITS, Proceedings of IEEE/NPSS Symposium Fusion Engineering, pp. 367-370, 2003.

[24] *E. P. Loewen, A. T. Tokuhiro*, Status of research and development of the lead-alloy-cooled fast reactor, Journal of Nuclear Science and Technology, Vol. 40, No. 8, p. 614-627, August 2003.

[25] *I. Silverman, A. L. Yarin, S. N. Reznik, A. Arenshtam, D. Kijet, A. Nagler*, High heat-flux accelerator targets: Cooling with liquid metal jet impingement, International Journal of Heat and Mass Transfer 49 (2006) 2782-2792.
[26] *C. C. Yang, S. Kraus*, A large electro-magnetic pump for high temperature LMFBR applications, Nuclear Engineering and Design 44 (1977) 383-395.
[27] *V. Fireţeanu*, Electromagnetic pumping of liquid metals (in Romanian language), Technical Press, Bucharest, 1986.
[28] *I. Doležel, V. Kotlan, B. Ulrych*, Magnetohydrodynamic pumps for molten salts in cooling loops, of high-temperature nuclear reactors, Przeglad Elektrotechniczny (Electrical Review), ISSN 0033-2097, R. 87 Nr 5/2011.
[29] *J. Etay, V. Fireţeanu, Y. Fautrelle, C. Roman*, Proceedings of 12th International Conference on Optimization of Electrical and Electronic Equipment (OPTIM), ISSN 1842-0133, ISBN 978-973-131-080-0, pp. EMID.2.1.03, May 2010.
[30] *C. Roman, J. Etay, Y. Fautrelle, V. Fireţeanu*, An overview on solar energy, molten salts and electromagnetic pumping technologies, Proceedings of 10th International Conference on Environment and Electrical Engineering (EEEIC), Rome, Italy, 2011.
[31] *C. Roman, J. Etay, Y. Fautrelle, V. Fireţeanu*, Study on electromagnetic pumping systems for molten salts based on 3D finite element models, Proceedings of ELECTRIMACS Conference, June 2011.
[32] *C. Roman, V. Fireteanu*, The 3D multiphysisc model and finite element analysis of conduction electromagnetic pumping system for molten salts, Proceedings of 7th International Symposium on Advanced Topics in Electrical Engineering (ATEE), ISSN 2068-7966, pp. 353-356, 2011.
[33] *D. LeBlanc*, Molten salt reactors: A new beginning for an old idea, Nuclear Engineering and Design 240 (2010) 1644-1656.
[34] *E. Sauvage*, Modélisation numérique thermo-hydrodynamique et inductive d'une fonte verrière élaborée en creuset froid inductif (PhD Thesis at Grenoble Institute of Technology), 2009.
[35] *J. A. Shercliff*, A textbook of magnetohydrodynamics, Pregamon Press, London, 1965.
[36] *SirD. Humphrey*, Magnetic field deflects arc, Phil. Trans. Roy. Soc. p. 427, 1821.
[37] *M. Faraday*, Induceed e.m.f.s and currents in moving liquids, Phil. Trans. Roy. Soc. p. 163, 1832.
[38] *W. Ritchie*, Electromagnetic force propels liquid, Phil. Trans. Roy. Soc. p. 294, 1832.
[39] *C. Wollaston*, Induced e.m.f.s in sea, measured in 1851, J. Soc. Tel. Engrs, 1881.
[40] *L. Leduc*, MHD magnetometer, J. Phys. Theor. Appl. (2e serie) 6, 84, 1887.
[41] *E. F. Northrup*, Theory and experiments on pinch-efect; electromagnetic pump, Phys. Rev. 24, 474, 1907.
[42] *Sir J. Larmmor*, Suggestion of solar dynamo, Engineering 108, 461, 1919.
[43] *C. Petersen*, MHD generator (U.S. Patent 1443091), 1919.
[44] *F. B. Young et al.*, Induced e.m.f.s in sea, Phil. Mag. 40, 149, 1920.
[45] *E. J. Williams*, Fluid motions due to electric currents in non-uniform fields, Phil. Mag. 50, 27, 1925.
[46] *J. Hartmann*, Mercury jet wave rectifier, Engineering 124, 338 and 377, also 132, 354, 1927.
[47] *A. Einstein, L. Szilard*, DC and AC electromagnetic pumps, Brit. Patent 344881, 1929.
[48] *E. J. Williams*, Flow in pipes under transverse magnetic field, Proc. Phys. Soc. 42, 466, 1930.
[49] *T. G. Cowling*, Solar dynamo theoy, Mon. Not. Roy. Astr. Soc. 94, 39, 1934.
[50] *W. Bennet*, Theory of pinch-effect in plasma, Phys. Rev. 45, 890, 1934.
[51] *B. Karlowitz, D. Halasz*, MHD generator (U.S. Patent), 1936.

[52] *J. Hartmann*, Flow in pipes under transverse magnetic field, Math.-fys. Medd. 15, Nos. 6 and 7, 1937.
[53] *V. C. A. Ferraro*, Behaviour of magnetic field in rotating star, Mon. Not. Roy. Astr. Soc. 97, 458, 1937.
[54] *L. Biermann*, Magnetic field inhibits convection, Vierteljahrschrift Astr. Geophys. 76, 194, 1941.
[55] *H. Alfven*, Discovery of Alfven waves, Nature 150, 405, 1942.
[56] *C. Walen*, Another view of Alfven waves, Ark. Math. Astr. Fys. 30A, No. 15, 1944.
[57] *S. Molokov, R. Moreau, H. K. Moffatt*, Magnetohydrodynamics – Historical Evolution and trends, ISBN 978-1-4020-4833-3, Springer, 2007.
[58] *E. F. Northrup*, Some newly observed manifestation of forces in the interior of an electrical conductor, Phys. Rev. 24 (6), pp. 474, 1907.
[59] *G. Dannen*, The Einstein-Szilard refrigerators, Sci Am, 276(1): 90-5, 1997.
[60] *H. Etherington*, Nuclear engineering handbook, McGraw-Hill, New York, 1958.
[61] *M. Trainer*, Albert Einstein's patents, World Patent Information 28 (2006) 159-165.
[62] *A. F. Kolesnichenko*, Electromagnetic processes in liquid material in the USSR and Eastern European Countries, Iron and Steel Institute of Japan (ISIJ) 30(1) pp. 8-26, 1990.
[63] *P. Sporn, A. Kantrowitz*, Magnetohydrodynamics: Future power process?, Power 103(11), pp. 62-65, 1959.
[64] *L. Steg, G. W. Sutton*, Prospects of MHD power generation, Astronautics 5, pp. 22-25, 1960.
[65] *P. Graneau*, Electrodynamic seawater jet: an alternative to the propeller?, IEEE Transactions on Magnetics 25(5) pp. 3275-3277, 1989.
[66] *S. Morota, K. Imaichi, M. Nakato, S. Takezawa*, An outline of the R&D project on supra conducting MHD ship propulsion, Proceedings MHDS Conference, pp. 53-68, 1991.
[67] *A. Tsinober*, MHD flow drag reduction, Viscous Drag Reduction in Boundary Layers, 1990.
[68] *C. C. Baker, R. W. Conn, F. Najmabadi, M. S. Tillack*, Status and prospects for fusion energy from magnetically confined plasmas, Energy 23 (7/8), pp. 649-694, 1998.
[69] *C. A. Borghi, A. Cristofolini, M. Fabbri*, Study of the design model of a liquid metal induction pump, IEEE Transactions on magnetics, Vol. 34. No. 5, September 1998.
[70] *P. Blanc, T. T. Xuan, R. Deshais*, Design calculations for annular induction electromagnetic pumps based on the finite element method, IEEE Transactions on magnetics, Vol. Mag.-18, No. 2, March 1982.
[71] *L. Liyi, C. S. Mei, Z. Ping, G. Xiangcheng, C. Shukang, W. Ying*, Experimental study on a novel linear electromagnetic pumping unit, IEEE Transactions on magnetics, Vol. 37, No. 1, January 2001.
[72] *P. J. Wang, C. Y. Chang, M. L. Chang*, Simulation of two-dimensional fully developed laminar flow for a magneto-hydrodynamic (MHD) pump, Biosensors and Bioelectronics 20 (2004) 115-121.
[73] *A. Demenko, J. K. Sykulski, R. Wojciechowski*, Calculation of inducted currents using edge elements and T-T_0 formulation, IEEE Transactions on magnetics 38(2), pp. 1305-08, 2008.
[74] *R. M. Kojciechowski, C. Jedryczka, W. Szelag, A. Demenko*, Description of multiply connected regions with induced currents using T-T_0 method, Progress In Electromagnetics research B, Vol. 43, 279-294, 2012.
[75] *R. Specogna, S. Suuriniemi, F. Trevisan*, Geometric T-Ω approach to solve eddy currents coupled to electric circuits, International Journal for Numerical Methods in Engineering 74:101-115, 2008.

[76] *S. Kanerva*, Simulation of electrical machines, circuits and control systems using finite element method and system simulator (PhD Thesis at Helsinki University of Technology, 2005).
[77] *L. Leboucher, P. Marty, A. Alemany*, An inverse method in electromagnetism applied to the optimization of inductors, IEEE Transactions on magnetics, Vol. 28, No. 5, September 1992.
[78] *A. M. Georgescu, S. C. Georgescu, S. Bernad, C. I. Coşoiu*, COMSOL multiphysics versus FLUENT: 2D numerical simulation of the stationary flow around a blade of the Achard turbine, Scientific Bulletin of the POLITEHNICA University of Timişoara, Transactions on mechanics, Tom 52(66), Fascicola 3, 2007.
[79] *S. Vantieghem*, Numerical simulations of quasi-static magnetohydrodynamics using an unstructured finite volume solver: development and applications (PhD Thesis at Université Libre de Bruxelles, 2011).
[80] *S. Aleksandrova, S. Molokov, C. B. Reed*, Modelling of liquid metal duct and free-surface flows using CFX, available electronically at http://www.doe.gov/bridge.
[81] *I. R. Kirilov, D. M. Obukhov, A. P. Ogorodnikov, H. Araseki*, Comparisn of computer codes for evaluation of double-supply-frequency pulsations in linear induction pumps, Nuclear Engineering and Design 231 92004) 17-185.
[82] *G. Sposito, M. Ciofalo*, One-dimensional mixed MHD convection, International Journal of Heat and Mass Transfer 49 (2006) 2939-2949.
[83] *N. Takorabet*, Computation of force density inside the channel of an electromagnetic pump by Hermite projection, IEEE Transactions on magnetics, Vol. 42, No. 3, March 2006.
[84] *R. Samulyak, Y. Prykarpatskyy*, Richtmyer-Meshkov instability in liquid metal flows: influence of cavitation and magnetic fields, Mathematics and Computers in Simulation 65 (2004) 431-446.
[85] *I. R. Kirilov, A. P. Ogorodnikov, V. P. Ostapenko*, Experimental investigations of flow nonuniformity in a cylindrical linear induction pump, 1980.
[86] *I. R. Kirilov, V. P. Ostapenko*, Local characteristics of a cylindrical induction pump for Rms>1, 1987.
[87] *B. G. Karasev, I. R. Kirilov, A. P. Ogorodnikov*, 3500 m^3/h MHD pump for fast breeder reactor, 1989.
[88] *F. Werkoff*, Finite-length effects and stability of electromagnetic pumps, Experimental Thermal and Fluid Science 4:166-170, 1991.
[89] *H. Araseki, I. R. Kirilov, G. V. Preslitsky, A. P. Ogorodnikov*, Double-supply-frequency pressure pulsation in annular linear induction pump. Part I: Measurement and numerical analysis, Nuclear Engineering and Design 195 (2000) 85-100.
[90] *H. Araseki, I. R. Kirilov, G. V. Preslitsky, A. P. Ogorodnikov*, Double-supply-frequency pressure pulsation in annular linear induction pump. Part II: Reduction of pulsation by linear winding grading at both stator ends, Nuclear Engineering and Design 200 (2000) 397-406.
[91] *I. R. Kirilov, D. M. Obukhov*, Two dimensional model for analysis of cylindrical linear induction pump characteristics: model description and numerical analysis, Energy Conversion and Management 44 (2003) 2687-2697.
[92] *C. Yamahata, C. Lotto, E. Al-Assaf, M. A. M. Gijs*, A PMMA valveless micropump using electromagnetic actuation, Microfluid Nanofluid (2005) 1:197-207.
[93] *H. Araseki, I. R. Kirilov, G. V. Preslitsky, A. P. Ogorodnikov*, Magnetohydrodynamic instability in annular linear induction pump. Part I. Experiment and numerical analysis, Nuclear Engineering and Design 227 (2004) 29-50.
[94] *H. Araseki, I. R. Kirilov, G. V. Preslitsky, A. P. Ogorodnikov*, Magnetohydrodynamic instability in annular linear induction pump. Part II.

Suppression of instability by phase shift, Nuclear Engineering and Design 236 (2006) 965-974.

[95] *H. Araseki, I. R. Kirilov, G. V. Preslitsky*, Sodium flow rate measurement method of annular linear induction pumps, Nuclear Engineering and Design 243 (2012), 111-119.

[96] *T. Ando, K. Ueno, S. Taniguchi, T. Takagi*, Induction pump for high-temperature molten metals using rotating twisted magnetic field: molten gallium experiment, IEEE Transactions on magnetics, Vol. 40, No. 4, July 2004.

[97] *K. Ueno, T. Ando, S. Taniguchi, T. Takagi*, Axial driving force induced by rotating twisted magnetic field, Proceedings of International Symposium Electromagnetic Processing of Materials, pp. 491-496, 2000.

[98] *T. Ando, K. Ueno, S. Taniguchi, T. Takagi*, Induction pump for high-temperature molten metals using rotating twisted magnetic field: Thrust measurement experiment with solid conductors, IEEE Transactions on magnetics, Vol. 38, pp. 1789-1796, 2002.

[99] *T. Ando, K. Ueno, S. Taniguchi, T.* Takagi, Visual system experiment of MHD pump using rotating twisted magnetic field applicable to high-temperature molten metals, Iron and Steel Institute of Japan (ISIJ), Vol. 43, pp. 849-854, 2003.

[100] *V. Teotia, S. Malhotra, K. Singh, U. Mahapatra*, Analysis and design of electromagnetic pump, Proceedings of the COMSOL Conference, India, 2010.

[101] *P. Sharma, L. S. Sivakumar, R. R. Prasad, D. K. Saxena, V. A. Suresh Kumar, B. K. Nashine, I. B. Noushad, K. K. Rajan, P. Kalyanasundaram*, Design, development and testing of a large capacity annular linear induction pump, Energy Procedia 7 (2011) 622-629.

[102] *H. R. Kim, Y. B. Lee*, MHD stability analysis of a liquid sodium flow at the annular gap of an EM pump, Annals of Nuclear Energy 43 (2012) 8-12.

[103] *Y. Feng, J. Seyed-Yagoobi*, Understanding of electrohydrodynamic conduction pumping phenomenon, Physics of fluids, Vol. 16, No. 7, July 2004.

[104] *R. Bonnefille, M. Kant*, Application de la théorie du champ électromagnétique aux machines linéaires, a induction, Revue de physique appliqué, Tome 5, p. 743-757, 1970.

[105] *R. S. Baker, M. J. Tessier*, Handbook of electromagnetic pump technology, Elsevier, New York, 1987.

[106] *S. J. Chapman*, Electric machinery fundamentals, McGraw Hill International Edition, 1998.

[107] *S. Poitout, P. J. Costa Branco*, Theoretical modeling and experimental tests of an electromagnetic fluid transportation system driven by a linear induction motor, IEEE Transaction on magnetics Vol. 42, No. 9, September 2006.

[108] *X. Dong, G. Mi, L. He, P. Li*, 3D simulation of plane induction electromagnetic pump for the supply of liquid Al-Si alloys during casting, Journal of Materials Processing Technology (2013), DOI: http://dx.doi.org/doi:10.1016/j.jmatprotec.2013.03.006.

[109] *A. T. Al-Halhouli, M. I. Kilani, S. Büttgenbach*, Development of a novel electromagnetic pump for biomedical applications, Sensors and Actuators A 162 (2010) 172-176.

[110] *J. K. Sykulski*, Modern design of electromechanical devices, Proceedings of XLIIIrd International Symposium on electrical Machines, Poznan, Poland, 2007.

[111] *S. H. Seong, S. O. Kim*, Analyses of annular linear induction pump characteristics using a time-harmonic finite difference analysis, Nuclear Engineering and Technology, Vol. 40, No. 3, April 2008.

[112] *N. Shamsuddeen, A. Ankit, J. Rajendrakumar, V. Krishna, V. Jayashankar*, Design and analysis of annular linear induction pump (ALIP), IEEE Transactions on magnetics, 2008.

[113] *L. Le Boucher, D. Villani, P. Marty*, Linear-induction electromagnetic machine with optimized magnetic flux distribution and use, U.S. Patent 5415529, 1995.

[114] *S. Cho, S. H. Hong*, The magnetic field and performance calculations for an electromagnetic pump of a liquid metal, Journal of Physics 31 (1998) 2754-2759.
[115] *K. V. Namjoshi, P. P. Biringer*, Analysis of magnetic field in linear induction pumps with extended teeth, IEEE Transactions on magnetics, Vol. Mag-19, No. 5, September 1983.
[116] *G. Vinsard, B. Laporte, N. Takorabet*, An analysis of the rotational forces in the secondary of an electromagnetic pump, IEEE transactions on magnetics, Vol. 34, No. 5, September 1998.
[117] *L. Leboucher, D. Villani*, Slot design of optimized electromagnetic pump, IEEE Transactions on magnetics, Vol. 29, No. 6, November 1993.
[118] *L. Leboucher, P. Boissonneau*, Channel shape optimization of electromagnetic pumps, IEEE Transactions on magnetics, Vol. 31, No. 3, May 1995.
[119] *E. Gierczak, E. A. Mendrela, E. M. Mendrela*, Calculation of an electromagnetic field in a three-phase induction pump with a compensating winding, IEEE Transactions on magnetics, Vol. 29, No. 5, September 1993.
[120] *H. Ota, K. Katsuki, M. Funato, J. Taguchi, A. W. Fanning, Y. Doi, N. Nibe, M. Ueta, T. Inagaki*, Development of 160 m^3/min large capacity sodium-immersed self-cooled electromagnetic pump, Journal of Nuclear Science and Technology, Vol. 41, No. 4, p. 511-523, April 2004.
[121] *A. Oto, N. Naohara, M. Ishida, T. Kuroki, K. Katsuki, R. Kumazawa*, Sodium-immersed self-cooled electromagnetic pump design and development of a large-scale coil for high temperature, Journal of Nuclear Technology, Vol. 110, Issue 2, pp. 159-167, May 1995.
[122] http://www.cea.fr/energie/astrid-une-option-pour-la-quatrieme-generation
[123] *A. Fanning, G. Kliman, W. Kwant, L. Dahl, T. Inagaki, M. Ueta, N. Nibe, H. Ota, K. Katsuki, Y. Doi, I. Maekawa*, Giant electromagnetic pump for sodium cooled reactor applications, Journal of Nuclear Technology, 2003.
[124] *A. Homsy, V. Linder, F. Lucklum, N. F. de Rooij*, Magnetohydrodynamic pumping in nuclear magnetic resonance environments, sensors and Actuators B 123 (2007) 636-646.
[125] *J. Zhong, M. Yi, H. H. Bau*, Magneto hydrodynamic (MHD) pump fabricated with ceramic tapes, sensors and Actuators A 96 (2002) 59-66.
[126] *A. V. Lemoff, A. P. Lee*, An AC magnetohydrodynamic micropump, Sensors and Actuators B 63 (2000) 178-185.
[127] *V. Singhal, S. V. Garimella*, Induction electrohydrodynamics micropump for heat flux coolging, Sensors and Actuators A, 2006.
[128] *H. R. Kim*, Design and experimental characterization of an EM pump, Journal of the Korean Physical Society, Vol. 35, No. 4, pp. 309-214, Octomber 1999.
[129] *G. S. Park, S. H. Park*, design of magnetic fluid linear pump, IEEE Transactions on magnetics, Vol. 35, No. 5, September, 1999.
[130] *S. Kikuchi, K. Murakami*, Behavior of a new DC electromagnetic pump using superconducting magnet, IEEE Transactions on magnetics, Vol. Mag-13, No. 5, September 1977.
[131] *P. Del Vecchio, A. Geri, G. M. Veca*, Superconducting magnets for electromagnetic DC pumps, IEEE Transactions on magnetics, Vol. Mag-21, No. 2, March 1985.
[132] *I. Bucenieks*, Perspectives of increasing efficiency and productivity of electromagnetic induction pumps for mercury basing on permanent magnets, Proceedings of ICONE14 International Conference on Nuclear Engineering, 2006.
[133] *C. Roman*, Studies of the annular linear induction pumps for sodium circuits use in nuclear plants, Proceedings of International Youth Conference on Energy, IEEE Catalog Number: CFP1335J-USB (pendrive); ISBN 978-1-4673-5554-4 (pendrive), Siofok, Hungary, 2013.
[134] *C. Roman, M. Dumont, Y. Fautrelle, V. Fireteanu, S. Vitry, F. Rey*, Study of the influence of traveling field frequency and wave length on pressure – flow rate

characteristic and modeling of MHD coupling in annular linear induction pump, Journal of Iron and Steel Research International, Vol. 19, pp. 463-466, 2012.

[135] ***C. Roman, M. Dumont, S. Letout, C. Courtessole, S. Vitry, F. Rey, Y. Fautrelle*****, Modeling of fully coupled MHD flows in large size annular linear induction pumps, Proceedings of International Conference on Heating by Electromagnetic Sources (HES), Padua, Italy, May 2013.**

[136] *M. Butzek, I. Bucenieks*, Proposed mercury pump for ESS, Proceedings of 16th Meeting of the International Collaboration on Advanced Neutron Sources, Düsseldorf-Neuss, 2003.

[137] *C. I. Mocanu*, Theory of electromagnetic field (in Romanian language), Technical Press, Bucharest, 1979.

[138] *V. Fireţeanu*, Sensors and transducers (in Romanian language), Printech Press, Bucharest, 2006.

[139] *E. C. Gh. Isbãşoiu, S. C. Georgescu*, Fluid mechanics (in Romanian language), Techincal Press, ISBN 973-31-0841-3, Bucharest, 1995.

[140] *R. Temam*, Navier-Stokes equations. Theory and numerical analysis, North-Holland Publishing Company, ISBN: 07204 2840 8, 1977.

[141] *L. Dragoş*, Magnetodynamics of fluids, Academy Press, Bucharest, 1969.

[142] *H. Hasuike, Y. Yoshizawa, A. Suzuki, Y. Tamaura*, Study on design of molten salt solar receivers for beam-down solar concentrator, Solar Energy 80 (2006) 1255-1262.

[143] *O. Garbrecht, F. Al-Sibai, R. Kneer, K. Wieghardt*, CFD-simulation of a new receiver design for a molten salt solar power tower, Solar Energy 90 (2013), 94-106.\

[144] *M. Yang, Xiaoxi Yang, Xiaoping Yang, J. Ding*, Heat transfer enhancement and performance of molten salt receiver of a solar power tower, Applied Energy 87 (2010) 2808-2811.

[145] *Xiaoping Yang, Xiaoxi Yang, J. Ding, Y. Shao, H. Fan*, Numerical simulation study on the heat transfer characteristics of the tube receiver of the solar thermal power tower, Applied Energy 90 (2012) 142-147.

[146] http://en.wikipedia.org/wiki/Molten_salt_reactor

[147] http://www.eere.energy.gov/basics/renewable_energy/power_tower.html

[148] http://www.archimedesolarenergy.com

[149] FLUX 10.4 User Guide

[150] *Y. Chikazawa, Y. Okano, T. Hori, Y. Ohkubo, Y. Shimakawa, T. Tanaka*, A feasibility study on a small sodium cooled reactor as a diversified power source, Journal of Nuclear Science and technology, Vol. 43, No. 8, p. 829-843 (2006).

[151] *A. Alemany, Ph. Marty, F. Plunian, J. Soto*, Experimental investigation of dynamo effect in the secondary pumps of the fast breeder reactor Superphenix, Jounal of Fluid Mechanics, Vol. 403, pp. 263-276, 2000.

[152] *Y. Su, W. Chen, F. Cui, W. Zhang*, Analysis and fabrication process of an electromagnetically actuated valveless micropump with two parallel flexible diaphragms, Journal of Mechanical Engineering, Vol. 219, pp. 1007-1014, 2005.

[153] *H. Mitsui*, Progress in Japan in electrical insulation at high temperatures, IEEE Electrical Insulation Magazine, Vol. 12, No. 3, pp. 16-27, June 1996.

[154] ***C. Roman, V. Fireteanu, S. Vitry, F. Rey*****, Transient magnetic — Translating motion finite element model of the Annular Linear Induction Pump, Proceedings of International Conference on Applied and Theoretical Electricity, pp. 40-45, 2012.**

[155] ***C. Roman, V. Fireteanu, Y. Fautrelle, M. Dumont, S. Vitry, F. Rey*****, Study of the electromagnetic phenomena in the annular linear induction pump based on 3D finite element models, Proceedings of 8th International Symposium on Advanced Topics in Electrical Engineering, IEEE Catalog Number CFP1314P-CDR, ISBN 978-1-4673-5978, Bucharest, 2013.**

[156] *G. Preda*, Electromagnetic field of moving bodies (PhD Thesis in Romanian language at POLITEHNICA University of Bucharest), 1998.
[157] *N. Kleinknecht, S. A. Halvorsen*, High frequency magnetohydrodynamic calculations in COMSOL Multiphysics, Proceedings of the COMSOL Conference, Stuttgart, 2011.
[158] *B. Knaepen, S. Kassinos, D. Carati*, MHD turbulence at moderate magnetic Reynolds number, in annual Research Briefs of the Center for Turbulence Research, pp. 449-460, 2003.
[159] *O. D. Makinde*, On MHD boundary-layer flow and mass transfer past a vertical plate in a porous medium with constant heat flux, Engineering Papers and Reports, paper 13, http://dk.cput.ac.za/eng_papers/13, 2009.
[160] *R. Moreau, S. Smolentsev, S. Cuevas*, MHD flow in an insulating rectangular duct under a non-uniform magnetic field, PMC Physics B 2010 3:3.
[161] *A. Thess, D. Krasnov, T. Boeck, E. Zienicke, O. Zikanov, P. Moresco, T. Alboussière*, Transition to turbulence in the Hartmann boundary layer, GAMM-Mitt. 30, No. 1, 125-132, 2007.
[162] *R. Griesse, K. Kunisch*, Optimal control for a stationary MHD system in velocity-current formulation, http://www.ricam.oeaw.ac.at/people/page/griesse, http://www.kfunigraz.ac.at/imawww/kunisch.
[163] *D. Biskamp*, Magnetohydrodynamic turbulence, Cambridge University Press, Cambridge, 2003.
[164] *D. S. Krasnov, E. Zienicke, O. Zikanov, T. Boek, A. Thess*, Numerical study of the instability of the Hartmann layer, Journal of Fluid Mechanics, Vol. 504, pp. 183-211, 2004.
[165] *M. Wosnik, L. Castillo, W. K. George*, A theory for turbulent pipe and channel flows, Journal of Fluid Mechanics, Vol. 421, pp. 115-145, 2000.
[166] *D. P. Lathrop, W. L. Shew, D. R. Sisan*, Laboratory experiments on the transition to MHD dynamos, Institute of Physics Publishing, plasma Physics and Controlled Fusion 43 (2001) A151-A160.
[167] *R. Samulyak, J. Du, J. Glimm, Z. Xu*, A numerical algorithm for MHD of free surface flows at low magnetic Reynolds numbers, Journal of Computational Physics 226 (2007) 1532-1549.
[168] *M. Narula, A. Ying, M. A. Abdou*, A study of liquid metal film flow under fusion relevant magnetic fields, Fusion Science and Technology, Vol. 47, pp. 564-568, April 2005.
[169] *V. Yakhot, S. A. Orszag, S. Thangam, T. B. Gatski, C. G. Speziale*, Development of turbulence models for shear flows by a double expansion technique, Physics of Fluids A, Vol. 4, No. 7, pp. 150-1520, 1992.
[170] *K. H. Spitzer, M. Dubke, K. Schwerdtfeger*, Rotational electromagnetic stirring in continuous casting of round strands, Metalurgical Transactions B, Vol. 178, pp. 119-131, 1986.
[171] *P. A. Davidson, F. Boysan*, The importance of secondary flow in the rotary electromagnetic stirring of steel during continuous casting, Applied Scientific Research, Vol. 44, pp. 241-259, 1987.
[172] *H. K. Moffatt*, Electromagnetic stirring, Journal Physics of Fluids A, Vol. 3, No. 5, pp. 1336-1343, 1991.
[173] *K. Fujisaki, T. Ueyama*, Magnetohydrodynamic calculation of in-mold electromagnetic stirring, IEEE Transactions on Magnetics, Vol. 33, No. 2, pp. 1642-1645, 1997.
[174] *N. El-Kaddah, T. T. Natarajan*, Electromagnetic strring of steel: Effect of stirrier design on mixing in horizontal electromagnetic stirring of steel slabs, Proceedings of Second International Conference on CFD in the Minerals and Process Industries (CSIRO), pp. 339-344, Melbourne, Australia, 1999.

[175] *L. B. Trindade, A. C. F. Vilela, A. F.F. Filho, M. T. M. B. Vilhena, R. B. Soares*, Numerical model of electromagnetic stirring for continuous casting billets, IEEE Transactions on Magnetics, Vol. 38, No. 6, 2002.
[176] *R. M. Khristinich, V. N. Timofeyev, V. V. Stafievskaya, A. V. Velenteyenko*, Molten metal electromagnetic stirring in metallurgy, Proceedings of International Scientific Colloquium Modeling for Electromagnetic Processing, pp. 29-36, Hannover, 2003.
[177] *S. Y. Lin, S. K. Kuo*, Electromagnetic force predictions of a stand electromagnetic stirring system using an analytical model, China Steel Technical Report, No. 21, pp. 29-33, 2008.
[178] *G. Zhu, J. Xu, Z. Zhang, Y. Bai, L. Shi*, Annular electromagnetic stirring – a new method for the production of semi-solid A357 aluminum alloy slurry, Acta Metallurgica Sinica (English Letters), Vol. 22, No. 6, pp. 408-414, 2009.
[179] *K. Stransky, F. Kavicka, B. Sekanina, J. Stetina, J. Dobrovska, L. Stransky*, Electromagnetic stirring of the melt of concast billets and its importance, Journal of Metal 2009.
[180] *K. Stransky, F. Kavicka, B. Sekanina, J. Stenina, V. Gontarev, J. Dobrovska*, The effect of electromagnetic stirring on the crystallization of concast billets, Materials and Technology Vol. 45, No. 2, pp. 163-166, 2011.
[181] *R. Ya. Yakobshe, A. A. Kuchaev, V. L. Naidek, A. C. Nogovitsin, G. I. Kasyan, V. A. Belyi*, Influence of electromagnetic stirring of steel on the mold on solidification processes of billets 150 x 150 mm, Metallurgical and Mining Industry, Vol. 4, No. 1, 2012.
[182] *O. Tollerfield*, Start-up of new electromagnetic system for displacement of liquid aluminum, Light Metals 2005 edited by Halvor Kvande TMS (The Minerals, Metals & Materials Society, pp. 867-872, 2005.
[183] *G. Guest, S. Williams, P. Gastaldi*, Development of a new generation electromagnetic metal moving system, Light Metals 2012 edited by Carlos E. Suarez TMS (The Minerals, Metals & Materials Society), pp. 1013-1018, 2012.
[184] *C. Mapelli, A. Gruttadauria, M. Peroni*, Application of electromagnetic stirring for the homogenization of aluminum billet cast in a semi-continuous machine, Journal of Materials Processing Technology, Vol. 210, pp. 306-314, 2010.
[185] *E. Sauvage, A. Gagnoud, Y. Fautrelle, P. Brun, J. Lacombe*, Thermoconductive instabilities of molten glass heated by direct induction in a cold crucible, Proceedings of International Scientific Colloquium Modelling for Electromagnetic Processing, Hannover, 2008.
[186] *D. Hülsenberg, B. Halbedel, G. Conrad*, Electromagnetic stirring of glass melts using Lorentz forces – Experimental results, Journal of Glass Science and Technology, Vol. 77, No. 4, 2004.
[187] *U. Krieger, B. Halbedel D. Hülsenberg, A. Thess*, Homogenisation of electrically heated glass melts by Lorentz forces, Proceedings of International Congress of Theoretical and Applied Mechanics (ICTAM), Warsaw, Poland, 2004.
[188] *U. Krieger, B. Halbedel D. Hülsenberg, A. Thess*, Electromagnetic effects on glass melt flow in crucibles, Journal of Glass Science and Technology A, Vol. 49, pp. 33-40, 2008.